LBL-21951 c.2

Lawrence Berkeley Laboratory

UNIVERSITY OF CALIFORNIA

Materials & Molecular Research Division

RECEIVED
LAWRENCE
BERKELEY LABORATORY

OCT 16 1986

LIBRARY AND
DOCUMENTS SECTION

THERMOCHEMICAL PROPERTIES OF GROUP IVB AND VB TRANSITION METAL ALLOYS WITH PLATINUM GROUP METALS: ACID-BASE STABILIZATION

M.J. Cima
(Ph.D. Thesis)

July 1986

TWO-WEEK LOAN COPY

This is a Library Circulating Copy which may be borrowed for two weeks.

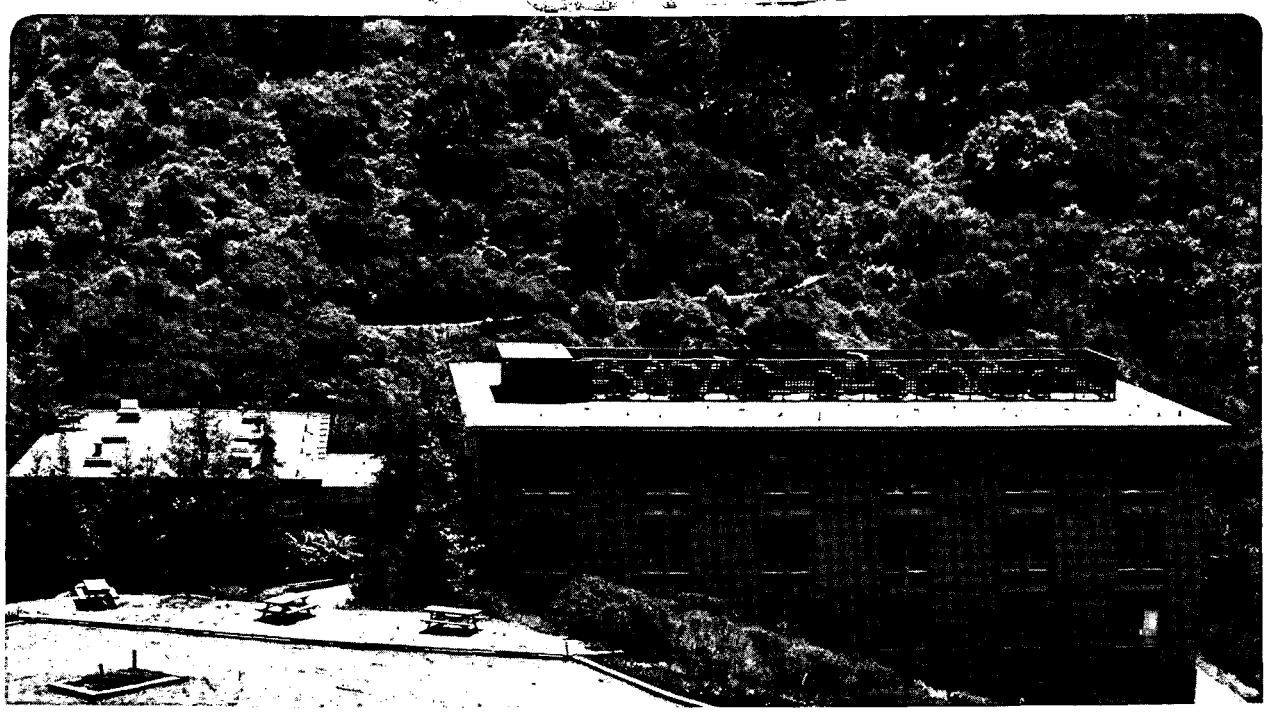

LBL-21951 c.2

Prepared for the U.S. Department of Energy under Contract DE-AC03-76SF00098

DISCLAIMER

This document was prepared as an account of work sponsored by the United States Government. While this document is believed to contain correct information, neither the United States Government nor any agency thereof, nor the Regents of the University of California, nor any of their employees, makes any warranty, express or implied, or assumes any legal responsibility for the accuracy, completeness, or usefulness of any information, apparatus, product, or process disclosed, or represents that its use would not infringe privately owned rights. Reference herein to any specific commercial product, process, or service by its trade name, trademark, manufacturer, or otherwise, does not necessarily constitute or imply its endorsement, recommendation, or favoring by the United States Government or any agency thereof, or the Regents of the University of California. The views and opinions of authors expressed herein do not necessarily state or reflect those of the United States Government or any agency thereof or the Regents of the University of California.

LBL-21951

Thermochemical Properties of Group IVB and VB Transition Metal Alloys with Platinum Group Metals : Acid-Base Stabilization

Michael John Cima

Materials and Molecular Research Division

Lawrence Berkeley Laboratory

and Department of Chemical Engineering

University of California

Berkeley, CA 94720

ABSTRACT

Solid-state galvanic cell measurements and oxide equilibration experiments are used to derive thermochemical quantities for a variety of acid-base stabilized alloys such as Nb-Pd, Nb-Rh, Ti-Pd, and Ti-Rh. The experiments have effectively resulted in the titration of palladium by niobium metal. The excess partial molar Gibbs energy of niobium at infinite dilution was determined to be -62 kcal/mole at 1000° C and the Gibbs energy of formation of $NbPd_{3.55}$ is -42 kcal/mole. These results and those for the other systems are used to assess the importance of crystal field effects in the context of the generalized Lewis acid-base theory.

The ternary phase diagrams for the Pd-Nb-O and Rh-Nb-O systems were obtained from the characterization of samples equili-

brated at 1000° C. Powder X-ray diffraction patterns were measured for several equilibrium oxides that are substoichiometric of Nb_2O_5 and are found to be consistent with crystal structures previously determined from single crystals of similar composition. An improved method was developed for composition measurements of binary metallic alloy grains using energy dispersive X-ray analysis and a scanning electron microscope.

The effects of different processing methods were also explored in the preparation of optically transparent yttria doped thoria (YDT) pellets, and techniques for the preparation of reliable YDT solid electrolytes are presented.

Acknowledgements

My deepest appreciation goes to the University of California, the staff of the Materials and Molecular Research Division at Lawrence Berkeley Laboratory, and the faculty and students of the Chemistry and Chemical Engineering Departments at U.C. Berkeley. I would also like to thank Prof. Leo Brewer for the guidance that has made this work possible and for inspiring a passion in me for the study of science and nature. I am fortuante to be among the countless number of students he has touched with his charm, never ending optimism, and keen insight.

I am indebted to my family for their support, especially my father and mother who have always been there when times were tough. A special thanks goes to my wife, Linda, for her love and faith. Lastly, I acknowledge my grandfather for teaching me to wonder how things work.

This work was supported by the Director, Office of Energy Research, Office of Basic Energy Sciences, Materials Sciences Division, U.S. Dept. of Energy under contract number DE-AC03-76SF00098.

Contents

Chapter 1

Acid-Base Stabilized Transition Metal Alloys

1.1 Introduction
1.2 Technical Importance
1.3 Transition Metal Valence Bond Model
1.4 Generalized Lewis Acid-Base Theory
1.5 Experimental Methods

Chapter 2

Experimental Methods for the Preparation and Characterization of Oxide-Alloy Equilibria

2.1 Introduction
2.2 Starting Materials
2.3 Consolidation and Hot Pressing
2.4 Sample Annealing
2.5 X-ray Diffraction
2.6 Polishing
2.7 Alloy Composition Measurement
2.8 Scanning Auger Microscopy

Chapter 3

Experimental Methods for the Measurement of Galvanic Voltages Generated by a Solid-State Cell

3.1 Principles of Operation
3.2 Defect Structure of Solid Oxide Electrolytes
3.3 Cell Kinetics
3.4 Arrangement of the Cell
3.5 Control and Measurement
3.6 Electrode Preparation and Polishing
3.7 Cell Operation

Chapter 4

Preparation of Transparent Yttria doped Thoria and the Preparation of Solid Electrolyte for use in High Temperature Galvanic Cells

4.1 Introduction
4.2 Attempts at Hot Pressing
4.3 Optimization of the Oxalate Precipitation Method
4.4 Electrolyte Prepared from Stock Powders
4.5 Performance of Electrolytes

Chapter 5

Observation and Conclusions

5.1 Palladium Alloy and Niobium Oxide Equilibration
5.2 Rh-Nb-O,Pd-Ti-O, and Rh-Ti-O Equilibration
5.3 Galvanic Cell Measurements
5.4 Results for Thermochemical Quantities
5.5 Discussion
5.6 Conclusions

Appendix 1

Calculation of X-ray Powder Diffraction Patterns

Appendix 2

Computer Programs

Chapter 1

Acid-Base Stabilized Transition Metal Alloys

1.1 Introduction

Transition metals are playing an ever increasing role in technology today, especially in areas that involve high temperatures or chemically reactive species. Thermochemistry plays an important part in predicting alloy behavior under a variety of conditions. In order to use it effectively, though, one has to adopt an approach that has some physical or chemical basis because a purely empirical one could not hope to yield information on all possible multicomponent alloys. This study focuses on the unusual stability of alloys from group IVB and VB metals with platinum group metals. Some of their intermetallic compounds have heats of formation in excess of -120 kcal/mole.

The strength of these interactions is remarkable. For comparison consider the heat released per hafnium atom when it is dissolved in an excess of carbon,

$$\mathrm{Hf} + \mathrm{C} = \mathrm{HfC} \qquad \Delta H^{\circ}_{298} = -58\mathrm{kcal/mole} \tag{1-1}$$

but when hafnium is dissolved in an excess of platinum

$$\mathrm{Hf} + 3\mathrm{Pt} = \mathrm{HfPt_3} \qquad \Delta H^{\circ}_{298} = -135\mathrm{kcal/mole}\ [4] \tag{1-2}$$

One normally considers carbides as rather stable compounds, so it is very surprising that an alloy has such greater stability. It is even more surprising when one considers that this compound of hafnium, when compared to other hafnium compounds, is second only in stability to hafnium oxide and hafnium

fluoride. The reaction in equation (1-2) is known to proceed at an explosive rate [1].

Although the hafnium platinide example was written as a compound, these materials exhibit many of the physical attributes that we normally associate with alloys. In particular, they show rather large variable composition regions. The phase diagram for the Nb-Pd system is shown in figure (1-1). In addition to the large mutual solubilities of the metals in bcc niobium and fcc palladium there are significant amounts of nonstoichiometry in the intermetallic phases. Considering the large heats of solution that are observed, the solutions that comprise the single phase regions of the diagram are extremely nonideal.

Brewer's theory [2], introduced some years ago, seeks to explain these strong interactions by the ability of the d-electron rich platinum group metals to share electrons with the hypo-electronic d-orbitals on the IVB and VB metals. The model proposes that the interaction is completely analogous to the Lewis acid-base concept used for nontransition elements.

Solution theories for metallic systems without strong chemical interactions between the constituent metals have been used successfully to understand their solution behavior. These methods model physical interactions between the metals such as internal pressure differences or the strain resulting from the size difference between atoms in the solid. These types of interactions are small in magnitude compared with the negative energies described above. No quantitative theory has yet been devised to make useful predictions on the stability of alloys of group IVB and VB transition metals with the platinum group. Clearly, the sign and magnitude of the heats involved in these alloys indicates that a chemical bonding description is appropriate. This study has revealed the effect

of several important aspects of the Lewis acid-base description in these alloys and thus has improved the predictive ability of this theory.

1.2 Technical Importance

Besides the obvious scientific interest in these alloys, there is growing technical interest. One well noted example is the reaction between platinum and ceramic insulators in high temperature thermocouples when used in reducing atmospheres [3]. Brewer's model indicates that d-electron bonding indirectly determines the s,p electron concentration, which has been shown to correlate well with substitutional diffusion coefficients in metals [4]. These alloys show extreme inertness toward oxidation at high temperatures [5] and are being considered for use as protective coatings.

In the area of catalysis there is great interest in what are called "metal-support interactions", which refers to the ability of some ceramic supports to influence the catalytic properties of platinum group catalysts. The methanation rate of CO and hydrogen is as much as 1000 times higher when a rhodium catalyst is supported on TiO_2 compared to when it is supported on SiO_2. The refractory oxides of the other IVB and VB are also known to influence reaction rates. There is evidence that the effect results from oxide creeping onto the platinum metal surface and somehow influencing the sites available for reaction or by directly taking part in the reaction. In view of the fact that the metals form extremely stable alloys it is not surprising that the platinum group metal and the IVB or VB oxide form a low energy interface that provides the driving force for the oxide to cover the catalyst' surface. It is possible that titanium atoms at the oxide alloy interface bond with both the platinum metal and oxygen which

results in the low energy interface.

The high stability of these alloys has been exploited recently to bond platinum to a silicon oxide substrate. The Pt–SiO_2 interface has rather poor adhesion characteristics but platinum is a convenient choice for conductors on VLSI devices that must undergo high temperatures during fabrication. Significant improvement has been achieved in bonding platinum to the SiO_2 surface by first depositing a thin film of Hf, Zr, or Ta followed by the platinum conductor [6]. When heat treated, the hafnium will react at the SiO_2 interface to form hafnium oxide and at the other interface it forms the very stable platinum intermetallic. The platinum is thus effectively glued to the substrate.

The IVB-VB, Pt group alloys have their analogs among the actinide-Pt alloys, which are also characterized by extremely high thermodynamic stability. Wijbenga [8] has measured the heat of formation of UPd_3 to be -130 kcal/mole. The fission products in spent nuclear fuel include large amounts of rhodium and palladium which will react with both the fuel and cladding materials [7]. Thermochemical models would be a great help in predicting the chemical integrity of these fuels and designing reprocessing schemes. The U.S. currently imports virtually all its supply of Rh and Pd. It has been proposed to recover these metals and Ru from spent nuclear fuel by extraction with molten lead [9] during the same process used to encapsulate the spent fuel in glass for long term storage. The process design must take into consideration the very low chemical activity of the platinum group metal in the fuel. Predictive models will greatly aid in understanding the chemistry of these complicated solid solutions.

1.3 Transition Metal Valence Bond Model

The electronic configuration of a metal in the solid state is not the same as that for the gaseous atom since upon condensation it may exploit bonding energy to make up for any energy needed for promotion to excited states. Brewer has reviewed [2] the successful assignment of the valence state in a metal to predict the crystal structures of all the d-bonded metals in the periodic chart where atomic spectra are known.

This point is best illustrated by an example. The gaseous ground state of Mg is the s^2 electronic configuration. If Mg were to remain in this configuration as it condensed the solid could only be held together by van der Waals bonding, because the Pauli exclusion principle forbids the overlap of the filled s orbitals. The promotion energy needed to excite the Mg atoms into the sp- electronic configuration is more than made up by the energy released upon the now allowed bonding in the solid. The same can be said for tungsten which has the gaseous ground state of d^4s^2. Promotion to the d^5s configuration leaves it with six bonding electrons instead of four.

The Engel-Brewer theory, as it is referred to, states that the crystal structure correlates with the concentration of s and p-electrons in the solid. The d-electrons indirectly influence the structure by providing a portion of the bonding energy needed to support a given sp-electron configuration. They examined the crystal structures of alloy systems where bonding could only be due to sp-electrons and assigned appropriate limits to the sp-electron concentration needed for the various crystal structures to be stable. The bcc crystal structure was shown to correlate with electron configurations from $d^{n-1}s$ to $d^{n-1.5}sp^{0.5}$ where n is the total number of valence electrons. The hcp and fcc crystal

structures correlate with $d^{n-1.7}sp^{0.7}$ to $d^{n-2.1}sp^{1.1}$ and $d^{n-2.5}sp^{1.5}$ to $d^{n-3}sp^{2}$, respectively.

These assignments were used to predict the thermodynamic stabilities of transition metals in the bcc and hcp crystal structures even when these structures are not observed for the pure element. To do this, estimates had to be made of the bonding energy of sp and d-orbitals. From the known heats of atomization of bcc and hcp transition elements and the relative energies of the atomic electron configurations $d^{n-1}s$, $d^{n-2}sp$, and $d^{n-2}s^{2}$ (obtained from atomic spectroscopy), a Born-Haber type cycle could be constructed to abstract the bonding energy for each electronic configuration. By assuming that the bonding ability of sp-orbitals varies in a smooth way across the transition series they could assign the bonding energy per d-electron.

The results of the analysis are shown in figure (1-2) for the 4d transition series. Note that the bonding ability of the d-orbitals is independent of crystal structure, enabling one to draw a curve that can be used to predict stability of phases that have not yet been observed. The predictions thus made have been shown to correctly predict the stable crystal structures of all the transition metals where atomic spectra are known [10].

A prominent feature of figure (1-2) is the significant decrease in the bonding energy of a d-electron to a minimum when five d-electrons are used per atom. As one moves further to the right in the transition series the excess electrons must be internally paired and cannot be used in bonding. This means that the average number of d-bonds per atom decreases and the bonding ability per d electron rises again. The total number of bonds, however, decreases past a maximum of five d-bonds per atom, which accounts for the decreasing internal

pressures of the elements to the right of the column which includes technetium. The decrease in bonding ability with increasing number of d-bonds can be attributed to two factors. There may be interference between the d bonds as they must be accommodated around the atom.

Another consideration, that will be shown to be important in acid-base stabilized alloys, is the fact that not all d-orbitals are the same because of the crystal field effect. When an atom is placed in a non spherically symmetric field, as in the crystal, the d-orbitals split in energy. Thus some of an atom's d-orbitals are more extended in real space because they are relatively higher in energy. This extension in space means that some of an atom's orbitals will have greater overlap with orbitals on neighboring atoms and therefore will yield a larger amount of bonding energy. The internally paired electrons are situated in the orbitals least available for bonding so that the bonding stabilization is maximized. The minimum occurs in figure (1-2) because as the number of unpaired d-electrons increases the bonding per d-electron is averaged over bonds that include progressively poorer d-bonding orbitals.

Similar variation of d and sp-bonding with number of unpaired d- electrons exists for the 3d and 5d transition elements [10]. The differences that do exist show that, as with the non-transition elements, the bonding ability of the sp-electrons decreases as one goes down a column in the periodic chart. Just the opposite trend, however, is observed with the average d-bond energy. The difference in trends can be attributed to the difference in orbital angular momentum between the s,p and d-orbitals. As one goes down a column in the transition series, atoms expand due to the increasing number of filled valence shells. Because of their lower angular momentum, the sp-electrons feel the

increasing nuclear charge more than the d-electrons. Thus the d-orbitals become more extended relative to the filled sp-orbitals of the core and may overlap better with neighboring atoms. It is for this reason that the melting and boiling points increase as one descends a column in the transition series while the opposite is true in the nontransition elements.

The role of the crystal field effect in the 3d metals is particularly important. In these metals, the d-orbitals are so split in energy that even orbitals that have unpaired electrons are localized enough to prevent them from bonding with neighboring atoms. These unpaired electrons cause the magnetism that occurs in the 3d metals.

A valence bond description of the electronic states in a metals can be consistent with the existence of bands of states with in the solid. All that is required is that states with in these bands maintain the character of that atomic valence state deemed most important by bonding considerations, eg. extent of d-character. The connection between atomic states and band structure is frequently made when referring to various features of transition metal bands such as the broad s and p bands and the narrow d-band so it is reasonable that these features would be correlated with realistic valence states. The atomic valence state is correlated to the electronic states of the condensed phase bands which in turn determines the bonding enthalpy of the crystal. Thus even though electronic states in the condensed phase are bands, a correlation between atomic valence state and bonding enthalpy will be maintained.

Some properties such as electrical conductivity and paramagnetism depend on the density of states at the Fermi level. The bonding energy, however, gives directly the integral over all occupied states within the band. Thus detailed

knowledge of the density of states at any particular energy is not needed.

Valence state descriptions such as $d^{n-1}s$ and $d^{n-2}sp$ are not single states even in the gaseous atoms. There are a variety of combinations of spin and orbital angular momenta of the electrons that correspond to different spectroscopic states and yet still have the correct contributions of atomic orbitals, [1,2]. Each of these states has a slightly different energy; thus even in the gaseous atom the state description occupies a band of energies.

1.4 Generalized Lewis Acid-Base Theory

Lewis acid-base reactions are those whose driving force is provided by the sharing of internally paired electrons on one species with energetically appropriate vacant orbitals on another species. The stability of the gaseous dimer of ammonia and boron triflouride observed in the reaction

$$BF_3 + NH_3 = F_3B{\cdot}NH_3 \tag{1-3}$$

is the result of ammonia's nonbonding electron pair being shared with the empty p orbital on boron.

The acid-base interaction in transition metal alloys occurs because internally paired d-electrons on one element may be shared with vacant d-orbitals on another. Metals of the platinum group have an excess number of electrons so they must be internally paired. Rhodium, for example, has the d^8s ground state for the gaseous atom, which has six internally paired d-electrons. The significant promotion energy required to obtain the d^6sp^2 is made up by an increase from three bonds per atom in the original electronic state to seven in the excited state. The d^6sp^2 state, characteristic of fcc metals, still has one internal pair that may not be used in the pure metal for bonding. The group IVB and VB

metals, on the other hand, are electron deficient and have vacant d- orbitals. Niobium has five valence electrons so that in the bcc metal the most significant electronic state is d^4s, thus it has one empty d-orbital and five bonds per atom.

The situation is depicted in figure (1-3), where boxes are drawn to represent the different orbitals on each of the atoms. Four of the boxes represent the one s and three p orbitals while the remaining five correspond to the five d-orbitals. The electron configuration in the solid is represented by arrows in the appropriate boxes. The $NbRh_3$ phase is known to have an ordered crystal structure based on an fcc lattice; therefore, the average sp-electron configuration in this alloy must be sp^2. The average number of electrons per atom in the alloy is eight, so that after three are used for the sp contribution five are left to be used in the d-bonds. The alloy electron configuration is also shown in figure (1-3), where it is clear that there are now eight bonding electrons per atom. The average for the two pure metals was $0.25*5 + 0.75*7 = 6.5$; the alloy thus has 1.5 bonding electrons per atom more than the pure metals. The additional bonding is the energy that provides the stability for the intermetallic compound. The niobium went from five to eight bonds per atom and the rhodium went from seven to eight, thus the rhodium has effectively made use of its nonbonding electrons by sharing them with the vacant niobium orbitals.

The bonds formed in the acid-base reaction are not as strong as those formed in the covalent type bonds formed when orbitals with a single electron are used for bonding. This is because a bond formed when two atoms each donate an electron will be stronger than a bond formed with the large amount of charge transfer that may be produced when a single atom brings both

electrons. If the heats were equivalent for the two type of bonds, figure (1-2) would suggest that the heat of formation of this compound would be approximately 3*(-28) = -84 kcal/mole while the experimental heat of formation is closer to -50 [11].

The clarification of the factors that influence the strength of these acid-base bonds is the major motivation for this study. Reliable thermochemical data suitable for establishing quantitative trends exist for only a few systems. Several qualitative trends are already known, however, the most striking of which is the dramatic increase in acid-base bonding ability as one goes down a column in the transition series. The 3d compound, $TiNi_3$, is known to have a heat of formation of approximately -30 kcal/mole [12] while its 5d analog, $HfPt_3$, has a heat of formation of -135 kcal/mole [4]. This trend results from the same effect which increases the strength of covalent d-bonding in the pure metals as a column is descended. The relative extension of the d-orbitals increases down the column so that overlap is greater with orbitals on neighboring atoms. This increases the ability of the base to share the nonbonding pair and strengthens the resulting bond.

The trend as one moves across a given transition series is more complicated because it is the result of several opposing effects. Wengert and Brewer [19] were able to establish limits on the relative basicity of the platinum group metals by the study of the phase equilibria in ternary zirconium-carbon phase diagrams. They used the excess partial molar Gibbs energy of zirconium at infinite dilution as the measure of the basicity. Their results, as extended by Gibson [16], are shown in figure (1-4). Note that although $\Delta\overline{G}^{xs}_{Zr,x_{Zr}=0}$ could not be unambiguously determined in most cases, definite limits could be presented. The results

clearly show that there is a maximum in the basicity as one proceeds across the platinum group.

The maximum in basicity across a transition series can be rationalized as the result of two effects. First, as one moves to the right across the platinum group, more electrons must be internally paired and may be used in acid-base bonding. Based on this effect alone, one would expect that atoms farther to the right in the series would be better bases. With increasing atomic number, however, there is an increase in nuclear charge which causes a contraction of the d-orbitals. This contraction decreases the degree to which the d-orbitals may overlap with orbitals on neighboring atoms. This trend, of course, decreases the basicity and is the reason silver and gold are such poor bases. It is interesting to note that for the acids the two trends support one another; zirconium has one more empty d- orbital than niobium and it has a lower nuclear charge so that these orbitals are also more expanded.

The role of the crystal field effect in these alloys has not been resolved. Its influence is so important in the pure metals that it seems unlikely that it should not be considered in alloys. One would expect that different nonbonding pairs on the same atom would have different degrees of overlap with neighboring atoms. Thus palladium with one more electron that rhodium and four internally paired electrons is effectively a polyfunctional base. Each one of its base functions has different degrees of basicity because each occupy orbitals split a different amount by the crystal field effect.

The experiments in this study are designed to carry out a titration of one metal by another just as one titrates H^+ and OH^-. Titrations provide a way of monitoring the extent of the acid-base reaction as a function of concentration.

Changes in the bonding character of the solutions as the concentration changes will separate the contributions of different d-orbitals. The idea is completely analogous to the titration of a polyfunctional aqueous base, where features in the titration curves represent the endpoints for the different functions. If the functional aqueous base, where features in the titration curves represent the endpoints for the different functions. If the acid-base interpretation of the metallic solutions is correct, then we should be able to explain the character of the different base pairs in terms of the effects discussed above.

Most of the experiments that have previously been performed on these alloys to obtain thermochemical data are resticted to a single composition or a very small range of compositions. Several investigators have explored a number of methods to measure activity coefficients as a function of composition. Schaller [13] measured the activity of zirconium in solutions rich in palladium and platinum by equlibria with ZrO_2 and H_2–H_2O mixtures. Meschter and Worrell [3],[14] studied the platinum rich alloys of Zr, Hf, and Ti by solid state galvanic cell measurements. Knudsen cell and mass spectroscopy were used to measure the vapor pressures over several compositions of the titanium and iridium system [15]. Gibson et al.[16] measured the palladium partial pressures above niobium- palladium alloys at three compositions, also using mass spectroscopy and Knudsen cell measurements. Kleykamp [11] used solid state galvanic cells to measure niobium activity in rhodium rich alloys.

These experiments involve either systems for which it is difficult to obtain reliable measurements or have the added complexity, from a theoretical view, of metals from different rows in the periodic chart. Ideally one would like to make measurements on alloys of intermediate stability so that several methods could

be used to verify the results, such as a combination of galvanic cell experiments and direct vapor pressure mesurements at high temperatures. Experiments on the Nb- Rh and Nb-Pd systems offer the possibility of determining the effect of palladium's additional base pair and to see if the crystal field effect is important in acid-base stabilized alloys. Kleykamp's [11] niobium activity measurements must be extended to higher concetrations to make a comparison with the Nb-Pd titration curve that will be determined. Gibson's [16] palladium vapor pressure measurement at $x_{Nb} = 0.18$, although it is at much higher temperature, will provide a good check on the results of our experiments.

1.5 Experimental Methods

The determination of thermodynamic properties of materials at high temperatures is a very difficult task. Two types of experiments have been performed in this study, both of which involve the equilibration of an acid-base stabilized alloy with the oxide of the hypo-electronic element.

Oxide Equilibration

Niobium, titanium, and vanadium have several oxides in their equilibrium phase diagrams. The oxygen phase relationship is quite complicated as seen in figure (1-5) which is the phase diagram for the niobium-oxygen system [17],[18]. Besides the familiar NbO, NbO_2, and Nb_2O_5, there are the many phases sub-stoichiometric to the pentoxide.

The equilibrium of any two of these oxides fixes the activity of both oxygen and the metal. If an alloy of this metal is equilibrated with these two oxides, then the metal activity in the alloy is also fixed to this value. The thermodynamics of these oxides is known; thus, study of the ternary diagrams of these

oxides with the platinum group metals yields information on the alloys.

As an example, consider a sample of NbO and NbO_2 that are in equilibrium. If a small amount of palladium is introduced into the sample, niobium dissolves in the palladium until its activity is the same as that in equilibrium with the two oxides. The following reaction takes place,

$$2NbO = NbO_2 + Nb_{(Pd)} \tag{1-4}$$

and the niobium activity would be determined from

$$0 = \Delta G_{(1-4)} = \Delta \overline{G}_{Nb} + \Delta G_f^{\circ}(NbO_2) - 2\Delta G_f^{\circ}(NbO) \tag{1-5}$$

where $\Delta G_f^{\circ}(NbO_2)$ and $\Delta G_f^{\circ}(NbO)$ are the Gibbs energies of formation of the two oxides and $\Delta \overline{G}_{Nb}$ is the partial molar Gibbs energy of niobium at equilibrium. The activities of niobium can thus be determined at a variety of compositions in palladium or rhodium solution by making use of the many oxides in the Nb-O phase diagram.

The method described above has the disadvantage that the thermodynamics of the oxides determines which alloy composition will be obtained. The activities in the alloy are a unique function of composition so that by fixing the niobium activity with the two oxides, the niobium concentration in the alloy is fixed and data may only be obtained for this composition. This is of course, a result of the Gibbs phase rule. The implications of the phase rule to the ternary diagrams determined in this study will be discussed in chapter 5.

Solid-State Galvanic Cell Measurements

The alloy compositions between those in equilibrium with two oxides will be in equilibrium with a single oxide. The partial pressure of oxygen and the

niobium activity are not fixed but there is a unique relationship between them. As an example, consider an alloy in equilibrium with NbO_2. The relationship between the the niobium activity and the partial pressure of oxygen is given by

$$\Delta G_f^o(NbO_2) = \Delta \overline{G}_{Nb} + RTlnP_{O_2} \tag{1-6}$$

Thus, if the partial pressure of oxygen were measured, the niobium activity could be determined at any composition. These partial pressure measurements are made by the use of a high temperature galvanic cell.

The solid state electrochemical cell used to make these measurements functions because of the unusual ability of certain ceramic materials to conduct oxygen anions at high temperature. Yttria doped thoria (YDT) is just one example of a material that is used for such applications. For the example above a typical cell would have the form

$$Pt/\ Nb_{(Pd)}, NbO_2\ /\ YDT\ /\ NbO_2, Nb_2O_{4.8}\ /\ Pt \tag{1-7}$$

The cathode of the cell has the oxygen partial pressure fixed by the equilibrium of two oxides, so the equation (1-7) can be thought of as a concentration cell where the voltage relates the difference in partial pressure of oxygen. Practically, one interprets the cell as functioning by two half reactions

$$2.5Nb_2O_{4.8} + 4e^- = 5NbO_2 + 2O^{-2} \tag{1-8}$$

$$Nb_{(Pd)} + 2O^{-2} = NbO_2 + 4e^- \tag{1-9}$$

The overall cell reaction is

$$2.5Nb_2O_{4.8} + Nb_{(Pd)} = 6NbO_2 \tag{1-10}$$

then by application of the Nernst equation the partial molar Gibbs energy of niobium in palladium solution is given by

$$\Delta\overline{G}_{Nb} = 6\Delta G_f^o(NbO_2) - 2.5\Delta G_f^o(Nb_2O_{4.8}) + 4F\epsilon \qquad (1\text{-}11)$$

where ϵ is the voltage and F is the Faraday constant. Further details on the use and properties of high temperature galvanic cells is given in chapter 3.

The two experimental techniques discussed above both require thermochemical data on the various oxides. Fortunately, there has been a recent review of the thermodynamics of the many oxides in the niobium system [17]. The thermodynamic values used in this study were obtained from the JANAF thermochemical tables [20] for most of the oxides. The JANAF tables are critical reveiws of the literature which reports the heat of formation, $H_{f,298}^o$, and Gibbs free energy function, gef, which is tabulated at temperature intervals of 100° K. Tabulation of gef ($gef = -(G^o - H_{298}^o)/T$) is convenient since it varies rather smoothly with temperature, does the change in Gibbs free energy function, Δgef. Relevent thermochemical data are reproduced in table (1-I).

Also included in table (1-I) are the Gibbs free energy functions and heat of formation for $Nb_2O_{4.8}$ that were derived from the data by Worrell [21] and Marucco [22]. Worrell performed high temperature galvanic cell experiments and Marucco used a combination thermogravimetric-resistivity measurement on the oxide while controlling oxygen partial pressure with gas mixtures. Both experiments yield very close values for the Gibbs energy change of the following reaction

$$2.5NbO_2 + 0.5\ O_2 = 1.25Nb_2O_{4.8} \qquad (1\text{-}12)$$

The Gibbs energy change can be fit to

$$\Delta G = -75290 + 19.95T \tag{1-13}$$

and ΔH^{o}_{298} is -73540 cal/mole. The tabulated values for the Gibbs energy functions of NbO_2 and O_2 can be used to obtain gef for $Nb_2O_{4.8}$ as a function of temperature

$$\mathrm{gef}(Nb_2O_{4.8}) = 24.24 + 0.0247T \tag{1-14}$$

This expression was used to evaluate the entries in table (1-I).

Chapter 1 References

[1] L. Brewer, Acta Met.,15(1967)p.553-556

[2] L. Brewer, Science, 161(1968)p.115

[3] P.J. Meschter, W.L. Worrell, Met. Trans. A, 8A(1977)p.503

[4] V. Srikrishnan, P.J. Ficalora, Met. Trans. A., 6A(1975)p.3] P.J. Meschter, W.L. Worrell, Met. Trans. A, 8A(1977)p.503

[4] V. Srikrishnan, P.J. Ficalora, Met. Trans. A., 6A(1975)p.2095

[5] Szymanski, Charcosset, Plat. Met. Rev., 30(1986)p.23

[6] 1984, U.S. Patent 4,423,087

[7] H. Kleykamp, "Behavior and Chemical State of Irradiated Ceramic Fuels", Procedings of Panel, August 1972; International Atomic Energy Agency, Vienna 1974, IAEA-PL-463/8 p.157

[8] G. Wijbenga, "Thermochemical Investigations on Intermetallic UMe_3 Compounds (Me = Ru,Rh,Pd)," Ph.D. Thesis, University of Amsterdam, Dec. 1981

[9] G. A. Jensen, "Recovery and Use of Fission Product Noble Metals", June 1980, PNL-SA-8358; A.W. Lautensleger, PNL-SA-11813

[10] L. Brewer, in P. Rudman, J. Stringer, and R.I. Jaffee (eds.), "Phase Stability in Metals and Alloys", McGraw-Hill, Inc., New York, 1967, p.39-61

[11] H. Kleykamp, J. Less Common Metals, 83(1982)p.105-113

[12] O. Kubaschewski, Trans. Faraday Soc., 54(1958)p.814-820

[13] H.J. Schaller, Ber. Bunsenges. 80(1976)p.999-1002

[14] P.J. Meschter, W.L. Worrell, Met. Trans. A, 7A(1976)p.299- 305

[15] M. Pelino, S.K. Gupta, L.R. Cornwell, K.A. Gingerich, J. Less-Common Metals, 68(1979)P31-P38; U.V. Choudary, K.A. Gingerich, L.R. Cornwell, J. Less-Common Metals 50(1976)p.201-11

[16] J.K. Gibson, L. Brewer, K.A. Gingerich, Met. Trans. A, 15A(1984)p.2075-85

[17] T. Matsui, K. Naito, Solid State Ionics, 12(1984)p.125-34

[18] R.P. Elliot,"Constitution of Binary Alloys",First Supplement, McGraw-Hill, 1965

[19] L. Brewer, P. Wengert, Met. Trans., 4(1973)p.83-104

[20] JANAF Thermochemical Tables, U.S. Dept. of Commerce, N.B.S., Inst. for Applied Technology, Michigan

[21] P.J. Metschter, W.L. Worrell, Met. Trans. B, 6B(1975)p.345-47

[22] J.F. Marucco, J. Solid State Chem., 10(1974)p.211-18

[23] B.C. Giessen et al., Met. Trans. A, 11A(1980)p.709-15

Table 1-I

Thermochemical Data for Nb and Several of its Oxides

Gibbs Energy Function, gef (cal/deg/mole)				
T(K°)	Nb	NbO_2	$Nb_2O_{4.8}$	Nb_2O_5
1100	12.278	22.349	51.328	53.709
1200	12.691	23.589	53.904	56.225
1300	13.084	24.772	56.374	58.627
1400	13.460	25.896	58.730	60.923
Heat of Formation $\Delta H^{\circ}_{f,298}$(kcal/mole)				
298	0.0	-190.0	-438.8	-454.0

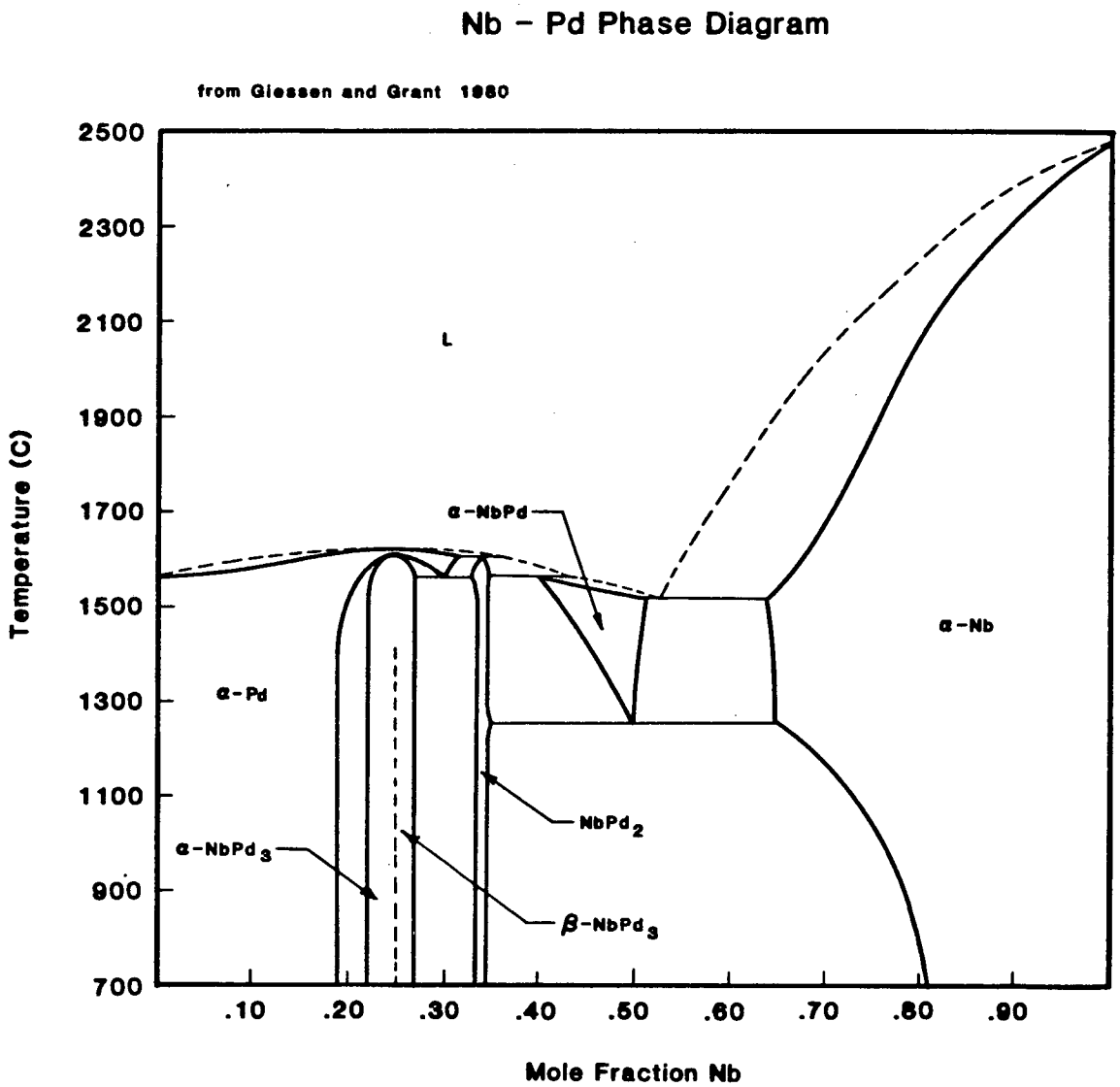

-- XBL 868-2900 --

Figure (1-1)
The niobium-palladium phase diagram determined by Giessen et al. [23]. Note that others have reported the existence of tetragonal σ–Nb_3Pd_2 which does not appear in this diagram (see chapter 5).

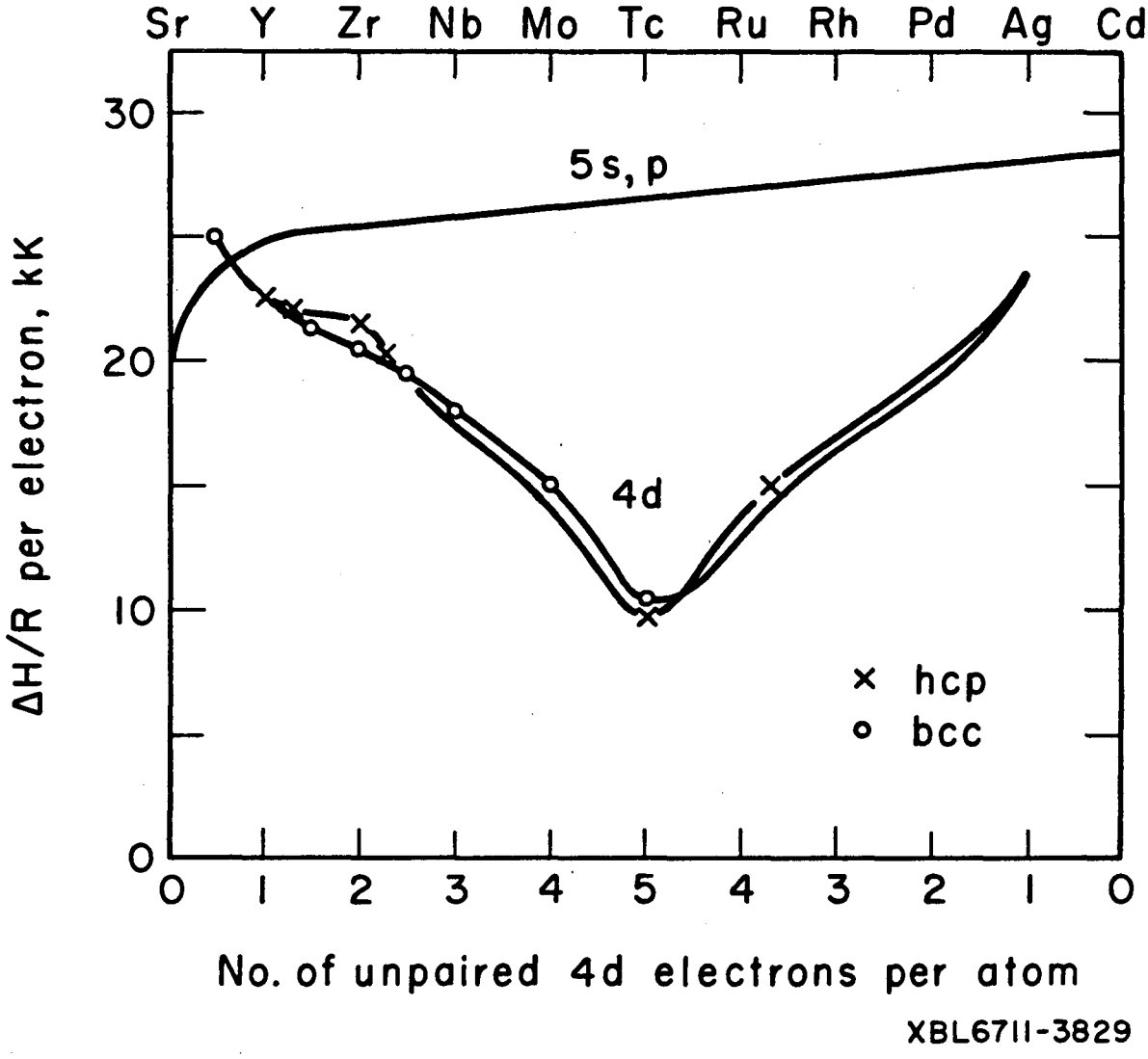

Figure (1-2)

Valence-state bonding energy in kilokelvin per mole per electron. The top curve is the bonding energy of the 5s and 5p electrons, versus element. The bottom curve represents the energy due to bonding of the 4d electrons as a function the number of unpaired d electrons. This diagram was provided by L. Brewer, details of his calculations can be found in reference [10].

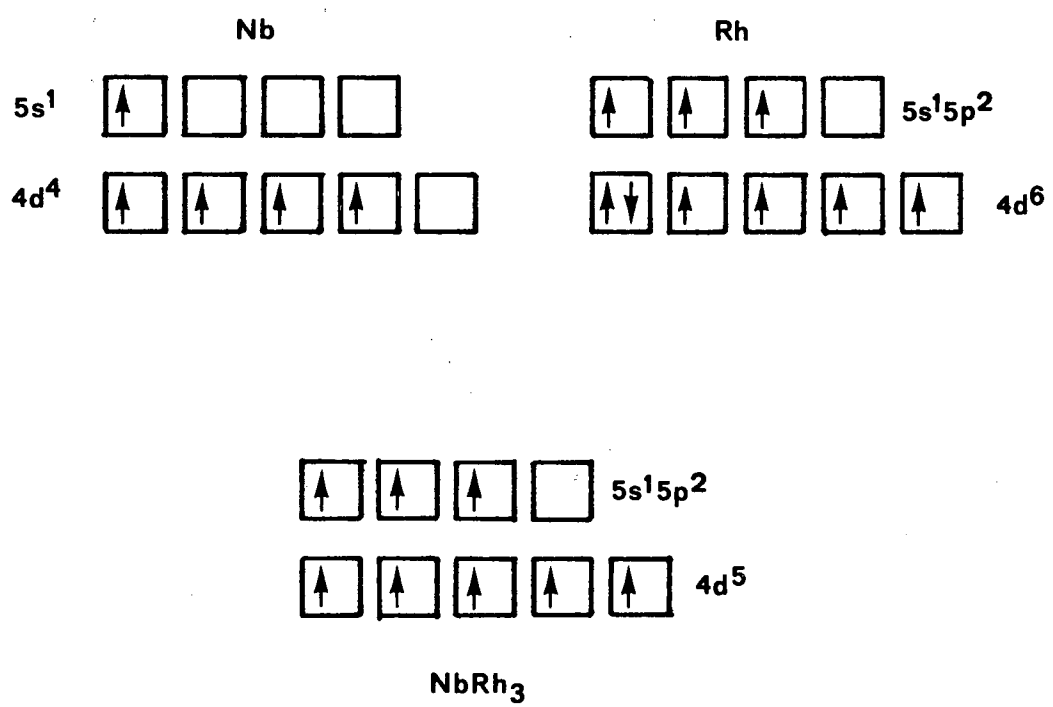

-- XBL 868-2901 --

Figure (1-3)
The electronic configurations of Nb, Rh and the average configuration on an atom in the $NbRh_3$ alloy are represented in this figure by nine boxes for each atom. The upper four represent the one 5s and three 5p orbitals while the lower five boxes represent the five 4d valence orbitals. Electrons appear as arrows which represents their spin.

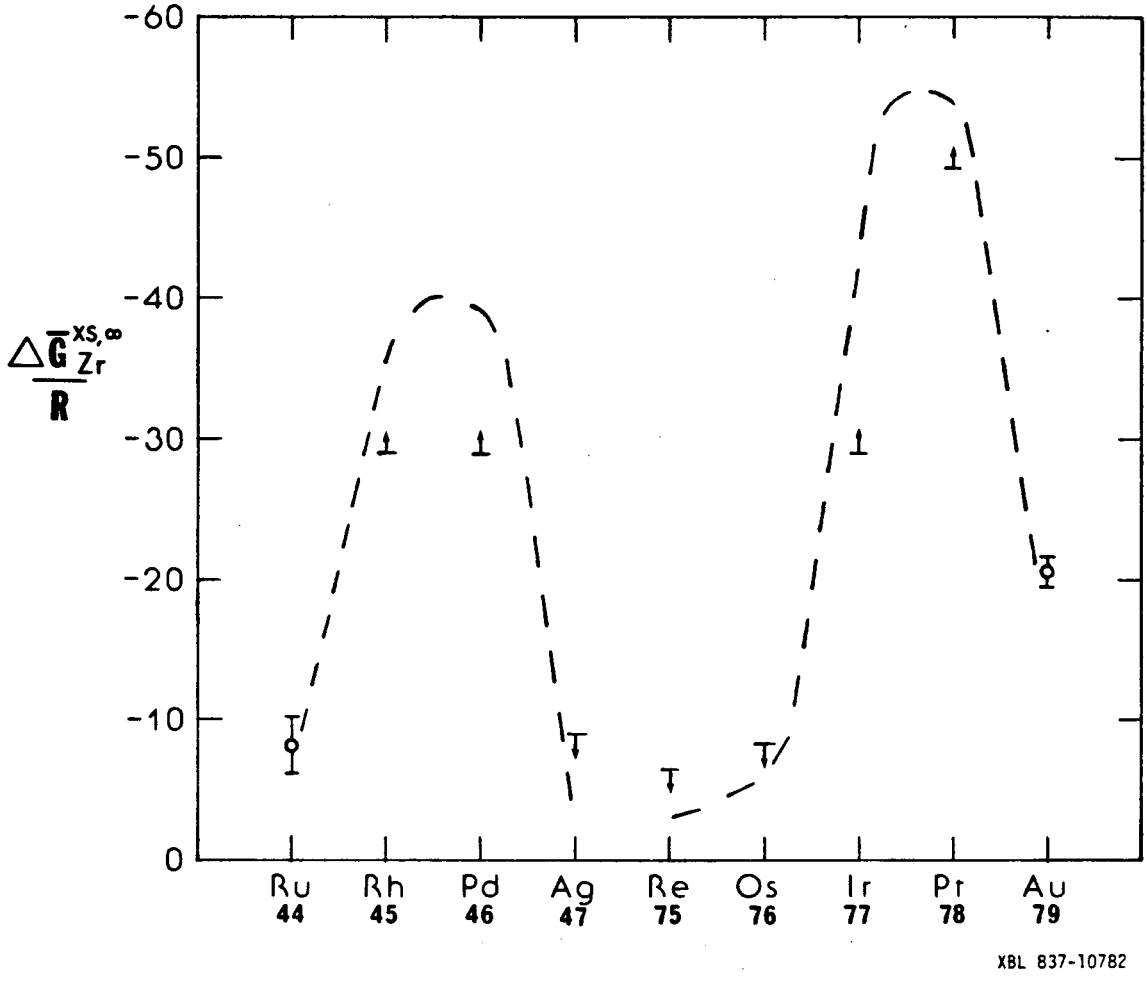

Figure (1-4)
The excess partial molar Gibbs energy of zirconium in kilokelvin/gm-atom in dilute solutions at 1800° K. This diagram was provided by L. Brewer, see reference [16].

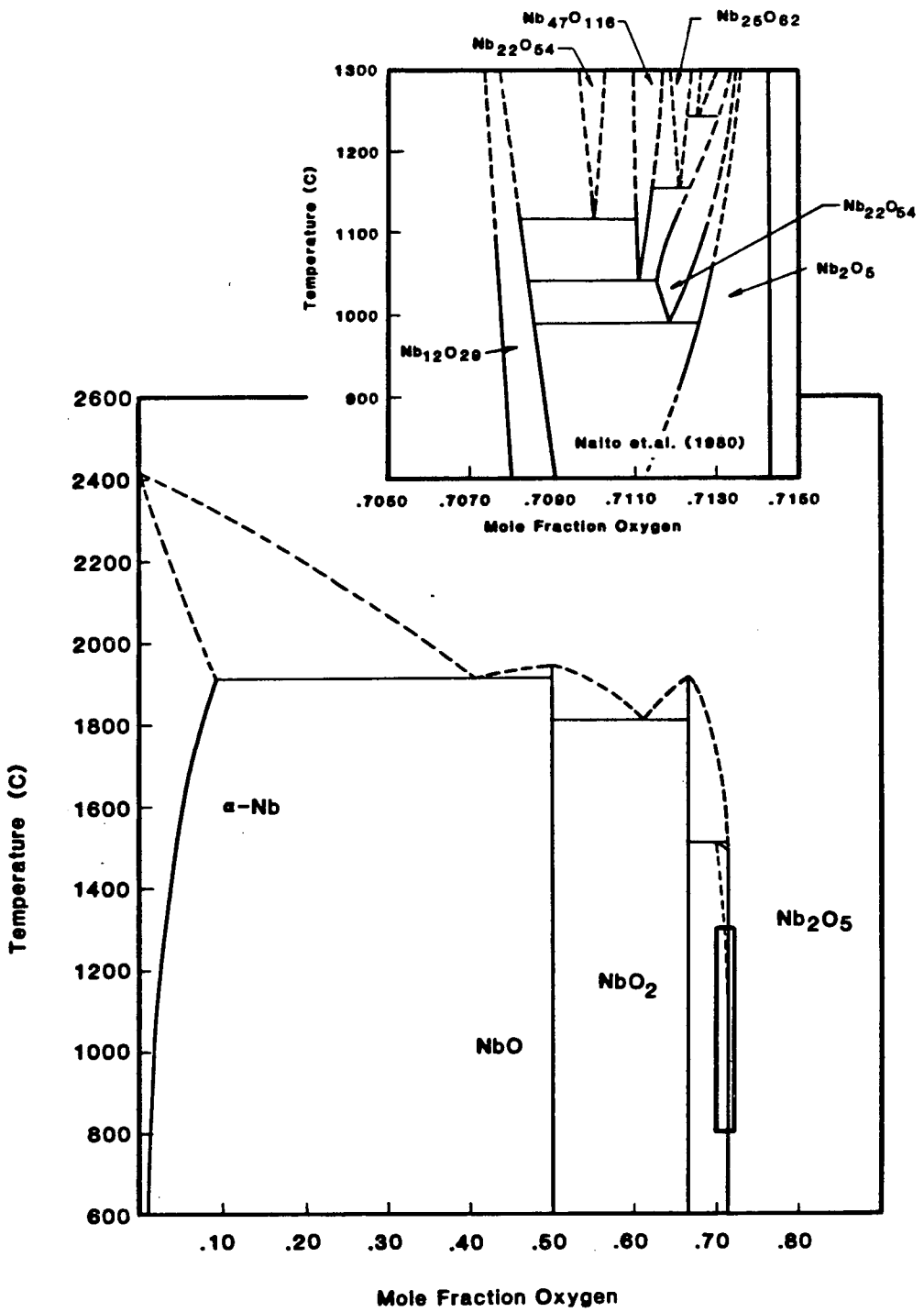

Figure (1-5)

The niobium-oxygen phase diagram. Inset is that determined by Naito et al. [17] which describes the complicated phase relationships in the region sub-stoichiometric to Nb_2O_5.

Chapter 2

Experimental Methods for the Preparation and Characterization of Oxide-Alloy Equilibria

2.1 Introduction

The experimental techniques discussed in this chapter were developed to characterize multiple phase samples used for the oxide equilibration study and the galvanic cell study. These methods were useful in determining whether the samples were in equilibrium and to reveal exactly which phases were present.

2.2 Starting Materials

Samples for the oxide equilibration experiment were prepared from stock powders of the metals and their oxides. Table (2-I) lists the origin of these powders and some of their characteristics. In several cases the powders were put through stainless steel classifier screens to reduce the degree of agglomeration. Agglomerates could not be broken up in the milling step and thus made mixing difficult since portions of the sample were composed of largely one phase.

The powders were weighed on a Mettler H20T semi-microbalance with an accuracy of ± 0.02 milligram into a small glass vial. The vial was tared after each component was added in order to account for any drift in the balance zero. Typical drifts were less than 0.07 milligram after the multiple weighings needed for a sample. Total mass of a sample was typically 2 grams.

Small glass beads (3 mm diameter) were then added to act as mixing balls. A small piece of parafilm was stretched over the mouth of the vial before the cap was secured. The parafilm prevented the segregation of the finer powders into the area between the cap and the glass. The vial was then placed in a slow speed rotating mixer operating at 50 to 100 rpm for several hours. The glass beads were removed by carefully picking them out with tweezers.

2.3 Consolidation and Hot Pressing

The powders were then cold pressed in a stainless steel die with a 7/16 in. bore. A load of 10,000 lb_f was maintained on the ram for several minutes and then the pressure was slowly released. This procedure yielded samples free of cracks and other pressing faults. The die was carefully cleaned before and after each sample was pressed. The outside of the resulting pellet was scraped clean with a glass slide in order to remove any possible steel contamination.

The samples were then surrounded by boron nitride in a graphite die. The bottom ram of the 1/2 in. i.d. (99.5% ATJ grade) graphite die was inserted into the die as shown in figure (2-1). A layer of boron nitride powder was then compacted into the die using the upper ram. More loose powder was then added on top so that when the sample pellet was dropped down the bore of the die the powder would completely surround it. The sample was then tamped down gently with the upper ram to make sure its faces were true with the rams. Boron nitride powder was then compacted on top of the sample to leave it isolated from the graphite die. This procedure was successful in preventing the reaction of the sample with the graphite die when the sample was hot pressed.

Uniaxial pressing of the die assembly while heating was accomplished in a

hot press designed and built at L.B.L., M.M.R.D. Heating was provided from a tungsten element constructed from sheet 1 in. wide and 0.010 in. thick. A diffusion pump and liquid nitrogen trap could evacuate the chamber to a pressure better than 10^{-4} mm Hg as measured by an ion gauge. The working ram was hydraulically driven and was used to apply variable pressure up to 4000 psi on the 1/2 in. sample ram.

The die assembly was set on the sample stage and the working ram lowered until it would just touch the upper ram of the assembly. No pressure was applied at this point because the working ram was to function only as a stop for evacuation of the chamber. If it were not in this position, the upper ram of the die assembly would pop off as the gasses rushed out of the die during chamber evacuation. The chamber was pumped on until the base pressure was below 10^{-5} mmHg.

The power to the filament was increased slowly until the die had reached a temperature of 1000° C. The temperature was measured by a 653nm Leeds and Northrup optical pyrometer. Sightings were made onto the top of the die through a quartz window.

A pressure of 3800 psi was then slowly applied to the die assembly. The pressure was applied to the hot sample because this procedure seemed to preserve the integrity of the sample pellet. Apparently at the higher temperatures the sample was plastic enough not to crack under the load.

The position of the working ram could be monitored by an attached dialometer gauge which had graduations at every 0.001 in. It quickly reached a steady state position as the temperature equilibrated. The power input was then gradually increased while closely monitoring the ram position. At constant

pressure it would begin to rise due to the increasing temperature and the thermal expansivity of the die assembly. Then abruptly the ram would begin to drop as the sample powders had begun to react and sinter together. A new steady state position would be reached in one or two minutes. The distance the ram traveled during the reaction was as little as 0.010 in. or as large as 0.060 in. The reaction temperature could only be estimated since this would all occur in a relatively short period of time compared with the time needed for the system to reach thermal equilibrium. This temperature did seem to be fairly consistent for samples of the same materials and varied from below 1100° C to 1450° C for the samples used in this study. The estimated temperatures are listed in Table (2-II). The heat treatment was concluded by cutting the power to the heating element, reducing the pressure on the ram, and letting the assembly cool under vacuum for several hours. The typical amount of time a sample spent above 1000° C was about twelve minutes.

The die could be disassembled with relatively little force to yield a very white pellet. The boron nitride would not sinter and would mostly flake off when touched to reveal the compacted sample pellet. Ultrasonic cleaning in ethanol would remove the rest of the boron nitride. The outside surface of the entire pellet would then be polished with silicon carbide paper just in case any small grains of boron nitride were embedded in its surface. Several test samples were cut open and examined metalographically without removing the BN in order to search for evidence of a reaction with the samples. No such evidence was ever observed. In addition no ternary phases were observed in X-ray powder diffraction patterns taken from the unpolished samples and no boron or nitrogen was noticed in the scanning Auger results to be discussed later.

2.4 Sample Annealing

The samples were then accuratly weighed ($\pm$0.02milligram) and annealed at 1000° C in a dynamic vacuum. Heating was supplied by a tungsten heating element and the vacuum was created by diffusion pump with a liquid nitrogen trap. The pressure was monitored by a vacuum ionization gauge and was typically 10^{-5}mm Hg. Temperature was measured by a platinum-platinum,13% rhodium thermocouple in contact with the 99.8% alumina crucible which contained the sample. The total heat treatment durations and the percentage mass changes for the samples are given in table (2-II). The mass changes were always very small. The crucible would appear gray after use but never appeared to react with the samples.

The samples were be periodically removed from the furnace so that they could be weighed and subjected to X-ray powder diffraction. The patterns were recorded and compared with earlier patterns to detect nonequilibrium phases since their peak intensities would change in time. The diffusion coefficient for niobium in palladium at 1000° C is $\approx 10^{-10}\text{cm}^2/\text{sec}$, [1] which can be assumed to be the limiting diffusion rate in the samples. Thus if 10 microns represents the average size of an alloy grain, a characteristic time for diffusion is $(10\times10^{-4}\text{cm})^2/(10^{-10}\text{cm}^2/\text{sec}) = 10^4\text{sec}$, or three hours, which is much shorter than the annealing time.

2.5 X-ray Diffraction

X-ray powder patterns were obtained on a Siemens D-500 diffractometer using Cu K_α radiation and a graphite monochrometer. Measurements were taken in step-scan mode every 0.1° or 0.05° (2θ) for one or two seconds. The

number of counts at each position was digitally recorded on a magnetic disk for plotting at a later time. This system offered a very convenient means to accurately compare patterns for different samples and for the same sample after further heat treatments. Data analysis was performed using the IDR routine in the DIFFRAC 11 software package [2]. This program determines peak positions, FWHM (full width at half maximum) and integrated intensities. Digital filtering techniques are used by the program to estimate and subtract the background as well as to eliminate $K_{\alpha 2}$ peaks from the analysis.

2.6 Polishing

Specimens were prepared for microscopic examination by cutting a wedge from the samples using a slow speed diamond saw with Buehler Isocut fluid [3] as the lubricant. Both pieces were then ultrasonically cleaned in ethyl alcohol and dried under an incandescent bulb. The position of the cut, figure (2-2), was chosen to obtain a face that had portions representative of both the center of the sample and the edges. Examination of such a face allows one to assess whether the sample might have reacted with either the crucible or the vapor space in the anealing furnace. The rest of the sample was often subjected to further heat treatments.

The specimens were then placed face down in the ram of a Buehler Pneumet I [3] hot mounting press. Several could be placed in the ram if they were separated by stainless steel rings. Buehler Konductomet I [3] was used as the mounting compound. It is a thermosetting phenolic resin that is filled with carbon powder to make it conducting. A conducting mounting material permitted electron beam examination of the specimens without having to coat them with

carbon or gold. A carbon coat would obscure the contrast when optically examining the samples, and gold's L_α emission conflicts with niobium's when performing energy dispersive analysis.

After removal from the mounting press the specimens were polished on wet silicon carbide paper. The grit sizes used were 240, 320, 400, followed by 600. These steps were performed by hand using a minimum of pressure so as to not preferentially remove grains of one phase over another. Optically smooth surfaces were then obtained by diamond paste and kerosene lubricant (Buehler [3] 6μm, 1μm, followed by 1/4μm) on a nylon fabric surface. The surface was rotated on a mechanical polishing wheel while the specimens were held by hand. Two or three minutes on each of the diamond grits was sufficient to proceed to the next polishing step. Ultrasonic cleaning was performed at each stage of the polishing scheme. No acid etching was performed in order to preserve the chemical composition of the surface.

2.7 Alloy Composition Measurement

The composition of alloy grains in the samples was obtained by energy dispersive X-ray analysis (EDAX). The equipment used was an scanning electron microscope made by AMR Corp. [4] with a drifted lithium silicon X-ray detector made by Kevex Corp. [5]. Spectra were obtained from 0.0 to 10.24 kev with a resolution of 10 ev/ch. Figure (2-3) is a portion of a niobium-palladium alloy spectrum that clearly shows the Nb(L_α) and Pd(L_α) peaks and demonstrates the resolution of the detector.

Quantex-Ray software [5] was used to remove silicon escape peaks and the background Bremstrahlung radiation from the X-ray spectrum emitted from the

sample. The net intensities could then be obtained from the characteristic lines in the spectrum. The Quantex-Ray software, however, was not found to include a reliable method to abstract the compositions from these peak intensities. Even with its ZAF routine and the use of standards, Quantex-Ray performed poorly. Studies indicated that the problem was the result of electron beam current fluctuations between measurements. If one alloy of known composition was treated as an unknown against other standards the results were better if the standards were measured during the same session as the unknown. If, however, the chamber was opened between measurements on the unknown and standards the results were unreliable. Presumably, one would never achieve the same beam current once the chamber was reevacuated. These problems may be avoided by measuring the beam current after each alloy measurement. In this way all intensities could be normalized by the beam current. The current measurement is accomplished by exchanging a Faraday cup for the sample without opening the chamber. The microscope used in this study did not easily allow such a procedure. Furthermore, if such a method had been adopted in our study, we would have had to assume that the beam current would stay constant throughout a session.

This study has developed a method that yields reliable and accurate compositions without resorting to the measurement of beam currents. The theory of electron beam interaction with solids is well developed and includes the understanding of the precision and sensitivity of electron microprobe analysis. Ziebold and Ogilvie [6] introduced a quasiempirical technique for determining calibration curves for multicomponent alloys. They noted that the theoretically predicted behavior of the X-ray intensity generated within a solid has the same

form as that which describes the X-rays emerging from the surface. Using this relationship the calibration curves for many alloy systems were fit to within the reproducibility of the data points.

The first order approximation for the form of the intensity versus composition generated in a binary alloy is

$$\frac{C_A}{K_A'} = \frac{\alpha_B}{\alpha_A} + \left(1 - \frac{\alpha_B}{\alpha_A}\right) C_A \tag{2-1}$$

where C_A is the weight fraction of A and K_A' is the ratio of the intensity of a particular characteristic X- ray peak for A in the alloy to that in pure A. The α_i terms represent the effects of both electron energy loss per unit depth of penetration and the back scattering efficiency of each species. Ziebold et al. [6] observed that the relative emergent intensity, K_A, had similar behavior. Data from a wide variety of binary transition metal alloys were shown to obey the following relations;

$$\frac{C_A}{K_A} = a_{AB} + (1 - a_{AB}) C_A \tag{2-2a}$$

$$\frac{C_B}{K_A} = a_{BA} + (1 - a_{BA}) C_B \tag{2-2b}$$

Their study included both light and heavy metals as well as both K and L lines. They were also able to give some theoretical justification to an expression relating a_{AB} and $\frac{\alpha_A}{\alpha_B}$. The relationship for the heavier species B in a binary alloy of A and B, is

$$a_{BA} = (\text{const}) \cdot \left(\frac{\sigma + \chi_{B,i}^{A}}{\sigma + \chi_{B,i}^{A}}\right)\left(\frac{\alpha_A}{\alpha_B}\right) \tag{2-3}$$

where $\chi^{B}_{A,i}$ and σ are given by

$$\chi^{B}_{A,i} = \left(\frac{\mu}{\rho}\right)^{B}_{A,i} \csc\theta \tag{2-4}$$

$$\sigma = 1820\left(\frac{30}{V}\right)^{2} \tag{2-5}$$

θ is the spectrophotometer take off angle and V is the beam voltage in kilovolts. $(\mu/\rho)^{K}_{J,i}$ is the mass absorption coefficient for line i of element A dissolved in element B which are published in a variety of sources [7].

Equation (2-3) may be futher simplified by accounting for the atomic number dependence of α_A and α_B. Ziebold et al. [8] point out that α's dependence on atomic number should be slight since the electron energy loss per unit depth tends to decrease with atomic number and the backscattering efficiency tends to increase with atomic number. They then proposed the relation

$$\frac{\alpha_A}{\alpha_B} = (\text{const})\cdot\left(\frac{Z_B}{Z_A}\right)^{n} \tag{2-6}$$

where the exponent n is small in magnitude. Substitution of equation (2-6) into equation (2-3) yields for the heavier element B,

$$a_{BA} = (\text{const})\cdot\left(\frac{\sigma + \chi^{A}_{B,i}}{\sigma + \chi^{B}_{B,i}}\right)\left(\frac{Z_B}{Z_A}\right)^{n} \tag{2-7}$$

Ziebold et al. [6] then reduced all their data for the heavy elements in the alloys using this expression to find the best value for n and the proportionality const. The following gave errors <1%

$$a_{BA} = 0.95\left(\frac{\sigma + \chi^{A}_{B,i}}{\sigma + \chi^{B}_{B,i}}\right)\left(\frac{Z_B}{Z_A}\right)^{0.28} \tag{2-8}$$

The light element requires a small correction due to the effect of secondary fluorescence which adds a multiplicative term

$$a_{AB} = 0.95 \left(\frac{\sigma + \chi^{B}_{A,i}}{\sigma + \chi^{A}_{A,i}} \right) \left(\frac{Z_A}{Z_B} \right)^{0.28} \left(\frac{1}{1+0.7\kappa} \right) \tag{2-9}$$

and κ is determined by

$$\kappa = \frac{\lambda_A}{\lambda_B} \frac{M_B}{M_A} \frac{(\mu/\rho)^{A}_{B,i}}{(\mu/\rho)^{B}_{A,j}} \sin\theta \tag{2-10}$$

$M_{J,w}$ is the molecular weight and λ_J is the wavelength of the absorbtion edge of atom J.

Equation (2-8) and (2-9) allow the calculation of a_{AB} and a_{BA} from known parameters. They do not however relieve the problems associated with the fluctuation of the electron beam current. The parameter K_A in equation (2-2) contains a measurement of the X-ray intensity over pure A at the same conditions as over the unknown since

$$K_A = \frac{I_{A,alloy}}{I_{A,pure}} \tag{2-11}$$

We have found that by combining equation (2-2) for each species an expression can be derived that provides accurate and reliable compositions by using standards. The method involves the measurement of the relative intensity of the characteristic lines of each component in the binary alloy. The relative intensity is defined

$$R_A = \frac{I_{A,alloy}}{I_{A,alloy}+I_{B,alloy}} \tag{2-12}$$

An equation like (2-2) may be substituted for each I_J but first a change to mole fraction is convenient

$$\frac{x_A}{K_A} = x_A + \bar{a}_{AB}x_B \tag{2-13a}$$

$$\frac{x_B}{K_B} = x_B + \bar{a}_{BA}x_A \tag{2-13b}$$

where

$$\bar{a}_{JK} = \frac{M_{w,K}}{M_{w,J}} a_{JK} \tag{2-14}$$

Substitution of equation (2-13a) and (2-13b) into equation (2-12) gives

$$R_A = \frac{x_A(\bar{a}_{BA}x_A+x_B)}{x_A(\bar{a}_{BA}x_A+x_B) + \lambda x_B(\bar{a}_{AB}x_B+x_A)} \tag{2-15}$$

The unknown parameter λ is the ratio $I_{B,pure}/I_{A,pure}$.

The utility of equation (2-15) is that none of the terms require the measurement of absolute line intensities. The beam current may vary but the relative intensities for each line should to a good approximation stay the same for a given sample since all the line intensities scale with the beam current in the same way. All the parameters may be derived from the equations above except for λ which must be obtained from standards.

Standards were made by arc melting carefully measured amounts of rod or sheet stock material. Bulk materials were used to prevent loss of small pieces when the arc was drawn. The samples were also weighed after melting to check if there was any change in mass. The standards were then homogenized at 1000° C for several hours under a vacuum of 10^{-5}mmHg. After cutting, mounting and polishing the standards were placed in the SEM for X-ray analysis.

Table (2-III) gives the results for niobium-palladium standards. Most of the measurements were obtained from a variety of locations on the surface of the

specimen to check for homogeneity and for reproducibility. The table lists the integrated intensities for the K_α lines and their relative intensities. The data in this table were taken over a period of a year in which the filament was exchanged several times. Note that the absolute intensities vary drastically while the relative intensities clearly follow a smooth function of concentration. Figure (2-4) shows a plot of relative intensity versus mole fraction niobium. Relative intensity measurements scatter wildly (not shown) from samples with 40% to 65% niobium indicating the presence of grains with different composition. This is consistent with the known phase diagram [9] since these compositions are within the two phase region at 1000° C.

The effective take off angle used was 20°±2° which was computed by considering not only the angle of incidence but the azimuthal angle between the tilt axis and the detector position. This calculation for the spectrometer is described in [8]. The electron beam voltage was 18.3 kev and the mass absorption coefficients used were 1160 and 759 for $(\mu/\rho)^{Pd}_{Nb,L_\alpha}$ and $(\mu/\rho)^{Nb}_{Nb,L_\alpha}$ as well as 2640 and 573 for $(\mu/\rho)^{Nb}_{Pd,L_\alpha}$ and $(\mu/\rho)^{Pd}_{Pd,L_\alpha}$ [7].

Application of equations (2-8), (2-9) and (2-14) yields 1.7±0.2 and 1.1±0.1 for $\overline{a}_{Pd,Nb}$ and $\overline{a}_{Nb,Pd}$ respectively. A least squares analysis was applied to equation (2-15) and the data in table (2-III) to obtain a value of 1.14 for λ. The curve in figure (2-4) is this best fit with an average deviation from the measured relative intensities of less than 0.005. Note that the curve has the correct behavior at both low and high niobium concentration. The quality of the fit is quite insensitive to variation in the $\overline{a}$ parameters as shown in table (2-IV), thus their assigned error has little consequence and little would be gained by using a multivariable minimization method to determine all three parameters.

Tables (2-V), (2-VI), and (2-VII) present the measurements for Ti-Pd, Ti-Rh, and Nb-Rh standards respectively. The $\overline{a}$ parameters were again determined by equations (2-8), (2-9) and (2-14) ($\overline{a}_{Ti,Pd}$, 1.87; $\overline{a}_{Pd,Ti}$, 0.49; $\overline{a}_{Ti,Rh}$, 1.80; $\overline{a}_{Rh,Ti}$, 0.50; $\overline{a}_{Nb,Rh}$, 1.10; $\overline{a}_{Rh,Nb}$, 1.60). Least squares analysis produces values for λ equal to 0.964, 0.799, and 0.678 for $\lambda_{Ti,Pd}$, $\lambda_{Ti,Rh}$, and $\lambda_{Nb,Rh}$. The results are presented against the data in figures (2-5), (2-6), and (2-7). Equation (2-15)'s performance is again quite good in all cases except the Nb-Rh solutions where the average deviation of the data from the predicted value was 0.014. It is possible that these alloys were not as homogeneous as the others since Nb-Rh alloys are higher melting and the equilibration temperature 1000° C does not allow fast enough diffusion. The intermetallics in the Nb-Rh system also have substantially smaller ranges of composition and there are many more of them, see figure (2-8), so that some of the alloy buttons may actually have been two phase. Arc melting produces rather large grains in the sample. Crystallites frequently extend from the bottom of the button to the top, figure (2-9). Thus, cutting a small sample from the arc melted sample may give a grain of just that one composition and skew the results since random EDAX measurements on the slice would yield the same relative intensities for the components.

2.8 Scanning Auger Microscopy

A limited number of samples were examined at the Scanning Auger Microscopy facility at M.M.R.D.,L.B.L. The instrument used was the Physical Electronics 590 Scanning Auger Microprobe [10]. The sample holder required much smaller samples than were used in the SEM so small pieces were cut from the pellets and polished on a diamond wheel by hand. Mounting material could not

be used because the carbon contamination on the surface would obscure analysis of the bulk material. The quality of the polish was inferior to the samples prepared in mounting material but was adequate for the types of measurements taken.

Auger microscopy has the advantage that it is sensitive to the light elements such as carbon and oxygen. The distribution of oxygen in the phases of the sample was mapped by recording the generation of Auger electrons from oxygen as a function of position on the surface.

Chapter 2 References

[1] A. Brunsch, S. Steeb, Z. Metallk., 62(1971)p.247-51

[2] DIFFRAC11, Fortran Software System, Version 2.0 RSX-11M, Siemens Corp. (1984)

[3] Beuhler LTD., Lake Bluff Illonois

[4] AMRay Corp., Bedford MA

[5] Kevex and Quantex-Ray Software, Foster City, CA

[6] T.O. Ziebold, R.E. Ogilvie, Anal. Chem. 36(1964)p.322-27

[7] L.S. Birks, "Electron Probe Microanalysis", second ed., Wiley-Interscience, 1971

[8] T.O. Ziebold, R.E. Olgilvie, Anal. Chem. 35(1963)p.621-27

[9] D.L. Ritter, B.C. Giessen, N.J. Grant, Trans. of the Met. Soc. AIME, 230(1964)p.1250-59

[10] Physical Electronics, Eden, Minnesota

Table 2-I

Starting Materials

Pd	Alfa Products	-60 mesh, 99.9%
Pd	Johnson Matthey Inc.	0.3 micron, 99.99%
Pd	Lawrence Livermore Lab stock	0.030 in. sheet
Rh	American Platinum Works	sponge, 99.9%
Rh	Lawrence Livermore Lab stock	0.030 in sheet
Nb	Teledyne, Wah Chang Corp.	-400 mesh, 99.9%, air classified
Nb	Materials Research Corp.	1/8" rod, Marz grade (99.9%)
Nb_2O_5	Noah Chemical Corp.	-325 mesh, 99.95%
Nb_2O_5	Alfa Products	99.9%, powder
NbO_2	Cerac Inc.	-200 mesh, 99.9%
NbO	Cerac Inc.	-100 mesh, 99.8%
Ti	Cerac Inc.	-325 mesh, 99.5%
Ti	Orion Chemical Co.	1/16" rod, 99.9%
TiO_2	Cerac Inc.	-325 mesh, 99.9%
Ti_2O_3	Cerac Inc.	-325 mesh, 99.8%
TiO	Cerac Inc.	-325 mesh, 99.9%
Fe	Materials Research Corp.	powder, 18ppm C
Fe_2O_3	Alfa Products	-325 mesh, 99.8%

Table 2-II

Reactants and Heat Treatments

Sample	Starting Materials (wt.%)	Hot Press. Temp.	Annealing Temp.	Mass Change (wt.%)
NP01	Pd (53.5) Nb (5.3) Nb_2O_5 (41.2)	1100C	2wk 1030C	-0.01
NP02	Pd (53.7) Nb (5.2) Nb_2O_5 (41.1)	1100C	2wk 1030C	-0.01
NP03	Pd (50.4) Nb (10.1) Nb_2O_5 (39.5)	1100C	2wk 1030C	-0.0
NP04	Pd (33.8) Nb (19.7) Nb_2O_5 (46.5)	1100C	2wk 1030C	+0.01
NP05	Pd (54.7) NbO (45.3)	1100C	3wk 1000C 24hr 1225C 19hr 1315C 16hr 1025C	-0.6
NP06	Pd (52.0) Nb (19.9) Nb_2O_5 (28.1)	1100C	24hr 1225C 19hr 1315C 16hr 1025C	-0.3
NP07	Pd (41.6) Nb (15.9) NbO_2 (42.5)	1100C	3wk 1000C 24hr 1225C 19hr 1315C 16hr 1025C	-1.25
NP08	Pd (40.6) Nb (15.6) NbO (43.8)	1100C	24hr 1225C 19hr 1315C 16hr 1025C	-0.3
NP09	Pd (29.5) Nb (38.8) Nb_2O_5 (31.7)	1100C	24hr 1225C 19hr 1315C 16hr 1025C	-0.06
NP10	Pd (25.9) Nb (34.0) NbO_2 (40.1)	1100C	3wk 1000C 24hr 1225C 19hr 1315C 16hr 1025C	-1.39
NP11	Pd (24.6) Nb (32.4) NbO (43.0)	1100C	3wk 1000C 24hr 1225C 19hr 1315C 16hr 1025C	-1.41
NP12	Pd (6.1) Nb (49.9) NbO_2 (44.0)	1100C	24hr 1225C 19hr 1315C 16hr 1025C	+0.1
NP13	Pd (6.1) Nb (49.4) NbO (44.6)	1100C	24hr 1225C 19hr 1315C 16hr 1025C	+0.4
NP14	Pd (35.7) Nb (52.0) NbO (12.3)	1450C	5dy 1000C	-0.0
NP15	Pd (29.9) Nb (57.4) NbO (12.7)	1350C	5dy 1000C	+0.0

Table 2-II (cont.)

Reactants and Heat Treatments

Sample	Starting Materials (wt.%)	Hot Press. Temp.	Annealing Temp.	Mass Change (wt.%)
NR01	Rh (11.9) NbO_2 (57.5) Nb_2O_5 (30.6)	1275C	48hr 1030C 6dy 1000C	-1.0
NR02	Rh (49.5) NbO (22.0) Nb_2O_5 (28.5)	1310C	48hr 1030C 6dy 1000C	-0.8
NR03	Rh (47.3) Nb (14.3) NbO_2 (38.4)	1375C	48hr 1030C 6dy 1000C	-0.2
NR04	Rh (40.4) Nb (47.2) NbO (12.4)	1375C	48hr 1030C 6dy 1000C	-0.1
NR05	Rh (18.5) NbO (59.1) NbO_2 (22.4)	1350C	48hr 1030C 6dy 1000C	-0.8
NR06	Rh (27.1) Nb (37.2) NbO (35.7)	1475C	48hr 1030C 6dy 1000C	-0.1
NR07	Rh (32.0) NbO_2 (13.0) Nb_2O_5 (55.0)	1150C	48hr 1030C 6dy 1000C	-1.8*
TR01	Rh (9.4) TiO (47.6) Ti_2O_3 (43.0)	1325C	7dy 1000C	+0.0
TR02	Rh (10.1) Ti_2O_3 (74.2) TiO_2 (15.7)	1425C	7dy 1000C	+0.0
TP01	Pd (9.3) TiO (48.0) Ti_2O_3 (42.7)	1400C	8dy 980C	+0.0

* small piece fell off during heat treatment.

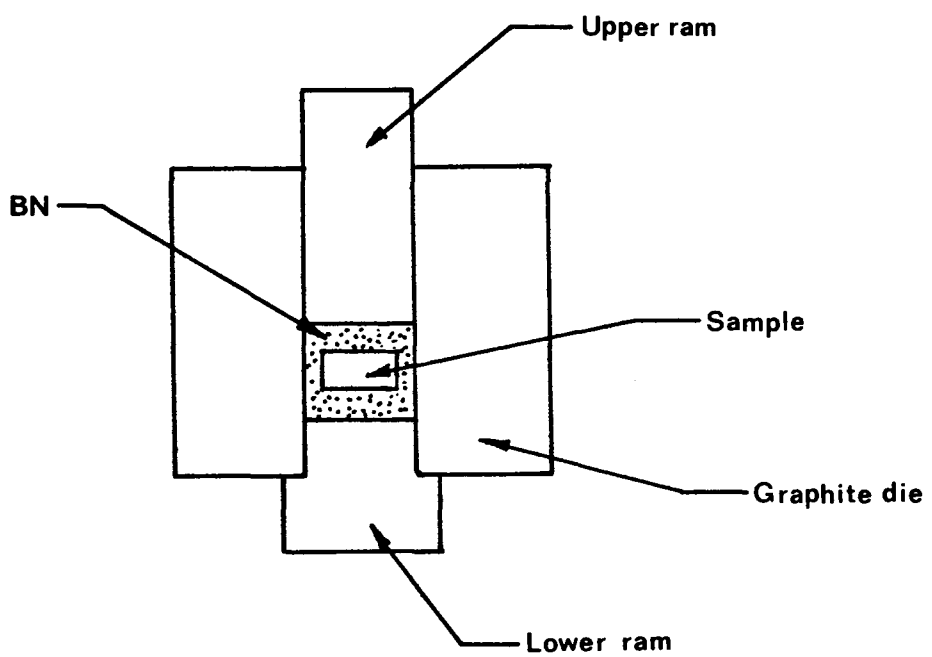

-- XBL 868-2903 --

Figure (2-1)
Graphite die used to hot-press samples. The prepressed pellets are surrounded by boron nitride powder to prevent reaction with the die.

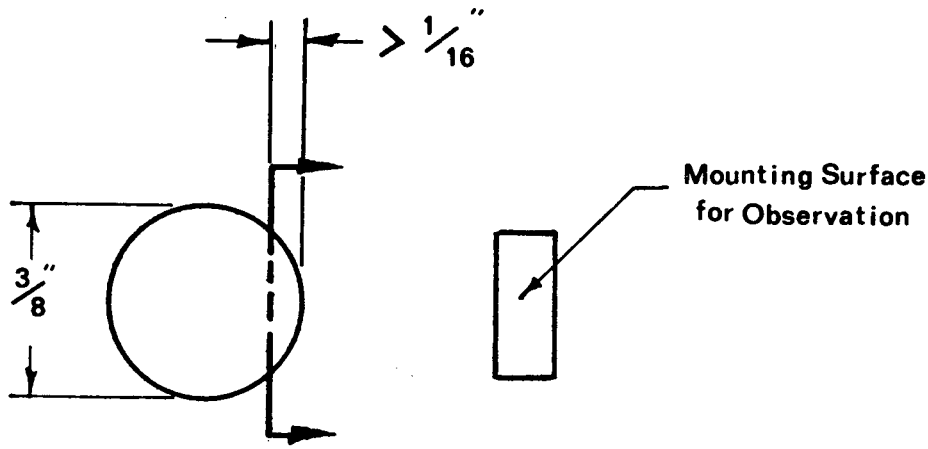

-- XBL 868-2904 --

Figure (2-2)
Sections used to microscopically examine the alloy oxide samples and electrodes used in this study.

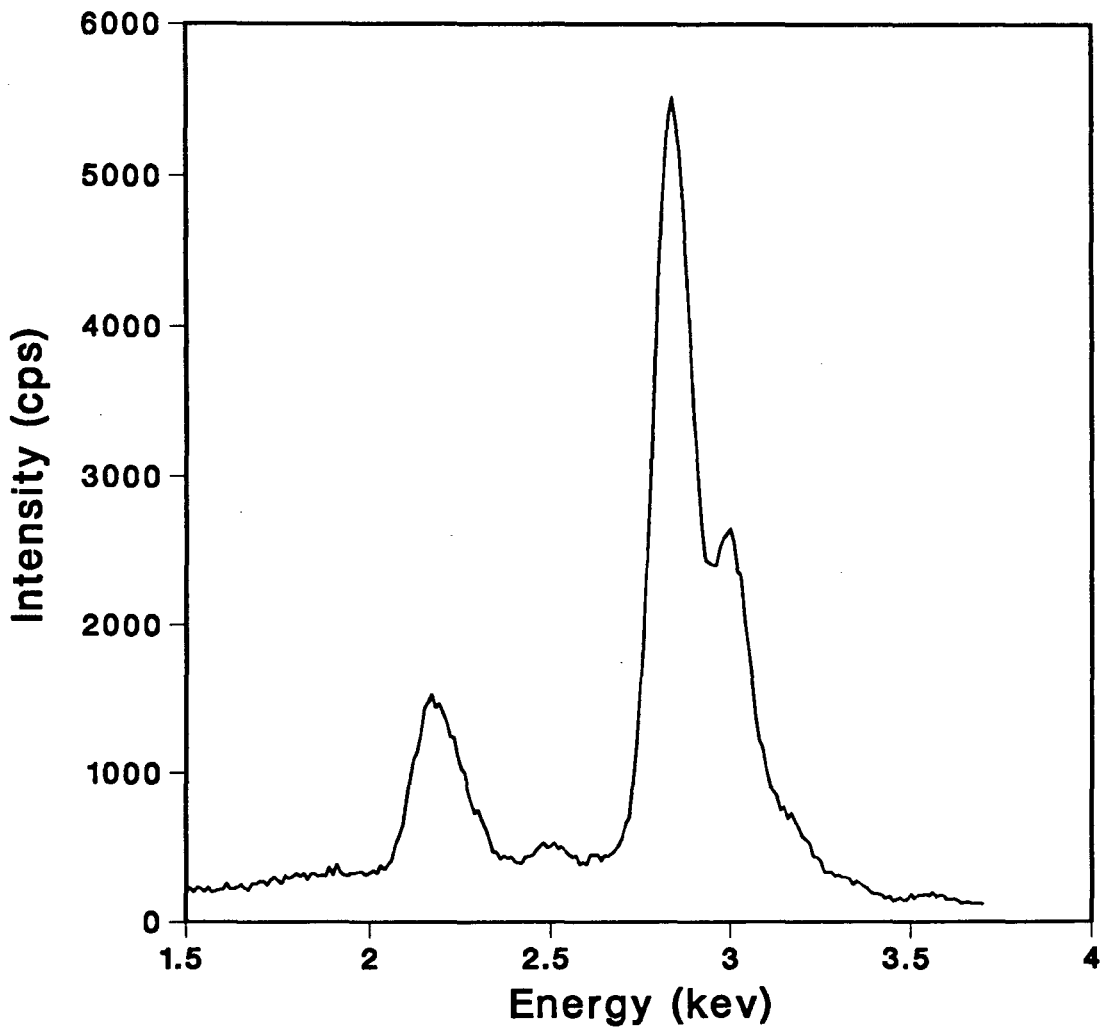

-- XBL 868-2905 --

Figure (2-3)
EDAX spectrum of a Nb-Pd alloy. The Nb(L_α) peak is at 2.2 kev and the Pd(L_α) peak is at 2.8 kev. Note that the Pd(L_β) is resolved but that for the niobium is not.

Table 2-III

Results for Nb-Pd Standards

$\bar{a}_{Pd,Nb} = 1.7$ $\bar{a}_{Nb,Pd} = 1.10$ $\lambda = 1.14$

x_{Nb}	intensity (cps) $L_\alpha(Nb)$	$L_\alpha(Pd)$	r	r_{calc}	% diff
0.061	5.75	102.50	0.053	0.052	-0.162
	11.31	111.60	0.092		-0.129
	10.26	107.10	0.087		0.331
	10.97	111.80	0.089		0.138
	26.46	245.30	0.097		-0.663
0.104	19.75	183.00	0.097	0.091	-0.668
	31.92	332.30	0.088		0.309
	28.38	309.60	0.084		0.676
	26.84	270.10	0.090		0.034
	3.73	34.01	0.099		-0.820
	8.50	71.90	0.106		0.269
	8.74	68.98	0.112		-0.400
	11.73	96.13	0.109		-0.032
0.122	35.24	311.10	0.102	0.108	0.668
	41.25	328.40	0.112		-0.316
	36.70	300.00	0.109		-0.057
	4.62	35.79	0.114		-0.583
0.172	16.80	86.29	0.163	0.158	-0.453
0.180	16.29	85.65	0.160	0.167	0.713
	26.53	74.37	0.263		-0.185
	22.85	63.81	0.264		-0.259
	20.19	58.81	0.256		0.552
0.267	11.24	32.32	0.258	0.261	0.305
	66.84	201.50	0.249		1.200
	72.93	215.70	0.253		0.841
	68.14	208.40	0.246		1.469
0.650	82.41	35.36	0.700	0.696	-0.369
	124.80	15.15	0.892		-0.693
0.848	129.80	13.79	0.904	0.885	-1.914
	122.00	13.02	0.904		-1.875
	241.80	13.52	0.947		-0.587
0.918	238.90	14.03	0.945	0.941	-0.336
	290.80	16.86	0.945		-0.402
	235.60	4.57	0.981		-0.019
0.972	221.80	3.93	0.983	0.981	-0.183
	216.10	3.36	0.985		-0.391

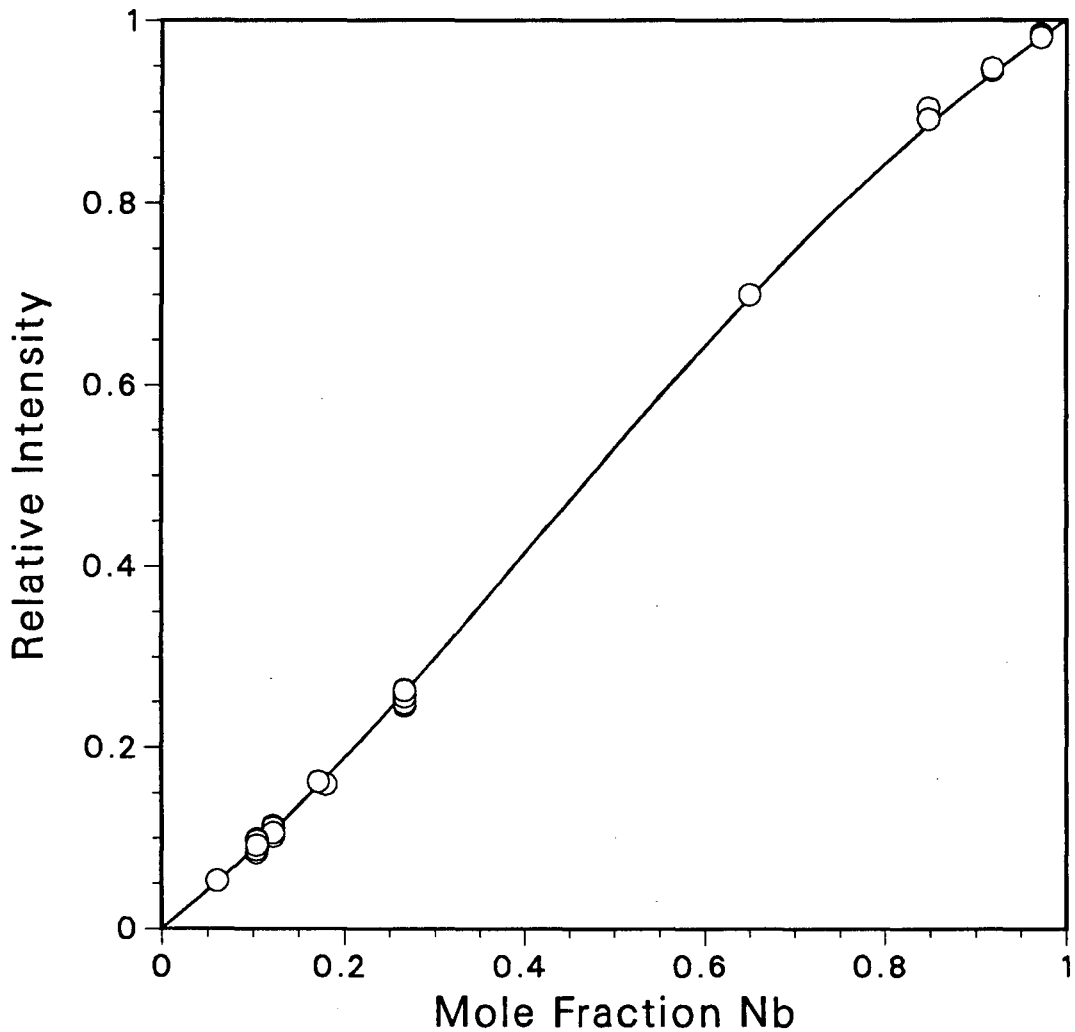

Figure (2-4)
The relative intensity of Nb(L_α) and Pd(L_α) peaks as a function of x_{Nb} in Nb-Pd alloys. The curve is generated by the parameters presented in table 2-III.

Table 2-IV

Sensitivity of Fit

Table of $|r_{Nb,calc} - r_{Nb}|_{ave}$

for different values of $\bar{a}_{AB}$ and $\bar{a}_{BA}$

(calculations were performed using the Nb-Pd data and $\lambda = 1.14$)

		$\bar{a}_{BA}$		
		1.5	1.7	1.9
$\bar{a}_{AB}$	1.0	0.008	0.006	0.005
	1.1	0.007	0.005	0.005
	1.2	0.006	0.005	0.005

Table 2-V

Results for Ti-Pd Standards

$\bar{a}_{Pd,Ti} = 0.49 \quad \bar{a}_{Ti,Pd} = 1.87 \quad \lambda = 0.964$

x_{Ti}	intensity (cps) $K_\alpha(Ti)$	$L_\alpha(Pd)$	r	r_{calc}	% diff
	3.27	67.52	0.046		-1.150
0.061	2.27	55.62	0.039	0.035	-0.447
	2.76	65.71	0.040		-0.557
	6.52	72.88	0.082		-0.726
0.128	6.42	73.41	0.080	0.075	-0.550
	6.31	74.01	0.079		-0.371
	7.51	57.23	0.116		-0.500
0.185	8.18	61.48	0.117	0.111	-0.643
	8.88	69.33	0.114		-0.258
0.200	26.43	191.00	0.122	0.121	-0.080
	24.66	177.40	0.122		-0.129
	15.17	85.22	0.151		-0.628
0.236	15.79	90.50	0.149	0.145	-0.373
	16.09	90.78	0.151		-0.573
	12.83	70.81	0.153		-0.857
	37.11	203.30	0.154		0.005
0.250	37.11	203.30	0.154	0.154	0.005
	42.47	235.90	0.153		0.184
	12.26	50.81	0.194		-1.760
0.282	10.28	45.11	0.186	0.177	-0.881
	12.29	53.54	0.187		-0.991
0.300	57.82	257.50	0.183	0.190	0.631
	50.57	214.10	0.191		-0.139
	73.58	260.40	0.220		0.639
0.350	73.58	260.40	0.220	0.227	0.639
	58.19	204.80	0.221		0.544
0.400	70.46	193.70	0.267	0.266	-0.108
	83.65	235.90	0.262		0.388
	90.43	204.40	0.307		-0.001
0.450	90.43	204.40	0.307	0.307	-0.001
	61.08	138.80	0.306		0.113
0.501	123.30	240.80	0.339	0.351	1.233
	128.40	249.60	0.340		1.130
0.551	152.00	232.50	0.395	0.397	0.166
	138.80	215.50	0.392		0.522
0.600	174.80	216.90	0.446	0.445	-0.143
	157.60	200.80	0.440		0.510

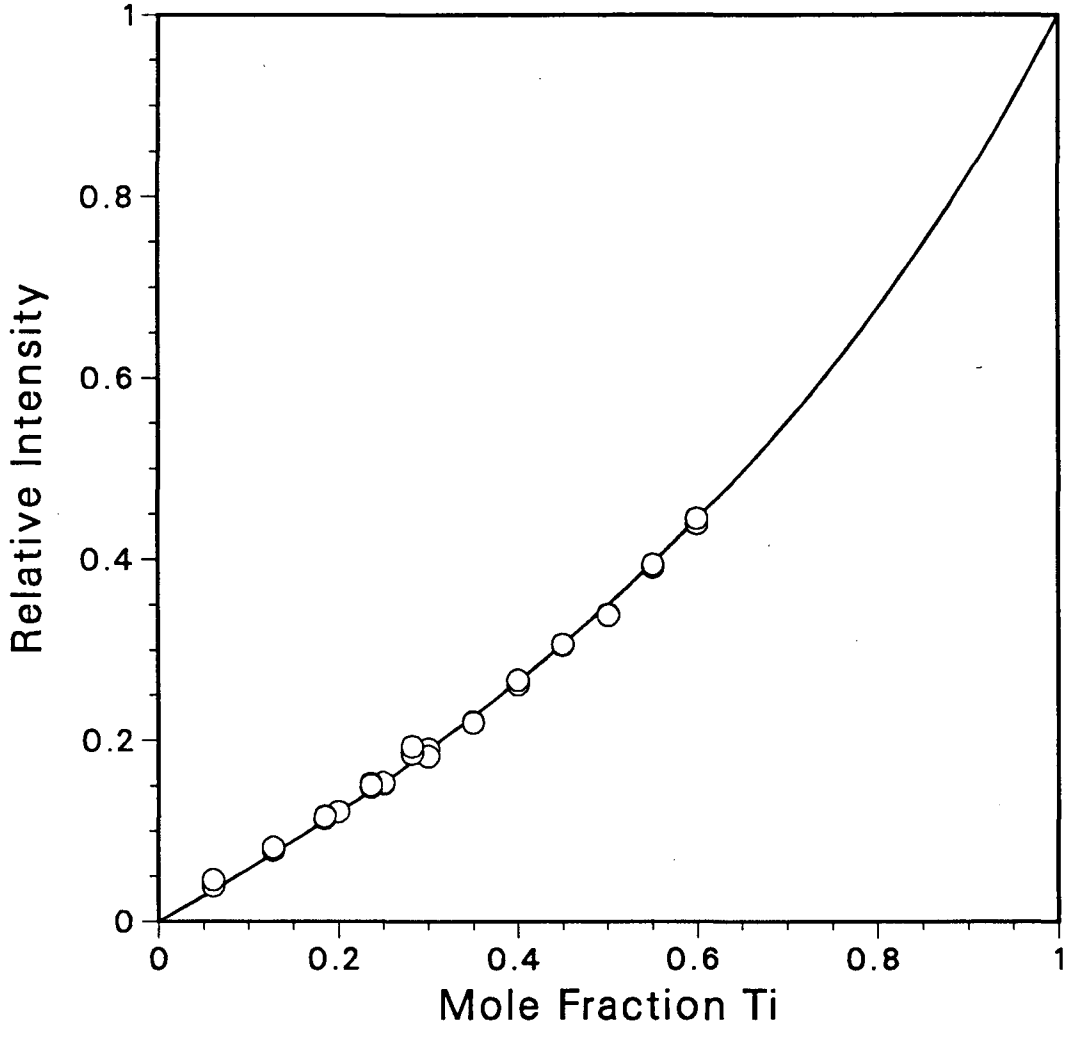

-- XBL 868-2907 --

Figure (2-5)
The relative intensity of Ti(K_α) and Pd(L_α) peaks as a function of x_{Ti} in Ti-Pd alloys. The curve is generated by the parameters presented in table 2-V.

Table 2-VI

Results for Ti-Rh Standards

$\bar{a}_{Rh,Ti} = 0.50$ $\bar{a}_{Ti,Rh} = 1.80$ $\lambda = 0.799$

x_{Ti}	intensity (cps) $K_\alpha(Ti)$	$L_\alpha(Rh)$	r	r_{calc}	% diff
	1.13	24.64	0.044		-1.285
0.044	1.89	38.42	0.047	0.031	-1.596
	0.87	32.14	0.026		0.447
	3.33	40.32	0.076		-0.424
0.101	3.62	40.62	0.082	0.072	-0.972
	3.13	37.16	0.078		-0.557
	10.00	42.49	0.191		-0.558
0.249	9.33	40.82	0.186	0.185	-0.111
	9.84	43.83	0.183		0.159
	16.39	40.08	0.290		-0.287
0.373	12.79	33.62	0.276	0.287	1.179
	15.23	38.26	0.285		0.265
	24.26	51.44	0.320		1.591
0.429	24.26	51.44	0.320	0.336	1.591
	24.56	51.79	0.322		1.470
	22.95	47.76	0.325		1.182
	23.58	37.72	0.385		0.172
0.484	23.58	37.72	0.385	0.386	0.172
	22.12	35.74	0.382		0.409
	18.53	29.62	0.385		0.155
	154.10	123.20	0.556		-0.401
0.651	154.10	123.20	0.556	0.552	-0.401
	146.30	120.70	0.548		0.377
	147.50	124.80	0.542		1.002
	157.90	99.50	0.613		-0.863
0.700	250.20	163.00	0.606	0.605	-0.071
	173.30	111.20	0.609		-0.433
	44.38	16.02	0.735		-1.341
0.800	45.57	16.15	0.738	0.721	-1.698
	279.90	112.10	0.714		0.732
	52.88	8.56	0.861		-0.910
0.900	48.85	7.60	0.865	0.852	-1.382
	56.35	9.40	0.857		-0.555
	57.67	4.03	0.935		-1.155
0.950	57.67	4.03	0.935	0.923	-1.155
	68.63	4.99	0.932		-0.920
	66.12	5.23	0.927		-0.365

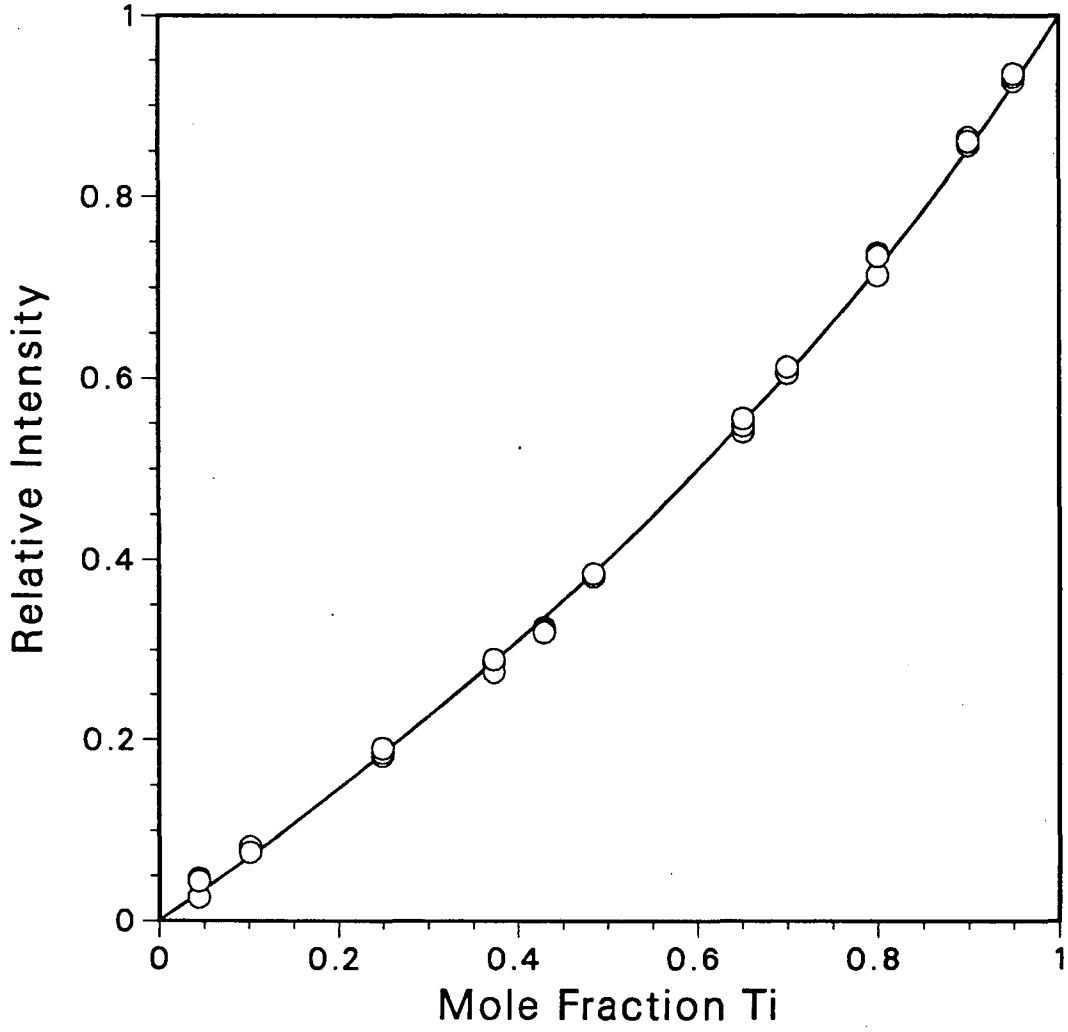

-- XBL 868-2908 --

Figure (2-6)
The relative intensity of Ti(K_α) and Rh(L_α) peaks as a function of x_{Ti} in Ti-Rh alloys. The curve is generated by the parameters presented in table 2-VI.

Table 2-VII

Results for Nb-Rh Standards

$\bar{a}_{Rh,Nb} = 1.60$ $\bar{a}_{Nb,Rh} = 1.10$ $\lambda = 0.678$

x_{Nb}	intensity (cps) L_α(Nb)	L_α(Rh)	r	r_{calc}	% diff
0.044	2.56	29.88	0.079	0.060	-1.903
	1.99	24.58	0.075		-1.492
	2.36	29.65	0.074		-1.401
	10.64	141.40	0.070		-1.018
0.210	8.73	21.23	0.291	0.290	-0.103
	8.24	21.62	0.276		1.438
	7.93	20.19	0.282		0.851
0.269	12.56	19.49	0.392	0.370	-2.180
	13.23	19.24	0.407		-3.737
	12.61	18.98	0.399		-2.909
0.332	14.77	17.69	0.455	0.452	-0.322
	12.37	14.61	0.458		-0.668
	14.61	17.33	0.457		-0.562
	67.30	85.83	0.439		1.231
0.423	82.42	70.40	0.539	0.562	2.245
	72.88	64.24	0.532		3.027
	87.39	71.66	0.549		1.233
0.601	114.40	40.67	0.738	0.744	0.633
	123.40	43.67	0.739		0.545
	129.40	46.24	0.737		0.733
0.936	41.90	2.00	0.954	0.971	1.653

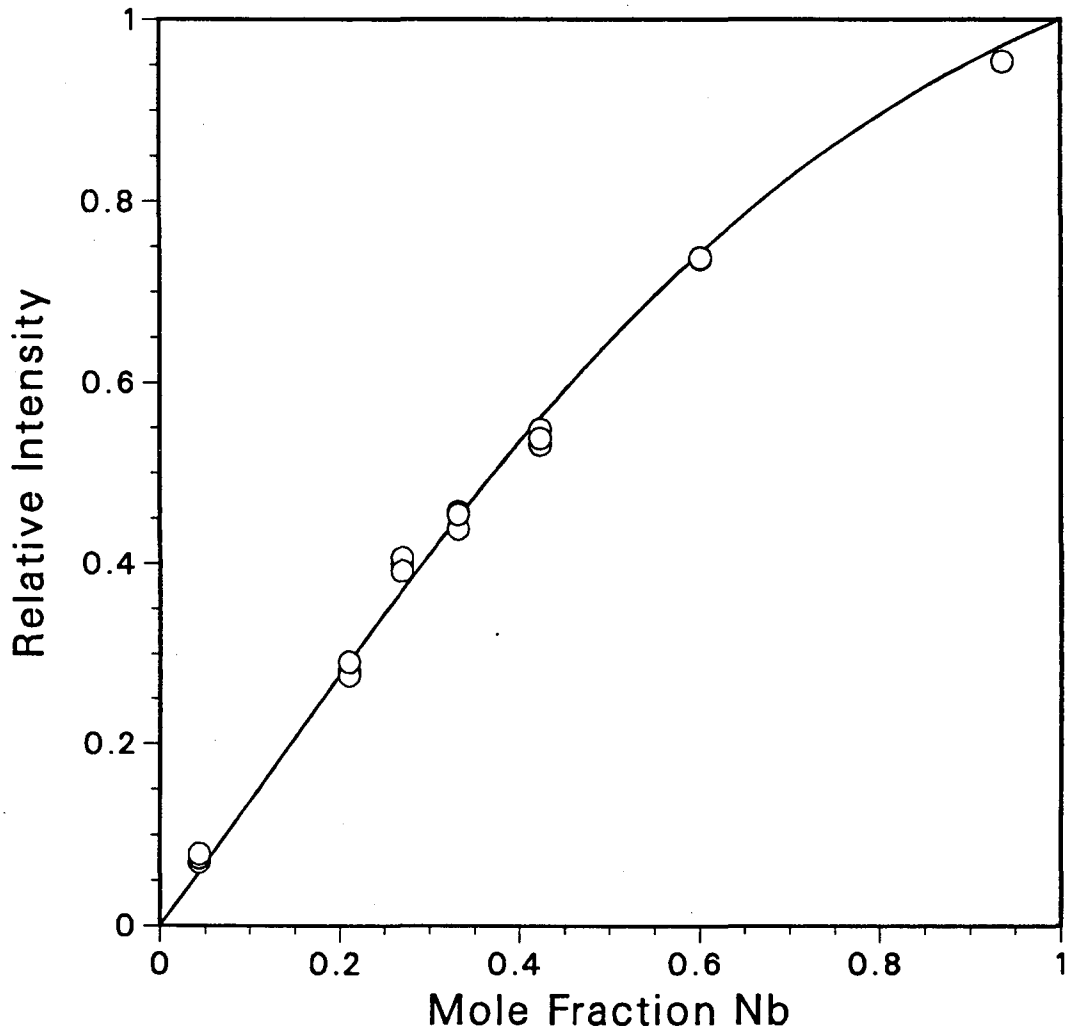

Figure (2-7)
The relative intensity of Nb(L_α) and Rh(L_α) peaks as a function of x_{Nb} in Nb-Rh alloys. The curve is generated by the parameters presented in table 2-VII.

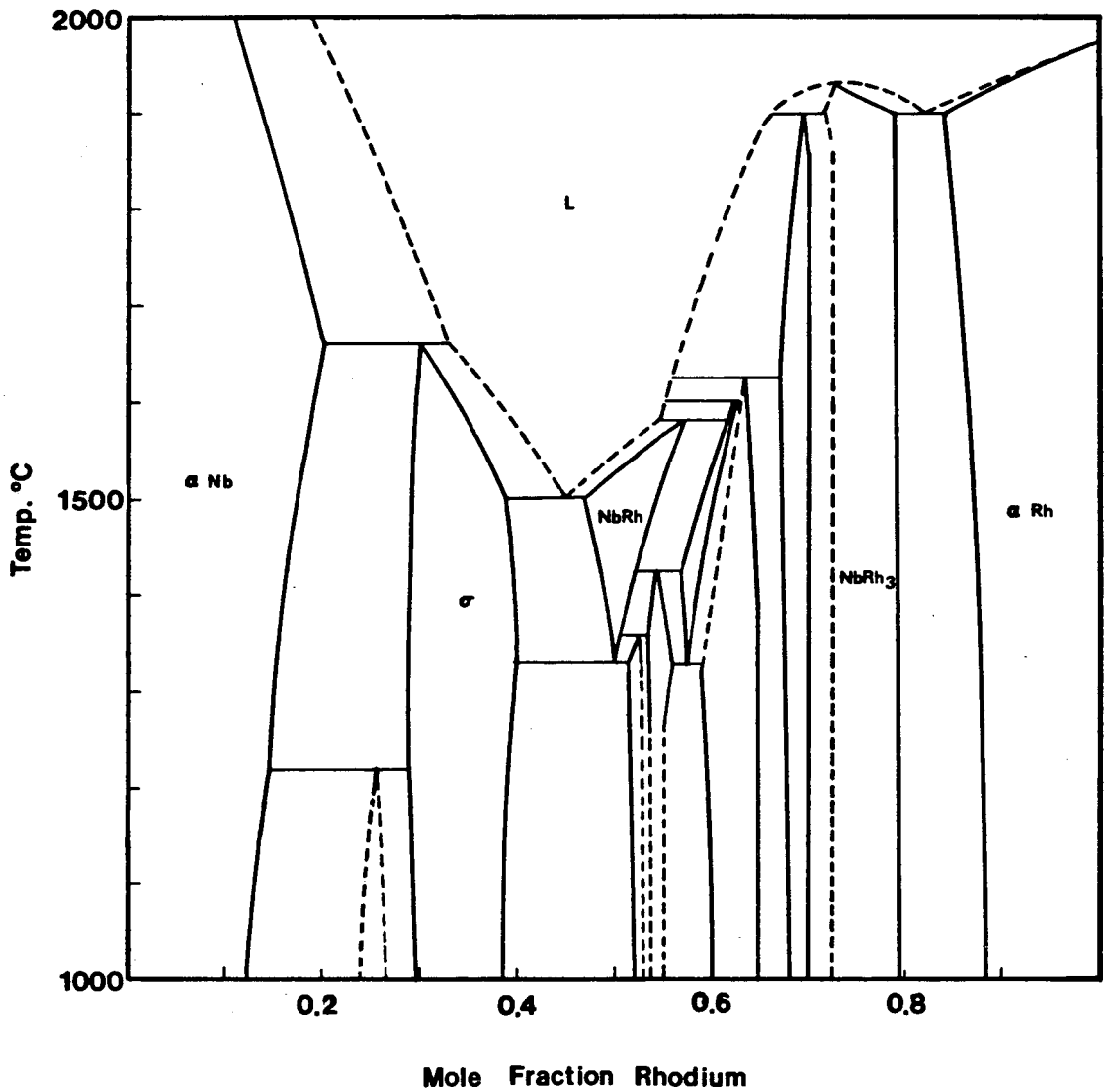

-- XBL 868-2910 --

Figure (2-8)
The niobium-rhodium phase diagram as determined by Ritter and Giessen [9].

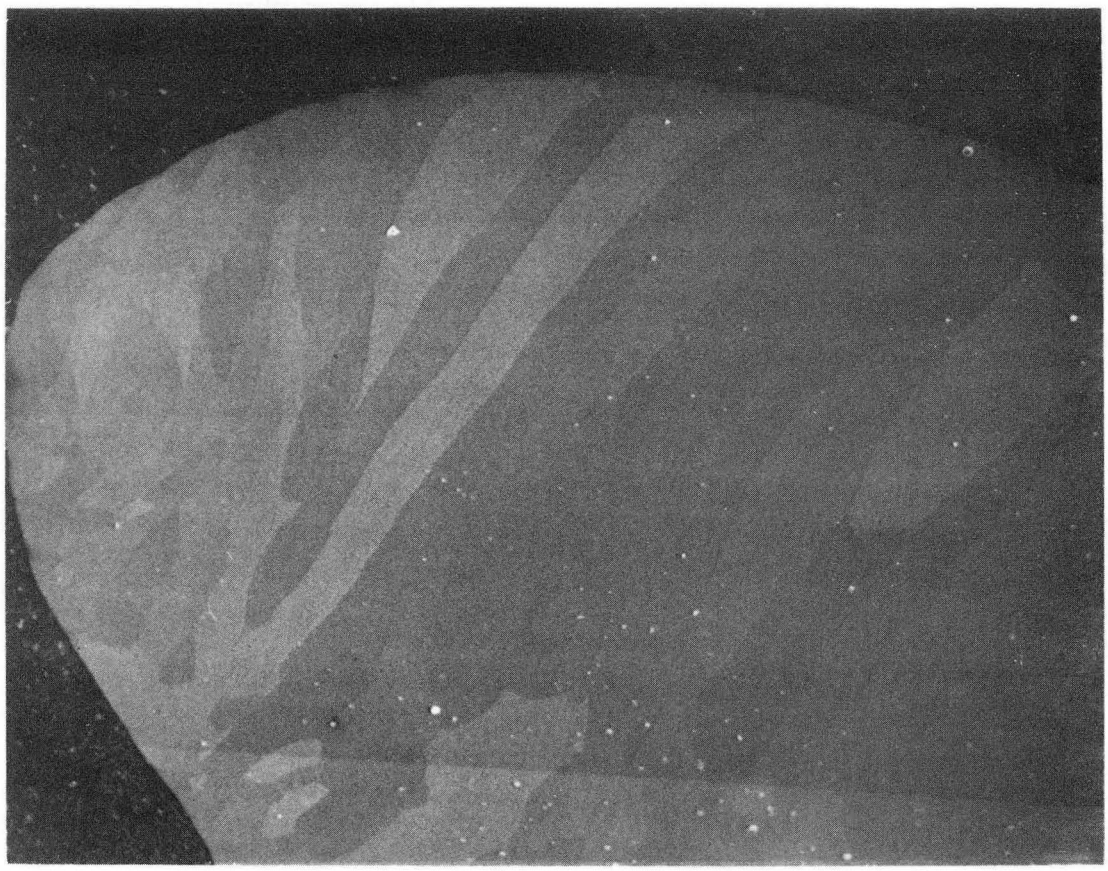

XBB 867-5539

Figure (2-9)

Scanning electron micrograph (20 X) of an Nb-Pd alloy button prepared by arc melting. The alloy has 2.7 atomic percent Nb and has been annealed at 1000° C for 4 hrs. Note that the grains extend from one side of the button to the other.

Chapter 3

Experimental Methods for the Measurement of Galvanic Voltages Generated by a Solid State Cell

3.1 Principles of Operation

The basic design of a solid state galvanic cell is very simple. The solid electrodes are made to intimately contact each side of a solid electrolyte. The EMF is then measured by electrical leads attached to each electrode. As was discussed in chapter 1 the cell functions because of the unusual ability of the solid electrolyte (superionic conductor) to conduct ions. The electrolytes of interest to this study are ones that conduct oxygen ions. There are several materials that have this property, most notable is calcia-stabilized zirconia (CSZ) which is of interest for use in fuel cells and is currently used in exhaust gas sensors for automobiles. Materials based on cerium, hafnium, and thorium oxides are also superionic conductors. They are all very refractory ceramic materials that share the same crystal structure in their ionically conducting form. Oxygen's relative ease of movement through the electrolyte's crystal lattice is a result of a large concentration of oxygen vacancies present in the crystal and the low activation energy required for an oxygen anion and a vacancy to exchange positions.

Thorium oxide has the fluorite crystal structure which is a fcc arrangement of thorium cations with the oxygen anions occupying all the tetrahedral interstitial positions of the thorium lattice. The structure is said to be "open" because

all the octahedral sites are unoccupied so that oxygen anions might move easily through the open lattice. Pure zirconium oxide is monoclinic at useful operating temperatures, while the tetragonal and cubic modifications are stable only at much higher temperatures. Its fluorite structure is formed, however, when amounts of calcium, yttrium, or a variety of rare earth or alkaline earth oxides are dissolved in it and it is for this reason the electrolyte is said to be stabilized. These oxide additions also play an important role in modifying the defect structure of the electrolyte as will be discussed.

3.2 Defect Structure of Solid Oxide Electrolytes

At any temperature above absolute zero all solids have a finite concentration of point defects. The defects that are important to the conductivity of a material are those that are charged such as electron-hole pairs, ion-pair vacancies (Schottky defects), and vacancy-interstitial pairs (Frenkel defects). The concentration of these defects is determined by thermodynamics. Frenkel, Schottky, and Wagner [1] realized that because of this, point defects could be treated as chemical entities in themselves.

Charged defects are of course subject to the restriction that electroneutrality be maintained throughout the crystal. It is known that anionic Frenkel defects are the predominant ionic defects present in oxides with the flourite structure. Thus electroneutrality requires

$$2C(O_i'') + C_e = 2C(V_O^{\cdot\cdot}) + C_h \tag{3-1}$$

where C_e and C_h are the concentrations of conduction band electrons and valence band holes. The other terms represent the concentrations of oxygen interstitials and oxygen vacancies denoted in the usual Kroger-Vink notation.

The conduction band in these ionic solids is primarily made up of cation orbitals while the valence band is made up of anion orbitals. This means that in thorium oxide a conduction band electron can be thought of as a Th^{+3} site while a valence band hole is equivalent to O^-.

Electrical conduction in these materials is the movement of charged defects under a potential gradient. The conductivity is to first order proportional to their charge, mobility, and concentration. Thus it is usually written as the sum of contributions from all the charged defects

$$\sigma = Fc_e q_e \mu_e + Fc_h q_h \mu_h + F\sum_i c_i q_i \mu_i \qquad (3\text{-}2)$$

where c, q, and μ represent concentration, charge, and mobility respectively and F is the Faraday constant. The first two terms are the contribution from free electrons in the conduction band and holes in the valence band while the third is a summation over all the ionic defects, i. Steele [2] has pointed out that the lowest observed electron or hole mobility is equal to or greater than the largest known ionic mobility. Thus, unless the concentration of ionic charge carriers is many orders of magnitude greater than the concentration of electronic defects the total conductivity will have contributions from two conduction mechanisms.

The defects are subject to a variety of chemical equilibria that serve to relate the concentrations appearing in equation (3-1). Worrell [3] has presented a concise description of the behavior of these oxide electrolytes and his method represents the approach taken by many studying solid electrolyte conductivity. Each of the relevant equilibria is used to construct a mass action type expression relating the concentrations of the various defects and an equilibrium constant. The important assumption made is that the long range interaction

between the charged defects can be neglected so that they then form an ideal solution. This approach has been surprisingly effective in describing the general behavior of the conductivity to changes in the chemical enviroment and chemical make up of the solid electrolyte and will be briefly summarized here so that the properties of the cell may be rationalized.

The equilibria between conduction band electrons and valence band holes as well as that between interstitial oxygen and oxygen vacancies are intrinsic to the solid electrolyte since they involve defects that are inherently present. Conduction electrons and holes may recombine by the equation

$$0 = e' + h^{\bullet} \tag{3-3a}$$

$$K_{3-3} = C(e')C(h^{\bullet}) \tag{3-3b}$$

The equilibrium between oxygen vacancies and interstitials is written

$$O_O = O_i'' + V_O^{\bullet\bullet} \tag{3-4a}$$

$$K_{3-4} = C(O_i'')C(V_O^{\bullet\bullet}) \tag{3-4b}$$

In addition the oxygen activity may be fixed by an external chemical equilibria such as the fixed partial pressure of oxygen in the atmosphere surrounding the electrolyte. The gaseous oxygen will react with the defects until equilibrium is achieved. In our experiments the oxygen partial pressure in the electrodes can be quite low. Under these conditions the predominant defects present will be oxygen vacancies and conduction electrons, so the relevant equilibrium is

$$O_O = V_O^{\bullet\bullet} + 2e' + \frac{1}{2}O_2 \tag{3-5a}$$

$$K_{3-5} = C(V_O^{\bullet\bullet})C_e^2 P_{O_2}^{1/2} \tag{3-5b}$$

Electroneutrality requires that $C(V_O^{\cdot\cdot}) = 1/2\ C_e$ so that rearrangement of equation (3-5b) gives

$$C_e = (2K_{3-5})^{1/3} P_{O_2}^{-1/6} \tag{3-6}$$

Thus that part of the total conductivity due to conduction electrons (n-type) will decrease with increasing P_{O_2} with a power of 1/6 if the concentration of vacancies is kept nearly constant.

Similarly at high partial pressure of oxygen the predominant defects are oxygen interstitials and holes in the valence band.

$$1/2\ O_2 = O_i'' + 2h^{\cdot} \tag{3-7}$$

which for the same assumptions as equation (3-6) gives

$$C_h = (2K_{3-7})^{1/3} P_{O_2}^{1/6} \tag{3-8}$$

This implies that the hole conduction or p-type conductivity will increase with increasing P_{O_2} with a power of 1/6.

Most electrolytes used, however, contain aliovalent cations which substitutionally replace thorium ions. This is the case when Y_2O_3 is dissolved in thoria. The presence of this new type of defect requires that the electroneutrality equation be modified to read

$$C_h + 2C(V_O^{\cdot\cdot}) = C_e + 2C(O_i'') + C(Y_{Th}') \tag{3-9}$$

$C(Y_{Th}')$ is easily made larger than the other terms on the right in equation (3-9) but it is only determined by experiment that this charge defect is predominantly compensated for by oxygen vacancies and not by holes. Subbarao et al. [4] demonstrated this by comparing the densities of YDT samples with that predicted assuming the formation of holes or the formation of oxygen vacancies. Thus equation (3-9) can be simplified to

$$C(V_O^{\cdot\cdot}) \approx 1/2\, C(Y_{Th}{}')\qquad (3\text{-}10)$$

The analysis that lead to equations (3-6) and (3-8) now results in

$$C_e = (2K_{3\text{-}5}/C(Y_{Th}{}'))^{1/2}P_{O_2}^{-1/4} \quad \text{or} \quad C_e = (\text{const})P_{O_2}^{-1/4}\qquad (3\text{-}11)$$

for low P_{O_2}, while for high P_{O_2}

$$C_h = (C(Y_{Th}{}')K_{3\text{-}7}/2K_{3\text{-}4})^{1/2}P_{O_2}^{1/4} \quad \text{or} \quad C_h = (\text{const})P_{O_2}^{1/4}\qquad (3\text{-}12)$$

Thus the P_{O_2} is now 1/4 and the magnitude of the electron and hole conductivity will depend on the yttrium concentration.

At an intermediate oxygen partial pressure the conductivities due to electrons and holes may both be small, compared to the ionic conductivity due to the abnormally high vacancy concentration. Thus the conductivity is expected to be independent of P_{O_2} over some range of oxygen partial pressure. Experimental measurements of total conductivity as a function of P_{O_2} are graphed in figure (3-1) for YDT and CSZ. At low P_{O_2} the electrolyte is an n-type conductor and at high P_{O_2} it is a p-type. The region in the middle is where the conductivity is nearly all ionic and is said to have an ionic transference number t_{ion} ($\sigma_{ion}/\sigma_{total}$) equal to one. This region is called the electrolytic conduction domain. Patterson [16] has reviewed the conductivity data on several oxide superionic conductors and assigned lower and upper P_{O_2} limits of the electrolytic domain as a function of temperature. It is known that YDT is an ionic conductor to a much lower P_{O_2} than CSZ while CSZ is better at higher partial pressures [16]. The lower boundaries are difficult to reproduce due to the effect of small amounts of impurities. The influence of these multiple valent impurities will be discussed in the next section.

3.3 Cell Kinetics

Measurement of true thermodynamic voltages is difficult for any type of cell since it is often subject to a variety of systematic errors. This is particularly true for high temperature solid state cells of the type used in this experiment. There are several sources of irreversible processes which can affect the measured EMF. They can be broadly classified into three main areas: electrode polarization, electrode passivation, and mixed potentials.

The solid oxide electrolytes used in these cells do not under all conditions have an ionic tranference number near one; i.e., an appreciable amount of their conductivity may be due to valence band holes and conduction band electrons. In the design of a cell each side of the electrolyte may have a different partial pressure of oxygen so that there is a thermodynamic driving force to move oxygen from the high P_{O_2} side to the low P_{O_2} side. An electrolyte in a galvanic cell allows the net flow of ions only when electrons flow through an external circuit. A potentiometer placed in this external circuit stops the flow of electrons and correspondingly stops the movement of oxygen ions through the electrolyte so that the EMF measured is that under open circuit (reversible) conditions. If, however, electrons are allowed to flow within the electrolyte as shown in figure (3-2), then oxygen ions may move even though no electrons flow in the external circuit. This unchecked flow of oxygen depletes the high P_{O_2} electrolyte-electrode interface of oxygen and oxidizes the low P_{O_2} electrolyte-electrode interface so that the measured EMF is that due to a cell under irreversible conditions. Electrodes with these characteristics are considered polarized since diffusion within the electrode may be slow. Diffusion potentials also exist within the electrolyte under these conditions as discussed by Bullard [7], and Wagner

[10].

There are several causes of electronic conduction in these materials. One is the effect of the partial pressure of oxygen disscussed in detail in the last section. Clearly, care must be taken to insure that the appropriate electrolyte is used for the partial pressures of oxygen in equilibrium with the electrodes. YDT has demostrated an ionic transference number of one to a very low P_{O_2} and is recommended for use at 1000° C to as low as 10^{-26} atm [5], while Patterson suggests 10^{-21} atm [16]. Lasker and Rapp [6] studied the influence of yttria concentration on ionic tranference number and found an optimum near 15 mole percent $YO_{1.5}$ in thoria. One would expect improvement by increasing yttrium addition since as was shown in the last section the oxygen vacancy concentration will increase with yttrium concentration. At higher concentrations, however, significant amounts of ordering are thought to occur which would decrease the mobility of the oxygen vacancies.

A very important source of electronic conduction is the presence of aliovalent impurities that may assume several oxidation states. Vest and Tallan [8] observed appreciable electronic conductivity when small amounts of iron chromium and vanadium were added to CSZ. There is no doubt that these impurities will modify the electronic defect concentration since they can either provide conduction electrons or valence band holes. The large effect by such small amounts of iron impurities compared with the amount of calcium or yttrium is not rationalized by such a simple picture. Kroger [9] has proposed that in actuality many of the oxygen vacancies introduced by calcium or yttrium doping are not free but are clustered about the Ca or Y. This would imply that the concentration of free vacancies and iron impurities are

comparible.

Electrode passivation concerns the rate at which the electrochemical process of interest proceeds. The rate of an electrochemical reaction is described by the exchange current density, i_o, which is completely analogous to the rate constant of a normal chemical reaction. Electrochemical reactions proceed with the movement of charge so rates are in terms of a current density. For small overvoltages the current density at an electrode is a linear function of overvoltage,

$$i = \frac{i_o F \eta}{RT} \tag{3-13}$$

which serves as a definition for i_o. The overvoltage is η, F the faraday constant, R the gas constant, and T the temperature. The exchange current density plays a fundamental role in the measurement of cell voltages since it is a measure of how reversible the electrode is. The situation is depicted in figure (3-3). A potentiometer works by applying the voltage necessary between two leads so that no current flows. What a potentiometer considers to be zero current depends on the potentiometer. In figure (3-3) the zero current level is the quantity Δi. For a given Δi the electrode with the larger i_o will have the better defined equilibrium voltage since the error in determining the necessary voltage will be smaller (see equation 3-13). Thus in order to measure accurate EMF's one must use a potentiometer that draws a minimum of current. Such a potentiometer will have an input impedence much larger than the total cell resistance.

The exchange current, i_o, must also be made as large as possible. i_o contains all the kinetic information of the electrochemical reaction such as the concentrations of reactants and products as well as rate constants. Very little work

has been done on the kinetics of the solid electrolyte - solid electrode interface especially in cases where the electrode has several phases. Worrell and Iskoe [11] have proposed a model for the electrochemical reactions occuring at a metal-metal oxide electrode on a solid electrolyte. They assume that the rate of the electrochemical reaction is completely controlled by diffusion of oxygen through the metal grains of the electrode. It is a simple matter to show that the exchange current density that results from this assumption is

$$i_o = \frac{2(Dc)F}{\Delta y} \tag{3-14}$$

where (Dc) is the solubility-diffusivity product of oxygen in the metal phase and Δy is a characteristic length for oxygen diffusion in the electrode. Δy is assumed to be the average size of the metal grains in the electrode. They had great success predicting exchange currents from known solubility- diffusivity products in the copper, iron, and nickel. More recently Iwase et al. [12] have applied this technique to Mo,MoO_2 electrodes.

Inspection of equation (3-14) shows that in order to increase the reversibility of the cell the metal grains in the electrodes should be made as small as possible to minimize the diffusion resistance. This mechanism is not the only one that may be important in these cells because electrodes containing only oxides are known to provide fast enough kinetics to be reversible. Several binary oxide electrodes, such as NbO_2–$Nb_{12}O_{29}$, are in fact used for reference electrodes . Thus electrochemical reactions in these cells must also occur with the oxide directly.

Another way an electrode may be passivated is when a reaction occurs between it and the electrolyte. These reactions leave a product phase separating

the electrolyte from the bulk electrode. One of the advantages of thorium oxide over zirconia is its improved chemical stability. Reactions are, however, known to occur between the doping element in the electrolyte and common electrode materials. Worrell reports [13] that $YFeO_3$ forms at temperatures as low as 900° C between YDT and Fe-FeO electrodes. A bluish product layer has been attributed to $YNbO_4$ when YDT is reacted with NbO_2,$Nb_{12}O_{29}$ at 1050° C or higher [14]. This compound and other yttrium niobates have been the subject of a recent crystallisation kinetics study [15].

The electrode-electrolyte interface is invariably in contact with a gaseous phase which is usually purified helium or argon. Electrochemical reactions can occur with chemical species in the gaseous phase and may lead to a mixed potential. To describe this condition consider the hypothetical situation depicted in figure (3-4). A solid electrolyte is bounded on one side by a reversible reference electrode with a fixed partial pressure of oxygen $P_{O_2,ref}$. The other side has solid electrode consisting of two oxides, MO and MO_2, as well as a gaseous atmosphere of helium. The helium is contaminated with a small amount of oxygen with partial pressure, P_{O_2}, but because of the slow oxidation kinetics of the electrode this pressure is actually higher than that one would calculate from equilibrium in the reaction

$$MO_2 = MO + 1/2\ O_2 \tag{3-15}$$

Two electrochemical reactions are possible in this situation,

$$MO + O^{-2} = MO_2 + 2e^- \tag{3-16}$$

$$1/2\ O_2 + 2e^- = O^{-2} \tag{3-17}$$

In these equations we have ignored the mechanistic subtleties involved with the

transfer of two electrons and mean them only to represent two overall electrochemical reactions. If equilibrium could be achieved only with respect to reaction (3-16) then the EMF generated by the cell would be

$$\epsilon_{MO,MO_2} = -(RT/4F)\ln(P_{MO,MO_2}/P_{O_2,ref}) \tag{3-18}$$

where P_{MO,MO_2} is the partial pressure of oxygen in equilibrium with the oxides. If reaction (3-16) were eliminated, however, then the observed EMF would be

$$\epsilon_{O_2} = -(RT/4F)\ln(P_{O_2}/P_{O_2,ref}) \tag{3-19}$$

Note that these voltages are different for any situation where the electrode is not in equilibrium with the gas.

The situation where both reactions (3-16) and (3-17) occur can be understood by use of the kinetics of each of the reactions. Figure (3-5) shows a plot of the current response as a function of electrode potential for each of the reactions separately as well as their sum. The curvature of each of the indivdual responses is a result of the Butler-Volmer type kinetics usually found in electrochemical reactions and/or diffusion control of species involved in the reaction. The parts of the curves near their respective overvoltages of zero are the regions where the linearized Butler-Volmer equation, (3-13), may be used. The potential that is actually measured is that where the net electrode current response is zero and is in general different from either of the individual potentials as shown in figure (3-5).

The exchange current densities of each of the reactions determines where the measured potential lies between ϵ_{O_2} and ϵ_{MO,MO_2}. If these two potentials are not too far apart both reactions can be described by equation (3-13). As shown in figure (3-6) the effective electrode response will be

$$i = \frac{F i_{o,tot}}{RT}(\epsilon - \epsilon_{eff}) \tag{3-20}$$

where $i_{o,tot} = i_{MO,MO_2} + i_{O_2}$ and ϵ_{eff} is given by

$$\epsilon_{eff} = \left(\frac{i_{o,MO,MO_2}}{i_{o,MO,MO_2} + i_{o,O_2}} \right) \epsilon^{o}_{MO,MO_2} + \left(\frac{i_{o,O_2}}{i_{o,MO,MO_2} + i_{o,O_2}} \right) \epsilon^{o}_{O_2} \tag{3-21}$$

Equation (3-21) means that the reaction with the higher exchange current will have a potential closer to that measured. One expects that the exchange current for a reaction will be proportional to the concentration of reactants to some small power just as in any rate expresion. For a gaseous reactant, concentration is equivalent to partial pressure, thus as the partial pressure of the contaminant is reduced the exchange current is decreased so that the other reaction should have greater influence on the measured voltage.

Although this example is a bit contrived it can be used to illustrate why a cell design where both electrodes are not physically isolated from one another will work in some cells and not in others. Consider a cell where the electrodes on each side of the electrolyte are in contact with the same gaseous enviroment. If the electrodes are Nb,NbO and NbO,NbO_2 then the electrodes possess different equilibrium oxygen potentials. The NbO,NbO_2 electrode will contaminate the gas with an amount of oxygen too high to be in equilibrium with the Nb,NbO electrode. The effect will be negligible, however, because the magnitude of the partial pressures at operating temperatures is less than 10^{-20} atm and can not impart a significant current drain on the reactions involving only the solids. The situation is quite different when an Mo,MoO_2 electrode is used. The partial pressure of oxygen in equilibrium with this electrode is also very low but there is a significant partial pressure of molybdenum oxide species. These gaseous

molybdenum oxides may undergo electrochemical reactions and transport molybdenum and oxygen throughout the chamber. The use of this type of electrode requires that the two electrodes be separated into different compartments so that gaseous transport can be prevented.

As another example consider two gas streams of helium one contaminated with just oxygen and the other with carbon oxides. If both are passed over an oxygen getter they may both emerge with nearly the same thermodynamic partial pressure of oxygen. The stream with the carbon contamination, however, may have an appreciable partial pressure of CO since the carbon has reduced the chemical activity of the oxygen. The two streams have very different electrochemical behavior because in the former case the partial pressure of electrochemically reactive species is very low, while in the latter it is very high. The larger contaminant partial pressure may increase the exchange current density for the parasitic reaction so much that it could dominate the electrode kinetics even though both streams by themselves would give the same equilibrium voltage.

3.4 Arrangement of the Cell

The basic design of the experiment is fashioned after that used by Meschter and Worrell [17]. The cell furnace and gas purification system are shown in figures (3-7) and (3-8). A schematic of the control and measurement system is presented in figure (3-9).

The high temperatures required to perform the experiment were provided by a specially designed three zone furnace and control system. The 30 in. cell furnace [21] had three independently controlled and powered Kanthal heating

elements that provided a 3.5 in. diameter hot zone. The setpoints of the two end sections were fixed to the temperature of the center section so that the load on the end elements would work to offset the heat loss out the ends of the tube. The three temperature controllers and SCR power supplies were manufactured by Eurotherm Corporation [22]. This technique was very successful in providing a 12 in. constant temperature zone accurate to within 0.2° C. in the center section of the furnace.

A 99.8% alumina tube (2 in. i.d., 0.125 in. wall, 24 in. length) was used to enclose the cell. The tube was closed at one end and specially ground on the open end so that it permitted a leak tight seal to be made using a Viton O-ring and a watercooled brass collar. Electrical noise from the furnace windings was eliminated by a grounded Kanthal sheath placed between the furnace elements and the cell tube. A stainless steel end cap was bolted to the top of the collar using another Viton O-ring to make the seal. This cap served as the mounting surface for all the support members used to hold the cell together. The main structural support was provided by a solid 99.8% alumina rod (1/2 in. dia., 16 in. long) which fit into a sleeve in the end cap.

Two 1/8 in. dia. alumina tension rods and an alumina disk were used to keep the cell under compression during operation. The ends of the tension rods had threads ground in them so that connections could be made. Special stainless steel fittings were used to attach these rods to stainless steel springs fixed to the end cap. The ends of the rods in the hot zone passed through holes in the alumina disk. Two tantalum nuts could then be screwed onto the rods so that the disk would compress the cell assembly against the support rod.

The cell assembly consisted of an electrolyte pellet sandwiched by two electrodes. The EMF leads were made of 20 mill platinum wire that were spot welded to two polished platinum disks. These disks were placed on the ends of the two electrodes so that they would also be held under compression. The leads were insulated by hollow alumina rods and alumina beads up to ceramic feedthroughs welded in the end cap. Alumina or thoria spacers were used between the cell assembly and the alumina disk to account for any variation in the thickness of the electrodes of electrolyte. They were choosen to keep the cell in roughly the same amount of compression each time it was run. The temperature of the cell was measured by a Pt-10%Pt,Rh thermocouple placed within 1/16 in. of the cell. Once secured to the end cap the cell assembly and support pieces were mounted vertically in the cell tube so that the end cap was on top.

During operation the cell chamber was continuously flushed with inert gas, which was made to pass down the length of the cell tube through an alumina tube to a forechamber below the cell assembly. This chamber was constructed from 10 mill tantalum sheet spot welded into the form of a tube and was packed with corrugated zirconium foil [19]. Dushman [20] has recommended the use of zirconium for an oxygen getter since experiments indicate that oxygen dissolution into the bulk of the metal at 1000° C is fast and thus the surface does not become coated with an oxide. The gas would then flow over the zirconium and then up past the cell to a exit in the end cap. Additional zirconium foil was wrapped around the cell assembly taking care to insure that it would not touch the electrolyte, electrodes or any of the electrical leads. The cell would not function without the presence of gettering material even when the gas was pretreated in an external gettering chamber. Presumably, contaminants

adsorbed on the alumina surfaces were enough to ruin the measurements. The end cap surface was protected from radiative heating by a series of tantalum heat shields mounted between it and the hot zone.

The inert gas used to flush the cell chamber was purified helium. Ultrapure helium (99.999%) [18] was first passed through a stainless steel tube immersed in a liquid nitrogen bath. The gas (now free of condensables) would then flow through a hot Rene 41 stainless steel tube (5/8" i.d.) packed with zirconium sheet [19]. The sheet was corrugated and rolled tightly into the tube in order maximize the surface area available for reaction with any oxygen containing species present in the helium. The tube passed through two Kanthal-wound furnaces with hot zones roughly 6 to 8 in. in length. During operation the first furnace was set to 1000° C while the second was at 600° C to 700° C. Hydrocarbon contaminants would crack on the high temperature zirconium surface forming zirconium carbide and hydrogen. The solubility of hydrogen in the metal at high temperature is very low compared to that at 600° C so that the low temerature zone could be used as a hydrogen absorber.

After exiting the cell furnace through the end cap, the gas would pass through a 1/4 in. stainless steel tube in a liquid nitrogen bath to a rotometer so that its velocity could be measured. The gas would then flow through a throttling valve and on to a mechanical pump. This system was very effective in preventing any back flushing of contaminants during transients in the flow of gas. Steady state flow rates were routinely 25 cc/min or lower. Check valves were ineffective at these low flow rates.

3.5 Control and Measurement

Figure (3-9) is a schematic of the control and measurement system designed and built at M.M.R.D.,L.B.L. EMF measurements were made using a Keithley [23] Model 610C solid state electrometer with an input impedance of greater than 10^{14} ohms with shielded coaxial cable between the cell cap and the electrometer. This model is equipped with a one milliamp output for full scale input deflection. The signal generated by this output was connected to a Doric [24] potentiometer that is part of the computerized data acquisition system.

This system was a slightly modified version of the one designed by Katz, Bethly, and Severns [25] which is based on a simple Z80 microprocessor on a CPU card built by Monolithic Systems [26] for use in industrial environments. It conforms to the INTEL Multibus standard used to connect with peripheral devices. The CPU has 48 programmable I/O lines used for input from the Doric potentiometer and a Doric trendicator used to measure the cell temperature. In addition a D/A card provided a programmable analog output to be used for the furnace setpoint. A 16k EPROM card was installed with a BASIC interpreter [27] and machine language routines for reading temperature and EMF as well as changing the furnace setpoint.

The most significant change made to the system design was an improvement to data and program storage which previously had been a simple teletype equipped with a paper tape storage device. Instead of installing more modern disk storage devices compatible with Multibus it was decided to replace the teletype with an IBM PC [28] and write appropriate software so that data collected by the MSC CPU [26] could be stored on the S-100 format used by the IBM PC. This approach led to immediate conversion to a more contemporary format

which was a great aid in processing and visualizing the data.

3.6 Electrode Preparation and Polishing

The electrodes were prepared in exactly the same way as the samples used in the oxide-alloy equilibration study described in chapter 2 except that the pellets were always kept dry following annealling. It was discovered that those samples that had been wet polished before use in a cell would give EMF measurements that would vary wildly whenever the temperature was changed. Figure (3-10) is a EMF and temperature trace as a function of time for the cell,

$$NbO,NbO_2/YDT/NbO_2,Nb_{12}O_{29} \tag{3-22}$$

where the electrodes had been wet polished and dried before use. The EMF varies to values almost twice that expected by the known thermodynamics of the oxides used in the cell. Clearly this phenomenon is the result of residual water absorbed within the electrodes. Even after hot pressing, the electrode pellets are still porous due to the change in volume accompanying the change from reactants to products in the annealling step. The high surface area generated by the pores then absorbed water which would crack and liberate hydrogen when heated to high temperatures. This idea is supported by the fact that the electrolyte could be sonic cleaned in ethyl alcohol followed by drying and still perform well. The electrolyte is very near theoretical density, as will be discussed in chapter 4, so that it has a minimum of surface area to absorb water.

The interfacial contact between the electrodes and the electrolyte must be good, so that these surfaces are required to be flat. A device was made to hold the electrode pellets at a fixed angle with respect to a rotating polishing wheel. The pellet was secured to the brass device by double sided tape. A small ledge

milled in the brass prevented the pellet from being knocked off by the lateral force imparted to it during polishing. This technique prevented the rounding of the edges that occurs when pellets are held by hand when polished. Clean and dry silicon carbide paper was used as the polishing medium. The grit sizes used were 320 followed by 600. When both sides of the electrode are polished in this way two flat and parallel faces are produced. Any residue that might be left from the tape was removed by lightly polishing the pellet faces by hand on 600 grit silicon carbide paper.

Chapter 4 details the preparation of the yttria doped thoria used as the solid electrolyte in these experiments. It was made to a slightly larger diameter than the electrodes (1/2 in. compared with 7/16 in.) so that the curvature of the edges imparted when it was polished by hand had little consequence. In addition it was very hard so that this curvature was only slight. This was fortunate since it meant that the YDT pellets could be polished inside a glove box which prevented the contamination of the laboratory. The polishing was again done on silicon carbide paper starting with grit size 320 and ending with 600.

3.7 Cell Operation

The polishing of the electrodes and electrolyte as well as the assembly of the cell were performed without touching any of the parts to be used with bare hands. Surgical gloves that had been washed with soap and water followed by ethyl alcohol were worn throughout the assembly process. The ceramic parts to the apparatus were frequently fired in air for several hours at 1000° C.

After the conductivity of all the leads was checked the cell assembly and support would be inserted in the cell tube and bolted into place. The chamber

would be evacuated by opening a gate valve between the gettering furnaces and the cell tube. Pumping was provided by a mechanical pump through a molecular sieve. The liquid nitrogen traps in the system and between the system and the mechanical pump would be filled once the pressure had reached 50 microns. The cell furnace would then be slowly ramped up to 200° C under these conditions for several hours in order to degas the chamber. Helium flow would then be started and the gettering furnaces brought to operating temperatures. After an hour the experiment would begin by ramping the cell furnace through the preprogramed temperature schedule.

Typical ramp rates between constant temperature periods were 100° C/hr to 150° C/hr. These slow ramp rates were needed to prevent cracking of the alumina cell tube which was much more susceptible to thermal shock than any of the other parts. Temperature, EMF, and the time were recorded approximately every minute during the entire experiment. Control of the temperature was within 0.3° C during the constant temperature periods the duration of which was assigned based on experience. Two to three hours was usually sufficient at temperatures near 1000° C to obtain voltages constant to within 0.2 millivolt for two hours. Much longer times were needed for lower temperatures. Attempts to write the operating program so that it would not proceed to the next constant temperature period unless the EMF had been constant met with little success. The behavior of the cells varied so much between electrode materials that appropriate criteria could not be predicted.

Several simple tests were used to check the reversibility of the cell .Temperature schedules were also choosen so as to collect EMF data on both increasing and decreasing temperatures in order to check for the presence of

irreversible changes in the cell with time. The gas flow was changed or even stopped during an experiment to check for variation in the measured voltage. A change in the EMF when the helium flow rate was changed would indicate reactions with gaseous contaminants. On several cells the EMF leads were shorted to see if the voltage would recover when reconnected to the electrometer.

The duration of the experiment was from two to three days. Figure (3-11) is a typical trace of a cell's EMF and temperature schedule as a function of time. The protocol for accepting an EMF as the reversible one was based not only on it being relatively constant with time (± 0.2 millivolt/hr) but also on the cell's behavior to some of the tests discussed above and its performance at other temperatures.

Chapter 3 References

[1] There are many references but those frequenly cited are; J. Frenkel, Z. Phys. 35(1926)652-669; W. Schottky, Z. Phys. Chem. B29(1935)335-355; C. Wagner, W. Schottky, Z. Phys. Chem. B11, (1930)163-210; C. Wagner, Z. Phys. Chem. B22,(1933)181-194

[2] B.C.H. Steele ,"Solid State Chemistry", Inorganic Chemistry, Series One, Vol. 10, ed. L.E.J. Roberts (Butterworths, London 1972) p.117-149

[3] W.L. Worrell, "Topics in Applied Physics", Vol. 21, ed. S. Geller (Springer-Verlag,New York,Berlin,1977) p.143-68

[4] E.C. Subbarao, P.H. Sutter, J.Hrizo, J. Am. Cer. Soc. 48[9](1965) p.443-46; also see J.E. Bauerle, J. Chem. Phys. 45,(1966)4162

[5] T.H. Estell, S.N. Flengas, Chem. Rev., 70(1970)p.339-76

[6] M.F. Lasker, R.A. Rapp, Z. Phys. Chem. N.F., 49(1966)p.198

[7] G.L. Bullard, Ph.D. dissertation, Dept. of Chemistry, U.C. Berkeley, 1978

[8] R.W. Vest, N.M. Tallan, J. Appl. Phys. 36[2](1965)p.543-47

[9] F.A. Kroger, J. Am. Cer. Soc., 49[4](1966)p.215-18

[10] C. Wagner, "Adv. in Electrochemistry and Electrochemical Eng." ed. P. Delahay (Wiley Interscience, Vol. 4, 1966) p.1-46

[11] W.L. Worrell, J.L. Iskoe, "Fast Ion Transport in Solids", ed. W. vanGool, (North Holland Publishing Co., 1973)p.513-21

[12] M. Iwase, T. Kanazawa, T. More, Solid State Ionics, 2(1981)p.331-36

[13] W.L. Worrell, "Thermodynamics, Vol. 1", (International Atomic Energy Agency, Vienna, 1966),p.131

[14] P.J. Metscher, Ph.D. dissertation, University of Pennsylvania, 1974

[15] I.A. Bondar',M.G. Degen, L.N. Koroleva, E.V. Morozova, Zhurnal Neorganicheskoi Khimii, 21(1976)p.349-53

[16] J.W. Patterson, J. of Electrochem. Soc., 118[7](1971)p.1033-39

[17] P.J. Meschter, W.L. Worrell, Met. Trans. A, 7A(1976)p.299- 305

[18] Scientific Gas Products Inc., Santa Clara, CA

[19] 99.8%, 0.127mm thick, Johnson Matthey Inc., Seabrook NH, cold rolled to 0.004 in. thick before using

[20] S. Dushman, "Scientific Foundations of Vacuum Technique", (John Wiley & Sons, New York; Chapman & Hall Ltd., London, 1949) see p.670 for details of clean up by zirconium and titanium.

[21] Lindberg 54357 Tube furnace,Lindberg Co., Watertown WI

[22] Eurotherm Corp., Reston, Virginia; digital temperature cotrollers model No. 919, SCR units model No. 932.

[23] Keithley Instruments Inc., Cleveland, Ohio

[24] Doric Scientific, San Diego, CA

[25] J.E. Katz, M. Bethly, J. Severns, "A Microprocessor Furnace Control System", Lawrence Berkeley Laboratory, LBID-142

[26] Monolithic Systems Corp., San Diego, CA

[27] P.R. McGoldrick, J. Dickinson, T.G. Allison, "LLL 8080 BASIC II Interpreter User's Manual", UCID-17752, 1978

[28] International Business Machines Corporation

[29] J.W. Patterson, E.C. Bogren, R.A. Rapp, J. Electrochem. Soc., 114[7](1967)p.752-58

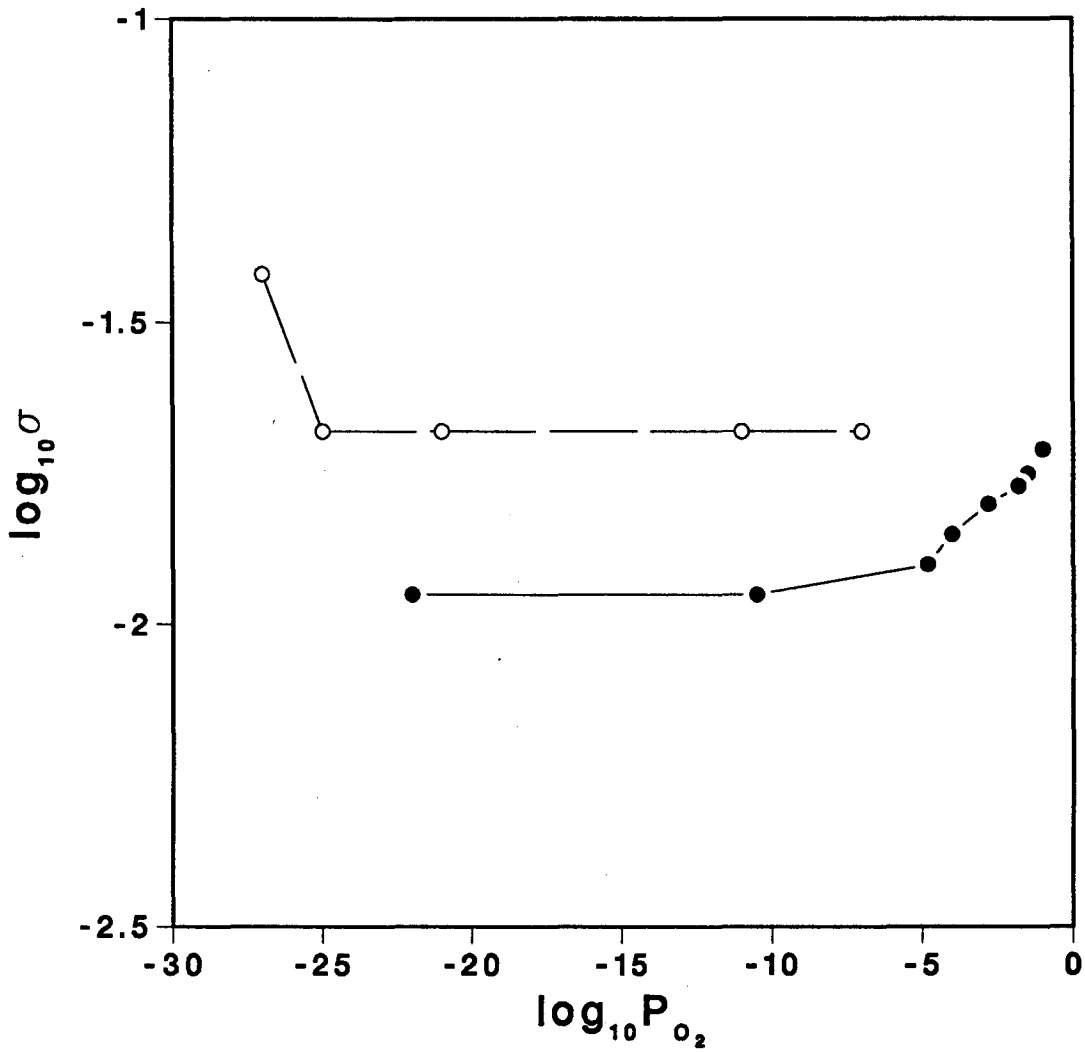

-- XBL 868-2911 --

Figure (3-1)
Electrical conductance of solid electrolytes versus $\log_{10}P_{O_2}$ at 1000° C. The filled circles are the data obtained by Lasker and Rapp [6] for $(ThO_2)_{0.85}(YO_{1.5})_{0.15}$. Open circles were data measured by Patterson et al. [29] on $(ZrO_2)_{0.85}(CaO)_{0.15}$.

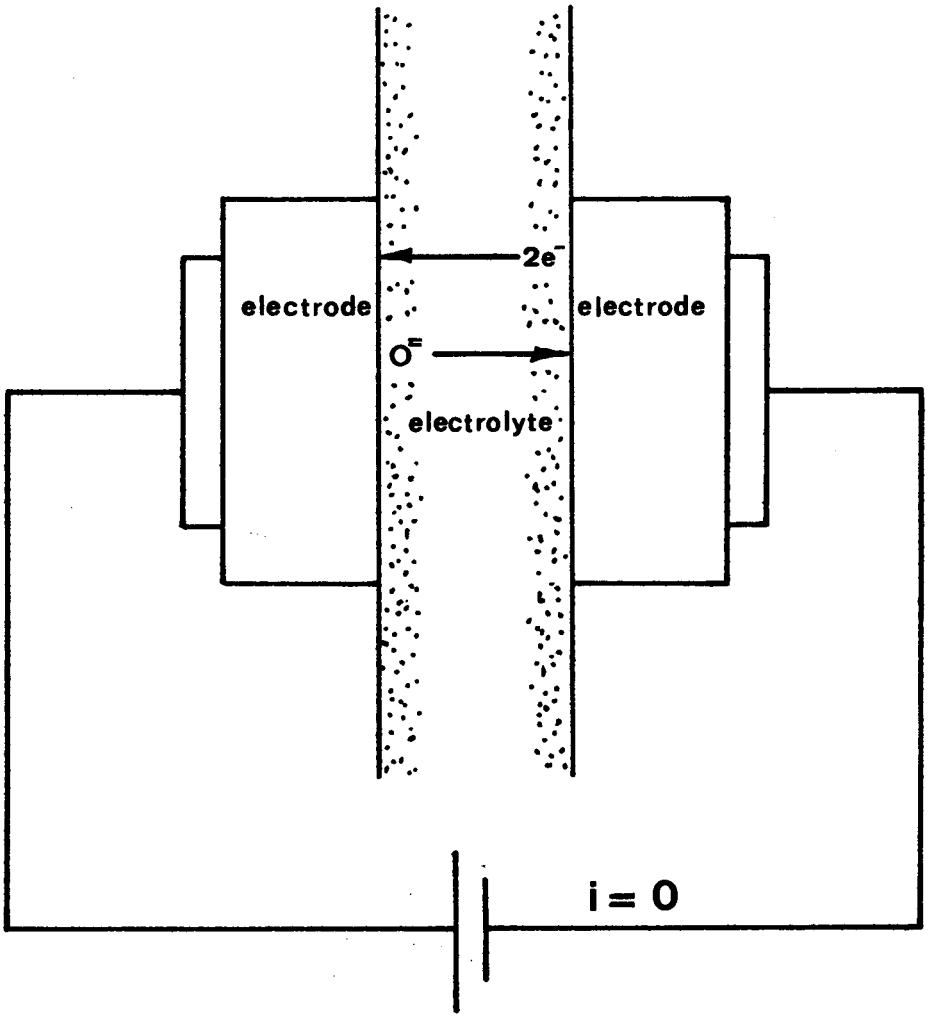

-- XBL 868-2912 --

Figure (3-2)
The short circuit of an high temperature galvanic cell by electronic leakage current.

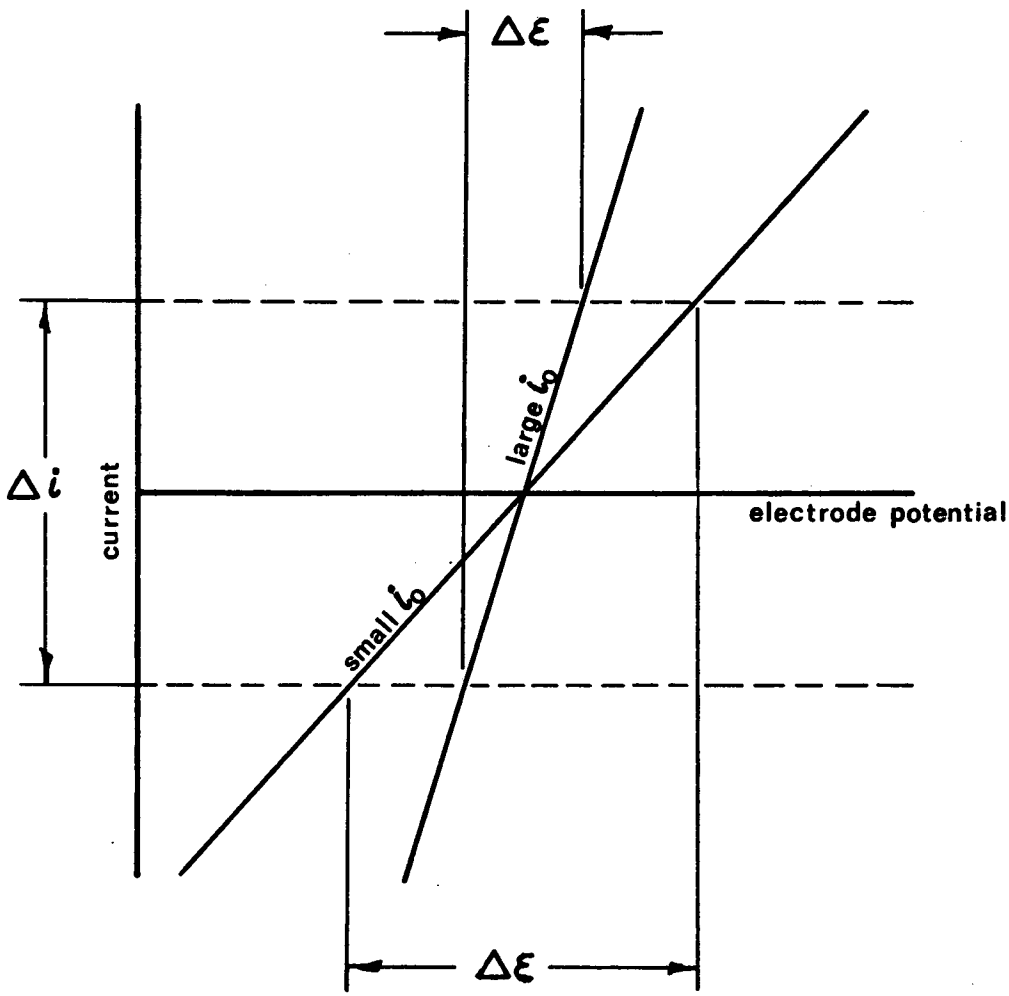

-- XBL 868-2913 --

Figure (3-3)
The effect of exchange current density on the performance of galvanic cells.

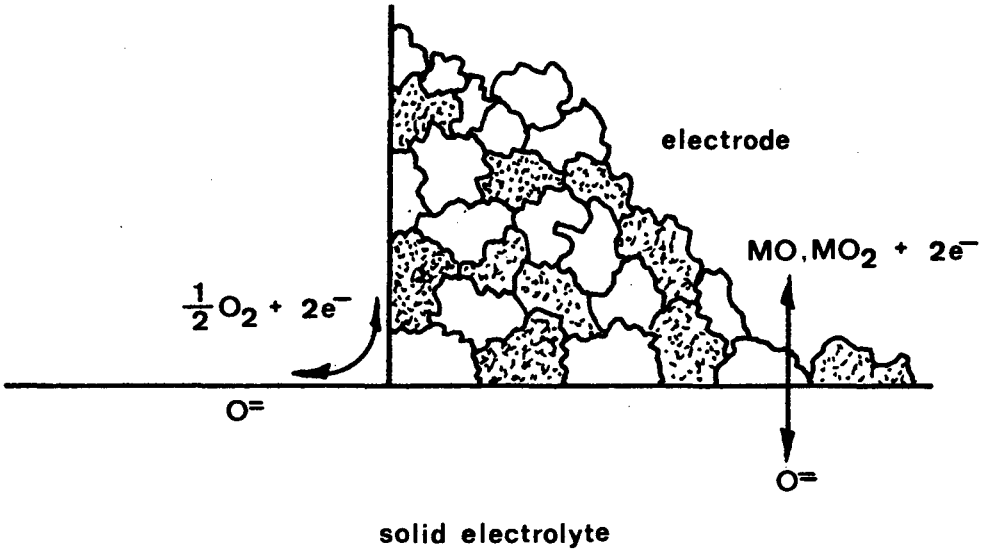

-- XBL 868-2914 --

Figure (3-4)
Parallel electrochemical reactions that may take place in solid state cells.

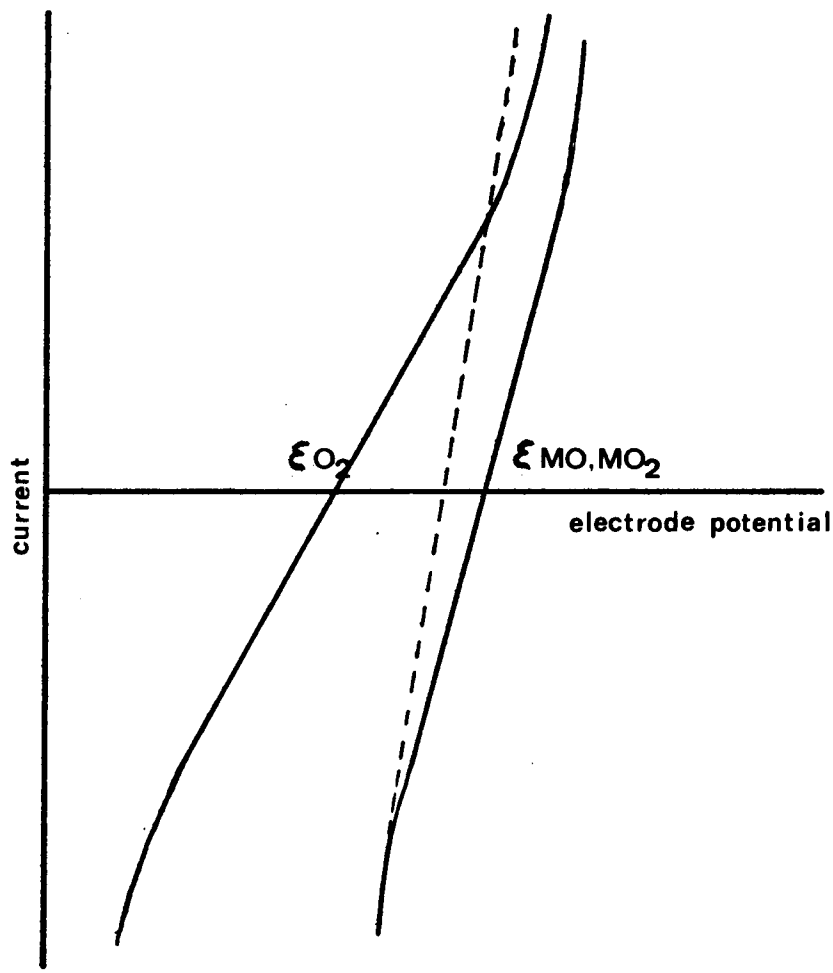

-- XBL 868-2915 --

Figure (3-5)
The current response as a function of electrode potential for each of the parallel electrochemical reactions. The dashed line is the effective electrode response, which is the sum of the individual reaction curves.

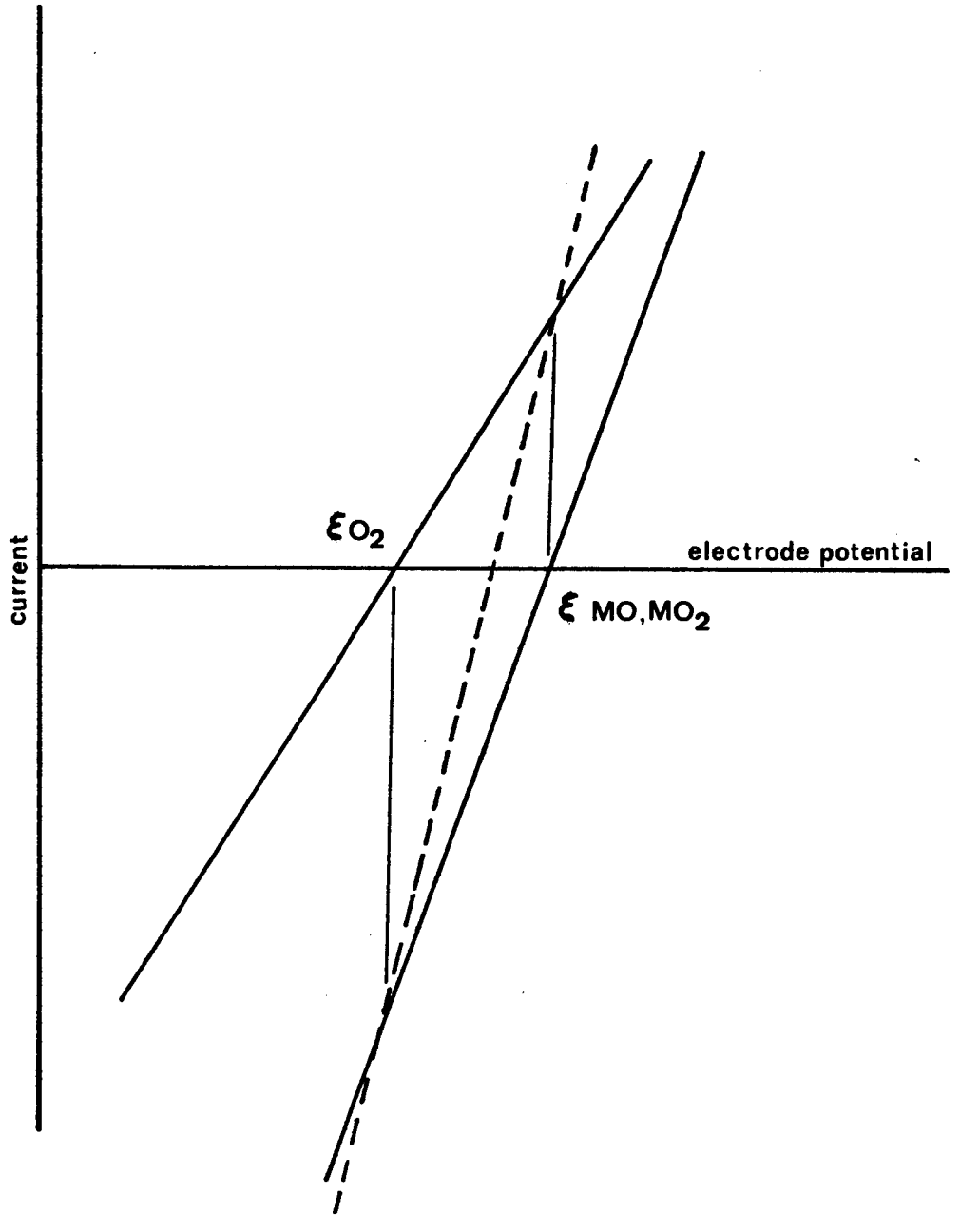

-- XBL 868-2916 --

Figure (3-6)
The linearized response of each electrochemical reaction is used to derive the approximate relation between exchange current densities and the measured cell voltage.

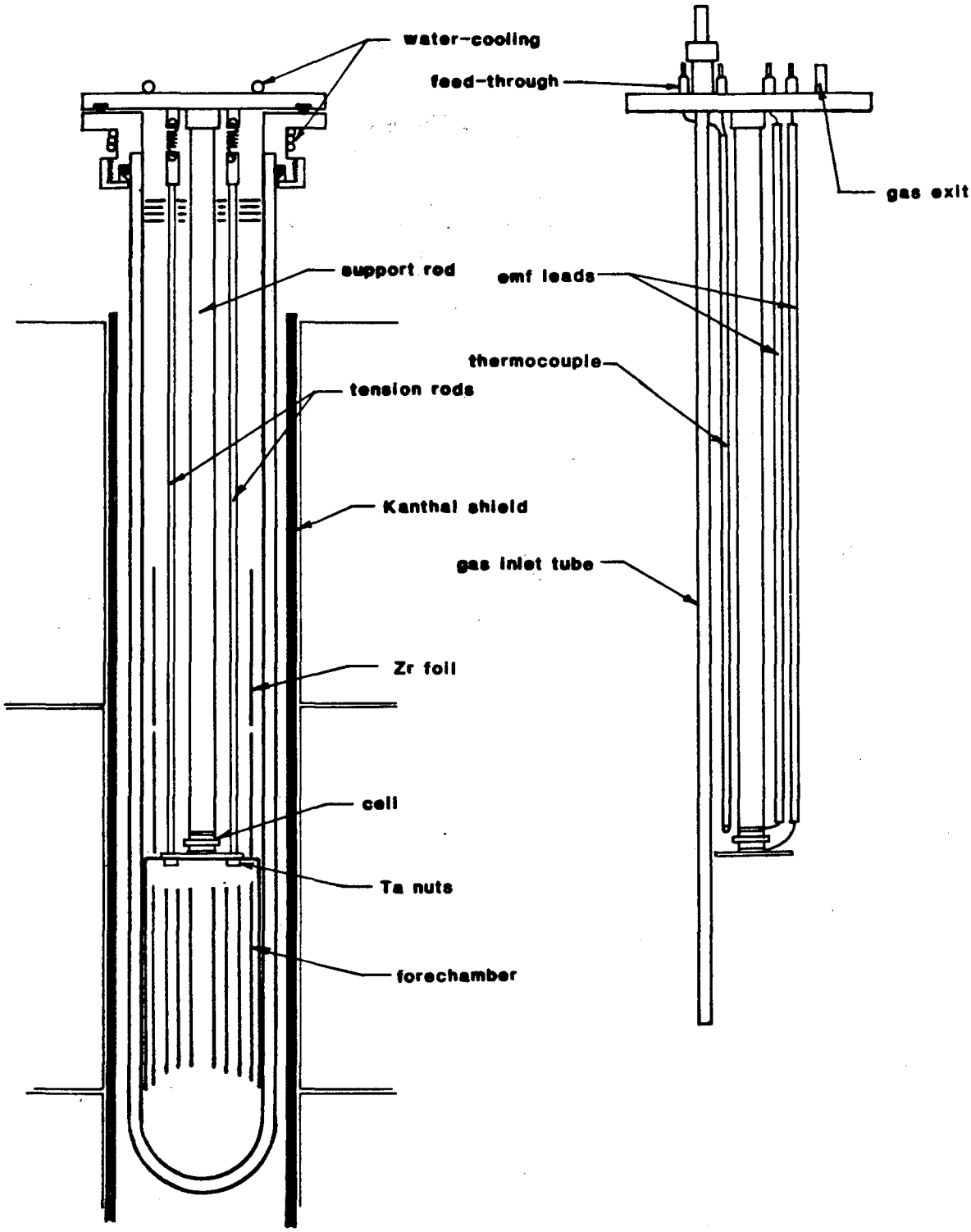

-- XBL 868-2917 --

Figure (3-7)
Cell assembly and gas manifold.

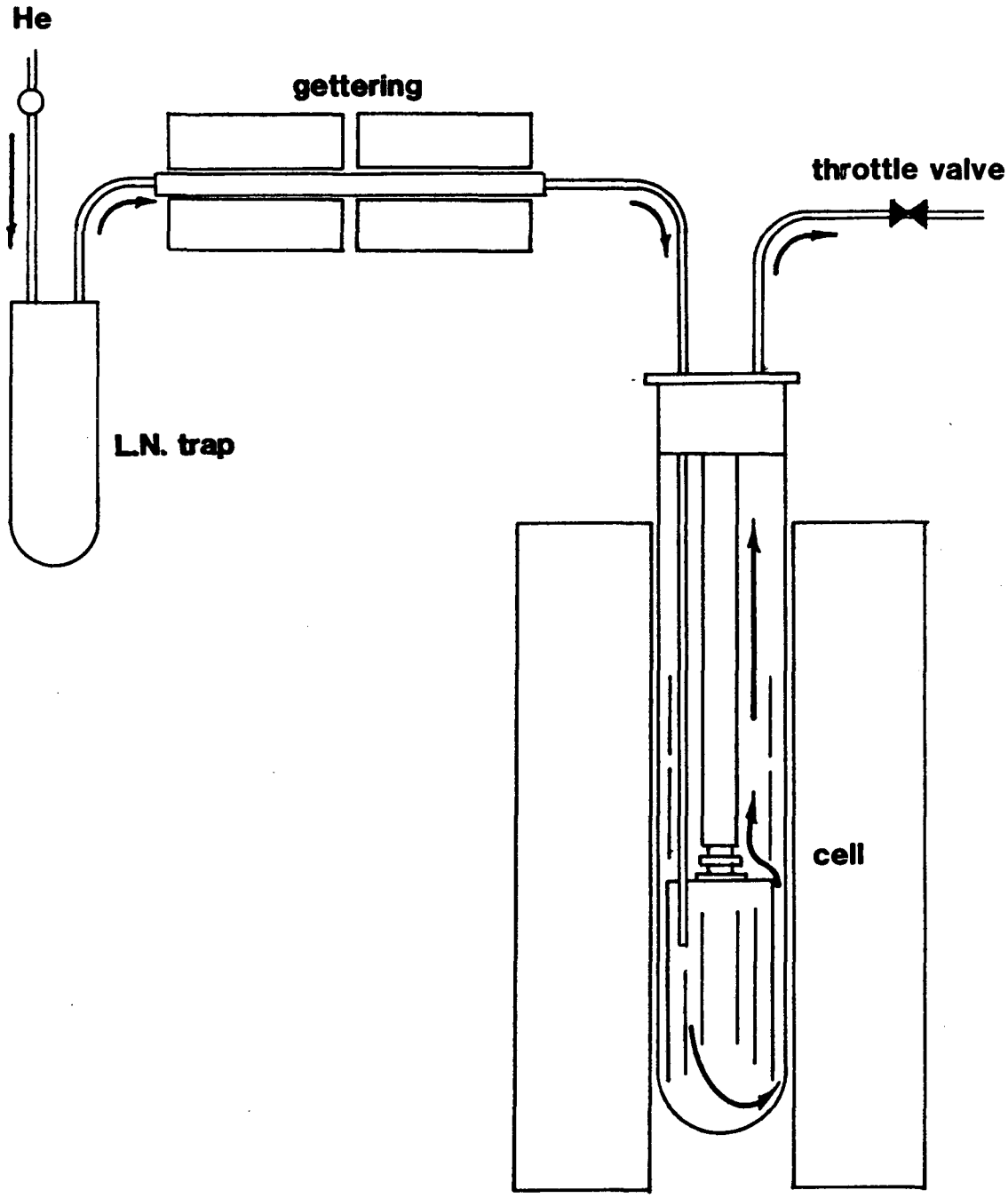

-- XBL 868-2918 --

Figure (3-8)
Schematic of the gas purification system.

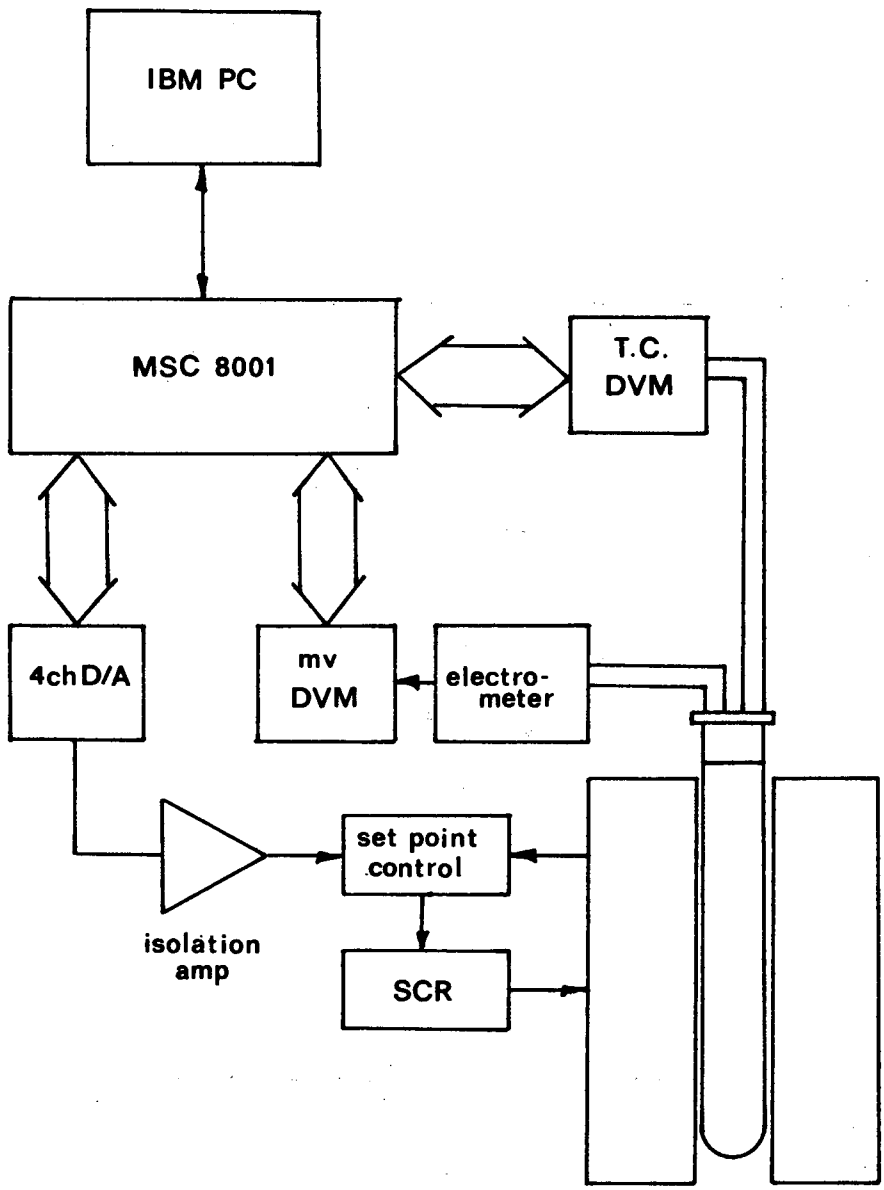

-- XBL 868-2919 --

Figure (3-9)
Schematic of control and measurement system.

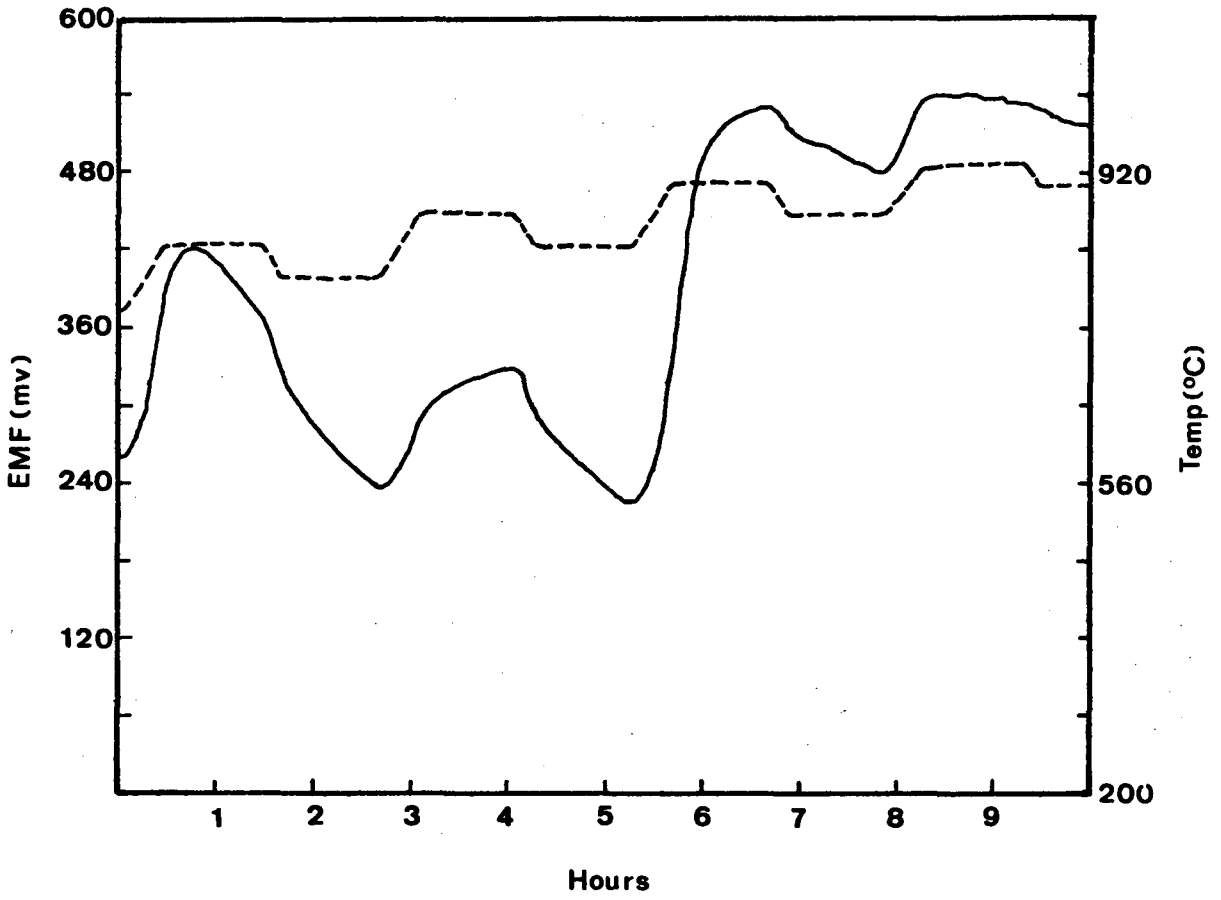

-- XBL 868-2920 --

Figure (3-10)
Performance of $NbO,NbO_2/YDT/NbO_2,Nb_{12}O_{29}$ when the electrodes had been wet polished before use. The dashed curve is the programmed temperature profile and the solid curve is the measured EMF.

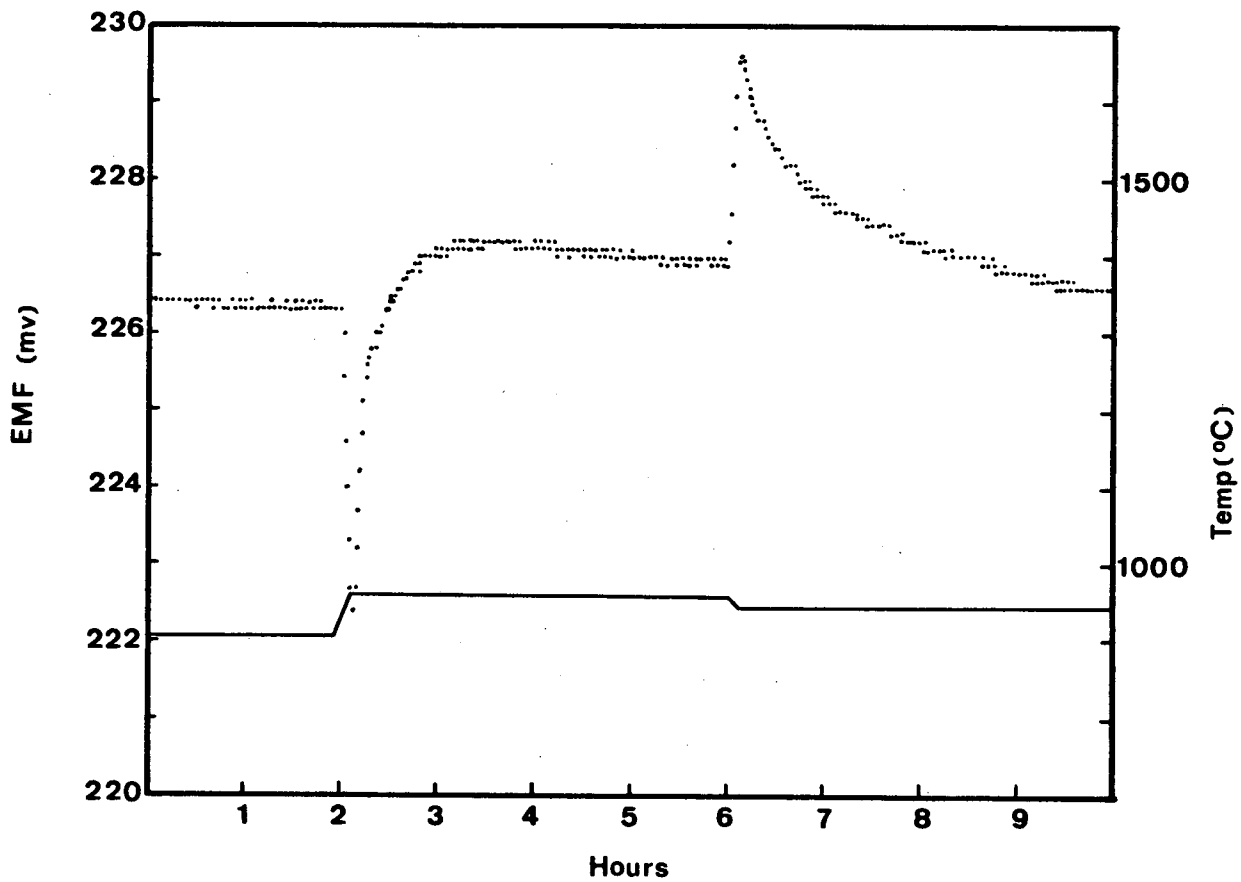

-- XBL 868-2921 --

Figure (3-11)

Typical performance of the solid state cells built in this study. This is the trace of the cell $NbO,NbO_2/YDT/Nb(Pd),NbO_2$. The sharp spikes in EMF when the temperature is changed are commonly observed. They could be the result of the cell being temporarily not being in thermal equilibrium. Because of its long time constant, however, it is likely that these transients are the result of the slow rate of diffusion in one of the electrodes as material moves to establish a new state of equilibrium.

Chapter 4

Preparation of Transparent Yttria doped Thoria and the Preparation of Solid Electrolyte for use in High Temperature Galvanic Cells

4.1 Introduction

This study is primarly interested in the preparation of a reliable solid electrolyte for solid-state galvanic cell experiments. High purity must be maintained in producing calcia stabilized zirconia (CSZ) and yttria doped thoria (YDT) electrolytes since their electronic conductivity is greatly influenced by small amounts of contaminants. High density material is also important to increase the structural integrity of the ceramic and prevent vapor phase oxygen transport through the electrolyte. There is also general interest in the production of high density refractory oxides for a variety of technical applications.

The techniques discussed here have lead to the preparation of fully dense YDT bodies that are transparent. This unusual state is difficult to obtain in refractory ceramics without introducing significant amounts of impurities. The transparent material produced here is largely free of such impurities although the small amounts of contaminants that do exist make this material inferior to those of lower density for use in galvanic cells. Its properties do however offer intriguing possibilities for use as a high temperature window to confine discharges of reactive gasses. Greskovich et al. [1] have produced transparent Y_2O_3 and YDT by a scheme similar to that used here except that

they did not explore the effect of different processing techniques on the powder's ability to give transparent material. Transparent alumina [2] is currently used in high pressure sodium lamps.

Several methods exist for producing ceramic powders with particle size less than 1 μm. They all rely on small particle size precursors that are carefully oxidized to form the oxide without increasing the grain size. Two methods often used to produce multicomponent powders are controlled hydrolysis of metal alkoxides first used by Mazidiyasni, Lynch, and Smith [3] and coprecipitation of the metal oxalates [4].

4.2 Attempts at Hot Pressing

Traditionally, highly dense ceramic bodies of cylindrical shape are produced by hot pressing. Several pellets were prepared by surrounding prepressed YDT compacts with boron nitride powder in a graphite die and hot pressing at 1400°C for 15 min. The product was very dense but had a dark color. Heat treatments in air at 950°C made the samples lose mass, indicating the presence of a contaminant and not reduced thoria, figure (4-1). Thoria reduction would mean that oxidation would occur with an increase in mass. The color never completely disappeared even after many days under these conditions.

Rhodes [5] observed similar behavior in hot pressed ZrO_2 and attributed it to carbon contamination from the furnace atmosphere. The form that carbon takes in the sample is difficult to say but its presence in the electrolyte would be detrimental to the performance of a solid state galvanic cell since it could increase the electronic conductivity and short circuit the cell. Rhodes

argues that carbon could be trapped in the pores of the densifying ceramic in the form of gaseous carbon oxides. CO could be produced by residual water vapor reacting with the graphite die. CO would disproportionate to C and CO_2 depending on the presence of trace amounts of metals which would catalyze the reaction. When oxidized the sample could only lose mass if the C diffuses to the surface to react with oxygen because reaction within the ceramic would lead to a mass increase. A simple analysis of the mass changes in figure (4-1) assuming only C diffusing out leads to a diffusivity of around $1\times10^{-8}cm^2/sec$ at 950°C which is a value not unlike the known diffusivity of carbon in similar materials.

4.3 Optimization of the Oxalate Precipitation Method

The removal of carbon from the completely dense material would seem to be a difficult task since the diffusion path length is quite long. The oxalate precipitation method for the preparation of dense YDT has proved to be very effective. Carbon present in thorium oxalate is removed by oxidation of the thorium oxalate powder, thus the diffusion path length can be made quite small. The principle advantage of this technique is that the final partical size can be made small to maximize the driving force for densification.

The starting materials were high purity thorium oxide and yttrium oxide. These oxides are very inert toward acid attack but a method was found to dissolve 50 to 100 gram amounts in a resonable amount of time. Concentrated nitric acid reacts only slowly with ThO_2 even when heated but when catalytic amounts of HF are added the reaction proceeds. The HF seems to continually etch the surface of the ThO_2 increasing the rate of dissolution.

The round bottomed pyrex flask containing the powder and acid was attached to a water cooled condenser to prevent the escape of HF vapors. This meant that an excess of HF was not needed and only a drop or two of 48% HF solution was used. No attack of the flask was noted presumably because the HF concentration was low and the surface area of the flask compared to the powder was small. Too much HF left noticeable crystals of thorium fluoride. Solutions were always filtered through a fritted glass disk before the precipitation step. Fifty grams of powder could be dissolved in an hour in 150cc conc. HNO_3 and 50cc distilled water when the flask was refluxed with an electric heating mantle.

An optimization study was carried out to determine a method by which high density YDT could be obtained from the nitrate solution prepared above. The investigation is shown schematically in figure (4-2). The procedure divides naturally into five basic operations. The first is copreciptation with oxalic acid solution followed by isolation of the resulting thorium and yttrium oxalates. The powders must then be dried and oxidized to obtain the metal oxides. Sintering is the last step in which the oxide powders are heat treated to achieve final density.

The precipitation reactions were carried out by adding the nitrate solution to a quickly stirred 80% saturated oxalic acid solution that exceeds the amount needed to preciptate all of the thorium and yttrium by 100%. The nitrate solution was added dropwise from a burrette.

White, et al. [6] noted the strong temperature dependence of particle size in thorium oxalate precipitations. Their results suggest that lower temperatures favor the precipitation of smaller crystallites. Nucleation and

growth phenomena frequently have such temperature effects since nucleation mechanisms are frequently independant of temperature while growth mechanisms involve a transport component which increases with temperature. The precipitation temperature of early experiments averaged 50°C due to the heat of solution of conc. nitric acid. Two changes were made: the nitric acid solution was brought to a pH of about 4 by addition of conc. NH_3 and the precipitation was carried out in an ice bath. The acidity of the final solution is required to prevent the precipitation of thorium hydroxide. The hydroxide does form as NH_3 is added but is dissolved as the solution is stirred.

Room temperature thorium oxalate slurries are hard to filter but it was discovered that cold solutions could be filtered if care was taken to have a layer of distilled water already passing into the Buchner funnel as the slurry was added. If the filter paper [7] was just moist, the small particles would creep under the paper and prevent a good seal.

Agglomerates have long been known to play an important role in the sintering behavior of ceramic materials. Recently, there has been great interest in quantitatively characterizing their effect. This study indicates some of the effects of agglomerates but is in no way quantitative. In early experiments the wet powder was dried on a hot plate. This lead to large, cracked agglomerates that had to be milled with zirconia mixing balls before they could be oxidized. Drying with a heat lamp yielded softer, more uniform agglomerate that also had to be milled. Samples processed in this way typically show greater variety in pore size and shape after sintering. They include small, spherical pores and large oddly shaped ones as shown in figure (4-3). Presumably, the large ones originate from the voids between

agglomerates.

Many of the problems from agglomerates can be eliminated by freeze drying the wet slurry. The freeze drier was constructed out of a large liquid nitrogen trap for a diffusion pump and the vacuum was supplied by a mechanical pump. The ends of the trap were sealed with appropriately constucted flanges so that a 250cc round bottom flask could be fitted to one end and the pump to the other. The slurry was placed in the r.b. flask and immersed in liquid nitrogen until frozen. The flask could be attached to the bottom of the trap and evacuated. The system worked very effectively and could sublime 75cc of water in 10 to 15hr. A very fine flocculent powder was produced. This powder needed no milling or grinding at all.

The thorium oxalate powder produced by this method is a hydrate with the formula $[Th(C_2O_4)_2]_{0.85}[Y(C_2O_4)_{1.5}]_{0.15}\cdot 6.8H_2O$ which was determined by thermogravimetric analysis. White et al. [6] observe for pure thorium oxalate only the dihydrate. They however, dried powders at 115°C before analysis. White et al.[6] also note that if oxidized at high temperature too quickly the powder may begin to fuse due to the low melting temperature of the hydrate. They show SEM micrographs of samples fired in this way that indicate the particles fuse creating large voids and making it impossible to obtain high green densities. Figure (4-2) shows that our experiments also achieved better results by first forming the anhydrous oxalate at 300°C and then decomposing it at 950°C.

Experiments indicate that even after 24 hr in air at 950°C as much as 1% by weight residual carbon is still present in the powder. When sintered at 2000°C the reducing power of this carbon creates a high vapor pressure of

ThO and the ceramic decomposes. Heating in pure oxygen for several hours eliminates this problem.

Cold pressing of the pellets was performed in a 1/2 in. stainless steel die without the use of any type of binder. Improper die pressing often resulted in rather large defects in the compacted pellet which of course did not disappear upon sintering. Rather low loads on the die gave the best results; only 5000 lb_f applied for several minutes. The rate at which pressure was applied and removed was made as slow as possible. The travel of the die's rams was distributed evenly by applying the same load to both the upper and lower ram and allowing them both to move freely. Frequently experimenters leave the lower ram statically in place which tends to yield uneven compaction. The body of the die, charged with powder, was held by hand between the anvils of the hydraulic press so that both the upper and lower rams extended out each side of the die. As the load was applied and the powders began to compact, the die would become locked in place and would no longer have to be held. The pellet was carefully ejected through the tapered end of the die by the use of a V-block at that end and applied pressure to the other. Teflon disks cut to fit the bore of the die were used several times to see if the quality of the compacts improved. The powders were placed between two prepressed Teflon disks ($\approx$ 1/32" thick) and compacted in the normal way. This method offered, however, little improvement of the samples and was abandoned. The entire pressing operation described thus far was performed with the die, rams, and sample inside a sealed plastic bag so as not to contaminate the hydraulic press with thorium oxide powders. The compacted pellets were prepared for sintering by first scraping off the outside of the pellet with a glass slide. This was done in order to minimize

contamination from the steel die.

Sintering was performed in a tungsten resistence furnace made by Centorr Associates [8] and a vacuum supplied by an oil diffusion pump with an attached L.N. trap. The vacuum and control systems were designed and built at M.M.R.D.,L.B.L. This furnace was capable of operating at 2200° C for extended periods of time. A high temperature tungsten rhenium thermocouple proved to be unreliable for use as a control thermocouple due to the extremely high temperatures involved which severely limited its lifetime. Thus temperature control had to be provided by linear variation in power input. This of course meant that set point control yielded a highly nonlinear temperature output. Ramp rates were always chosen with regard to the highest rate of temperature change between the initial and final set point. The temperature ramp rate was such that the soaking temperature was reached after four or five hours inorder to minimize thermal stress.

The sample was supported during sintering by a devise designed to minimize contact with foreign materials. The samples were placed on five vertical tungsten wires (0.0625 in. dia.) so that contact was limited to their tips. These wires were fixed in position by holes electric discharge machined in a molybdenum pedestal. Figure (4-4) depicts this devise and its use. The tungsten mesh heating element provided a hot zone of about 2 in. in diameter by 3.5 in. in length. The heat shields were made from tungsten sheets in a variety of thicknesses and surrounded the element on all sides.

Finally the influence of sintering atmosphere was investigated. It was found that the presence of hydrogen greatly improved the final density. For safety reasons initial experiments used only nonexplosive mixtures such as 4%

H_2–Ar until proper modifications could be made to the tungsten resistance furnace. It has long been known that a gas insoluble in the lattice will inhibit pore shrinkage when it becomes entrapped at the point of pore closure. This would indicate that the very small spherical pores in figure (4-4) could be elliminated if pure H_2 was used. Indeed, transparent samples are produced by use of a pure H_2 atmosphere as is shown in figure (4-5) and figure (4-6).

X-ray diffraction studies and a correlation of lattice parameter with respect to yttrium concentration [1] gives the yttrium concentration to be 17 mole percent as $YO_{1.5}$. The theoretical density calculated from this concentration is 9.1561 gm/cc and means that the bulk densities in figure (4-2) range from 94.3% to 99.8% of theoretical.

4.4 Electrolyte Prepared from Stock Powders

Material of lower density was prepared directly form the stock powders in order to compare with the performance of the high density electrolyte. The stock powders were carefully weighed into a small glass vial in the proportion $(ThO_2)_{0.85}(YO_{1.5})_{0.15}$. Several small glass beads were added and the top of the vial was covered with parafilm and capped. The vial was then mixed on a slow speed rotary mixer for several hours followed by removal of the glass beads with tweezers.

The powders were cold pressed in the same way as the material from the oxalate precipitation study and as before the pellets were cleaned with a glass slide. The sintering conditions of 2000°C under hydrogen were maintained for a period of several hours while ramping between temperatures at approximately 150°C/hr to 250°C/hr. The final density of the pellets varied from 92% to 95%

of theoretical density.

4.5 Performance of Electrolytes

The criterion we used to screen electrolyte material was performance of the cell

$$NbO, NbO_2 \ / \ YDT \ / \ NbO_2, Nb_2O_{4.8}$$

with overall reaction

$$NbO + 1.25Nb_2O_{4.8} = 3.5NbO_2$$

The electrodes are composed of oxides with known thermodynamics thus the cell emf and temperature coefficient can be predicted. Figure (4-7) is a third law plot based on the entropy change given in the literature (see chapter 5). Included in the figure are data from Worrell [9] and from two cells using electrolyte prepared from the stock oxide powders which were sintered in H_2 to 94% of theoretical density. It is clear from figure (4-7) that electrolytes prepared by oxalate precipitation give anomalous temperature coefficients. One possible reason for this is that small amounts of residual carbon have increased the electronic conductivity to a value that causes polarization of the cell. This material can not therefore be used in the galvanic cell experiments. The material produced from the stock powders performed well, however, and was used in the thermodynamic studies.

Chapter 4 References

[1] C. Greskovich, C.R. O'Clair, M.J. Curran. J.Am.Cer.Soc., 55 324 (1972); C. Greskovich, K.N. Woods. J.Am.Cer.Soc.Bull. 52 No.5 p.473 (1973).

[2] R. Coble, U.S. Patent No. 3,026,210, March 20, 1962

[3] K.S. Mazdiyasni, C.T. Lynch, J.S. Smith. J.Am.Cer.Soc. 50 No.10 p.532 (1967).

[4] R.W.M. D'Eye, P.G. Sellman. J. Inorg. and Nuclear Chem., 1 p.143 (1955); R. Beckett, M.E. Winfield. Australian J. Scient. Res. 4 p.644 (1951).

[5] W.H. Rhodes, R.M. Haag. "High Purity Fine Particulate Stabilized Zirconia", Air Force Materials Laboratory, 1970, AFML-TR-70-209.

[6] G.D. White, L.A. Bray, P.E. Hart. "Optimization of Thorium Oxalate Precipitation Conditions Relative to Thorium Oxide Sinterability", Pacific Northwest Laboratory, 1980, PNL- 3263

[7] Filter paper used was Whatman No. 50.

[8] Centorr Associates Inc., Suncook, N.H.

[9] W.L. Worrell. "Measurements of the Thermodynamic Stabilities of the Niobium and Tantalum Oxides using a High Temperature Galvanic Cell". Lawrence Radiation Laboratory, 1965, UCRL-11957

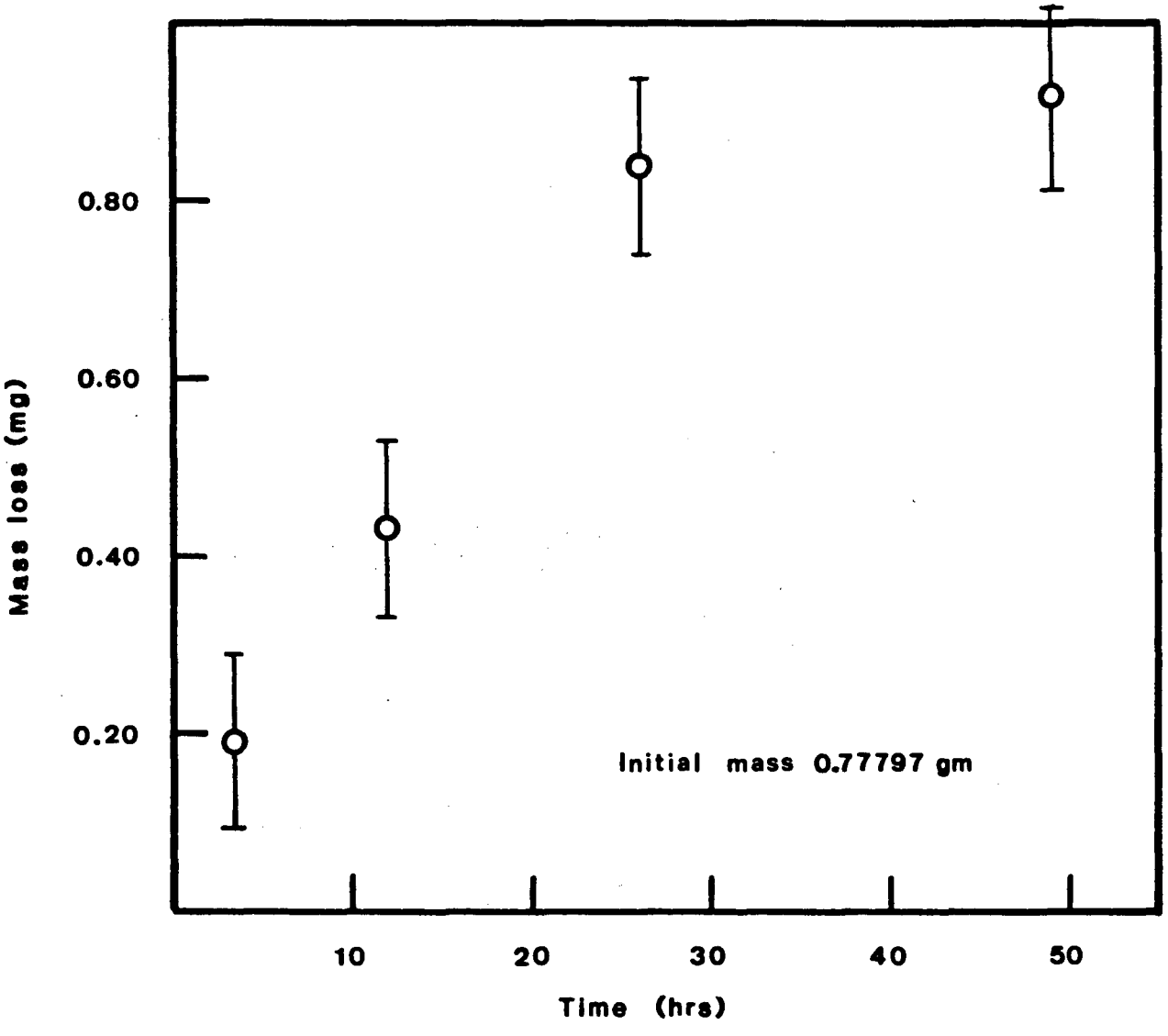

-- XBL 868-2922 --

Figure (4-1)
Mass loss of hot pressed YDT when heated in air at 950° C.

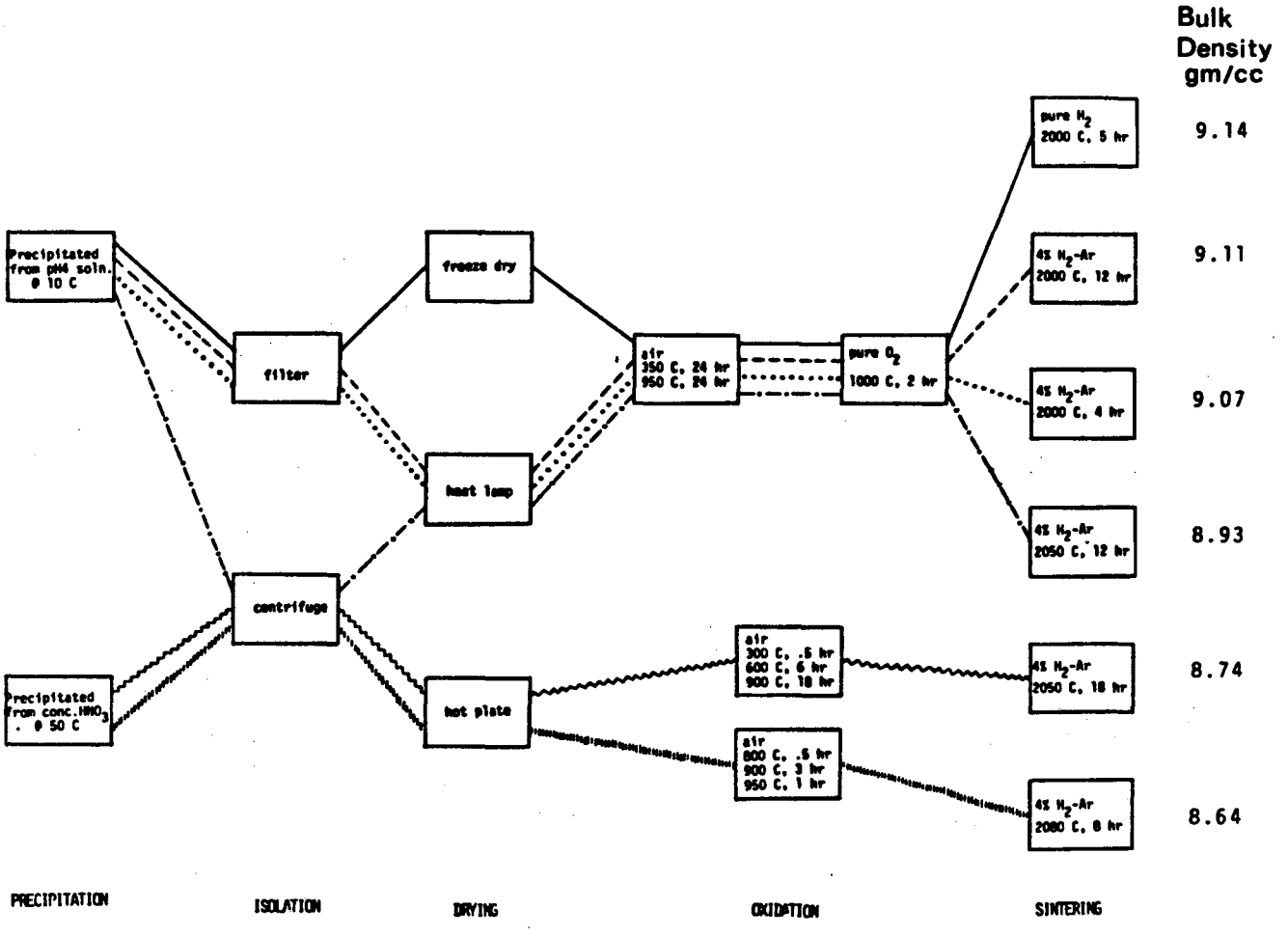

-- XBL 868-2923 --

Figure (4-2)
Optimization study for preparation of high density YDT by the oxalate precipitation method.

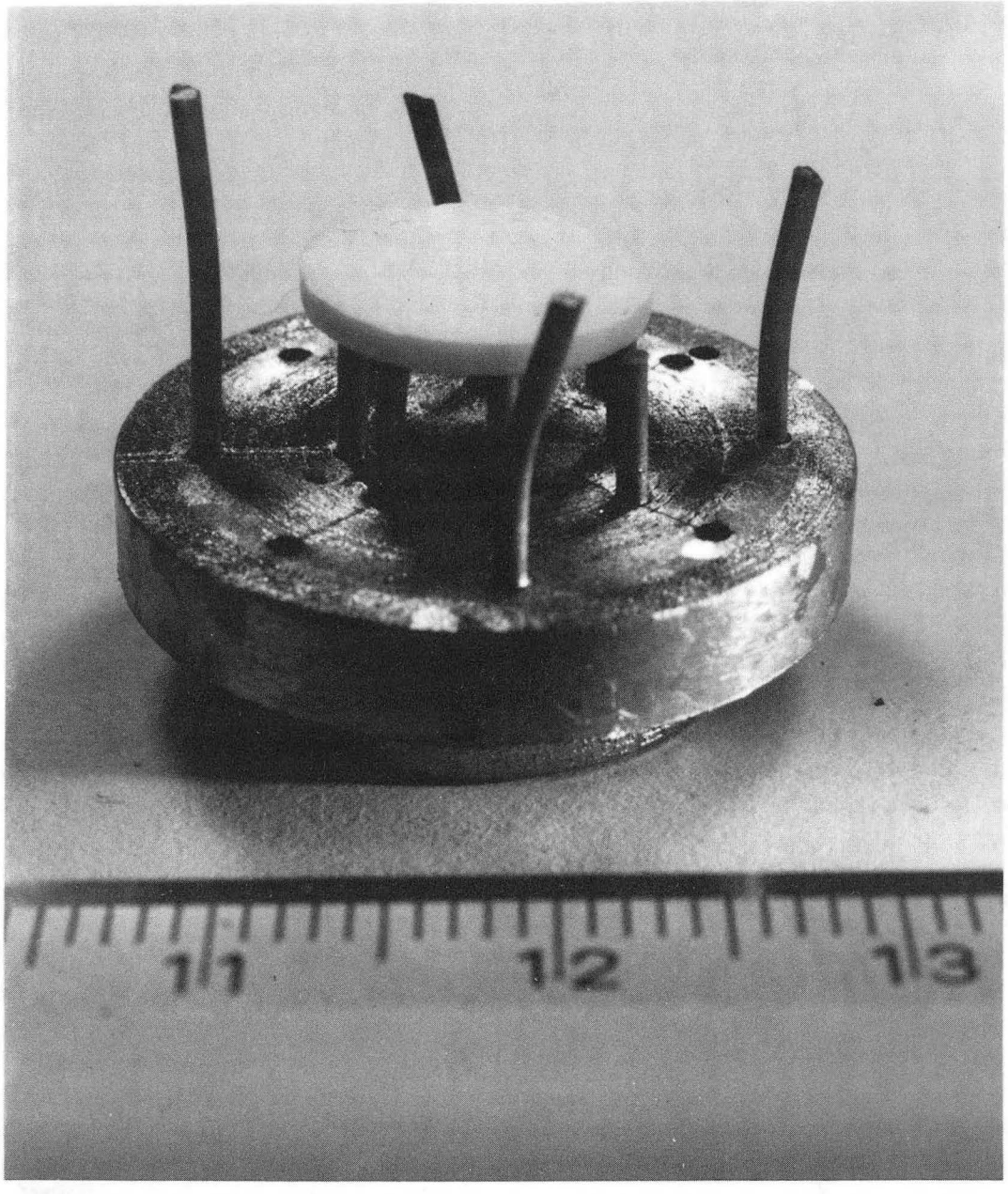

XBB 867-5545

Figure (4-3)

Device for holding sample pellets during sintering. The tungsten wires are held in place by holes electric discharge machined in the molybdenum base. The longer wires on the side help prevent the sample from falling off the shorter ones. Note the hole placed in the side which is used as a black body for temperature measurement.

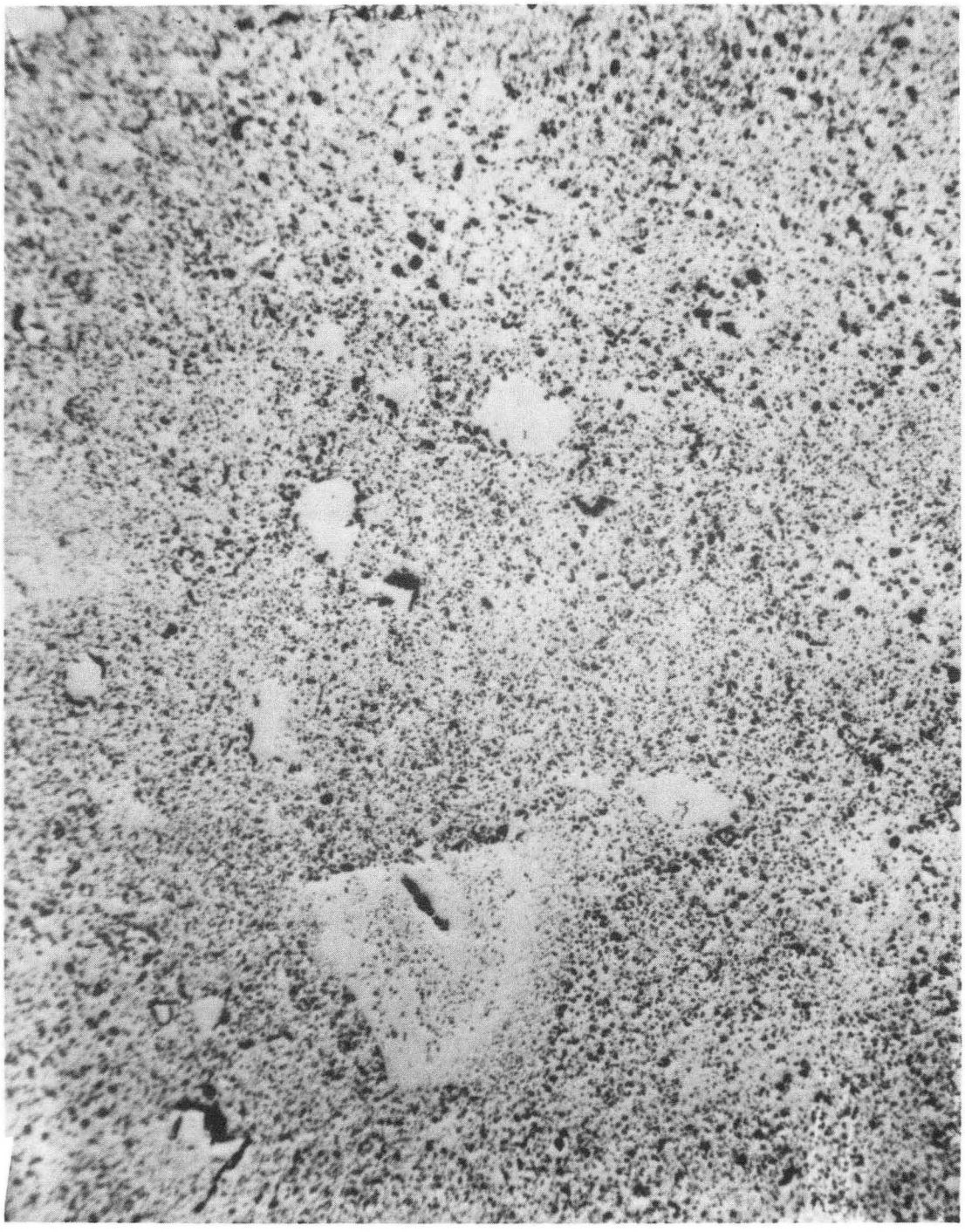

XBB 867-5546

Figure (4-4)
YDT sample, 8.64 gm/cc, as polished (25 X).

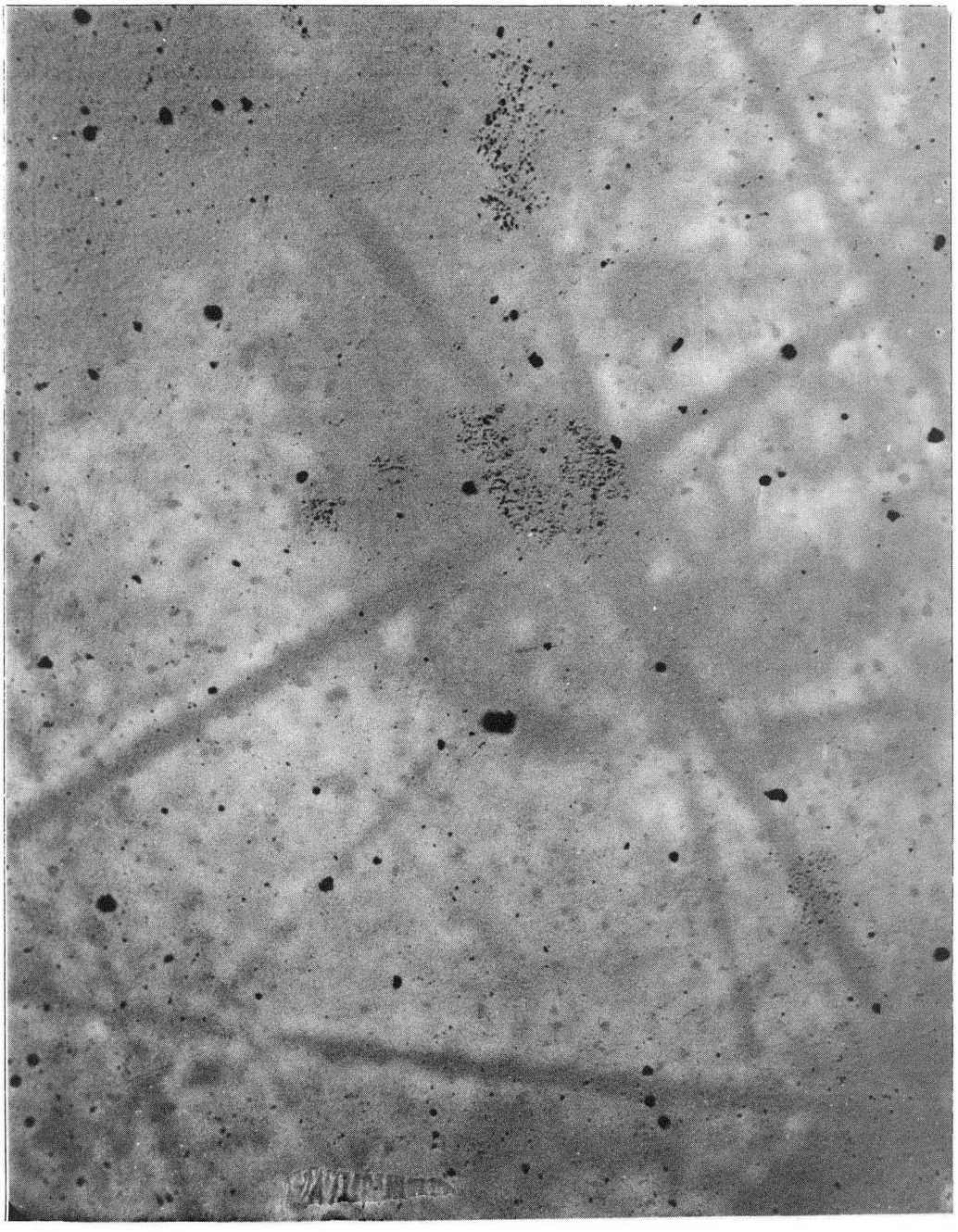

XBB 867-5547

Figure (4-5)

YDT sample, 9.14 gm/cc, as polished (25 X). Note sample is transparent: lines are from the underside of pellet.

XBB 867-5543

Figure (4-6)
YDT sample, 9.14 gm/cc. The letters YDT are typed on the paper underneath the pellet.

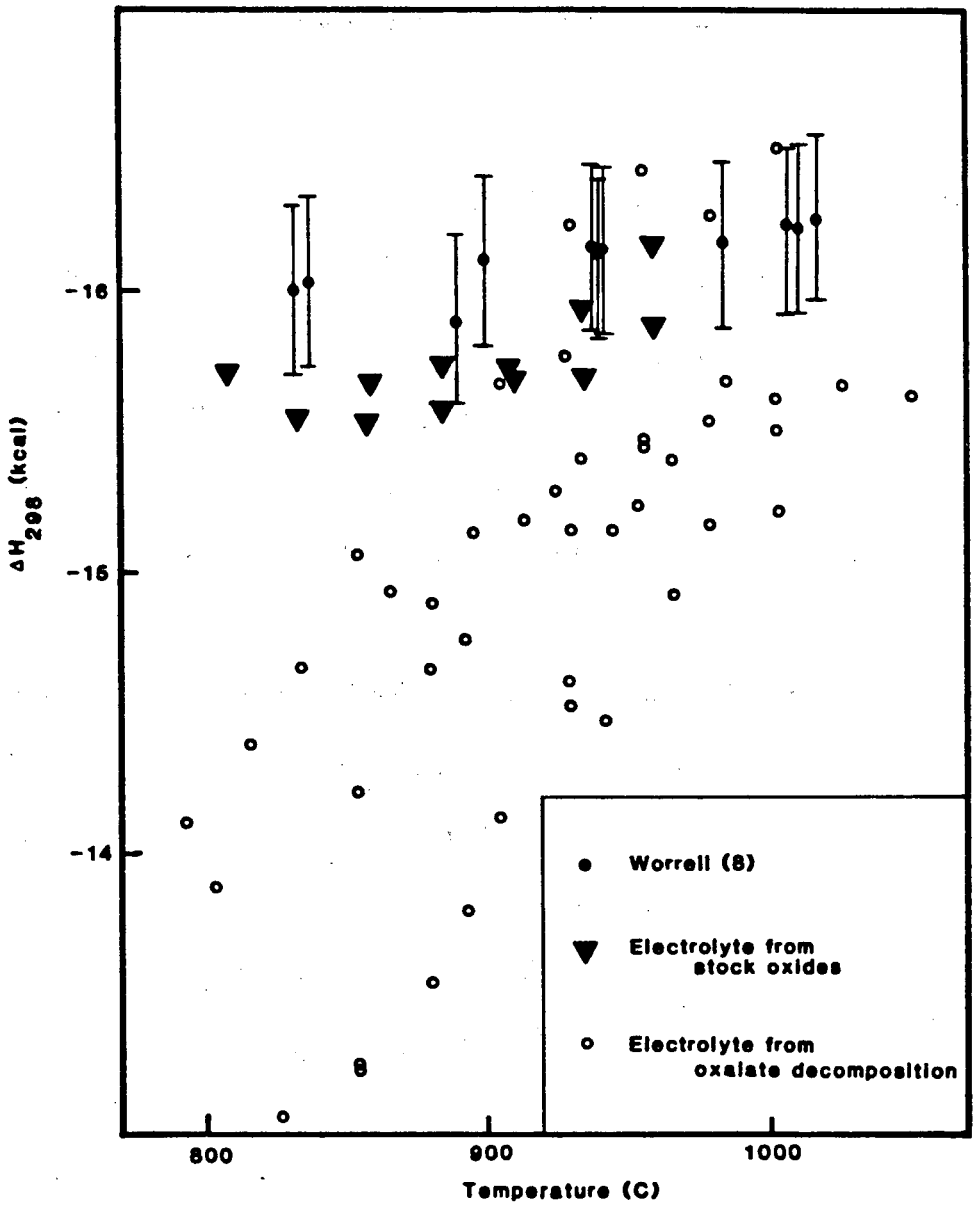

-- XBL 868-2924 --

Figure (4-7)
Third law plot for $NbO+1.25Nb_2O_{4.8}=3.5NbO_2$. Electrolyte prepared by oxalate decomposition performs poorly compared with material produced by sintering the stock oxides.

Chapter 5

Observations and Conclusions

5.1 Palladium Alloy and Niobium Oxide Equilibration

The niobium-oxygen and niobium-palladium binary systems were discussed in chapter 1. Our immediate goal is to use the observations presented here to sort out how these complicated binary systems interact to form the ternary phase diagram. A ternary system is in general more complicated than a binary because of an additional degree of freedom allowed by the phase rule. The Pd-Nb-O system and its analogs are greatly simplified by the experimental observation that the solubility of palladium in the oxides is very small. Similarly, the solubility of oxygen in the alloys is also very small in all but a few cases. Thus the ternary diagram is almost entirely made up of poly-phase regions and all the samples presented here can be expected to have at least two phases.

The multiple phases are clearly seen in optical micrographs of the polished samples. Figure (5-1) is the magnified polished surface of sample NB02. It possesses grains with a metallic luster as well as those with a dull gray hue. The black areas are residual pores. The metallic grains are as, expected, the alloy phase which can be easily shown by selective X-ray mapping of the surface or by scanning Auger microscopy which is discussed below. Note that this polished surface has not been chemically etched.

For a single degree of freedom the phase rule permits only three phases at equilibrium in a ternary system. With the pressure fixed to ambient, our experi-

ments then fix the temperature to a controlled value. Figure (5-2) is an optical micrograph of sample NP03. A metallic phase is present as well as the residual pores. The sample also has oxide grains with two different shades of gray when illuminated by unpolarized light. Evidence that two different oxides are indeed present can be seen in figure (5-3) which represents elemental maps of a surface of this sample taken by counting Auger electrons of specific energies. The oxygen map shows that there are regions which contain different amounts of oxygen within the gray material depicted in the secondary electron image of the same area. Secondary electron images do not produce pictures of great contrast, so it is difficult to tell if the changes in contrast observed in the optical micrograph correspond to regions of different oxygen content. These observations, however, do not conflict with the X-ray diffraction results presented below. Figure (5-3) also shows that the oxygen content in the alloy must be small. This is confirmed by comparison of the Auger spectrum obtained from the alloy taken during continuous sputtering (see figure (5-4)). The Auger spectrum for the oxide phase is shown for comparison. Energy dispersive X-ray analysis also confirms that the amount of palladium dissolved in the oxide is below the detection limit.

The number of oxide phases in the samples can in many cases be determined as above by using optical microscopy. The task is not always easy, because the lower oxides of niobium are very metallic in appearance. Figure (5-5) is an optical micrograph of sample NP08. This sample also has three phases, where one of the gray oxide phases is clearly present along with two phases that are metallic in appearance. The large cubic grains, however, are not those of an alloy phase, but are NbO crystallites which are very similar to the crystallites found in the starting NbO material. One of the reactants used in the prepara-

tion of this sample was NbO along with niobium and palladium powder. The reactants and number of oxide phases determined by optical microscopy are listed in table (5-I) for each of the Pd-Nb-O samples.

Optical microscopy does not yield much information on which oxide or alloy phases are present in a sample but it is an important tool because knowledge of the number of phases is a great help in understanding the complicated X-ray diffraction patterns generated by these polyphase samples. The niobium oxides between NbO_2 and Nb_2O_5 form several homologous series which have over one hundred atoms per unit cell. The intricate patterns in which the atoms are arranged produce many planes which will diffract X-rays. The powder patterns are further complicated by lines from other phases, thus one must be able to superimpose patterns from these phases in order to completely characterize the samples. Fortunately the crystal structures of all the phases we are concerned with are known in sufficient detail to allow their detection in the samples. Thus the crystal stuctures of the alloys discussed in chapter 1 can be used to generate theoretical powder patterns which can be superimposed on patterns of the pure oxides. Assignment of the lines observed in the sample's powder pattern can then be made by comparison. The procedure used to calculate these patterns is discussed in Appendix 1.

Inspection of the X-ray patterns of all the NP samples shows that they may be classified into groups that show related peaks. Samples NP08, NP09, and NP10 show identical patterns except for slight changes in the relative intensities of some of the lines. The upper three traces in figure (5-6) are a part of the patterns for these three samples taken with $Cu_{K\alpha}$ radiation. Note that there is a one to one correspondance for all the peaks. The lower trace in figure (5-6)

is the pattern for a sample of NbO and NbO_2 that had been equilibrated in the same way as the NP samples. Disregarding the change in relative intensity of the NbO and NbO_2 lines, all the oxide peaks can be found in the traces above. One must conclude that both oxides are present in these samples. Further evidence is found in the optical microscopy results shown in table (5-I). Two oxide phases were observed in each of these samples. The changes in relative intensities of the two oxide lines reflects the fact that they are in different volumetric proportion.

There are lines present in the sample patterns of figure (5-6) that do not correspond to lines in the binary oxide sample. These lines are, of course, those of the alloy phase. Comparison with the calculated patterns of Appendix 1 shows only those of the $NbPd_2$ phase are consistent with these extra peaks. The position and relative intensity of the lines for the $NbPd_2$ phase are superimposed on the binary oxide pattern at the bottom of the figure. This is done by drawing lines where the maxima to the peaks would be expected with heights representative of the relative intensity of the reflections. The complete assignment of all the lines in the sample patterns are presented in table (5-II).

The composition measurements confirm that the alloy phase in the samples above is indeed $NbPd_2$. The EDAX results for all the NP samples are presented in table (5-III). The $NbPd_2$ phase in samples NP08, NP09, and NP10 are found to have niobium mole fractions of 0.333 $\pm$0.001, 0.325 $\pm$0.003, and 0.323 $\pm$0.004 respectively. All these compositions seem to be the same within the experimental error of the method.

The optical, X-ray, and composition results all indicate that samples, NP08, NP09, and NP10 represent compositions in the ternary phase diagram

for which three phases are in equilibrium, i.e. NbO, NbO_2, and $NbPd_2$. The temperature was fixed during the heat treatment so that at equilibrium the concentrations in each of the three phases is fixed and is independent of the starting materials used to prepare the samples. This is the case as long as the overall composition lies within the ternary phase envelope. This last point is illustrated by the three samples just discussed. Sample NP08 was prepared from niobium, palladium, and NbO powders, while NP09 and NP10 used Nb_2O_5 and NbO_2 respectively instead of the monoxide. Thus the fact that this ternary phase region is independent of reactants provides a check that equilibrium is being attained.

The diffraction pattern for NP07 is considerably simpler than those discussed above and is depicted in the upper trace of figure (5-7). This is consistent with the results from optical microscopy which indicate that the sample has a single oxide phase. The lower trace in figure (5-7) is the pattern for the stock NbO_2 material. The similarity between these lines and many in the sample's pattern is unmistakable. Superimposed on the lower trace is the synthesized pattern of $NbPd_2$, again, which match the rest of the reflections in NP07's pattern. The complete assignment of the reflections in this pattern is given in table (5-IV). Reference to table (5-III) confirms that the composition of the alloy (niobium mole fraction 0.327 $\pm$0.007) is near that corresponding to $NbPd_2$.

A different set of three samples which have identical patterns is shown in the three upper traces of figure (5-8). Two of the samples, NP04 and NP06, were prepared from niobium, palladium, and Nb_2O_5 powders while the third, NP05, was prepared from just palladium and NbO powders. The X-ray patterns reveal that the single oxide phase observed by optical microscopy is again

NbO_2. The lower trace in figure (5-8) is the NbO_2 pattern which matches many of the reflections in the other patterns. There are many extra lines, however, which do not correspond to the $NbPd_2$ reflections seen in the pattern for NP07. Superimposed on the lower NbO_2 trace is the calculated pattern for beta–$NbPd_3$, which clearly confirms this compound's presence in these samples. The assignments of the observed reflections for the samples are presented in table (5-V).

Samples NP04, NP05, NP06, and NP07, are two-phase systems and as such have an extra degree of freedom over samples that are three-phase. This means that for the given equilibration temperature the compositions in each terminal phase can be varied. There must, however, be a one to one correspondence between the composition in one phase and that in the other. This relationship is frequently referred to as the tie lines between the two phases. Thus, different two-phase samples only have identical terminal phases if the overall compositions of the two samples lie on the same tie line. The homogeneous range of NbO_2 is so small that composition changes have negligible effect on the lattice constants for the phase so that no change is detectable by X-ray diffraction. The $NbPd_3$ compound though is known to have a relatively large homogeneous range. Giessen et al. [1] observed this phase from 23 to 26 atomic percent niobium while $NbPd_2$ supports only a small amount of nonstiochoimetry. This accounts for the difference in measured niobium concentrations for samples NP04, NP05, and NP06, which are 0.252 $\pm$0.005, 0.242 $\pm$0.002, and 0.236 $\pm$0.003 respectively.

Optical microscopy indicates that there are two oxide phases present in sample NP03 while only one was observed in NP01 and NP02. The overall

compositions in the samples are such that they allow one to guess that the oxides present would be those between NbO_2 and Nb_2O_5. The phase in equilibrium with oxygen saturated NbO_2 is thought to be the monoclinic form of $Nb_{12}O_{29}$. Schaffer et al. [2] made early observations of this as well as Marucco [3] and later Naito et al. [4]. $Nb_{12}O_{29}$ has also been prepared in an orthorhombic form [5], but the equilibrium phase appears to agree with the work of Norin [6] on a monoclinic single crystal. This fact is confirmed by comparing the powder pattern of a sample consisting of saturated NbO_2 and $Nb_{12}O_{29}$, prepared from NbO_2 and Nb_2O_5, to a pattern of pure NbO_2 and a calculated powder pattern from the crystal structure determined by Norin [6]. The patterns shown in figure (5-9) are in excellent agreement.

The X-ray pattern of sample NP03 is compared, in figure (5-10), with the pattern generated above for NbO_2 and $Nb_{12}O_{29}$. The lines match perfectly when the reflections corresponding to fcc palladium are added. The palladium solid solution range, as discussed in chapter 1, is quite large, so that the measured concentration of 0.135 $\pm$0.004 is consistent.

The patterns for samples NP01 and NP02 are identical and similar in appearance to that for NP03, but carefull examination of the patterns shown in figure (5-11) indicates that they are indeed different. There are slight shifts in the positions of some of the stronger reflections and the appearance of some new lines. There is good agreement with the powder pattern observed by Gruehn and Norin [7] shown in figure (5-12) for the phase $NbO_{2.483}$. Naito et al. [4] indicate that this is the only equilibrium phase between $Nb_{12}O_{29}$ and Nb_2O_5 at 1000°C. Many of the other phases that exist at higher temperature in this region are known to have X-ray patterns that are very similar to one another,

thus assignment of the phases in this region is very difficult.

The upper two traces in figure (5-13) are the patterns for NP14 and NP15. Reflections from NbO appear in the patterns and are shown in the sythesized pattern at the bottom of the figure. Giessen et al. [1] have shown that the lattice constant for bcc niobium changes from a value of 3.307 angstroms at pure Nb to 3.242 at 25 atomic percent palladium which is a much greater change than the variation in lattice parameter in the palladium solid solution. Our measurements yield a lattice parameter of 3.27 angstroms. This accounts for the shift in the positions of the niobium (110) and (200) reflections in NP14 and NP15's patterns but this does not explain the many weak lines that have appeared. These lines do seem to fit the positions of reflections observed by Greenfield and Beck [8] for the tetragonal σ phase of Nb_3Pd_2. The estimated intensities of these lines at the positions their work indicated are also shown at the bottom of figure (5-13). The assignment of two metal phases does not conflict with the composition measurements which lie between the compositions of the two phases and seem to scatter much more than the expected experimental error. This scatter is a result of randomly analyzing one or more grains of the two different phases.

Sample NP11 has reflections for both the σ phase and NbO as shown in figure (5-14). The bcc niobium lines have disappeared, while those of the $NbPd_2$ phase now are unmistakably present. Thus this sample also has two metallic phases, Nb_3Pd_2 and $NbPd_2$. The composition measurements again offer conformation since the 0.557 $\pm$0.063 mole fraction measured is intermediate to these phases and scatters even more wildly than measurements for NP14 and NP15 since the difference in composition of the two phases is greater.

The samples richest in niobium were difficult to characterize. The X-ray diffraction patterns for NP12 and NP13 indicate that they contain bcc niobium and NbO but the composition measurements for these samples seem to scatter more than the error expected for the method. Closer inspection of the X-ray pattern for NP12 shows that there are two weak lines present at positions corresponding to the strongest lines of NbO_2. Thus it is safe to conclude that this last sample has not reached eqilibrium. The liquidus temperature is known to rise rapidly from 1520° C at palladium saturated bcc niobium to the melting point of pure niobium at 2471° C [1]. A general rule is to try to equilibrate alloys at a temperature at least three quarters of the melting point in order to reach equilibrium in a finite amount of time. Thus these samples may not be able to equilibrate at the soaking temperature of 1000° C.

Table (5-VI) summarizes the phase assignments for the NP samples and their overall atomic composition calculated from the amounts of starting materials used. It is a trivial matter to construct the ternary phase diagram at 1000° C from the information in this table. The diagram consistent with it is shown in figure (5-15).

The inclusion of the σ phase conflicts with the most recent phase diagram study on the Nb-Pd system [1] but has been observed by other investigators [8]. Giessen et al. [1] suggest that it may be stabillized by a variety of impurities. Their experiments show that small amounts of tantalum or vanadium will precipitate the σ phase in Nb-Pd alloys, but they also say that carbon or oxygen will not. The presence of tantalum is difficult to exclude in our experiments since niobium frequently contains small amounts of it. The two ores are found together in nature and are difficult to separate in processing. The other

possiblity is that what we have observed is not the σ phase at all but a new ternary compound containing only a small amount of oxygen. Such compounds have been observed in analogous systems, such as Nb_5Pt_3O [9] and $Nb_{0.519}Ir_{0.296}O_{0.185}$ [10]. The lines defining the phase boundaries in this region are shown as tentative because the issues discussed above can only be resolved by a detailed study of this small region of the diagram.

5.2 Rh-Nb-O, Pd-Ti-O, and Rh-Ti-O Equilibration

Many of the difficulties experienced in preparing the Nb-Rh EDAX standards occured in the preparation of rhodium-niobium oxide samples. Initially trial samples were made in order to investigate the length of soaking period needed to reach equilibrium. The stock rhodium powder had not been classified for these test samples, so that it contained many agglomerates of particles in the 50 to 100 micron range. Figure (5-16) is an electron micrograph of one of these large grains in a sample that had been heated under vacuum for two days at 1225° C followed by seven days at 1000° C. Superimposed on the photo is a trace representing the intensity of niobium L_α X-rays as a function of position through the alloy grain. Note that there are two regions of different niobium concentration within this grain. The region of low niobium concentration is the rhodium solid solution and the higher is the $NbRh_3$ intermetallic phase.

The presence of the two alloy phases is not in itself a problem since these phases are in equilibrium in the binary system, but more careful analysis reveals that a niobium concentration gradient exists in the $NbRh_3$ phase. Figure (5-17) is a plot of the concentration of niobium averaged over 12 by 12 micron regions across the face of the grain pictured in figure (5-16). The graph indicates that there is as much as a 3 atomic percent drop in niobium concentration across the $NbRh_3$ phase. Thus this sample cannot be in thermodynamic equilibrium. The niobium diffusion coefficient in rhodium must be substantially smaller than that in palladium solutions because of the fact that rhodium's melting point is four hundred degrees greater than palladium's. This is the reason that the palladium samples equlibrated much more easily than the rhodium samples.

The rhodium powders used in samples NR01 to NR07, TR01 and TR02 were classified before use with a .2 mm sieve to help deagglomerate the starting material. This seemed to decrease the time required to reach equilibrium.

The reactants and number of oxide phases determined by optical microscopy are listed in table (5-VII) for all the Rh-Nb-O samples as well as the Rh-Ti-O and Pd-Ti-O samples. Also included in the table are their overall atomic compositions and alloy compostions. The identities of the oxides detected by X-ray diffraction are also presented in this table.

The Rh-Nb-O samples of interest are those with two oxide phases, NR01 and NR05. It is clear from figure (5-18) that the two oxide phases in sample NR05 are NbO and NbO_2. This figure is a small section of the X-ray pattern for the sample as well as a pattern for a sample of just the two oxides. The X-ray pattern for NR01 shows significant amounts of $Nb_{12}O_{29}$, while only very weak lines for NbO_2 (see figure (5-19)) are present. This is consistent with the optical microscopy results, which show only a small volume percent of the second oxide phase. The overall composition and the assignment of one of the oxides to $Nb_{12}O_{29}$ and the measurement of a 21 atomic percent alloy forces one to conclude that the second oxide is indeed NbO_2 since any other choice would not be consistent with the overall mass balance of the sample. The phase diagram compatible with these the assignments for the NR samples is shown in figure (5-20). Kleykamp [19] studied the rhodium rich portion of this diagram and found very similar results.

Samples TR01, TR02, and TP01 were designed to yield three phases upon equilibration. This was accomplished by weighing out the correct proportions of two oxides such that the overall composition would lie in a two phase region of

the binary Ti-O system. A small amount of palladium or rhodium was added to this powder and then mixed well before hot-pressing. The small atomic percent of platinum group metal could not significantly change the relative amounts of the two oxides.

Figure (5-21) contains the X-ray patterns for TR01 and TP01 as well as a pattern for a sample containing only TiO and Ti_2O_3. All the reflections for the two oxides are present in the samples, but the small volume percent of the alloy prevents complete identification of any intermetallics that may be present. The reflections that are not those of the oxides do, however, coincide with the strongest reflections expected for rhodium or palladium alloys.

5.3 Galvanic Cell Measurements

The first galvanic cell experiments were performed with electrodes composed entirely of two oxide phases, specifically,

$$NbO, NbO_2 \text{ /YDT/ } NbO_2, Nb_{12}O_{29} \qquad \text{(cell-I)}$$

These experiments allowed us to check the reliability of our measurements since the voltages could be compared with those measured by other investigators. This cell's performance was not as good as those that had an alloy-oxide sample as one of the electrodes. When used at temperatures above 1000° C the voltage measured quickly degraded and the cell became unusable. It did work, however, at lower temperatures than the alloy-oxide cells since steady voltages were measured after several hours at temperatures as low as 800° C.

The measured voltages as a function of temperature for two cells of type I are presented in figure (5-22) and are fit by

$$\epsilon_I(\text{mv}) = 199.6 + 0.054\text{T}(^\circ\text{K}) \tag{5-1}$$

The separate runs agree very well and depart from the linear fit by only several millivolts out of 260 mv. Worrell's [12] measurements for a type I cell are also plotted in figure (5-22). He assigned an error of 10 mv to each of these points since the EMF varied with the flow of inert gas though the cell container. Variation with flow rate was not noted in our experiments. His measurements are, however, consistently higher than ours. Nonetheless, our results are in excellent agreement with Worrell's when one considers that they only differ by 5 mv out of 265 mv.

The Nb-Pd-O samples used in the galvanic cell measurements were prepared by referring to the phase diagram that was constructed in the alloy-oxide equilibration experiment. The proportion of reactants was chosen so as to yield a single oxide phase and alloy phases with niobium concentrations from that in $NbPd_3$ down to one atomic percent. The reactants and heat treatments used for the samples are described in table (5-VIII). All but the last of these samples was prepared especially for use as electrodes, with special care not to contaminate them before the cell experiment. Sample NP23 was obtained from NP04, which had previously been used in the oxide-alloy equilibration study. Before use as an electrode, however, it was heated under vacuum for 24 hrs at 1150° C to insure that the specimen was dry. The procedures discussed below to identify the phases present in the electrode were performed after the samples were used in the cell experiments.

The annealling temperatures were not limited to 1000° C, particularly for samples with only a small amount of niobium metal as a reactant. These sam-

ples, with relatively isolated grains of niobium, have greater diffusion distances over which to equilibrate. Unfortunately, these samples also have the greatest palladium activity, which means palladium loss due to vaporization is greatest in these samples. The largest palladium loss was in sample NP16 which decreased in mass by 6%. The vapor pressure of palladium at 1400° C is known to be 2.7×10^{-8} atm [11]. The Langmuir equation may be used to estimate the amount of mass loss expected over the period of six days. This calculation yields 0.003 gm/cm^2 while the total mass lost was 0.083 gm. The sample had a superficial area of 3 cm^2 but because it was not completely dense it is not unreasonable to assume that the total area was between 5 and 10 cm^2. The entire surface area, of course, is not available for vaporization since the partial pressure of palladium within the porous body will be near its equilibrium value and thus only grains near the surface will contribute to the vaporization area. This still yields a lower loss than that measured but it is the correct order of magnitude.

Even with a 6% change in the mass of NP16 there is only a slight effect on the concentration expected in the alloy. Originally its reactants were weighed out to give one atomic percent of niobium in the alloy. From the known amounts of reactants and the loss of 0.083 gm Pd, one can calculate that the expected final composition should be a niobium mole fraction of 0.024. This is close to the measured final mole fraction of 0.030 ± 0.007. Thus although the mass loss was large in sample NP16, it has little effect on our experiments since we measure the composition of the alloy by EDAX after the heat treatment. Note also the mass loss quickly diminishes as the niobium concentration in the alloy increases due to the expected drop in palladium activity.

X-ray diffraction reveals that sample NP23 still retains the NbO_2 and $NbPd_3$ phases present in sample NP04. Examination of this pattern and that for NP22 which are presented in figure (5-23) reveals that it also has reflections that are attributed to the $NbPd_3$ phase. The EDAX measurements on NP22, however, scatter between 18 and 22 atomic percent niobium which indicates that there are two alloy phases in this sample; $NbPd_3$ and saturated palladium. Giessen et al. [1] also find that these alloys are in equilibrium with one another at temperatures below 1300° C. Saturated palladium's presence is difficult to confirm by X-ray diffraction since the palladium reflections lie very close to those of $NbPd_3$.

The X-ray patterns shown in figure (5-24) indicate that the phases present in samples NP20 and NP21 are NbO_2 and palladium solid solution. NP20 has an alloy of 13.9 atomic percent niobium while NP21 has 16.8%. The alloy concentrations found in samples NP20, NP21, and NP22 are in agreement with the phase diagram in figure (5-15), which shows that NbO_2 is in equilibrium with alloys between 0.134 and 0.33 mole fraction niobium.

The single oxide present in samples NP16, NP17, and NP18 is the monoclinic form of Nb_2O_5. Small sections of their X-ray patterns are shown in figure (5-25) where they are compared with the reported positions and intensities of reflections of Nb_2O_5 [12]. The patterns are very similar to those observed from $NbO_{2.483}$ but the positions of the strongest reflections are measurably different. NP19 does show the reflections for $NbO_{2.483}$, which is consistent with the results for NP01 and NP02. These samples have an alloy composition very close to that in NP19 and are in equilibrium with the same oxide.

The cells used to measure the partial molar Gibbs energy of niobium in samples NP16 to NP23 all used the the NbO_2,$Nb_2O_{4.8}$ reference electrode. In addition NP16 was measured again against an Fe,$Fe_{0.95}O$ reference electrode to check for thermodynamic consistency.

The cells using the niobium oxide reference electrodes can be classified into three types. The first uses samples in which the alloy is in equlibrium with monoclinic Nb_2O_5. Thus samples NP16, NP17, and NP18 were used in cells of the type

$$NbO_2,\ Nb_2O_{4.8}\ /YDT/\ Nb_2O_5,\ Nb_{(Pd)} \qquad \text{(cell-II)}$$

The cells with electrodes NP16, NP17, and NP18 functioned sluggishly, especially NP17, which could only be made to work properly between 878° C and 968° C. Below this temperature range a steady and reproducible EMF was achieved only after several hours. The two regions were distinguished, however, by the lower region having an EMF with an abnormally large temperature coefficient. The region at higher temperature had a low temperature coefficient which is characteristic of cells with overall reactions involving only solids and thus have small changes in entropy. Presumably, below a critical temperature the electrode kinetics are too slow to counter the increasing effect of electronic conduction in the electrolyte. The EMF in the upper region is linear in temperature, see figure (5-26), for all these cells and can be fit to the following equations

$$\epsilon_{NP16}(mv) = 167.5 + 0.046T \quad (1120\text{–}1270^\circ\ K) \qquad (5\text{-}2)$$

$$\epsilon_{NP17}(mv) = 151.5 + 0.022T \quad (1150\text{–}1240^\circ\ K) \qquad (5\text{-}3)$$

$$\epsilon_{NP18}(mv) = 213.3 - 0.045T \quad (1145\text{–}1275^\circ\ K) \qquad (5\text{-}4)$$

The experiment with sample NP19 uses a cell of the second type since the alloy in this electrode was not in equilibrium with Nb_2O_5 but was shown above to contain $NbO_{2.483}$. In order to maintain similarity with the equations that will be derived for the cells of type II, we will regard this compound as $Nb_2O_{4.966}$. The cell is described by

$$NbO_2, Nb_2O_{4.8} /YDT/ Nb_2O_{2.483}, Nb_{(Pd)} \qquad \text{(cell-III)}$$

The EMF measurements for this cell, see figure (5-26), may be fit to the following expression

$$\epsilon_{NP19}(mv) = 134.2 - 0.047T \quad (1225\text{–}1305^\circ\ K) \qquad (5\text{-}5)$$

The third type of cell that used an NbO_2,$Nb_2O_{4.8}$ reference electrode was that for samples NP20, NP21, NP22, and NP23. The cell configuration is written

$$NbO_2, Nb_2O_{4.8} /YDT/ NbO_2, Nb_{(Pd)} \qquad \text{(cell-IV)}$$

The cell using the NP21 electrode was run a second time after replacing the reference electrode and electrolyte to check the reproducibility of the measurements, which agree within a millivolt. Figure (5-26) also includes the results for these cells. Their voltages are fit by the following expressions

$$\epsilon_{NP20}(mv) = -10.1 - 0.022T \quad (1160\text{–}1275^\circ\ K) \qquad (5\text{-}6)$$

$$\epsilon_{NP21}(mv) = -34.3 - 0.032T \quad (1230\text{–}1285^\circ\ K) \qquad (5\text{-}7)$$

$$\epsilon_{NP22}(mv) = -30.0 - 0.058T \quad (1170\text{–}1270^\circ\ K) \qquad (5\text{-}8)$$

$$\epsilon_{NP23}(mv) = -201.4 - 0.027T \quad (1180\text{–}1255^\circ\ K) \qquad (5\text{-}9)$$

An experiment was repeated on electrode NP16 using a $Fe,Fe_{0.95}O$ reference electrode so that the resulting cell configuration was

$$Fe, Fe_{0.95}O\ /YDT/\ Nb_2O_5, Nb_{(Pd)} \qquad \text{(cell-V)}$$

The voltage fit the expression

$$\epsilon_{NP16,Fe-Fe_{0.95}O}(mv) = -13.2 + 0.056T \qquad (5\text{-}10)$$

This cell had only marginal performance and only seemed to operate well in the range between 930° C and 1000° C. In addition a slight discoloration at the iron electrode electrolyte interface was noted when the cell was disassembled. This was undoubtedly the $YFeO_3$ reaction product that Meschter [13] describes as occuring at this interface when the cell temperature is above 800° C. The amount of this phase was not enough to be detected by X-ray diffraction. Meschter [13] observed that its presence makes the measured EMF slightly lower than the thermodynamic voltage that should be generated. Bullard [14] reasons that the magnitude of this decrease depends on the ionic transference number of the ternary oxide. It will be shown later that the voltage generated by cell V was indeed slightly low but the derived partial molar Gibbs energy for niobium is within experimental error of that derived from the cell of type II.

5.4 Results for Thermochemical Quantities

The ternary diagrams that were determined in sections 5.1 and 5.2 can now be used to calculate the partial molar Gibbs energy in the alloys at those compositions terminating ternary phase regions in which two of the phases are oxides. Regions that fulfill this condition are

$$NbO\text{–}NbO_2\text{–}NbPd_2, \qquad NbO_2\text{–}Nb_{12}O_{29}\text{–}Pd_{(x_{Nb}=0.135)}$$

$NbO-NbO_2-Rh_{(x_{Nb}=0.36)}$, $NbO_2-Nb_{12}O_{29}-Rh_{(x_{Nb}=0.21)}$

$TiO-Ti_2O_3-Pd_{(x_{Ti}=0.36)}$, $TiO-Ti_2O_3-Rh_{(x_{Ti}=0.51)}$

The equilibrium between NbO_2 and $Nb_2O_{4.8}$ fixes the niobium activity by the following equation

$$2.4NbO_2 = Nb_2O_{4.8} + 0.4Nb \tag{5-11}$$

At equlibrium the Gibbs free energy change for the reaction must be zero, thus

$$\Delta G = 0 = 0.4\Delta\overline{G}_{Nb} + \Delta G_f^o(Nb_2O_{4.8}) - 2.4\Delta G_f^o(NbO_2) \tag{5-12}$$

where $\Delta\overline{G}_{Nb}$ is the partial molar Gibbs energy of niobium in equilibrium with the two oxides. $\Delta G_f^o(Nb_2O_{4.8})$ and $\Delta G_f^o(NbO_2)$ are the Gibbs energy of formation of the two oxides which were shown in chapter 1 to have values of -311200 cal/mole and -135660 cal/mole respectively at 1000° C. Substitution of these values into equation (5-12) results in a $\Delta\overline{G}_{Nb}$ of -35.9 kcal/mole.

The partial molar Gibbs energy is related to the activity and the activity coefficient by the definition

$$\Delta\overline{G}_{Nb} = RTln a_{Nb} = RTln\gamma_{Nb}x_{Nb} \tag{5-13}$$

Substitution of the compositions of the samples in equilibrium with both NbO_2 and $Nb_2O_{4.8}$ gives for a niobium-palladium solution at 1000° C, $\log_{10}\gamma_{Nb(x_{Nb}=0.135)} = -5.30$, while for rhodium solution $\log_{10}\gamma_{Nb(x_{Nb}=0.21)} = -5.47$. Note that the activity of niobium has been reduced over five orders of magnitude from that which one would expect in an ideal solution of the two metals.

The niobium activity is fixed in samples with NbO and NbO_2 by the reaction

$$2NbO = NbO_2 + Nb \tag{5-14}$$

so that the partial molar Gibbs energy of niobium is given by

$$\Delta\overline{G}_{Nb} = 2\Delta G_f^{\circ}(NbO) - \Delta G_f^{\circ}(NbO_2) \tag{5-15}$$

The Gibbs energy of formation of NbO is -72880 cal/mole, as given in chapter 1, so that the partial molar Gibbs energy in equilibrium with NbO and NbO_2 is -10.1 kcal/mole at 1000° C. The resulting activity coefficients are $\log_{10}\gamma_{Nb(x_{Nb}=0.333)} = -1.26$ for the palladium solution and $\log_{10}\gamma_{Nb(x_{Nb}=0.36)} = -1.30$ for rhodium solution. Thus, in a relatively small composition range the activity coefficents have changed four orders of magnitude. This is an indication that the character of the solution is changing dramatically in this composition range.

The equilibrium of TiO and Ti_2O_3 fixes the titanium partial molar Gibbs energy at 1000° C to a value of -22.6 kcal/mole by the reaction

$$3TiO = Ti_2O_3 + Ti \tag{5-16}$$

Equation (5-13) then gives for the titanium activity in palladium solution $\log_{10}\gamma_{Ti(x_{Ti}=0.36)} = -3.44$ and in rhodium solution $\log_{10}\gamma_{Ti(x_{ti}=0.51)}=-3.59$.

The high temperature galvanic cell experiments had the advantage that the voltage generated could be used to calculate the partial molar Gibbs energy of niobium in alloys that were in equilibrium with only one oxide. In addition they allowed the evaluation of $\Delta\overline{G}_{Nb}$ at several temperatures.

The overall reaction for a type I cell is

$$NbO + 1.25Nb_2O_{4.8} = 3.5NbO_2 \tag{5-17}$$

Multiplication of the EMF data -nF results in the Gibbs energy for this reaction as a function of temperature. The number of equivalents in equation (5-17) is

two, so using equation (5-1) gives

$$\Delta G(\text{cal/mole}) = -9206 - 2.50T(^{\circ}K) \tag{5-18}$$

Worrell [12] did the same with his data and by weighting measurements from temperatures above 1200°K over lower temperatures measurements he arrives at

$$\Delta G(\text{cal/mole}) = -11150 - 1.38T(^{\circ}K) \tag{5-19}$$

The intercept and slope of equations (5-18) and (5-19) differ significantly even though the numerical values of ΔG are in good agreement over the temperature range of the experiment. This is because of temperature dependent errors, which may vary between investigators. These differences are common among high temperature thermodynamic data and indicate that second law estimates of ΔH and ΔS must be used with caution for most reactions.

The technique most frequently used to check for temperature dependent errors and to obtain accurate heats of reaction is the third law method [15]. The Gibbs energy function, gef, calculated from calorimetric measurements or by estimation, is used to calculate ΔH°_{298} for each of the equilibrium measurements. This scheme is equivalent to obtaining the entropy change for the reaction by independent means and calculating a ΔH for each ΔG measured. The advantage is that a heat of reaction is obtained for each measurement and not by fitting all of them to obtain just one. Secondly, estimates of the entropy change of a reaction can be made quite accurately so that even when calorimetric data is lacking one can reliably use the third law method. If there are no temperature dependent errors ΔH°_{298} will be independent of temperature. The free energy function for all the oxides in equation (5-17) were presented in chapter 1 and may be used to calculate Δgef° as a function of temperature for this reaction.

Each of the EMF measurements gives a value of ΔG° which may then be used in

$$\Delta H^\circ_{298} = T(\Delta G^\circ/T + \Delta gef^\circ) \tag{5-20}$$

Figure (5-27) is the third law plot for the data of the cells of type I and from Worrell [12]. The calculated value of ΔH°_{298} changes by by 0.3 kcal/mole over the temperature range where the experiments were conducted, which is considered quite good for high temperature galvanic cell experiments. The average value of ΔH°_{298} is -15.7 ± 0.2(kcal/mole) for our measurements while Worrell's gives -16.1 ± 0.1.

The overall reaction for a cell of type II is

$$5NbO_2 + 0.4Nb_2O_5 = 2.5Nb_2O_{4.8} + 0.8Nb_{(Pd)} \tag{5-21}$$

The Gibbs free energy change for the reaction is related to the standard Gibbs energy change by the equation

$$\Delta G = \Delta G^\circ + 0.8\Delta\overline{G}_{Nb} \tag{5-22}$$

where $\Delta\overline{G}_{Nb}$ is the partial molar Gibbs free energy of niobium the alloy oxide electrode. ΔG° at any given temperature is calculated by reference to the thermochemical data for the reactants and products in their standard states (see chapter 1). The Gibbs energy functions, gef°, were used to calculate ΔG° because of the ease of interpolating them between reference temperatures. The change in the Gibbs energy function for this reaction between 1100°K and 1400°K is approximated by

$$\Delta gef^\circ(cal/deg/mole) = 9.178 - 3.897\times10^{-3}T \tag{5-23}$$

and ΔH°_{298} is 34500 cal/mole. Substitution of $\Delta G = -nF\epsilon$ into equation (5-22) and using the relation $\Delta G^{\circ} = \Delta H^{\circ}_{298} - T\Delta gef^{\circ}$ gives

$$\Delta\overline{G}_{Nb} = 1.25(-nF\epsilon - \Delta H^{\circ}_{298} + T\Delta gef^{\circ}) \tag{5-24}$$

Equation (5-21), as written, has four equivalents so that n equals 4 in (5-24) and it may be used to calculate $\Delta\overline{G}_{Nb}$ at any temperature an EMF measurement is made on a cell of type II.

Rather than substitute (5-2), (5-3), or (5-4) into equation (5-24) the individual measurements were substituted so that the scatter resulting from variation in voltage may be appreciated from a plot of $\Delta\overline{G}_{Nb}$ versus T, shown in figure (5-28). The curves are very linear and fit to these expressions

$$\Delta\overline{G}_{Nb}(NP16)\ (cal/mole) = -54500 - 6.33T \tag{5-25}$$

$$\Delta\overline{G}_{Nb}(NP17)\ (cal/mole) = -53720 - 2.70T \tag{5-26}$$

$$\Delta\overline{G}_{Nb}(NP18)\ (cal/mole) = -60630 + 4.85T \tag{5-27}$$

Cell V can be used to check the thermodynamic consistency of our measurements. Its overall cell reaction is

$$0.4Nb_2O_5 + 1.9Fe = 0.8Nb + 2Fe_{0.95}O \tag{5-28}$$

so that the partial molar Gibbs energy of niobium is given by

$$\Delta\overline{G}_{Nb} = 1.25(-nF\epsilon + 0.4\Delta G_f^{\circ}(Nb_2O_5) - 2\Delta G_f^{\circ}(Fe_{0.95}O)) \tag{5-29}$$

Equation (5-28) is for four equivalents so that with the known thermodynamics of the oxides and the voltage of cell V we can evaluate $\Delta\overline{G}_{Nb}$. Meschter et al. [13] report that the Gibbs energy of formation of $Fe_{0.95}O$ is can be evaluated

from

$$\Delta G_f^\circ(Fe_{0.95}O)(cal/mole) = -63120 + 15.45T \quad (873\text{–}1633^\circ K) \qquad (5\text{-}30)$$

At 1000° C, equations (5-29) and (5-30) yield -60 kcal/mole for $\Delta\overline{G}_{Nb}$ in sample NP16, while equation (5-25) gives -62.5 kcal/mole. The agreement between the two values is not excellent but is close to the experimental uncertainty. The difference is understandable considering the presence of $YFeO_3$ at the electrolyte-electrode interface which will lower the EMF generated by the cell.

The cell of type III has an overall cell reaction, which when written for four equivalents, is

$$0.402Nb_2O_{4.966} + 5NbO_2 = 2.5Nb_2O_{4.8} + 0.805Nb_{(Pd)} \qquad (5\text{-}31)$$

The Gibbs energy function and heat of formation of $Nb_2O_{4.966}$ are not known explicitly, so they were estimated by a linear interpolation between those assigned to $Nb_2O_{4.8}$ and Nb_2O_5. This results in

$$\Delta gef^\circ(cal/deg/mole) = 9.338 - 3.960\times10^{-3}T \qquad (5\text{-}32)$$

and the ΔH°_{298} is 34500 cal/mole for reaction (5-31). Then as before the partial Gibbs energy of niobium is simply related to the measured EMF by

$$\Delta\overline{G}_{Nb} = (-nF\epsilon - \Delta H^\circ_{298} + T\Delta gef^\circ)/0.805 \qquad (5\text{-}33)$$

Direct substitution of the measurements was made into equation (5-33) so that the points for this cell could be plotted in figure (5-28). A fit of these points yields

$$\Delta\overline{G}_{Nb}(NP19)\ (cal/mole) = -50480 + 4.62T \qquad (5\text{-}34)$$

Cells of type IV have the overall reaction

$$6NbO_2 = 2.5Nb_2O_{4.8} + Nb_{(Pd)} \tag{5-35}$$

which is based on four equivalents. The change in the Gibbs energy function from the thermochemical values in chapter 1 is

$$\Delta gef^{o}(cal/deg/mole) = 12.323 - 5.315\times10^{-3}T \tag{5-36}$$

and the ΔH^{o}_{298} is 42900 cal/mole. The partial molar Gibbs energy of niobium is then related to the measured EMF by

$$\Delta\overline{G}_{Nb} = -nF\epsilon - \Delta H^{o}_{298} + T\Delta gef^{o} \tag{5-37}$$

Each EMF measurement was substituted directly into equation (5- 37) with the results depicted in figure (5-28). The partial molar Gibbs energies of niobium for these samples are fit by

$$\Delta\overline{G}_{Nb}(NP20)\ (cal/mole) = -34210 + 1.52T \tag{5-38}$$

$$\Delta\overline{G}_{Nb}(NP21)\ (cal/mole) = -31170 + 1.79T \tag{5-39}$$

$$\Delta\overline{G}_{Nb}(NP22)\ (cal/mole) = -32620 + 4.79T \tag{5-40}$$

$$\Delta\overline{G}_{Nb}(NP23)\ (cal/mole) = -17050 + 1.78T \tag{5-41}$$

5.5 Discussion

The specific interactions between solute and solvent are best described by the niobium partial Gibbs energy in excess of that expected by a perfect solution. The excess partial molar Gibbs energy is the difference between the partial molar Gibbs energy and the configurational Gibbs energy obtained upon perfectly random mixing. Thus the expressions for $\Delta\overline{G}_{Nb}$ in section 5.4, can be used to derive the excess partial molar Gibbs energy of niobium, $\Delta\overline{G}^{xs}_{Nb}$, from the equation

$$\Delta\overline{G}^{xs}_{Nb} = \Delta\overline{G}_{Nb} - RT\ln x_{Nb} \tag{5-42}$$

When this is applied to equations (5-25,26,27), (5-34), and (5-38,39,40,41) the following equations are derived in cal/mole

$$x_{Nb} = 0.03 \qquad \Delta\overline{G}^{xs}_{Nb} = -54500 + 0.64T \tag{5-43}$$

$$x_{Nb} = 0.037 \qquad \Delta\overline{G}^{xs}_{Nb} = -53720 + 3.86T \tag{5-44}$$

$$x_{Nb} = 0.067 \qquad \Delta\overline{G}^{xs}_{Nb} = -60630 + 10.2T \tag{5-45}$$

$$x_{Nb} = 0.104 \qquad \Delta\overline{G}^{xs}_{Nb} = -50480 + 9.12T \tag{5-46}$$

$$x_{Nb} = 0.139 \qquad \Delta\overline{G}^{xs}_{Nb} = -34210 + 5.44T \tag{5-47}$$

$$x_{Nb} = 0.171 \qquad \Delta\overline{G}^{xs}_{Nb} = -31170 + 5.30T \tag{5-48}$$

$$x_{Nb} = 0.18 \qquad \Delta\overline{G}^{xs}_{Nb} = -32620 + 8.19T \tag{5-49}$$

$$x_{Nb} = 0.22 \qquad \Delta\overline{G}^{xs}_{Nb} = -32620 + 7.49T \tag{5-50}$$

$$x_{Nb} = 0.255 \qquad \Delta\overline{G}^{xs}_{Nb} = -17050 + 4.49T \tag{5-51}$$

Equations (5-49) and (5-50) were both obtained from equation (5-40), since at equilibrium the partial molar Gibbs energy of niobium in saturated palladium, $x_{Nb} = 0.18$, must equal that at the lower phase boundary of $NbPd_3$, $x_{Nb} = 0.22$. The results for the alloys in equilibrium with NbO,NbO_2 and $NbO_2,Nb_{12}O_{29}$ can be used to calculate $\Delta\overline{G}_{Nb}^{xs}$ at 1000° C at niobium mole fractions 0.333 and 0.135 respectively. The partial molar Gibbs energies of -10.1 and -35.9 kcal/mole yield niobium excess partial molar Gibbs energy of -7.3 kcal/mole at $x_{Nb} = 0.333$ and -30.8 kcal/mole at $x_{Nb} = 0.135$.

The partial molar enthalpy and excess partial molar entropy are related to the excess partial molar Gibbs energy by $\Delta\overline{G}_i^{xs} = \overline{H}_i - T\overline{S}_i^{xs}$. Inspection of equations (5-42) through (5-51) reveals that the partial molar enthalpy tends to a less negative value with increasing niobium concentration. The uncertainty of the temperature coefficient in these equations makes it difficult to derive any trends in the partial molar entropy. Kubaschewski [16] has shown that for a wide variety of metallic solutions, the partial molar enthalpy and excess partial molar entropy at high dilution are approximately related by $\overline{H}_i = (3400 \pm 1400°\ K)\overline{S}_i^{xs}$. This relation is understood by considering that for solutions where there are large specific interactions between the solute and solvent there is a reduction in the lattice vibration contribution to the entropy. At higher concentration of the solute there is an additional tendency toward ordering because the solute atoms wish to surround themselves with solvent atoms. Thus, for the partial molar enthalpies in the equations (5-25) to (5-41), an excess partial molar entropy of the order of -10 cal/deg/mole is not unreasonable.

The activity coefficient, defined by equation (5-13), is plotted in figure (5-29) for the results of the galvanic cells at 1000° C. The activity coefficients for

the alloys in equilibrium with two oxides are also plotted in this figure. It is clear that the activity coefficient will decrease over nine orders of magnitude when a small amount of niobium is dissolved in palladium at 1000° C; this effect is a manifestation of the extremely strong bonds that are being formed upon dissolution. The curve in figure (5-29) is roughly sigmoidal, with steepest descent at mole fractions between 0.10 and 0.15. A plot of acid activity as it is titrated by a base also has such a sigmoidal shape thus the curve in figure (5-29) represents the titration of a metal acid, niobium, by a metal base, palladium. The curve, of course, is not continuous as it is in aqueous acid-base titration curves because the two solid metals are not completely miscible in all proportions.

The simplest model to describe the behavior of the palladium solid solution is the quasichemical type [17]

$$\Delta\overline{G}_{Nb}^{xs} = w(1-x_{Nb})^2 \tag{5-52}$$

where w is the interaction parameter. The data derived above indicate that w is not at all constant but is a strong function of concentration, which indicates that the character of the bonding in solution is changing rapidly as niobium is added. If one approximates this change in w as a linear function of x_{Nb} the result is at 1000° C

$$\frac{\Delta\overline{G}_{Nb}^{xs}(\text{kcal/mole})}{(1 - x_{Nb})^2} = -61.8 + 156.1x_{Nb} \tag{5-53}$$

Thus the interaction parameter changes from -62 kcal/mole at infinite dilution to -34 kcal/mole in saturated fcc palladium.

The $\Delta\overline{G}_{Nb}^{xs}$ of approximately -62 kcal/mole at infinite dilution of niobium can be compared to the substantially more negative value, -84.1 kcal/mole, for zirconium at infinite dilution in palladium which was obtained by Schaller [18]. This observation is entirely consistent with the Lewis acid-base model discussed in chapter 1. Zirconium, with a nuclear charge one less than niobium, has more expanded d-orbitals and one more vacant d- orbital; thus it can function as a better acid. The more negative value of zirconium's excess partial Gibbs energy reflects its enhanced ability to accommodate palladium's nonbonding electron pairs.

Kleykamp [19] performed high temperature galvanic cell experiments on the niobium-rhodium system. The excess partial molar Gibbs energy of niobium at infinite dilution in rhodium was found to be -48 kcal/mole, which is much more postive than the -62 kcal/mole we have observed in palladium solution. Palladium has one more valence electron than rhodium and therefore has one additional nonbonding pair available for Lewis base bonding. Clearly the electron pair used at infinite dilution in the palladium solution forms a stronger bond to niobium than rhodium forms with niobium at infinite dilution.

Figure (5-30) is a graph of $\log_{10}\gamma_{Nb}$ for both palladium and rhodium solutions. The data from figure (5-29) has been reproduced here, and superimposed are the results from our rhodium-niobium oxide experiments as well as the activity coefficients derived from Kleykamp's [19] EMF experiments for niobium-rhodium alloys. A slight irregularity does appear in Kleykamp's results; the niobium activity coefficient in the 0.069 niobium mole fraction alloy appears to be smaller than the activity coefficient at his 0.023 mole. This could only occur if there was a two phase region between the two samples. The Nb-Rh

phase diagram reported by Ritter et al. [20] shows that fcc rhodium exists to a niobium mole fraction of 0.13. It is not impossible, however, that a new intermetallic has gone undetected. The analogous Ti-Pt and Zr-Pt systems do form intermetallics rich in platinum that are roughly assigned the compostion $TiPt_8$ [21] and $ZrPt_8$ [22].

Figure (5-30) offers new insight on the strength of bonds formed with different nonbonding pairs. At low niobium concentration the activity of niobium at the same mole fraction is seen to be lower in palladium than in rhodium solution, as discussed above for the case of infinite dilution. At higher niobium concentration, however, the reverse is true. Rhodium is a stronger base at high niobium concentration while palladium is stronger at low niobium mole fraction. This behavior can be accounted for by several contributing effects described in the context of the Lewis acid-base theory.

The two electron pairs of palladium cannot be expected to have the same bonding ability. Just as with normal polyfunctional bases, the basicity of the second base pair is reduced from that of the first. This difference in transition metal bases stems in part from the crystal field effect. As discussed in chapter 1, when an atom is placed in the nonspherically symmetric field of a crystal lattice site, the d-orbitals split in energy. The outermost d-orbitals can be used most effectively in normal covalent bonds to neighboring atoms. These bonds are more stable than the acid-base bond because a bond formed where both atoms donate an electron will naturally be more stable than a bond where both electrons are donated by a single atom. Thus the nonbonding electron pairs are delegated to the least exposed of the of the five d-orbitals in the base. All things being equal, the single nonbonding orbital of rhodium would have the same

basicity as the innermost of palladium's two nonbonding pairs. The other pair of palladium should be a much more effective base than the innermost pair since it is more exposed and better able to overlap with orbitals on neighboring atoms.

The situation is complicated by the increase in atomic number on going from rhodium to palladium. The increasing nuclear charge contracts the orbitals of the base and thereby decreases the ability of nonbonding pairs to overlap with orbitals on adjacent atoms. This is the effect that eventually makes silver and gold such poor bases. Thus the innermost of palladium's two nonbonding orbitals must be a poorer base than the single nonbonding pair of rhodium. Figure (5-31) diagramatically explains the combination of the two effects. The nonbonding orbital on rhodium is drawn so that it is intermediate in extent to the two nonbonding pairs on palladium.

The unrefined Lewis acid-base interpretation of these transition metal solutions uses a greatly simplified picture of how electrons are distributed between the atoms. Much of the electron density that is said to be donated via d-orbitals from the base to the acid may actually be offset by polarization of the bond toward the base and movement of electron density back toward the base through other orbitals. The latter mechanism is similar to the "back bonding" observed in metal carbonyls in which electron density donated through the σ orbitals of the CO ligands is back donated to CO's π orbitals by symmetrically correct orbitals on the metal. Thus, the actual charge on any of the metal atoms will never vary appreciably from zero. To the extent that such charge transfer does occur, the electronegativity of the constituent atoms will play a role in polarizing the bonds that are formed back toward the more

electronegative atom. Polarization will weaken the bonds that are formed. Palladium is more electronegative than rhodium: thus, if Nb-Pd solutions and Nb-Rh solutions have the same amount of back bonding, the Nb-Pd bond will be weaker than the Nb-Rh bond, all other things equal.

The behavior of the two titration curves in figure (5-30) is completely explained by the combination of the these effects. At low niobium concentration, the presence of both of the nonbonding orbitals on palladium serve to make it a better base than rhodium. At higher niobium concentration palladium's nonbonding pair most available for bonding has been saturated so that the solution appears to be one of niobium atoms and palladium atoms already associated with niobium. The nonbonding pair available under these conditions is the least in bonding ability so rhodium is the better base.

The Ti-Pd and Ti-Rh systems show the same behavior at high titanium concentration. Samples TP01 and TR01 both contained TiO and Ti_2O_3 so that the titanium activity was fixed to the same value. Rhodium contains 51 atomic percent titanium while palladium contains 37 for this same titanium activity. Thus again at higher concentrations of the acid, rhodium is a better base.

The base activity must decrease as the acid concentration builds. Although our experiments do not measure palladium activity directly, the Gibbs-Duhem equation may be used to calculate how it changes with niobium concentration. The Gibbs-Duhem equation in differential form for a binary solution is written

$$d\log\gamma_1 = -\frac{x_2}{x_1} d\log\gamma_2 \qquad (5\text{-}54)$$

which, when integrated by parts from pure component 1 to a mole fraction of x_2

of component 2, gives

$$\log\gamma_1 = \frac{-x_2}{1-x_2}\log\gamma_2 + \int_0^{x_2} \frac{\log\gamma_2}{(1-x_2)^2}dx_2 \qquad (5\text{-}55)$$

Equation (5-53) may be substituted into (5-55) to give the palladium activity coefficient out to saturated fcc palladium at 1000° C. The calculated excess partial molar Gibbs energy of palladium is -3.7 kcal/mole at 0.18 mole fraction niobium and 1000° C. A resonable value for the excess entropy is -3 to -5 cal/deg/mole so that $\Delta\overline{G}_{Pd}^{xs}$ at 1515° K is -3 to -2.5 kcal/mole. This compares well with the the palladium partial pressure measurement performed by Gibson [23], who calculated an excess partial molar Gibbs energy of -2.2 kcal/mole for this alloy at 1515° K.

The partial molar Gibbs energies of niobium and palladium in saturated fcc Pd must be equal to those in the lower phase boundary of the $NbPd_3$ intermetallic. This boundary has the composition of $NbPd_{3.55}$. The Gibbs energy of formation for this phase is calculated from the two partial molar quantities. This gives a value of -41.5 kcal/mole at 1000° C or -9.1 kcal/g.atom. Kleykamp's results [19] indicate that $\Delta G_f(NbRh_{3.55})$ equals -47 ± 1 kcal/mole at 1000° C, which again reflects the fact that rhodium lowers the activity of niobium more than palladium at these concentrations. It is important to realize the meaning of basicity strength depends on context; deciding which species is a better base depends on whether the definition is based on the integral Gibbs energy or one of the individual partial molar quantities. One would have concluded that palladium was the better base at this composition if the decision was based solely on the activity of palladium, because the calculated value of the partial molar

Gibbs energy of palladium, -4.2 kcal/mole, is more negative than that calculated for rhodium, -0.3 kcal/mole, at $x_{Nb} = 0.22$. The difference of niobium activity in the two solutions, however, far outweighs the lower palladium activity when one calculates the Gibbs energy of formation. This is a particularly important consideration when the bonding ability of the different species changes so drastically with composition.

5.6 Conclusions

The titration curves for Nb-Pd and Nb-Rh solutions have been used to resolve the different contributions of the two electron pairs on palladium. The lower activity of niobium in dilute Nb-Pd solutions reflects the presence of the extra electron pair of palladium and this orbital's enhanced basicity is attributed to crystal field splitting. The lower activity of niobium at high concentrations in rhodium solution is a result of the increased nuclear charge on palladium, which decreases the ability of its second electron pair to be used in acid-base bonding.

The results of these experiments have clearly illustrated the relative importance of number of bonding orbitals, crystal field splitting, and increasing nuclear charge in rhodium and palladium alloys. All the observations are completely consistent with the Lewis acid-base concept applied to transition metal alloys. This work has been another step in a continuing effort to turn what is now a qualitative theory used to predict trends in the stabilities of alloys into one that is quantitative. These experiments were a successful step in this direction because the activity of one of the constituents was measured as a function of composition, thereby resolving the extent of the acid-base interaction. Future

studies should address similar measurements on related alloys of the transition series such as V-Pd, V-Rh, Zr-Pd, Zr-Rh, and completion of the titration curves for Ti-Pd and Ti-Rh.

Chapter 5 References

[1] B.C. Giessen et al., Met. Trans. A, 11A(1980) p.709-15

[2] H. Schafer, D. Bergner, R. Gruehn, Z. Anorg. Allg. Chem. 365(1969) p.438

[3] J.F. Marucco, Compt. Rend. Acad. Sci. Paris, 275(1972) p.275

[4] K. Naito, N. Kamegashira, N. Sasaki, J. Solid State Chem. 35(1980) p.305-11

[5] R. Norin, Acta Chem. Scand. 17(1963) p.1391-1404

[6] R. Norin, Acta Chem. Scand. 20(1966) p.871-80

[7] R. Gruehn, R. Norin, Z. Anorg. Allg. Chem., 355(1967) p.176- 81

[8] P. Greenfield, P. Beck, Trans. AIME, 206(1956) p.265-76

[9] R. Horyn, R. Andruszkiewicz, J. Less-Common Met. 71(1980)P9-P12

[10] R. Horyn, L. Folcik-Kokot, N. Iliev, J. Less-Common Met., 57(1978)P69-P74

[11] R. Hultgren, P. Desai, D. Hawkins, M. Gleiser, K. Kelly, D. Wagman, "Selected Values for the Thermodynamic Properties of the Elements", Amer. Soc. for Metals, Metals Park, Ohio, 1973

[12] W.L. Worrell, "Measurements of the Thermodynamic Stabilities of the Niobium and Tantalum Oxides Using a High Temperature Galvanic Cell", University of California, Lawrence Radiation Laboratory, UCRL-11957

[13] P.J. Metschter, W.L. Worrell, Met. Trans. B, 6B(1975)p.345

[14] G.L. Bullard, Ph.D. Dissertation, Dept. of Chemistry, U.C. Berkeley, 1978

[15] K. Pitzer, L. Brewer, "Thermodynamics", (a revision of that by G.N. Lewis and M. Randell), McGraw-Hill Book Co., N.Y., 1961

[16] O. Kubaschewski, High Temperatures - High Pressures, 13(1981)p.435-440

[17] There are many references but an early reveiw is G. Scatchard, Chem. Rev., 8(1931)p.321-33

[18] H.J. Schaller, Ber. Bunsenges. 80(1976)p.999-1002

[19] H. Kleykamp, J. Less-Common Metals, 83(1982)p.105-113

[20] D.L. Ritter, B.C. Giessen, N.J. Grant, Trans. Met. Soc. AIME, 230(1964)p.1250-59

[21] J.L. Murray, Bull. Alloy Phase Diagrams, 3(1982)p.329-35

[22] P.J. Meschter, W.L. Worrell, Met. Trans. A, 8A(1977)p.503-9

[23] J.K.M. Gibson, Ph.D. dissertation, Dept. of Chemistry, U.C. Berkeley, 1983

[24] Joint Committee on Powder Diffraction Standards, 1601 Park Lane, Swarthmore, Pennsylvania

Table 5-I

Optical Microscopy Results for the NP Samples

Sample	Reactants	Number of Oxide Phases
NP01	Nb,Pd,Nb_2O_5	1
NP02	Nb,Pd,Nb_2O_5	1
NP03	Nb,Pd,Nb_2O_5	2
NP04	Nb,Pd,Nb_2O_5	1
NP05	Pd,NbO	1
NP06	Nb,Pd,Nb_2O_5	1
NP07	Nb,Pd,NbO_2	1
NP08	Nb,Pd,NbO	2
NP09	Nb,Pd,Nb_2O_5	2
NP10	Nb,Pd,NbO_2	2
NP11	Nb,Pd,NbO	1
NP12	Nb,Pd,NbO_2	1
NP13	Nb,Pd,NbO	1
NP14	Nb,Pd,NbO	1
NP15	Nb,Pd,NbO	1

Table 5-II

Assignment of Reflections in Figure (5-6)

d values are in angstroms. Intensities, I, are in percent of maximum.
2θ values are given for Cu K_α radiation.
See [24] for NbO and NbO_2 powder data.
Powder data for $NbPd_2$ is derived in Appendix 1.

$NbPd_2$			NbO_2			NbO			NP08	NP09	NP10
(hkl)	d 2θ I		(hkl)	d 2θ I		(hkl)	d 2θ I		d 2θ I	d 2θ I	d 2θ I
						100	4.160 21.3 50		4.203 21.1 30	4.203 21.1 32	4.184 21.2 25
			400R	3.42 26.1 100					3.412 26.1 11	3.415 26.1 32	3.409 26.1 13
			321	3.21 27.8 30							3.194 27.9 2
						110	2.946 30.2 50		2.975 30.0 26	2.973 30.0 54	2.965 30.1 54
			222,520R	2.54 35.3 80					2.546 35.2 10	2.542 35.3 39	2.535 35.4 21
						111	2.416 37.1 50		2.427 37.0 100	2.428 37.0 100	2.422 37.1 86
101	2.292 39.3 100								2.289 39.3 91	2.289 39.3 87	2.283 39.4 62
031	2.267 39.8 96								2.268 39.7 77	2.275 39.6 37	2.263 39.8 45
						200	2.095 43.1 100		2.102 43.0 75	2.102 43.0 100	2.098 43.1 100
130	1.991 45.6 65								1.988 45.6 49	1.911 45.5 13	1.987 45.6 20
002	1.943 46.8 30								1.943 46.7 46.7	1.944 46.7 46.7	1.939 46.8 46.8
						210	1.873 48.5 50		1.882 48.3 10	1.881 48.4 11	1.878 48.4 14
			622R,650	1.754 52.2 80					1.751 52.2 9	1.753 52.1 28	1.748 52.3 10
			800R	1.712 53.5 50		211	1.713 53.4 50		1.719 53.3 4	1.717 53.3 18	1.714 53.4 26

Table 5-III

EDAX Measurements on the Alloy Phase in the NP Samples (x_{Nb})

NP01	NP02	NP03	NP04	NP05
0.100	0.101	0.134	0.254	0.244
0.104	0.103	0.140	0.250	0.244
0.105	0.101	0.139	0.244	0.239
0.100	0.101	0.131	0.250	0.242
0.100	0.103	0.131	0.252	
0.102	0.100	0.135	0.253	
			0.260	
NP06	**NP07**	**NP08**	**NP09**	**NP10**
0.237	0.322	0.333	0.325	0.317
0.238	0.322	0.333	0.328	0.324
0.238	0.337	0.333	0.326	0.326
0.231	0.327	0.331	0.322	0.325
NP11	**NP12**	**NP13**	**NP14**	**NP15**
0.503	0.777	0.920	0.645	0.618
0.566	0.792	0.905	0.667	0.667
0.561	0.731	0.873	0.649	0.625
0.571	0.754	0.881	0.626	0.683
0.531	0.796			
0.516				
0.668				
0.511				
0.659				
0.484				

Table 5-IV

Assignment of Reflections in Figure (5-7)

d values are in angstroms. Intensities are in percent of maximum.
2θ values are given for Cu K_α radiation.
See [24] for NbO_2 powder data.
Powder data for $NbPd_2$ is derived in Appendix 1.

$NbPd_2$		NbO_2		NP07
hkl	d 2θ I	hkl	d 2θ I	d 2θ I
		400R	3.42 26.1 100	3.418 26.0 72
		321	3.21 27.8 30	3.202 27.8 3
		222,520R	2.54 35.3 80	2.541 35.3 93
		440	2.422 37.1 50	2.421 37.1 6
		521	2.341 38.5 20	2.350 38.3 3
101	2.292 39.3 100			2.288 39.4 63
031	2.267 39.8 96			2.265 39.8 100
130	1.991 45.6 65			1.991 45.5 18
002	1.943 46.8 30			1.943 46.7 14
		640,213	1.897 48.0 20	1.894 48.0 4
		622R,650	1.754 52.2 80	1.753 52.1 42
		800R	1.712 53.5 50	1.711 53.5 27

Table 5-V

Assignment of Reflections in Figure (5-8)

d values are in angstroms. Intensities are in percent of maximum.
2θ values are given for CuK_α radiation.
See [24] for NbO_2 data.
Powder data for β-$NbPd_3$ is derived in Appendix 1.

β-$NbPd_3$		NbO_2		NP04	NP05	NP06
hkl	d 2θ I	hkl	d 2θ I	d 2θ I	d 2θ I	d 2θ I
		400R	3.42 26.1 100	3.417 26.1 100	3.409 26.1 32	3.415 26.1 28
		321	3.21 27.8 30			
		222,520R	2.54 35.3 80	2.543 35.3 80	2.539 35.3 24	2.541 35.3 35
		440	2.422 37.1 50	2.417 37.2 16	2.411 37.3 4	2.419 37.2 6
211	2.351 38.3 34	521	2.341 38.5 20	2.350 38.3 4		2.352 38.2 3
022	2.282 39.5 48				2.283 39.4 28	
006	2.267 39.8 92			2.263 39.8 91	2.262 39.8 100	2.262 39.8 100
212	2.252 40.0 91					
023	2.137 42.3 51			2.135 42.3 9		2.133 42.3 6
213	2.112 42.8 100			2.111 42.8 9	2.108 42.9 4	2.108 42.9 12
024	1.973 46.0 30					
214	1.954 46.5 58			1.952 46.5 2	1.941 46.8 7	1.952 46.5 20
		640,213	1.897 48.0 20			
		622R,650	1.754 52.2 80	1.753 52.1 58	1.751 52.2 17	1.752 52.2 27
		800R	1.712 53.5 50	1.709 53.6;53.6 20	1.707 53.5 5	1.711 7

Table 5-VI

Results for Palladium-Niobium Oxide Equilibration

Sample	Reactants	Composition			Phases Present (x_{Nb} alloy)
		x_{Pd}	x_{Nb}	x_O	(See Table 5-VIb)
NP01	Nb,Pd,Nb_2O_5	0.306	0.223	0.471	$NbO_{2.483}$,Pd(0.103)
NP02	Nb,Pd,Nb_2O_5	0.307	0.222	0.471	$NbO_{2.483}$,Pd(0.103)
NP03	Nb,Pd,Nb_2O_5	0.292	0.250	0.458	NbO_2,$Nb_{12}O_{29}$,Pd(0.135)
NP04	Nb,Pd,Nb_2O_5	0.181	0.320	0.498	NbO_2,β–$NbPd_3$(0.252)
NP05	Pd,NbO	0.382	0.309	0.309	NbO_2,β–$NbPd_3$(0.242)
NP06	Nb,Pd,Nb_2O_5	0.338	0.295	0.366	NbO_2,β–$NbPd_3$(0.236)
NP07	Nb,Pd,NbO_2	0.246	0.323	0.430	NbO_2,$NbPd_2$(0.327)
NP08	Nb,Pd,NbO	0.282	0.421	0.297	NbO,NbO_2,$NbPd_2$(0.333)
NP09	Nb,Pd,Nb_2O_5	0.181	0.429	0.390	NbO,NbO_2,$NbPd_2$(0.325)
NP10	Nb,Pd,NbO_2	0.155	0.437	0.409	NbO,NbO_2,$NbPd_2$(0.323)
NP11	Nb,Pd,NbO	0.169	0.543	0.288	NbO,σ–Nb_3Pd_2,$NbPd_2$
NP12	Nb,Pd,NbO_2	0.035	0.538	0.427	NbO,Nb(0.770)
NP13	Nb,Pd,NbO	0.041	0.669	0.291	NbO,Nb(0.896)
NP14	Nb,Pd,NbO	0.300	0.600	0.100	NbO,Nb(sat),σ–Nb_3Pd_2
NP15	Nb,Pd,NbO	0.248	0.649	0.103	NbO,Nb(sat),σ–Nb_3Pd_2

Table 5-VII

Results for NR, TR, and TP Samples

Sample	Reactants	Composition $x_{Rh\ or\ Pd}$	$x_{Nb\ or\ Ti}$	x_O	Phases Present ($x_{Nb\ or\ Ti}$ alloy)
NR01	Rh,NbO_2,Nb_2O_5	0.050	0.300	0.650	$NbO_2,Nb_{12}O_{29},Rh(0.21)$
NR02	Rh,NbO,Nb_2O_5	0.294	0.255	0.451	$Nb_2O_5,Rh(0.20)$
NR03	Rh,Nb,NbO_2	0.300	0.300	0.400	$NbO_2,Rh(0.22)$
NR04	Rh,Nb,NbO	0.348	0.551	0.101	NbO,Rh(0.56)
NR05	Rh,NbO,NbO_2	0.099	0.401	0.500	$NbO,NbO_2,Rh(0.36)$
NR06	Rh,Nb,NbO	0.200	0.552	0.248	NbO,Rh(0.56)
NR07	Rh,NbO_2,Nb_2O_5	0.150	0.250	0.600	$Nb_2O_5,Rh(0.07)$
TR01	Rh,Ti,Ti_2O_3	0.030	0.436	0.534	$TiO,Ti_2O_3,Rh(0.51)$
TR02	Rh,Ti_2O_3,TiO_2	0.032	0.380	0.588	? ,Rh(0.27)
TP01	Pd,TiO,Ti_2O_3	0.028	0.438	0.534	$TiO,Ti_2O_3,Pd(0.36)$

Table 5-VIII

Summary of Preparation and Characterization of Electrodes

Sample	Starting Materials (wt%)	Annealing Temp	Mass Change (wt%)	EDAX Measurements on alloy phase (x_{Nb})	Product Phases
NP16	Pd(51.9) Nb(1.0) Nb_2O_5(47.1)	6dy 1130C	-6	0.03 0.03 0.02	Nb_2O_5, Pd(s.s.)
NP17	Pd(54.9) Nb(2.5) Nb_2O_5(42.6)	8dy 1020C	-1.8	0.039 0.037 0.036 0.034	Nb_2O_5, Pd(s.s.)
NP18	Pd(53.5) Nb(4.1) Nb_2O_5(42.4)	3dy 1090C	-1.7	0.069 0.066 0.065 0.067	Nb_2O_5, Pd(s.s.)
NP19	Pd(51.4) Nb(6.1) Nb_2O_5(42.5)	3dy 1090C	-1.3	0.102 0.098 0.106 0.102 0.112	$NbO_{2.483}$, Pd(s.s.)
NP20	Pd(41.2) Nb(6.4) NbO_2(52.4)	6dy 1130C	-2.0	0.140 0.139 0.137 0.141	NbO_2, Pd(s.s.)
NP21	Pd(37.7) Nb(5.9) NbO_2(56.4)	6dy 1000C	-0.2	0.171 0.168 0.166 0.177	NbO_2, Pd(s.s.)
NP22	Pd(37.2) Nb(8.1) NbO_2(54.7)	6dy 1000C	-0.2	0.212 0.183 0.221 0.185 0.194 0.226 0.187 0.185	NbO_2, Pd(s.s), β–$NbPd_3$
NP23	NP04	24hr 1150C	-0.0	see NP04	NbO_2, β–$NbPd_3$

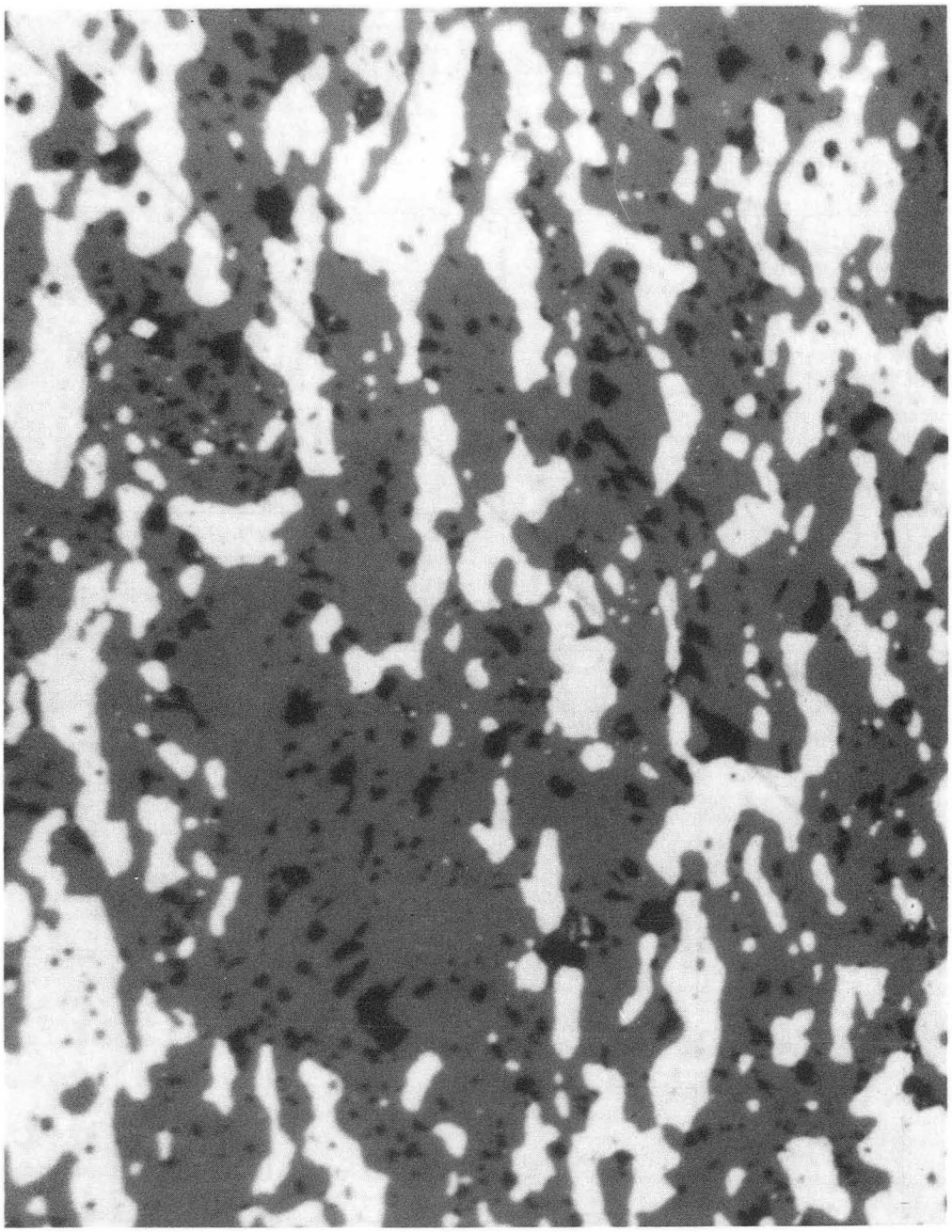

XBB 867-5548

Figure (5-1)

Optical micrograph of sample NP02, as polished at 400 X using unpolarized light. Note the presence of the light grey area which is the alloy and a single dark grey area; the black areas are voids. The dark grey material is the oxide in equilibrium with the alloy.

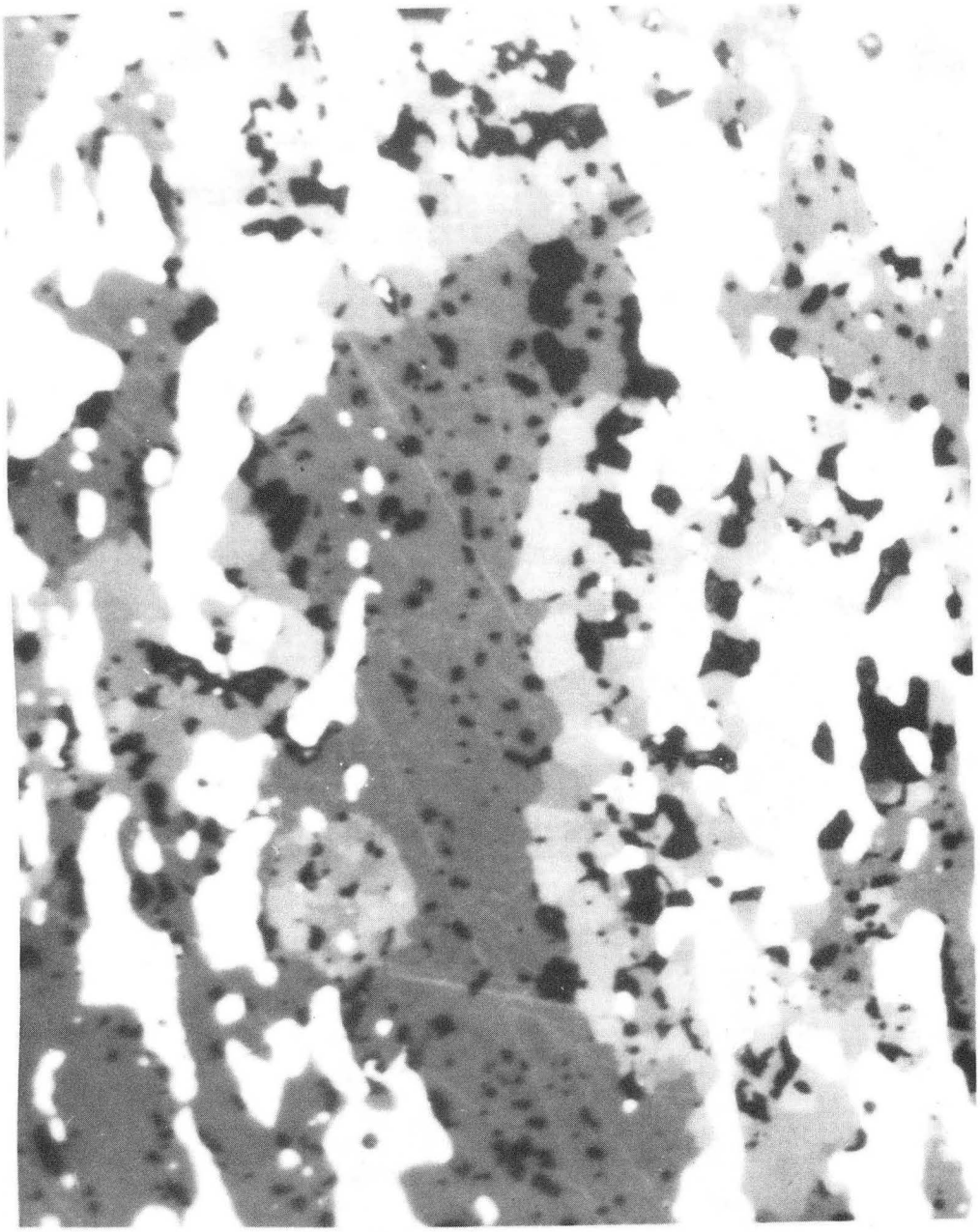

XBB 867-5540

Figure (5-2)

Optical micrograph of sample NP03, as polished at 400 X using unpolarized light. Besides the alloy and voids there are two areas of medium grey which are grains of two different oxides.

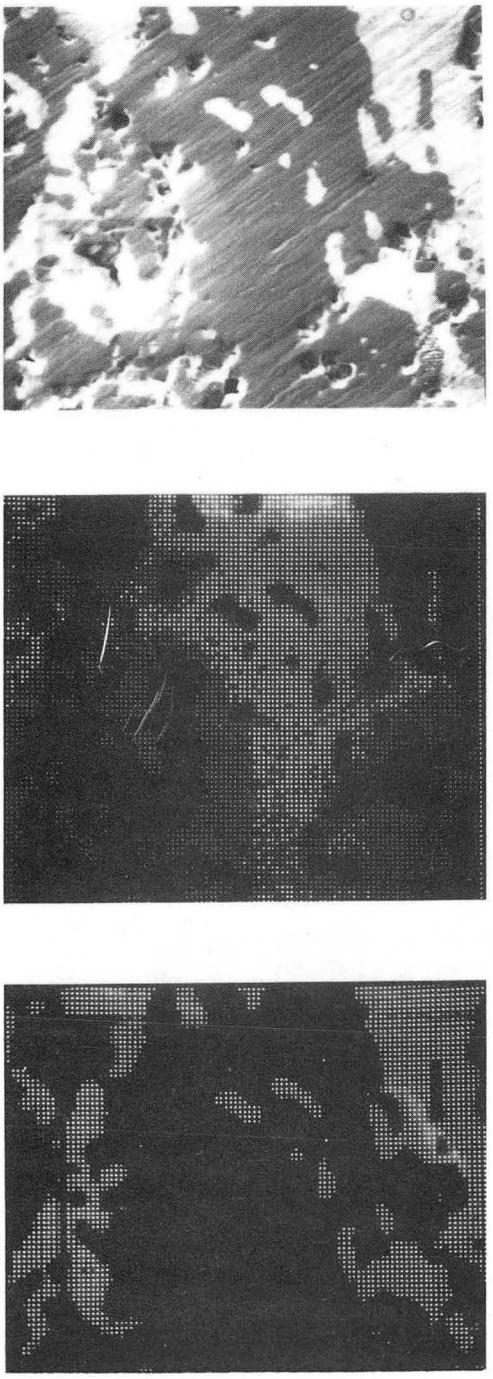

XBB 867-5541

Figure (5-3)

Electron micrographs of NP03 at 1000 X. The upper photo is the secondary electron image of the surface while the lower two micrographs are Auger electron maps of the same area. The bottom micrograph maps the presence of Auger electrons with energy corresponding to palladium while the middle maps that of oxygen. The palladium map clearly shows that the light area in the SEM image is the alloy. The oxide region shows areas of two different concentrations of oxygen corresponding to the two different oxides.

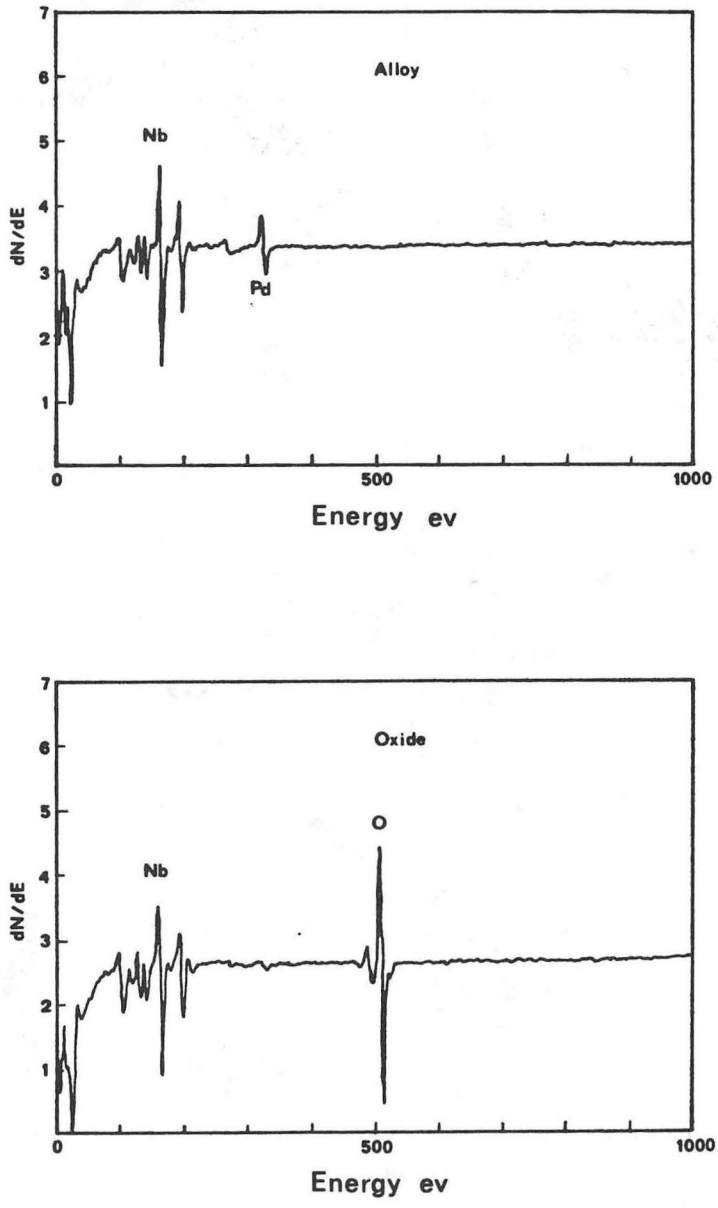

-- XBL 868-2925 --

Figure (5-4)

Auger electron energy derivative spectrums for different phases of NP13. The upper spectrum is for the alloy phase which shows no significant amounts of oxygen while the spectrum for the oxide does not indicate the presence of palladium.

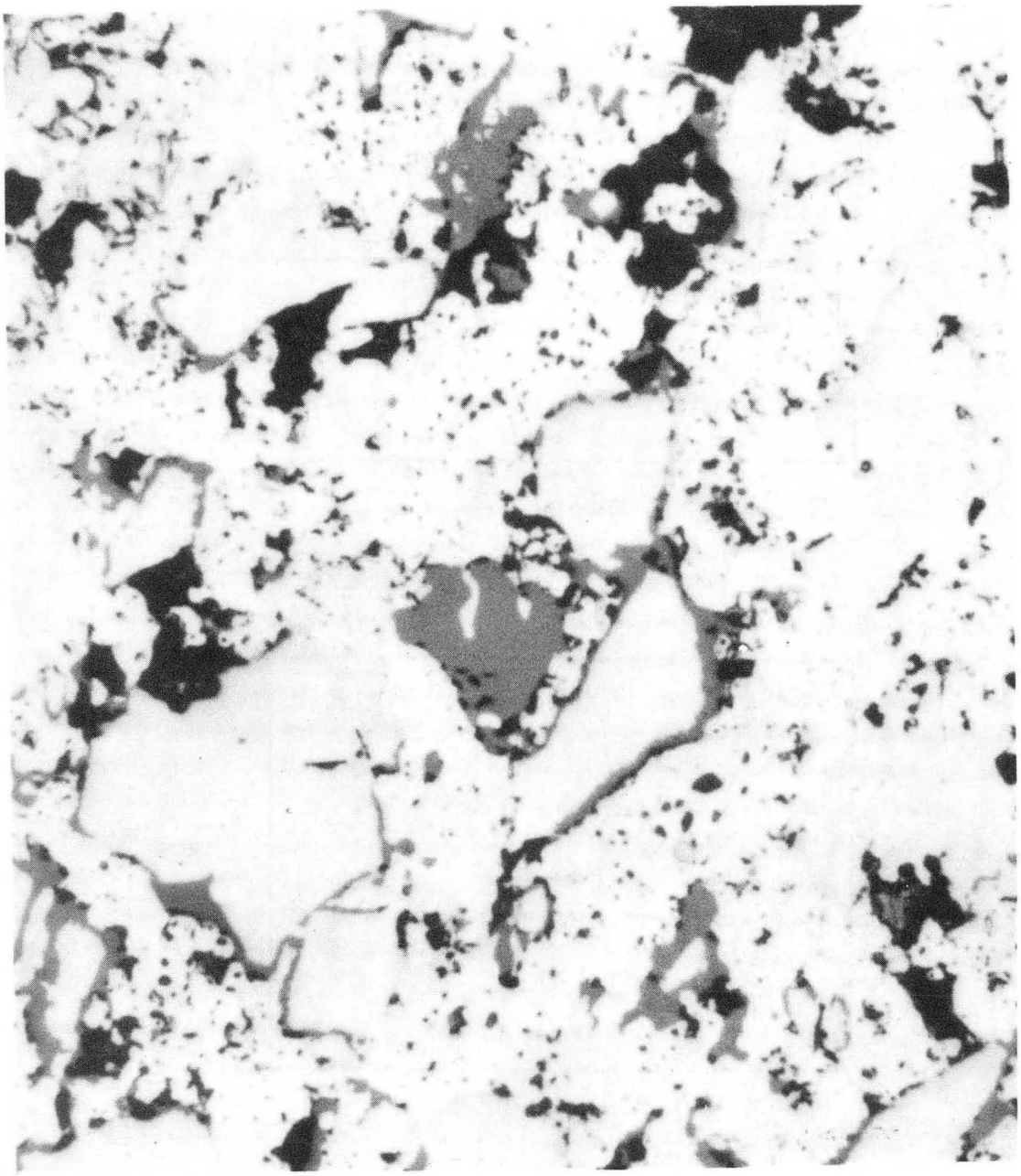

Figure (5-5) XBB 867-5549

Optical micrograph of NP08 (800 X). The large cubic grains are NbO crystallites. The darker grey grains are NbO_2.

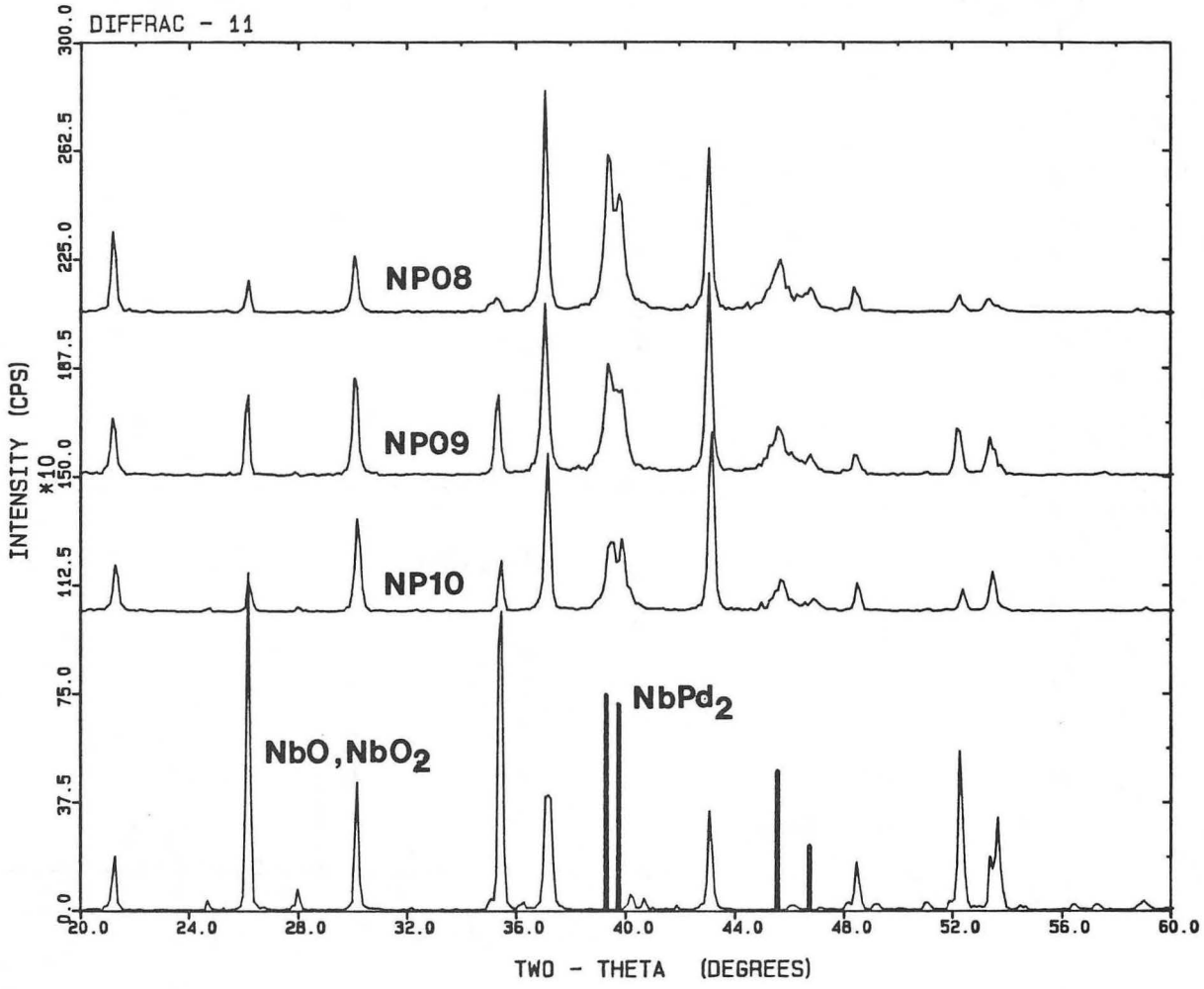

-- XBL 868-2926 --

Figure (5-6)

XRD patterns for NP08, NP09, and NP10 using Cu(K_α) radiation. The lower trace is a sample of NbO and NbO_2 in equilibrium. The calculated positions and relative intensities of $NbPd_2$ are included in the lower pattern.

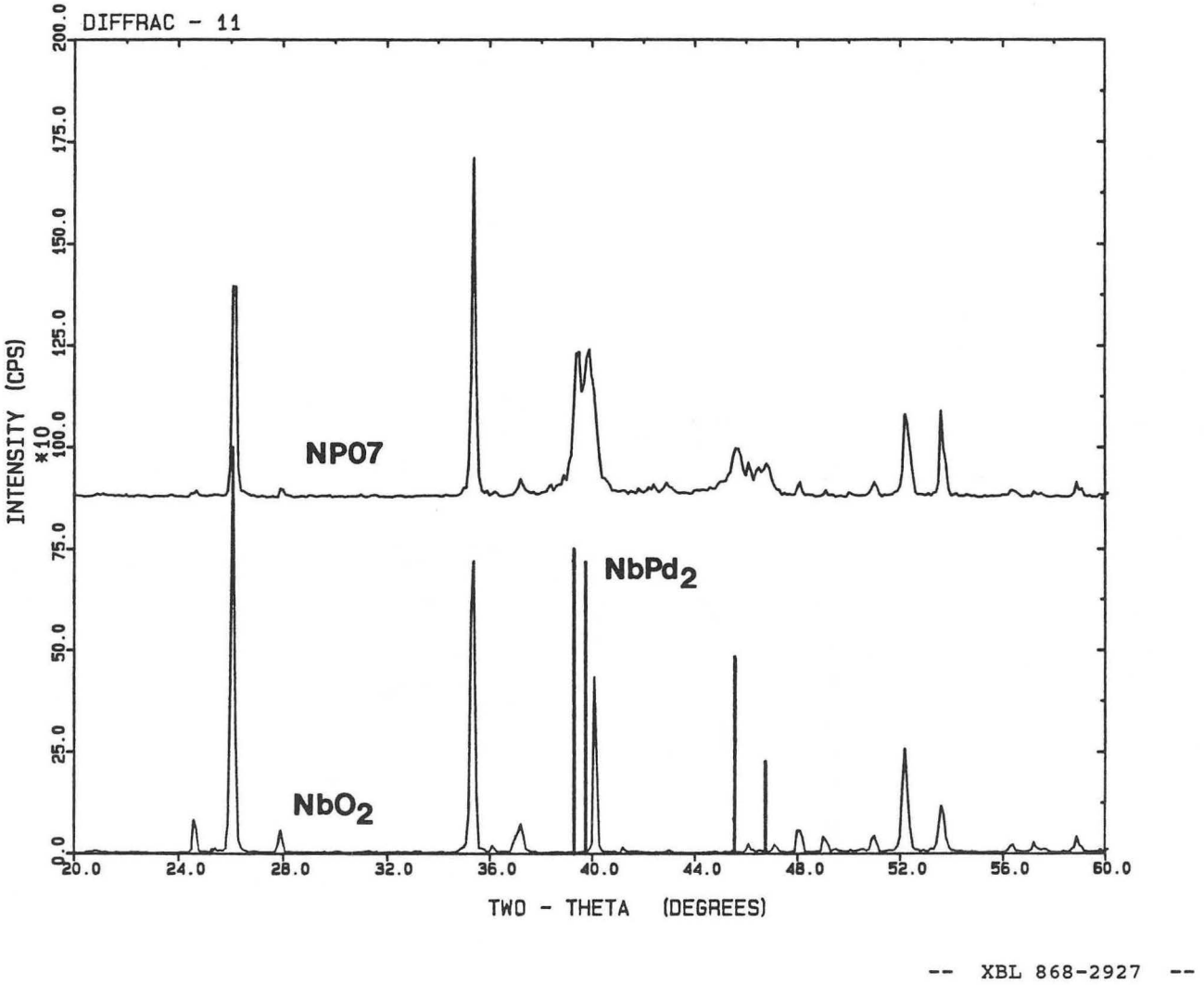

Figure (5-7)
XRD pattern for NP07 using Cu(K_α) radiation. The lower pattern is that for pure NbO_2 and that calculated for $NbPd_2$.

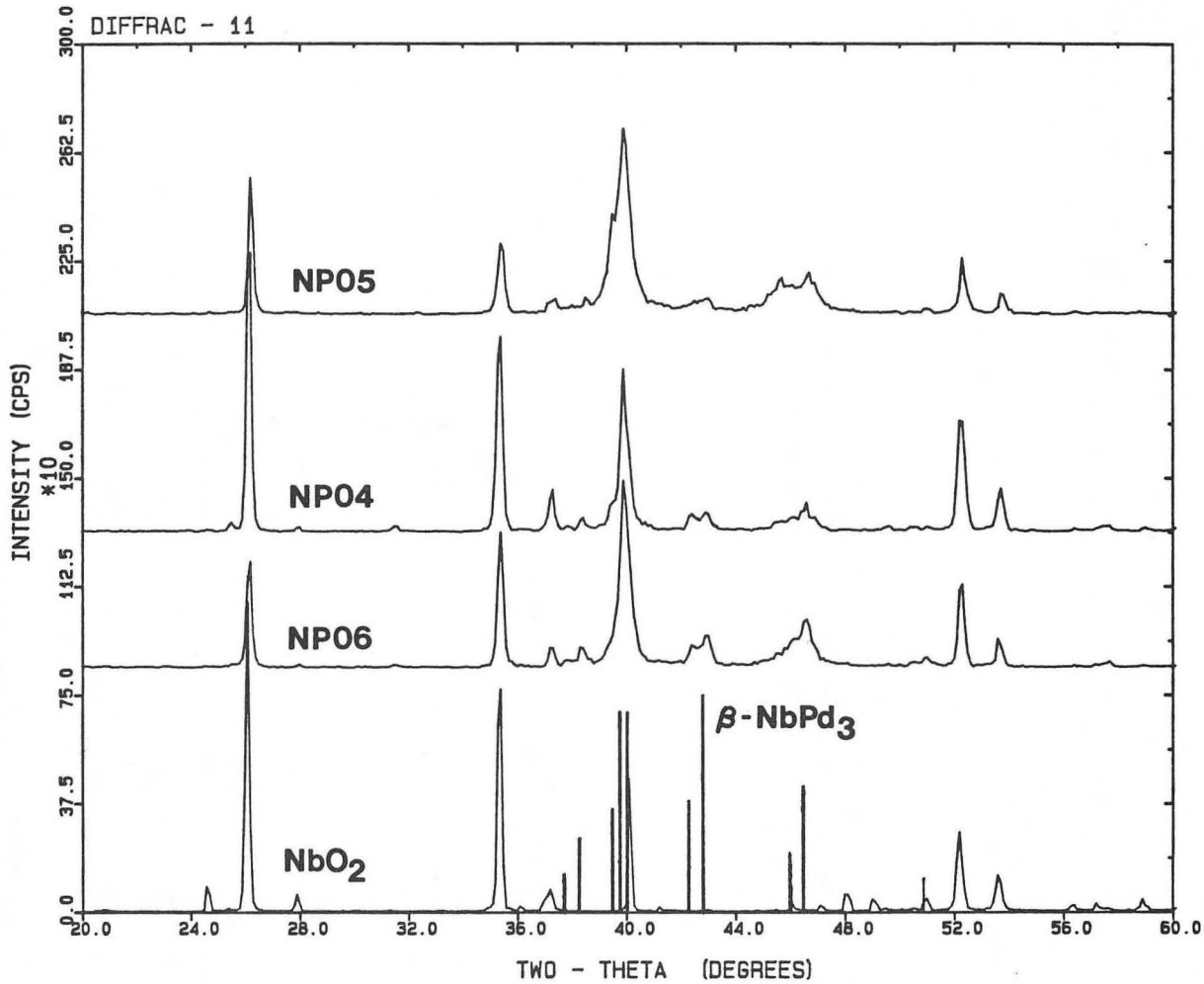

-- XBL 868-2928 --

Figure (5-8)
XRD patterns for NP04, NP05, and NP06 using Cu(K_α) radiation. The lower pattern is that for pure NbO_2 and that calculated for β–$NbPd_3$.

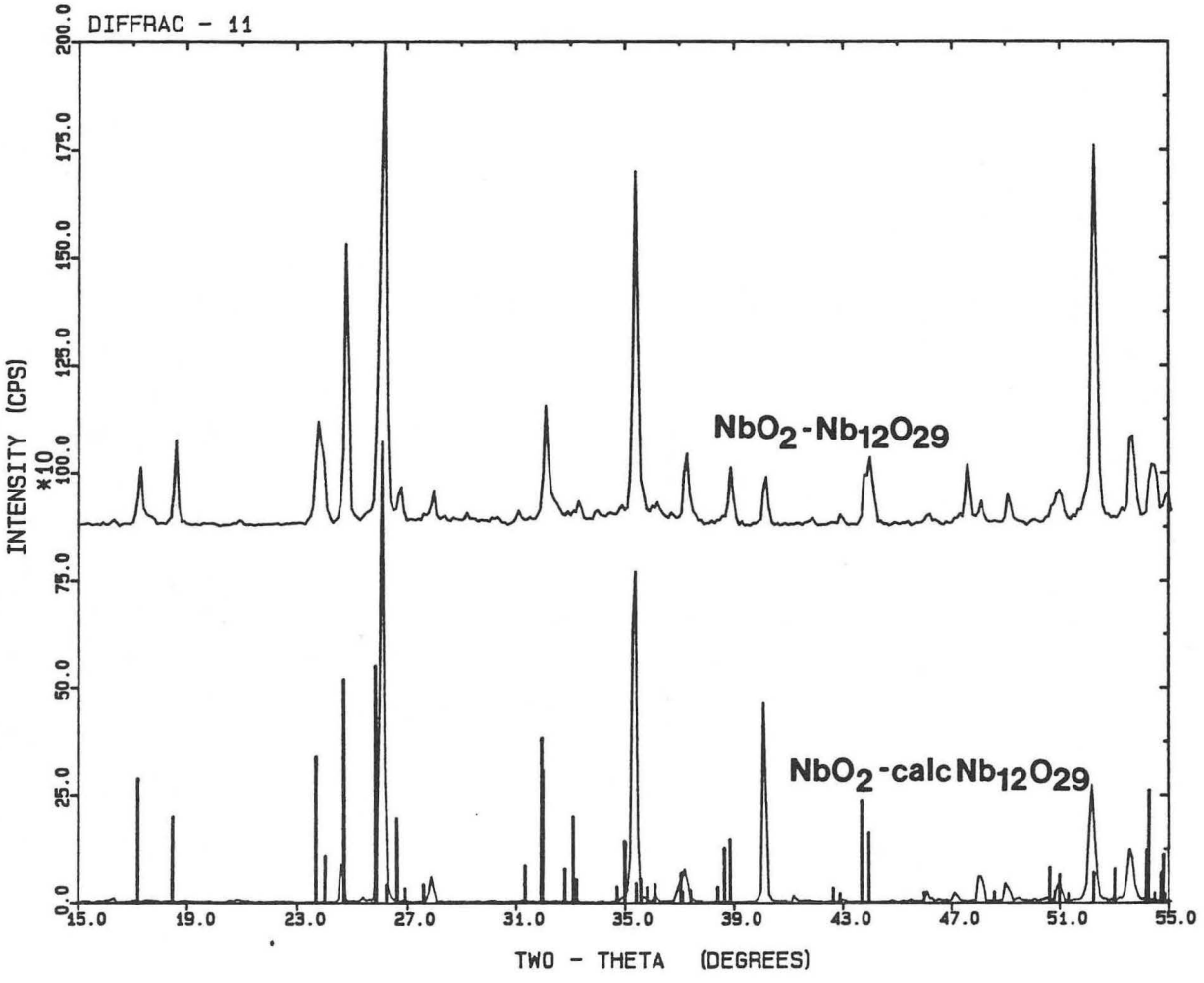

-- XBL 868-2929 --

Figure (5-9)

XRD pattern of a sample containing NbO_2 and $Nb_2O_{4.8}$. The lower pattern is that for pure NbO_2 and the calculated pattern for the monoclinic form of $Nb_{12}O_{29}$.

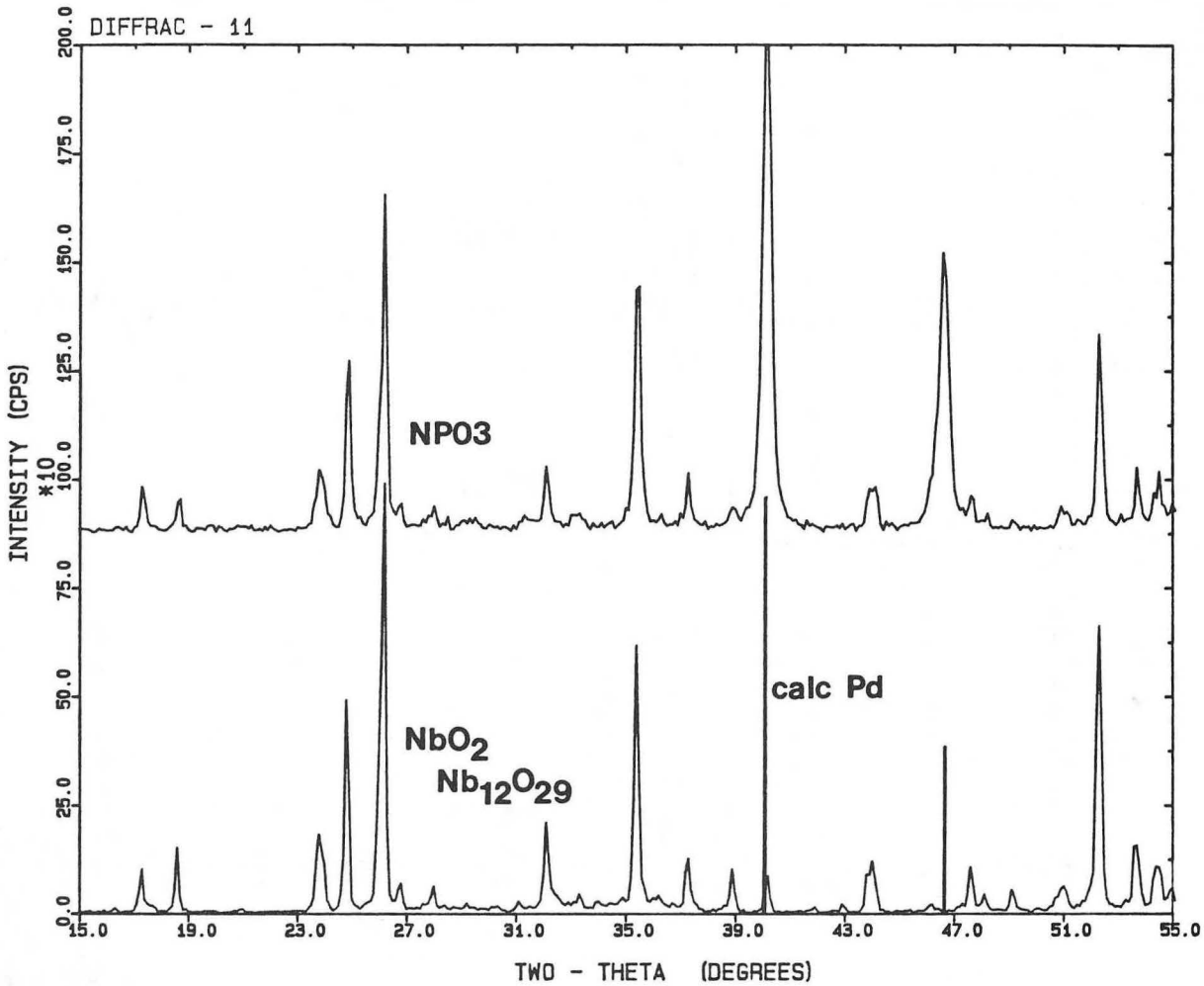

-- XBL 868-2930 --

Figure (5-10)

XRD pattern of sample NP03. The lower pattern is that from a sample containing NbO_2 and $Nb_{12}O_{29}$. Superimposed on the lowere pattern is the calculated pattern for fcc palladium.

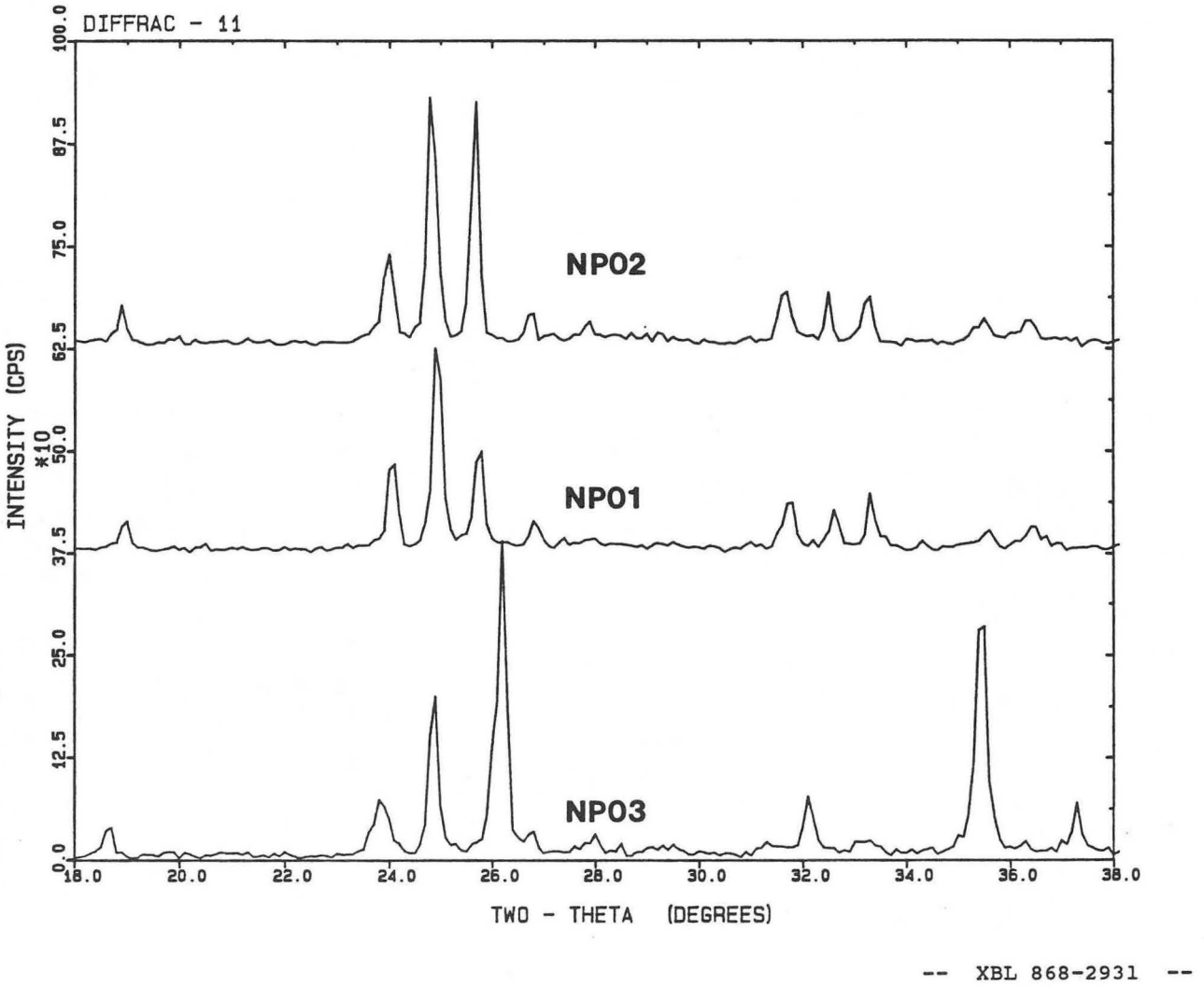

Figure (5-11)

A small portion of the XRD pattern for samples NP01, NP02, and NP03. Note that the patterns for NP01 and NP02 are identical while that for NP03 is different.

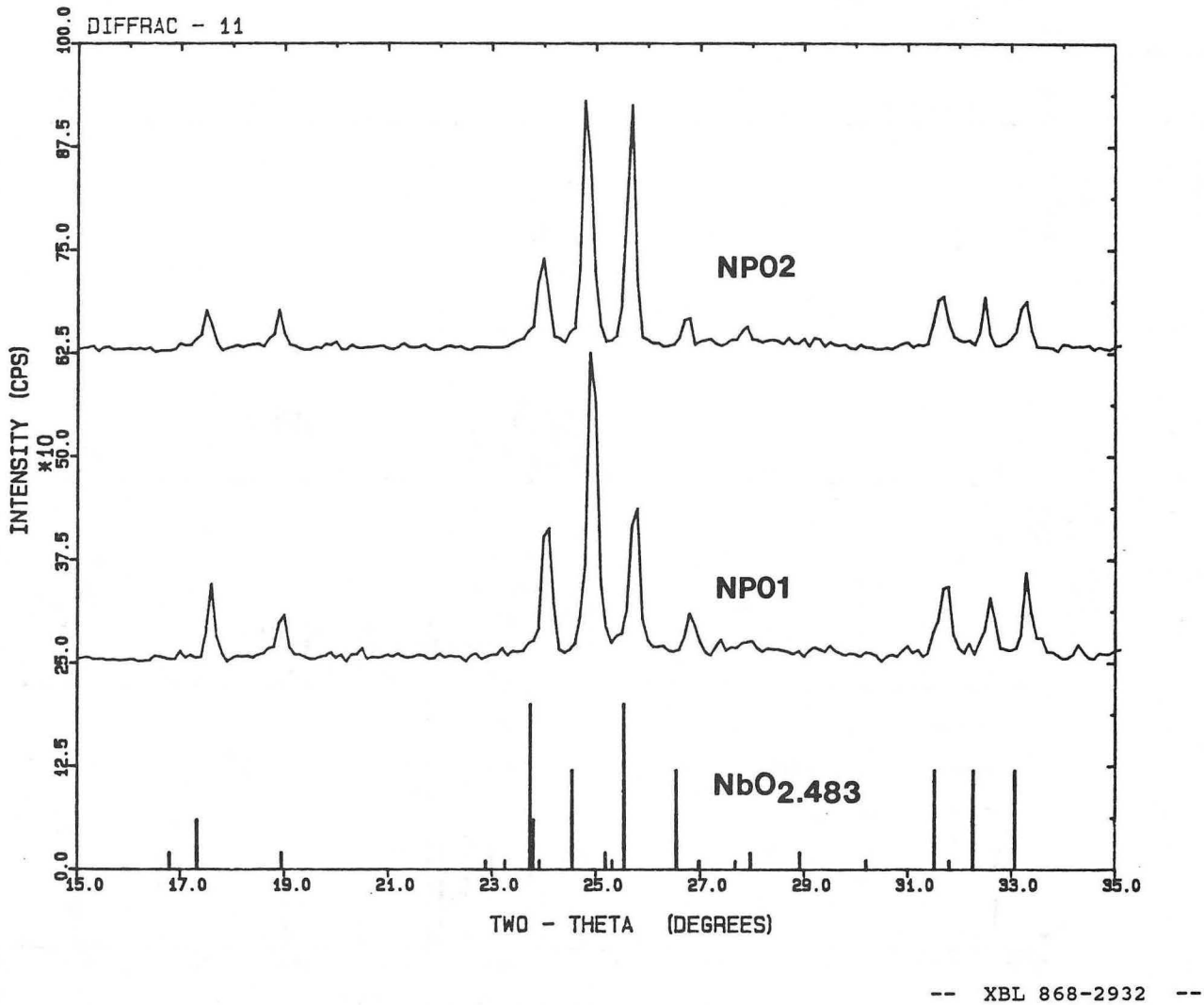

Figure (5-12)
XRD patterns for samples NP01 and NP02. The synthesized pattern below is that reported by Gruehn et al. [7] for $NbO_{2.483}$.

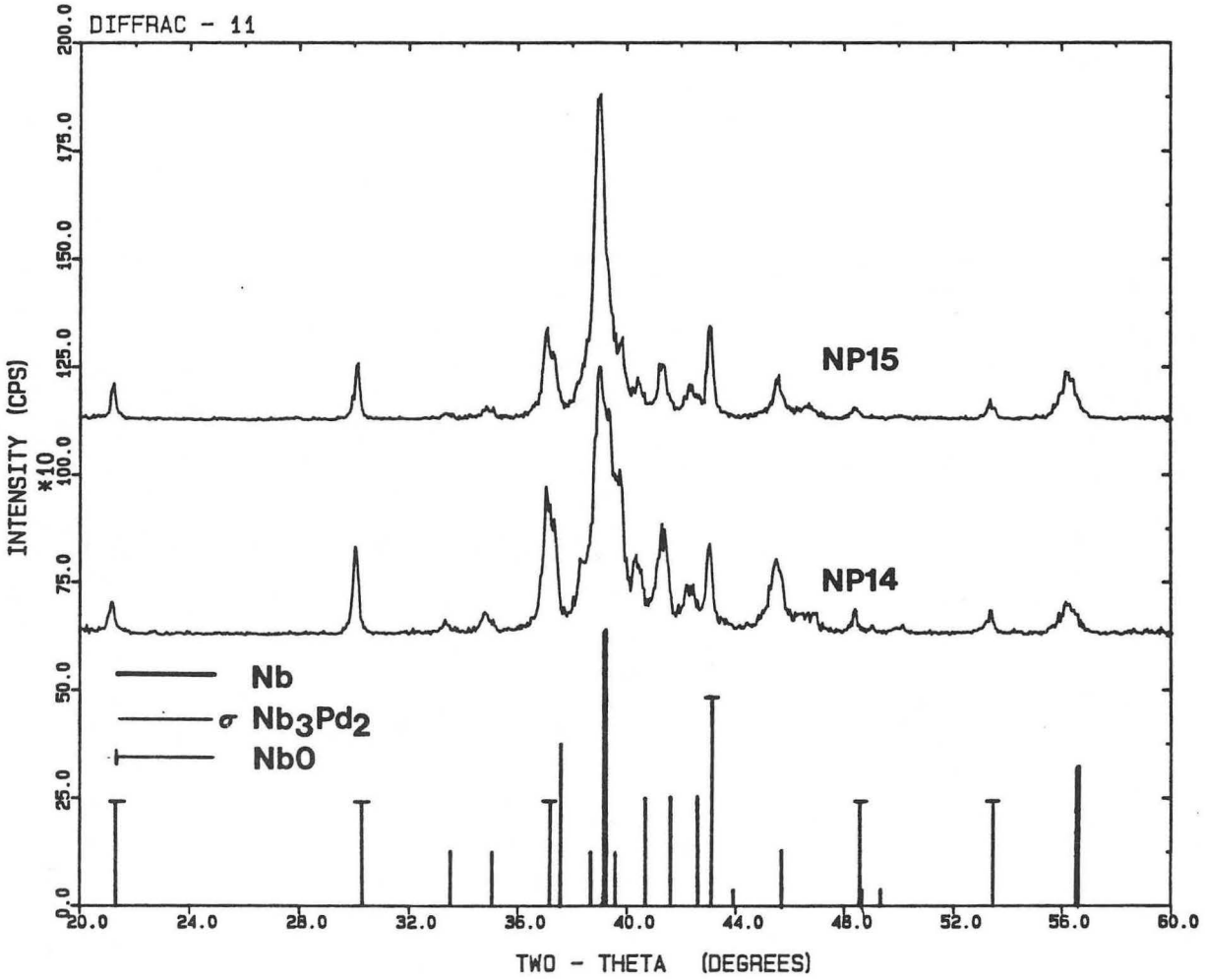

Figure (5-13)
The complicated patterns for NP14 and NP15 are compared with the synthesized patterns for NbO, bcc niobium, and σ–Nb_3Pd_2.

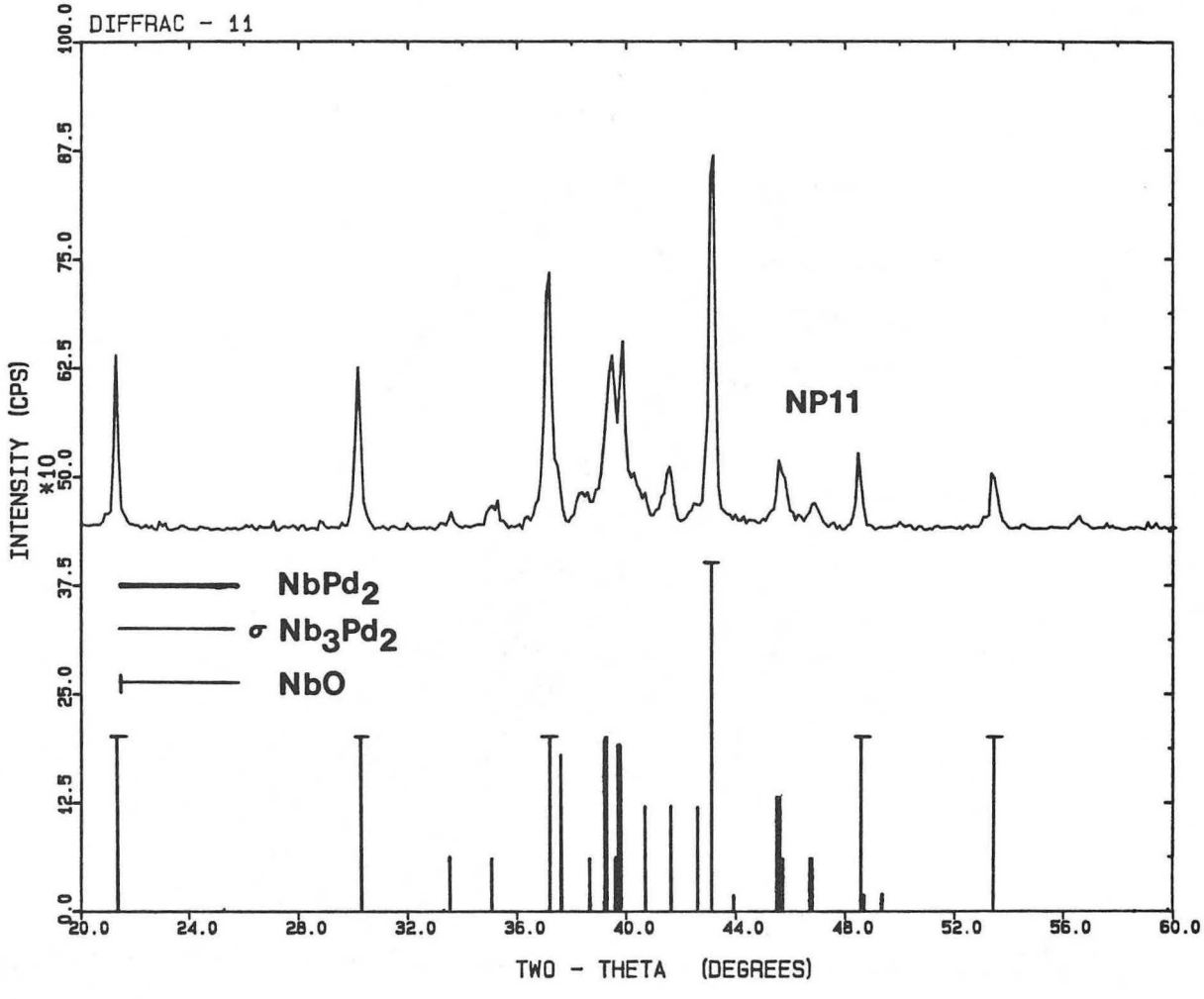

-- XBL 868-2934 --

Figure (5-14)
The XRD pattern for sample NP11 is compared to the synthesized patterns for NbO, σ–Nb_3Pd_2, and $NbPd_2$.

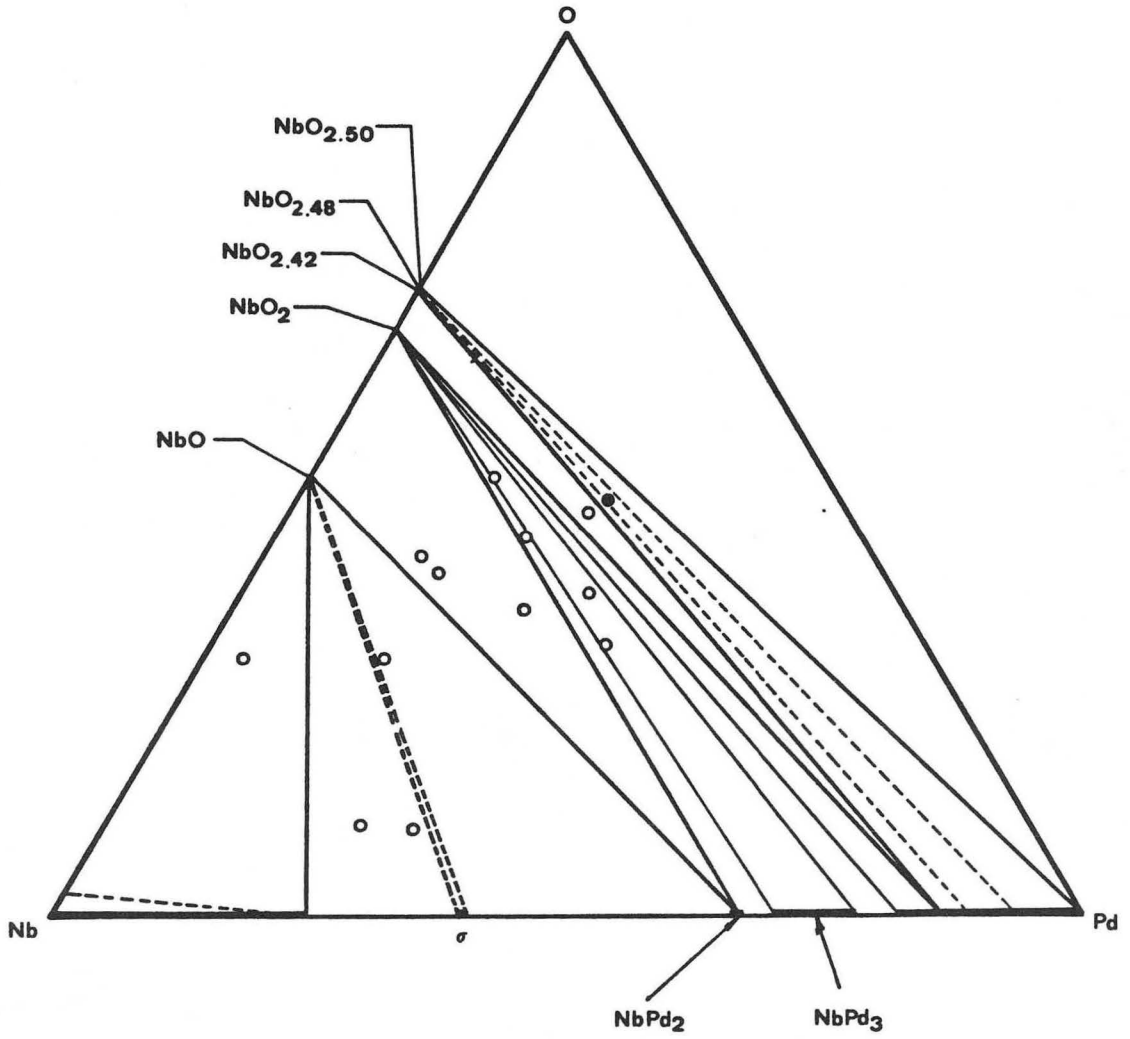

-- XBL 868-2935 --

Figure (5-15)

The Nb-Pd-O phase diagram at 1000° C deduced from the results of the oxide equilibration study. The circles represent the overall compositions of the samples used in this study which are tabulated in table 5-VI. The lines delineate the various phase regions uniquely determined by the phases found in the samples and the phase rule. The dashed lines indicating the presence of the σ phase, represent the controversial nature of its stability.

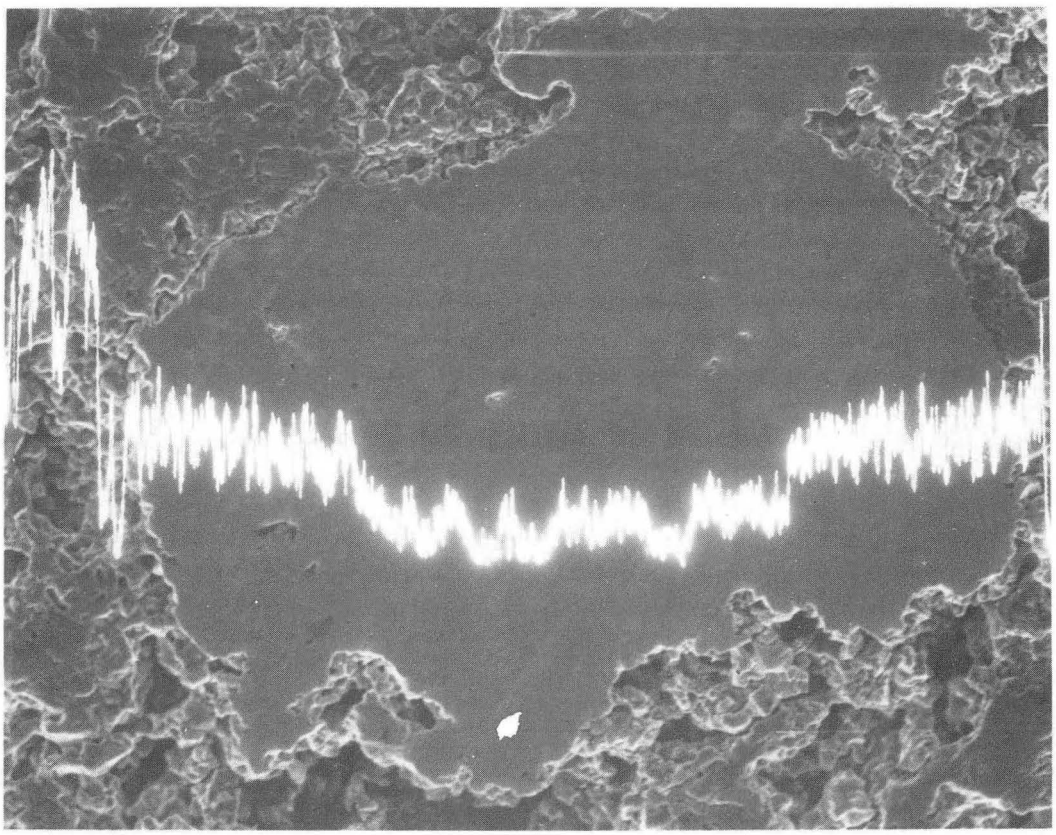

Figure (5-16) XBB 867-5544

Scanning electron micrograph (580 X) of a Rh-Nb-O sample where the rhodium starting material had not been classified. The line across the center of the photo is a trace representing the intensity of Nb(L_α) X-rays emitted as a function of position across the center of the large alloy grain. There is clearly a change in niobium concentration across the grain.

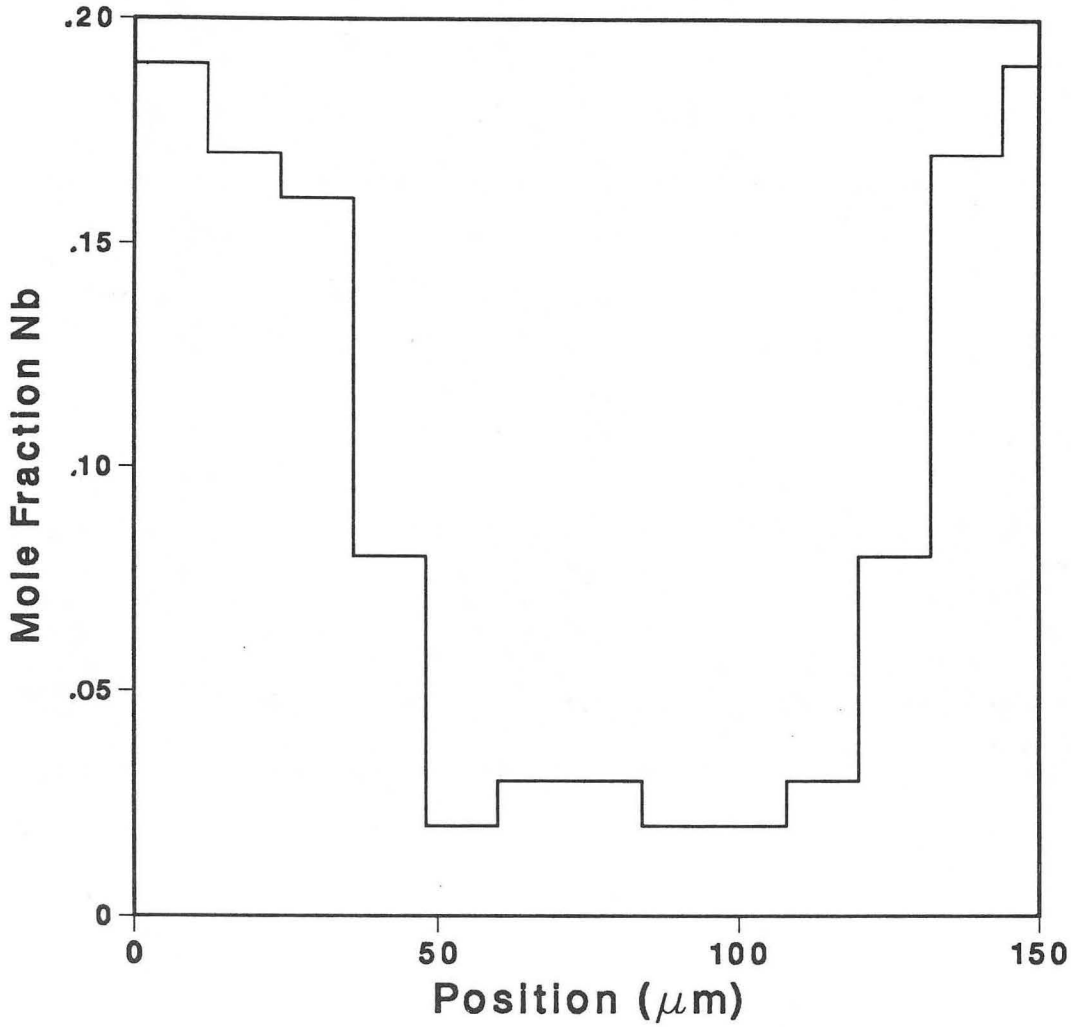

-- XBL 868-2936 --

Figure (5-17)

The average compositions measured by EDAX in 12X4 μm^2 regions across the Nb-Rh grain shown in figure (5-16). These measurements were made by consecutive 300 sec counts every 12 μm across the midline of the grain. The concentration profile clearly shows the presence of two alloy phases and a concentration gradient across the $NbRh_3$ phase.

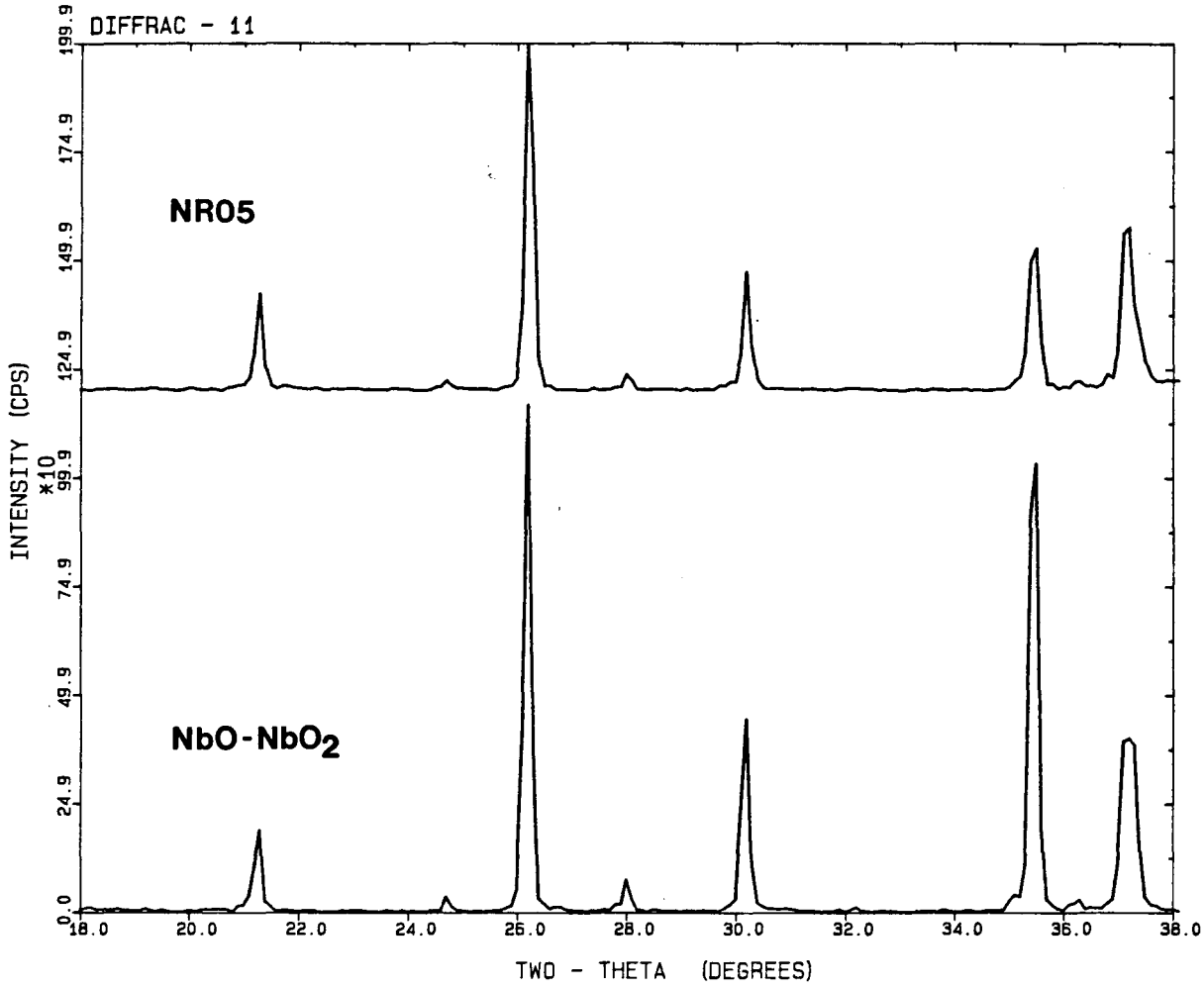

-- XBL 868-2937 --

Figure (5-18)
XRD pattern of sample NR05 compared with a pattern from a sample containing NbO and NbO_2.

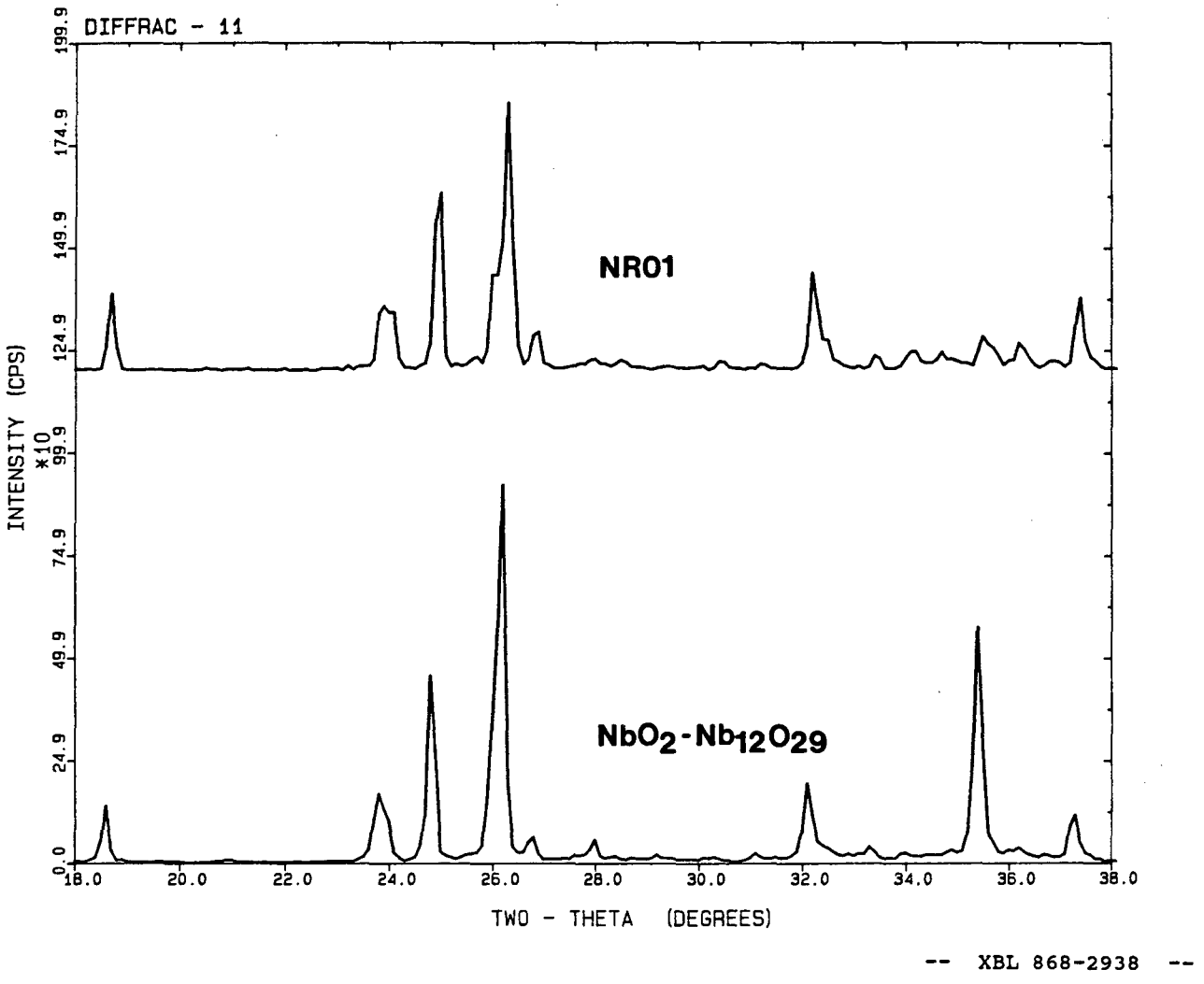

Figure (5-19)
XRD pattern for NR01 compared with a pattern from a sample containing NbO_2 and $Nb_{12}O_{29}$.

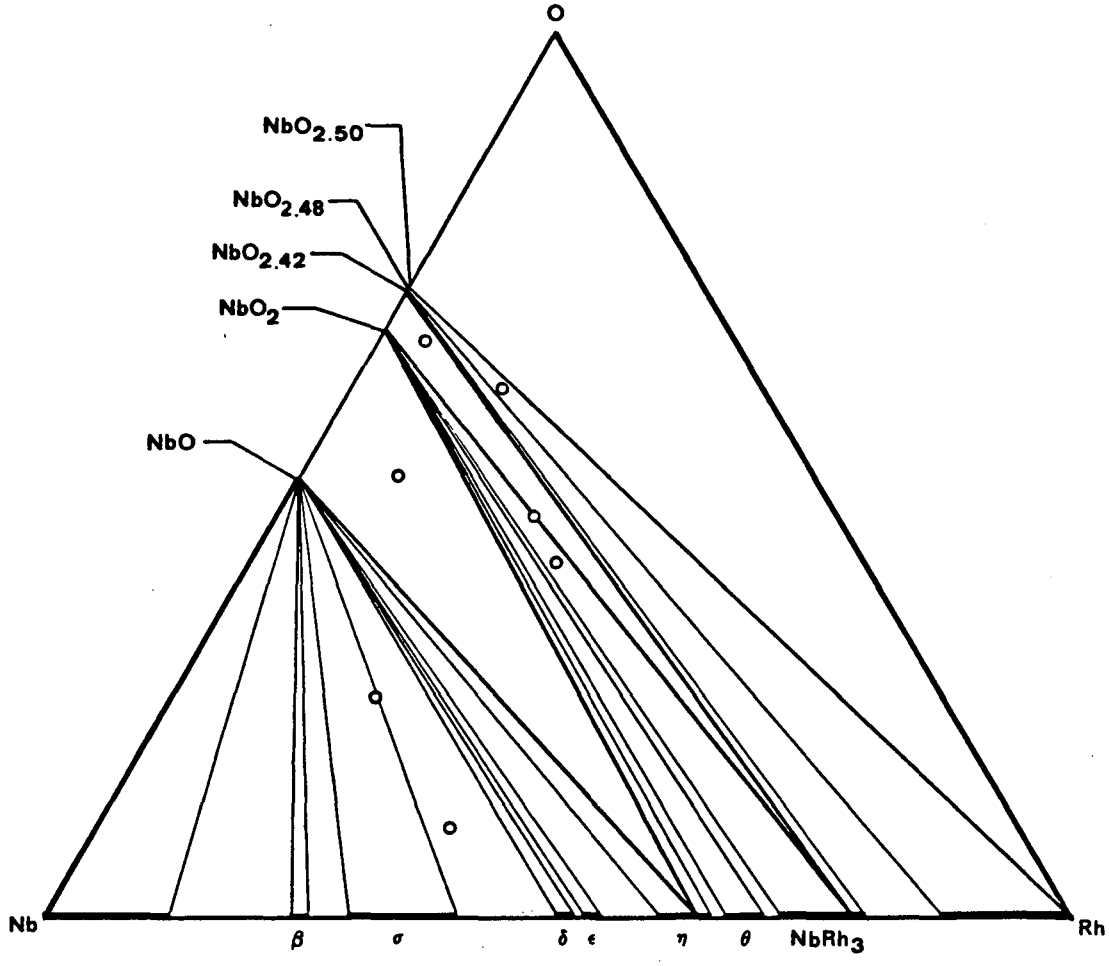

-- XBL 868-2939 --

Figure (5-20)

The Nb-Rh-O phase diagram at 1000° C consistent with the results from the NR samples. The overall compositions of these samples are shown as points within the phase diagram.

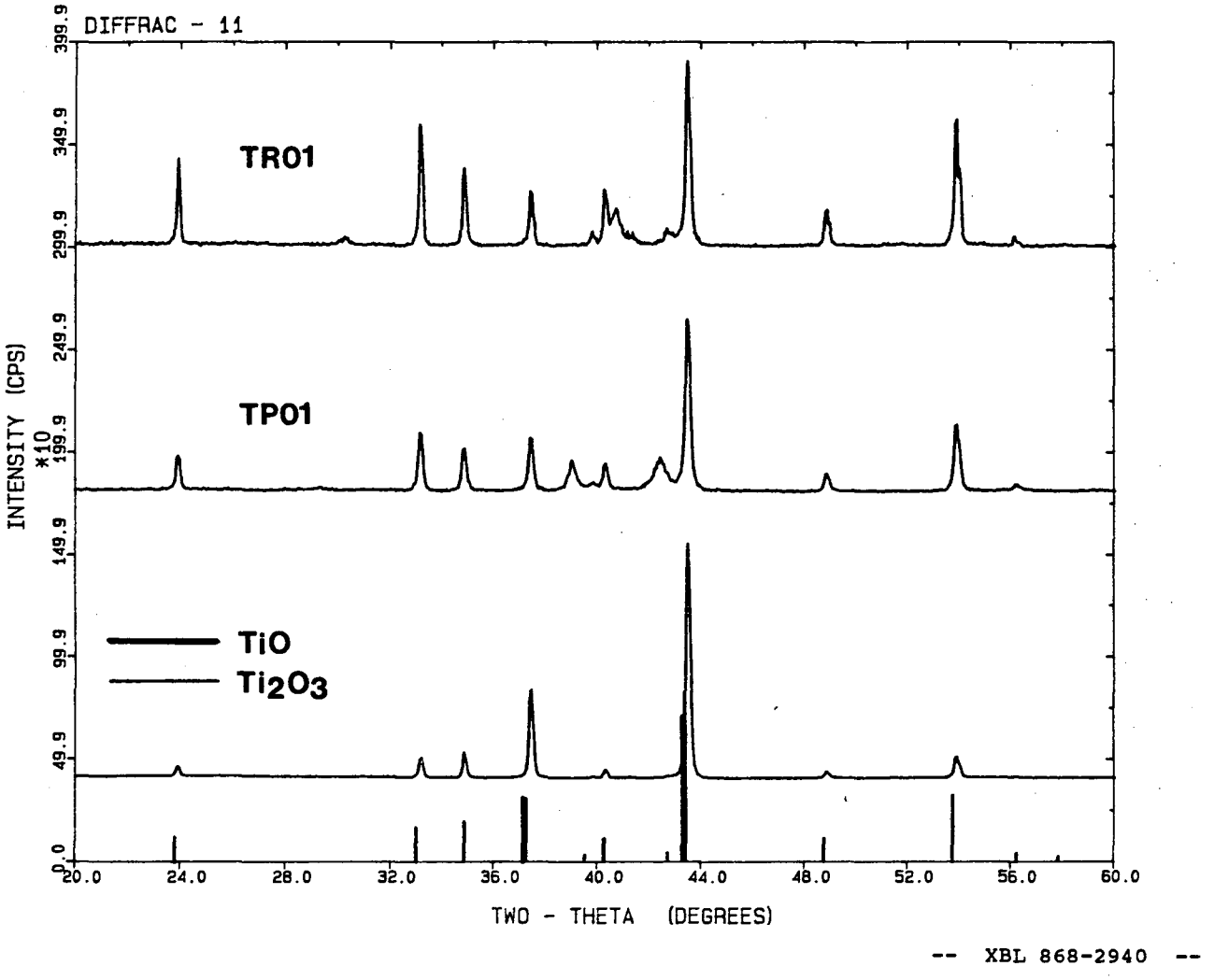

Figure (5-21)

The XRD patterns for samples TP01 and TR01 compared with the pattern from a sample which contains TiO and Ti_2O_3. The pattern reported in the JCPDS file for each of these oxides is included below the lowest pattern. The slight differences in thses patterns can be attributed to the different alloy reflections.

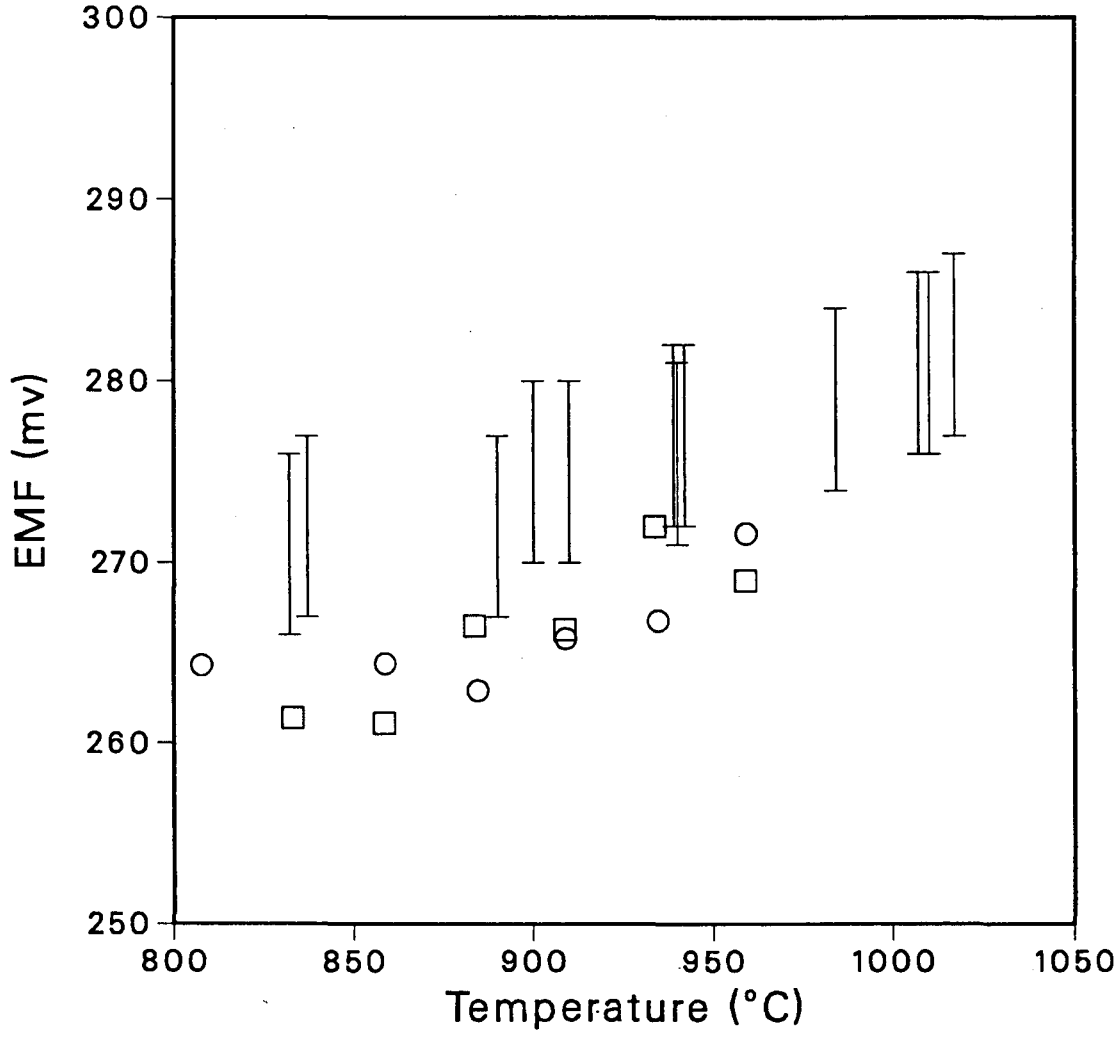

-- XBL 868-2941 --

Figure (5-22)

The voltage measured versus temperature is depicted above for the cell $NbO,NbO_2/YDT/NbO_2,Nb_2O_{4.8}$. The points represented by circles and squares were obtained by Worrell [12]. His error results from changes in voltage when the inert gas flow to the cell was changed. Voltage variation was not observed in our measurements.

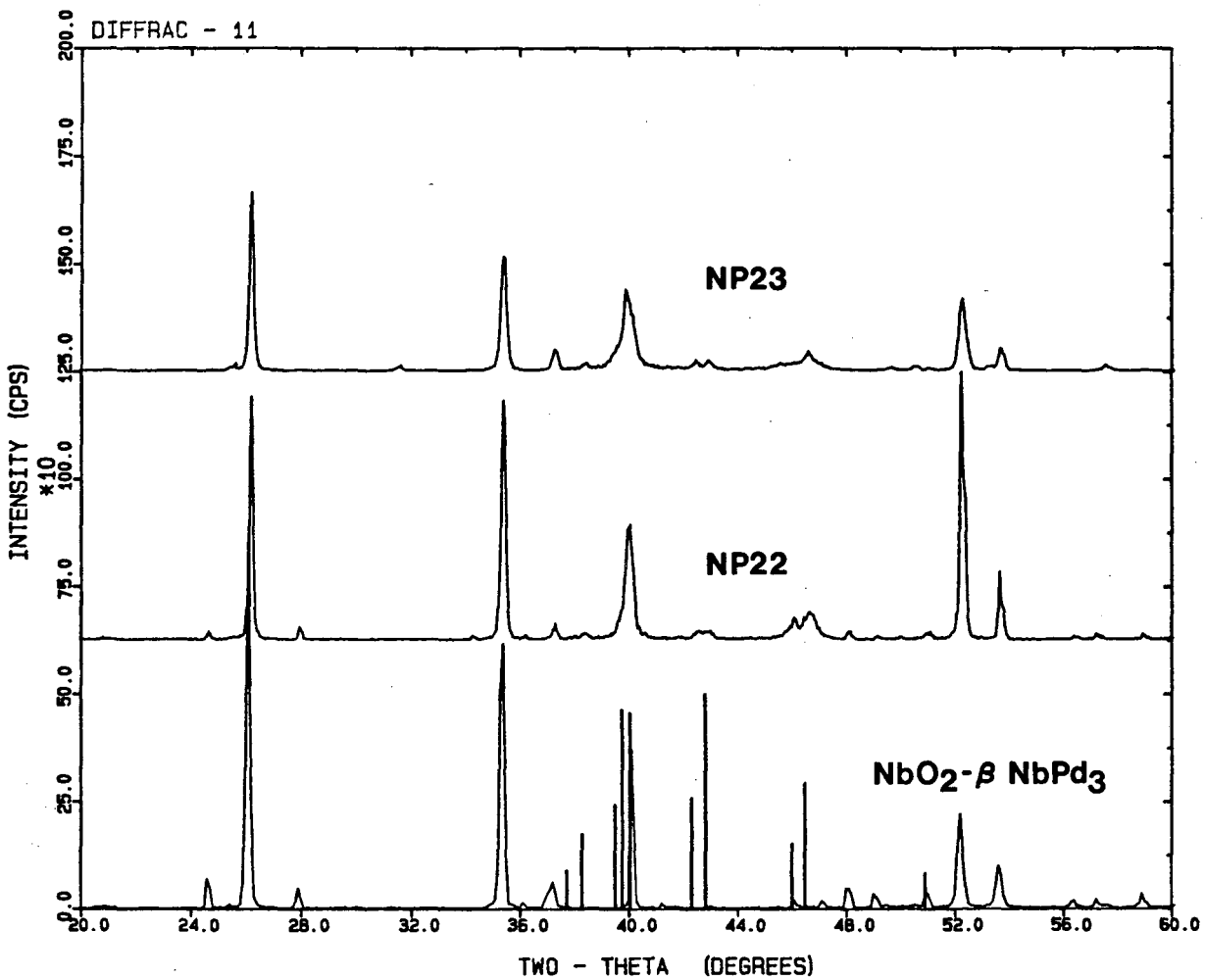

Figure (5-23)
XRD patterns for electrodes NP22 and NP23 compared with the pattern for pure NbO_2 and that calculated for β–$NbPd_3$.

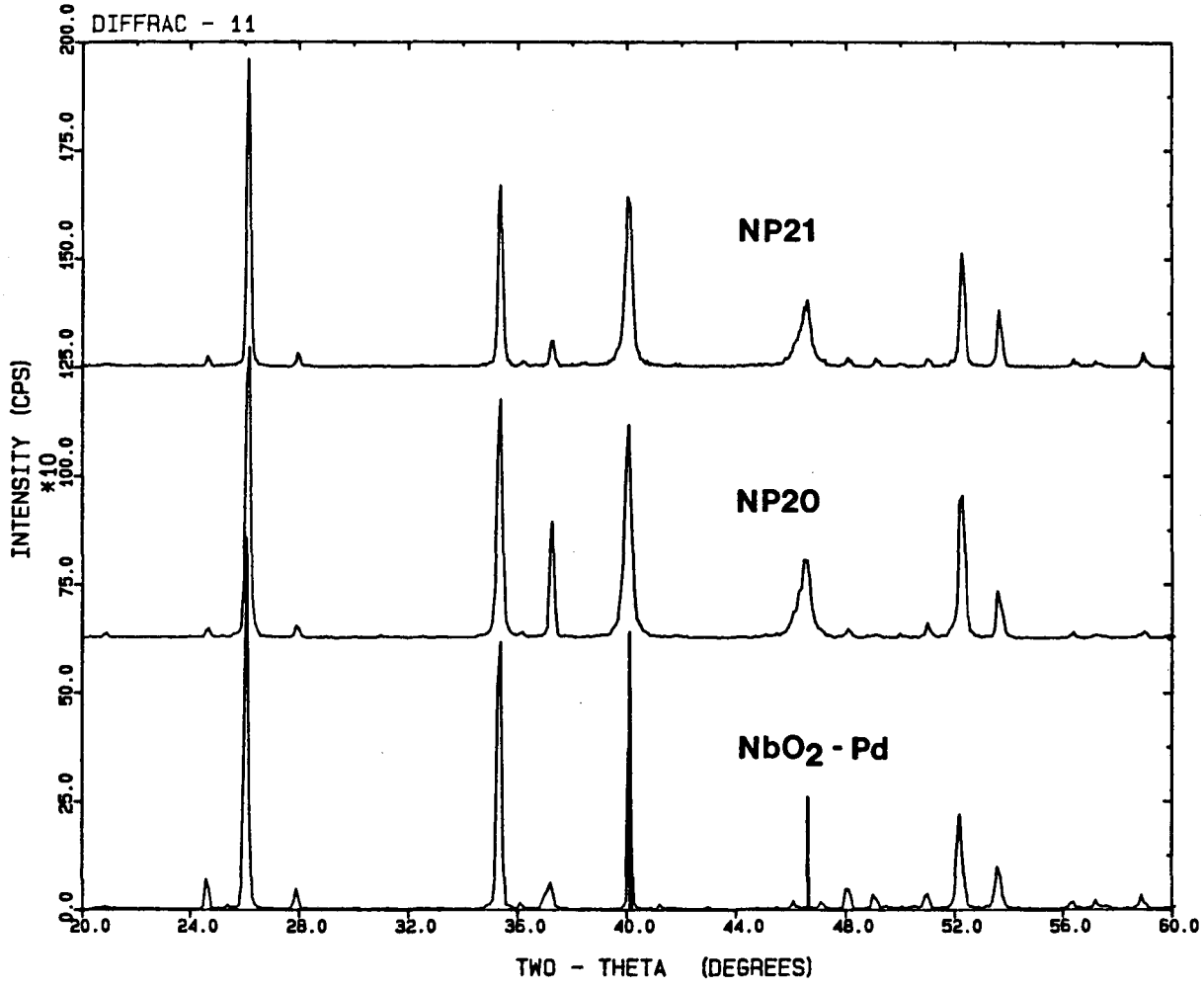

-- XBL 868-2943 --

Figure (5-24)
XRD patterns for electrodes NP20 and NP21 compared with the pattern for pure NbO_2 and that calculated fcc Pd.

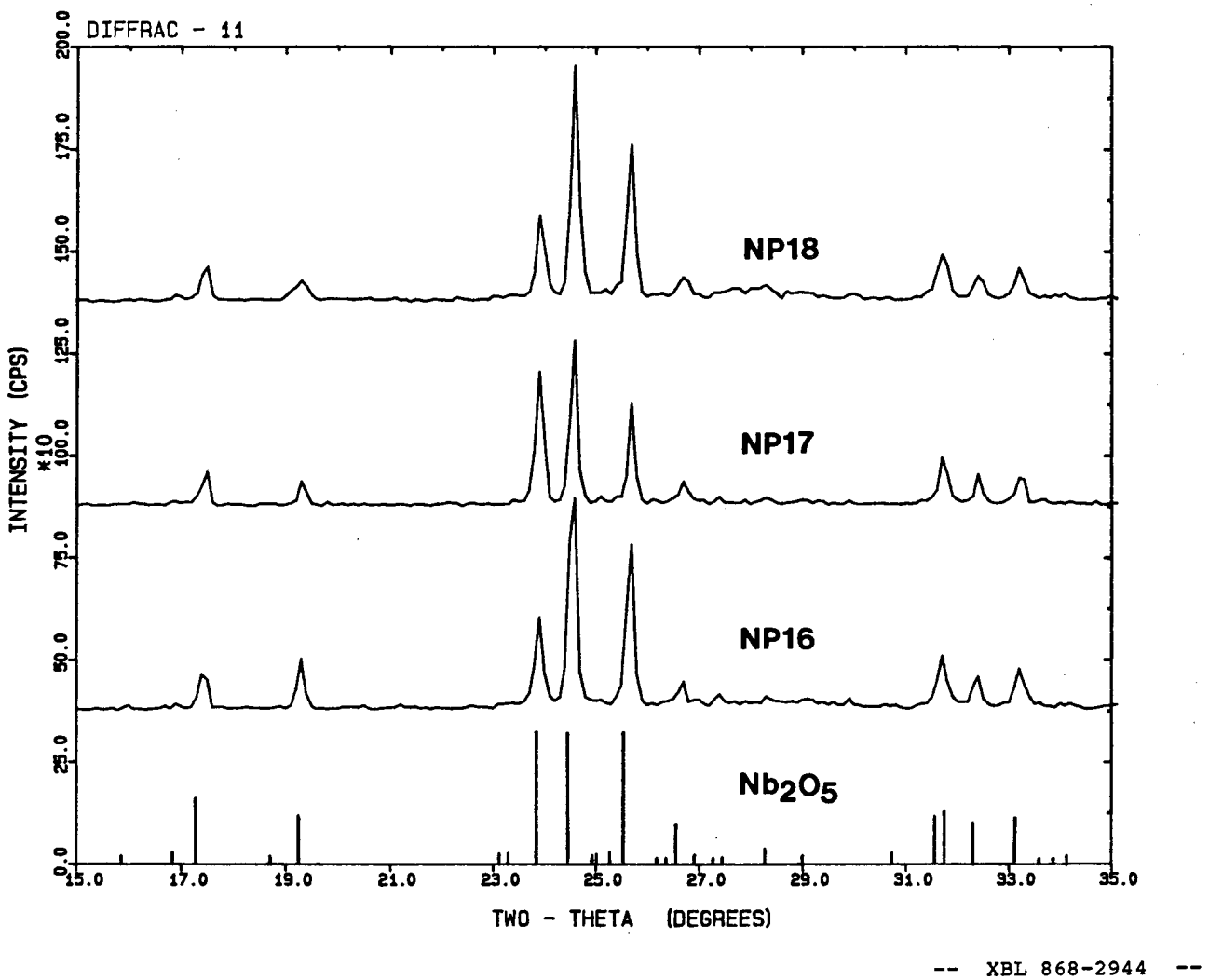

Figure (5-25)
XRD patterns for electrodes NP16, NP17, and NP18 compared with the pattern reported for monoclinic Nb_2O_5.

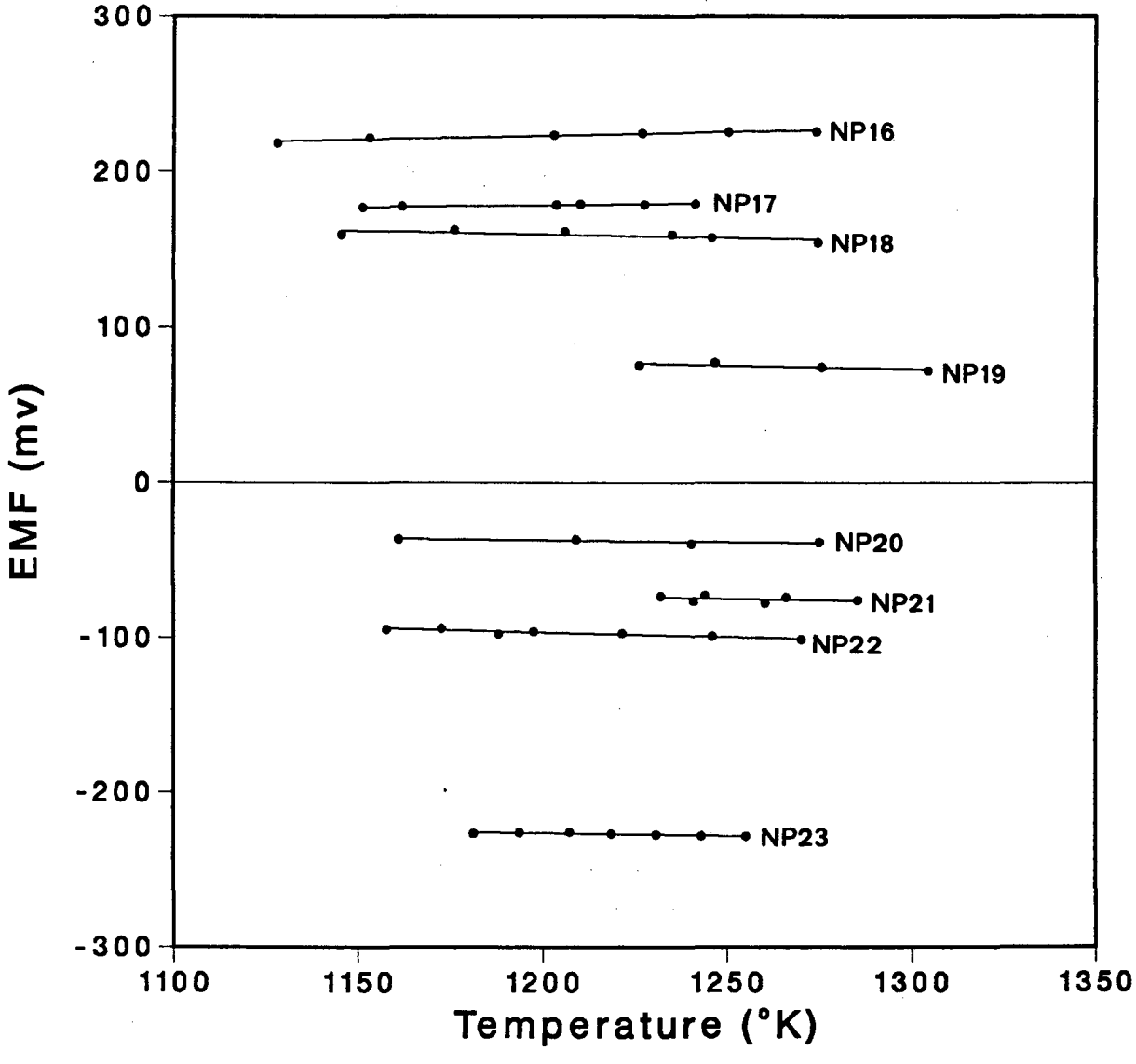

-- XBL 868-2945 --

Figure (5-26)
Voltage measured for each of the alloy-oxide electrodes versus temperature (°K). Each of these cells used the NbO_2,$Nb_2O_{4.8}$ reference electrode and the YDT electrolyte.

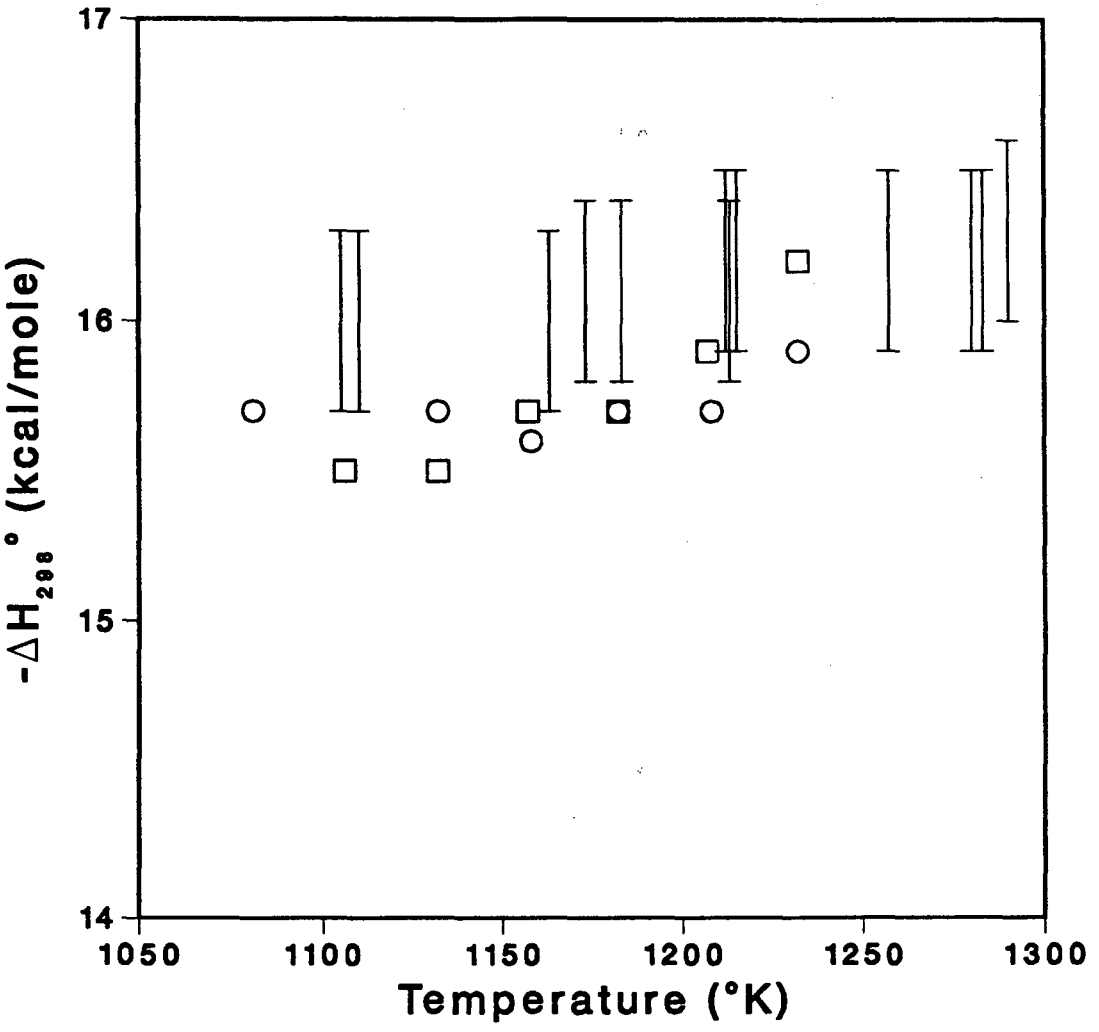

-- XBL 868-2946 --

Figure (5-27)

Third law plot for the reaction $NbO + 1.25Nb_2O_{4.8} = 3.5NbO_2$. The points represented by circles and squares were from two cells in our experiments while those described with error bars were derived from the results of Worrell [12].

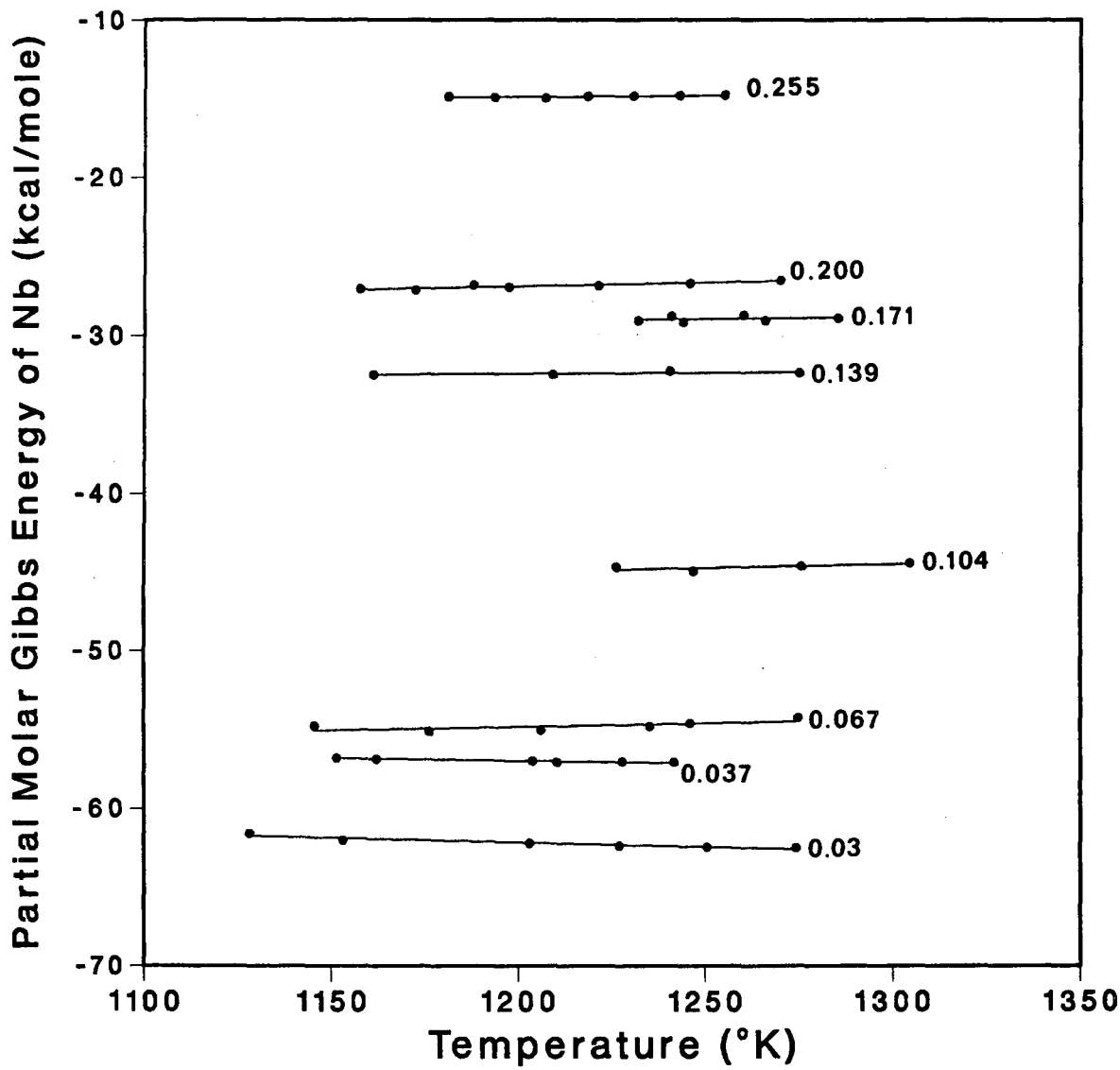

-- XBL 868-2947 --

Figure (5-28)
The partial molar Gibbs energy of niobium in palladium solution derived from the galvanic cell measurements. The numbers refer to the mole fraction of niobium in the alloy.

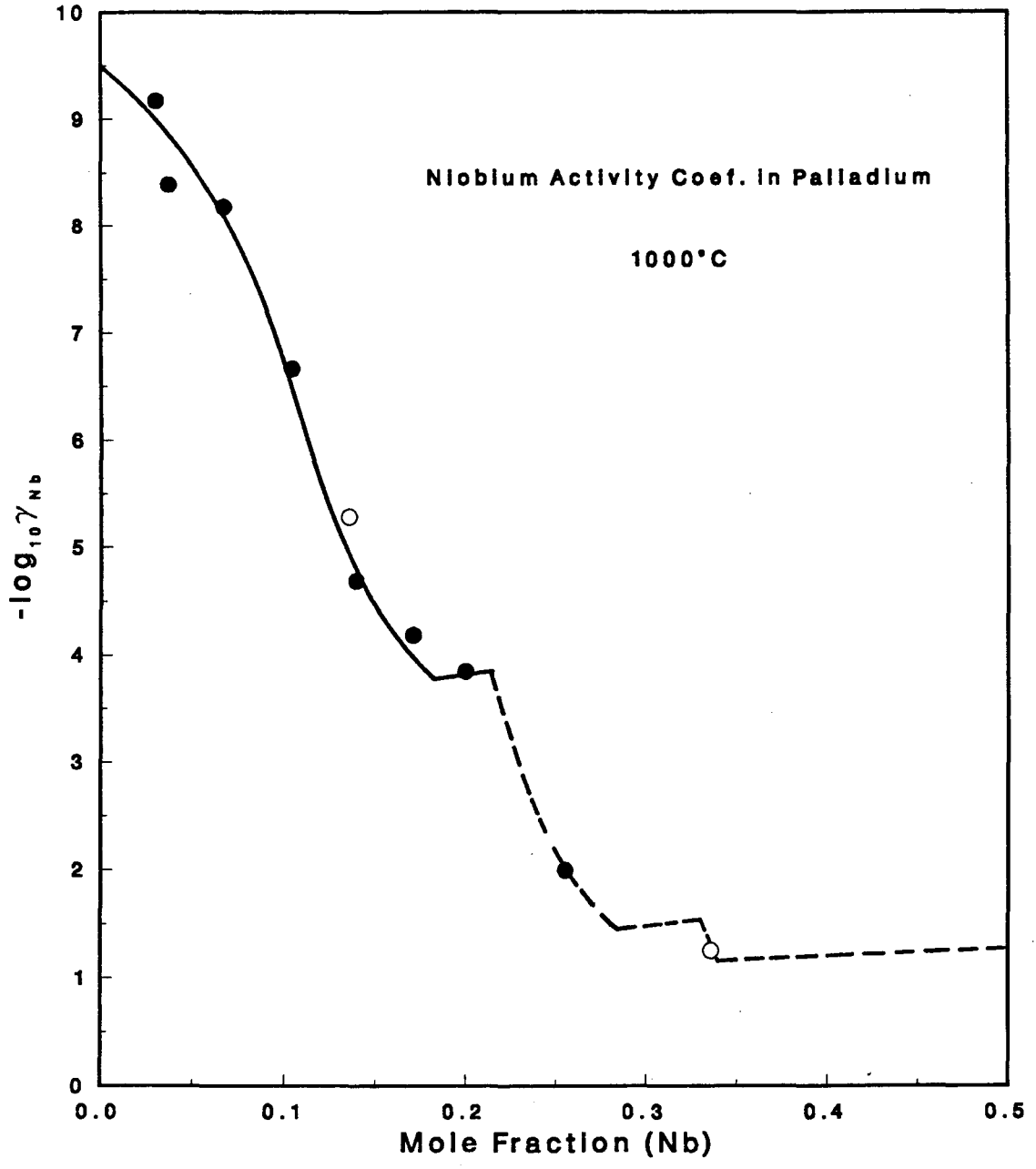

-- XBL 868-2948 --

Figure (5-29)

The niobium-palladium titration curve at 1000° C is shown above. The results from the galvanic cell measurements are filled circles and the results of the oxide equilibration study are rings. The discontinuities occur because the two metals are not miscible in all proportions.

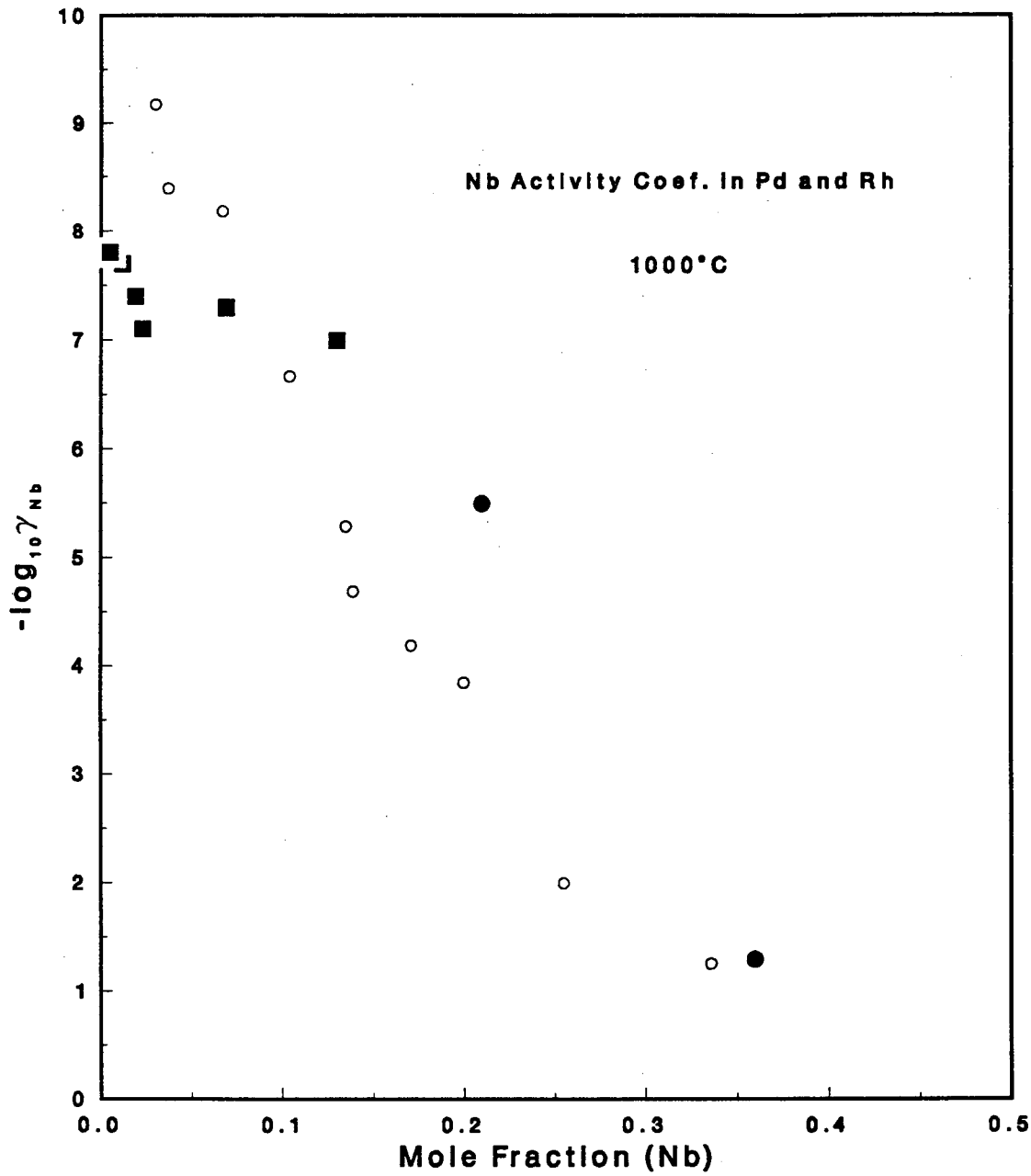

-- XBL 868-2949 --

Figure (5-30)

This figure compares the titration curves for Nb-Pd and Nb-Rh solutions. The rings are the points shown in figure (5-30) for the Nb-Pd titration. The filled blocks are derived from Kleykamp's experiments while the filled circles are from our oxide equilibration study on Nb-Rh alloys.

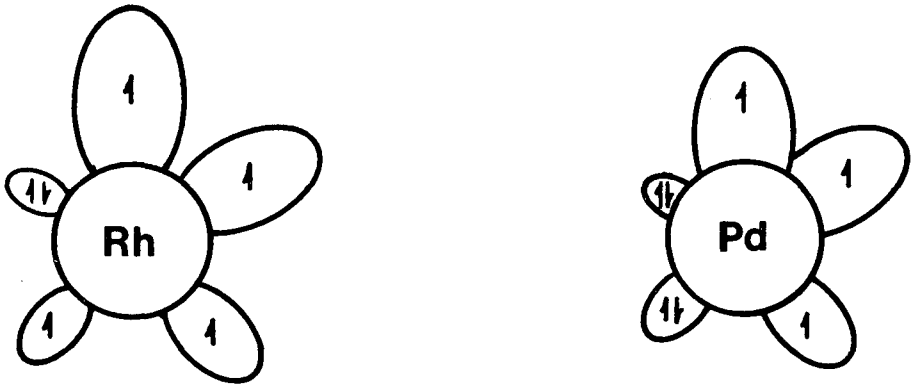

-- XBL 868-2950 --

Figure (5-31)
This is a schematic illustrating the effect of a crystal field on the relative ease of bonding of the five d-orbitals. Note also the contraction of the orbitals due to the increased nuclear charge on Pd.

Appendix 1

Calculation of X-ray Powder Diffraction Patterns

The assignment of a crystal's space group and unit cell dimensions can be made by measuring the positions of X-ray diffraction lines and by noting systematically absent reflections. Frequently, a unique assignment of the space group cannot be made by powder X-ray diffraction so that one must use the precession method on single crystals. Once the space group and lattice constants have been assigned it is a simple matter to determine which reflections will be present in the powder pattern and their positions. The simple presence or absence of a reflection is not all that we would like for their assignment since the reflection intensities may vary greatly.

The assigned space group is a classification of the symmetry elements of a crystal but frequently the atoms may arrange in a variety of fashions and still retain the correct elements of symmetry. Their exact positions are determined by measurement of the intensity of the reflections present in the diffraction pattern.

X-rays are scattered by electrons of the individual atoms that make up the crystal. The scattering power of an atom is a function of its atomic number. The scattered waves from other atoms constructively reinforce only in directions in which the path lengths of the waves differ by an integral number of wavelengths. Bragg[1] envisioned this condition as scattering from planes of atoms separated by a distance, d, in a direction related to the incident direction

by the famous Bragg equation. The scattering power of a plane and the intensity of its diffraction line is related to the number of atoms in that plane as well as their atomic numbers. The problem of determining the atomic positions in a crystal structure must be solved by single crystal measurements for all but the simplest of crystals.

The intensities of the lines in the X-ray powder pattern may be calculated from information obtained by single crystal studies and/or making knowledgable estimates of atom positions. Additional corrections must be made to account for various geometrical considerations inherent to the powder method and the angle dependence of scattering efficiency. All these effects are usually expressed by the following equation

$$I \approx j \cdot \frac{1+\cos^2 2\theta}{2} \cdot \frac{1}{2\sin^2\theta\cos\theta} \cdot F_{hkl}^2 \qquad \text{(AP-1)}$$

where I is the relative intensity of the reflection with Bragg angle θ and the factors j and F will be discussed below.

The first trigonometric term is the so called polarization factor. The incident unpolarized X-rays interact with the electrons of an atom so that they oscillate in the plane perpendicular to the incident direction. These vibrating charged particles emit photons in all directions. The photons are, however, polarized since those scattered in a direction θ have their horizontal component of the oscillation unchanged while the vertical is shortened. The intensity in the scattered direction is proportional to the sum of the squares of these two vectors, thus it must decrease with increasing θ. This effect was first worked out by J.J. Thomson in his early studies on the dynamics of charged particles.

The second trigonometric factor in equation (AP-1) is the Lorentz factor, which corrects for several effects. The most important contribution is that not all the power put into the diffracted beam is exactly at the Bragg angle. It is distributed over a small range about the Bragg condition, the breadth of which is a function of angle so that the measured peak intensity decreases as this range increases. This term also includes a second component that is due to the statistics of randomly oriented crystals. The X-rays diffracted from a polycrystalline sample are directed into cone-shaped regions since there are always a number of crystals in the sample with the correct orientations that are axially distributed. If a particular cone has its radiation spread over a small angle, $\delta\theta$, only those crystals oriented correctly to diffract into this envelope will contribute to the diffracted intensity. Thus the set of normals to the diffracting Bragg planes will also trace out a cone of angular breadth, $\delta\theta$. The area that this cone traces out on a sphere with unit area is the probability of finding a crystal in the sample with the proper orientation. This probability is a function of angle since the area subtended will change with angle. It is easy to see that the probability decreases as the Bragg angle increases so that the intensity of the diffraction peak will correspondingly decrease.

The F and j terms in equation (AP-1) represent the effect of crystal structure on the intensity. The multiplicity factor, j, accounts for the statistics of planes with equivalent d spacing. Several crystal systems have a number of sets of planes with different orientations but having the same d spacing. As an example consider the cubic system, which has planes with Miller indices (111), $(11\bar{1})$, $(\bar{1}\bar{1}1)$, and $(1\bar{1}1)$ that have different orientations yet have the same d spacing. There are, however, only three of the d spacing of the (100) plane, i.e.

(100), (010), and (001). Thus the probability that the {111} planes will have the correct orientation is greater than that of the {100} planes so that the intensity of the {111} reflection will be correspondinly higher all other things being the same.

The structure factor F, as its name implies, is the term representing the effect of symmetry, atom type, and position in the crystal. It is usually calculated by treating each of the atoms in the unit cell as individual scatterers of X-rays. The net scattering of the unit cell is found by summing these individual contributions, in a way that accounts for both the amplitude and phase of the component waves. This summation is most conveniently carried out by treating F as a complex number made up of component waves from the individual atoms. The magnitude of these components is given by the atomic scattering factor of the atom considered. The phase relation between the component waves is determined by the atomic positions in the unit cell. The equation for F then becomes a summation over all atoms of the unit cell,

$$F_{hkl} = \sum_{n=1}^{N} f_n e^{2\pi i(hx_n + ky_n + lz_n)} \qquad \text{(AP-2)}$$

where f_n is the atomic scattering factor for atom n, which is the ratio of the amplitude of the wave scattered by atom n to that scattered by an electron. The phase difference of the component waves depends on the direction of the diffracted beam and the atomic positions and is the dot product of the k vector for the reflection (given by Miller indices h,k, and l) and the position vector of the atom, n. This position vector has components that are the fractional coordinates of the atom in the unit cell. Thus, if the atom positions are known, the powder pattern may be calculated by use of equations (AP-1) and (AP-2).

These equations were used to calculate the powder patterns expected for the intermetallics in the Nb-Pd phase diagram, as well as that for the monoclinic form of $Nb_{12}O_{29}$. Atomic scattering factors at discrete values of $x = \sin\theta/\lambda$ were obtained for niobium and palladium from [2]. These values were fit to the following equations to ease computer calculation of the patterns.

$$f_{Nb} = 41.510-52.984x+10.605x^2+29.175x^3-16.454x^4 \qquad \text{(AP-3a)}$$

$$f_{Pd} = 46.497-55.628x+3.467x^2+40.743x^3-21.262x^4 \qquad \text{(AP-3b)}$$

The computer programs written to generate each of the powder patterns discussed below appear in the appendix 2.

The $NbPd_3$ intermetallic is reported to have two crystal structures for which the exact range of stability has not been agreed upon (see chapter 1). Dwight[3] determined that α–$NbPd_3$ has the tetragonal $TiAl_3$ type structure with lattice constants a = 3.895 and c = 7.913. The $TiAl_3$ structure has eight atoms per unit cell and possesses the symmetry of space group I4/mmm [4]. The Wyckoff positions that are occupied by atoms are listed in table (AP-I). The left column in the table is the atom while the center column represents the number and Wyckoff letter assigned to these positions [5]. Note the presence of the body centering translation (1/2,1/2,1/2) which is characteristic of I space groups.

The positions in table (AP-I) were used in equations (AP-1) and (AP-2) along with the proper multiplicity factors for the tetragonal system. The results for the relative intensities are compared in table (AP-II) with lines on a Debye-Scherrer film of α–$NbPd_3$, on loan from R.M. Waterstrat [6]. The agreement is excellent and could be used for the assignment of reflections should they appear in the patterns to be discussed below.

Giessen et al.[7] have assigned an orthorhombic structure to β–$NbPd_3$ with the space group Pmmn and 24 atoms per unit cell, so it has lower symmetry than the α form. They also report the lattice constants; a = 5.486, b = 4.845, and c = 13.602. The proposed Wyckoff positions of the atoms are given in table (AP-III). Note in this space group sites of general and special symmetry have a degree of arbitrariness in their positions, so that their exact positions depend on the crystal. Their assignment was based on powder patterns from a Debye-Scherrer camera so that the atom positions are only approximate and are given in the column on the right. The simulated powder pattern is presented in table (AP-IV).

$NbPd_2$ is also an orthorhombic crystal of the $MoPt_2$ type with the Immm space group [8] and lattice constants, a = 2.839, b = 8.376, and c = 3.886. The Wyckoff positions are given in table (AP-V) for the six atoms per unit cell. This crystal type requires that y_g be determined from the intensities of the reflections. Giessen et al. [8] determined that the related materials, VNi_2, VPd_2, VPt_2, $NbPt_2$, and $TaPd_2$ had a y_g equal to 0.334, 0.340, 0.341, 0.337, and 0.339, respectively. Thus this parameter seems to be constant among the related compounds so that an estimate of 0.34 would be quite accurate. The resulting synthesized powder pattern is presented in table (AP-VI).

The terminal solid solutions in the Nb-Pd system are extensive; as a result, the lattice constants are expected to change with concentration. Kudielka et al. [9] report that the lattice constant for the fcc palladium solid solution changes from 3.8916 at 1% niobium to 3.9002 at 12.2%. Giessen et al. [10] measured a change from 3.901 at 10% to 3.905 at 18% niobium, and as discussed in chapter 5 they report that the lattice constant for the bcc niobium solid solution

changes from 3.274 at 90% niobium to 3.242 at 25%. The best reported value for the pure metals is 3.3066 and 3.8907 for niobium and palladium respectively. These of course represent small but measureable changes in the powder pattern.

The oxide patterns needed for characterizing the samples in our study were obtained by several methods. In the cases where we had stock materials of the crystal we would measure the pattern directly. Thus NbO, NbO_2, and Nb_2O_5 were measured and compared with the JCPDS [11] reference listings for proper reflection position and intensity. For several of the other oxides patterns were reported in the literature for poly-crystalline samples, such as for $NbO_{2.483}$ [12].

Data for the monoclinic form of $Nb_{12}O_{29}$ was calculated by use of the reported F values from a single crystal [13] which was prepared by [14]. These values were substituted directly in equation (AP-1) to produce the synthesized powder pattern.

Appendix 1 References

[1] W. Bragg, "Introduction to Crystal Analysis",(G. Bell and Sons, Ltd., 1928)

[2] B.D. Cullity, "Elements of X-ray Diffraction",(Addison-Wesley Inc., Reading, MA, 1978)

[3] A.E. Dwight, "Columbium Metallurgy," (Interscience NY), AIME Met. Soc. Conf., 1961, vol.10, p.383-406

[4] W.B. Pearson, "A Handbook of Lattice Spacings and Structures of Metals and Alloys",(Pergamon Press,1967) Vol.2

[5] "International Tables for Crystallography, Vol. A, Space Group Symmetry", ed. L. Hahn, (D. Reudel Co., Boston, 1983)

[6] R.M. Waterstratt, National Bureau of Standards, Washington, DC 20234

[7] B.C. Giessen, N.J. Grant, Acta Cryst. 17(1964) p.615-16

[8] B.C. Giessen, N.J. Grant, J. Less Common Met. 8(1965) p.114- 19

[9] E. Kudielka-Artner, B.B. Argent, Proc. Phys. Soc. Lond., 80(1962)1143

[10] B.C. Giessen et al., Met. Trans. A, 11A(1980) p.709-15

[11] Joint Committee on Powder Diffraction Standards, 1601 Park Lane, Swarthmore, Pennsyvania

[12] R. Gruehn, R. Norin, Z. Anorg. Allg. Chem., 355(1967) p.176- 81

[13] R. Norin, Acta Chem. Scand., 20(1966) p.871-80

[14] R. Gruehn, D. Bergner, H. Schafer, Angew. Chem., 77(1965) p.1082

Table AP-I

Atomic Positions in α–$NbPd_3$

tetragonal, space group I4/mmm (DO_{22})
8 atoms per unit cell, a = 3.895, c = 7.913

body centering translations (0,0,0)+, (1/2,1/2,1/2)+

Nb	2(a)	(0,0,0)
Pd	2(b)	(0,0,1/2)
Pd	4(d)	(0,1/2,1/4),(1/2,0,1/4)

Table AP-II

α–$NbPd_3$ Calculated Powder Pattern

Measured positions obtained from a Debye-Scherrer film provided by R.M. Waterstrat [6] using $Cu(K_\alpha)$.
Sample composition $Nb_{22.5}Pd_{77.5}$; annealed at 900° C

hkl	d(angstroms)	int(%)	$2\theta_{calc}$	$2\theta_{meas}$	int(visual)
101	3.495	1	25.5		
112	2.260	100	39.9	40.1	vst
004	1.978	17	45.9	46.0	w
200	1.948	32	46.6	46.8	m
204	1.388	21	67.5	67.6	st
220	1.377	10	68.1	68.5	m
116	1.189	12	80.8	80.9	w
312	1.176	24	81.9	82.4	m
224	1.130	11	86.0	86.1	m

Table AP-III

Atomic Positions in β–$NbPd_3$

orthorhombic, space group $Pmmn(D_{2h}^{13})$
24 atoms per unit cell, a = 5.486, b = 4.845, c = 13.602
origin choice 2 in reference [5]

Nb	2(a)	$\pm(1/4,y_a,1/4)$		$y_a \approx 0$
Nb	4(e)	$\pm(1/4,y_{e1},z_{e1})$	$\pm(1/4,y_{e1},1/2-z_{e1})$	$y_{e1} \approx 2/3$ $z_{e1} \approx -1/12$
Pd	2(b)	$\pm(1/4,y_b,3/4)$		$b_y \approx 0$
Pd	4(e)	$\pm(1/4,y_{e2},z_{e2})$	$\pm(1/4,y_{e2},1/2-z_{e2})$	$y_{e2} \approx 1/3$ $z_{e2} \approx 1/12$
Pd	4(f)	$\pm(x_f,y_f,1/4)$	$\pm(1/2-x_f,y_f,1/4)$	$x_f \approx 0$ $y_f \approx 1/2$
Pd	8(g)	$\pm(x_g,y_g,z_g)$ $\pm(1/2-x_g,y_g,z_g)$	$\pm(1/2-x_g,y_g,1/2-z_g)$ $\pm(x_g,y_g,1/2-z_g)$	$x_g \approx 0$ $y_g \approx 1/6$ $z_g \approx -1/12$

Table AP-IV

Calculated XRD Pattern of β–$NbPd_3$

a = 5.486, b = 4.845, c = 13.602

hkl	d (angstroms)	I(%)	2θ Cu(K_α)
021	2.3850	18	37.72
022	2.3511	34	38.28
006	2.2670	92	39.76
212	2.2523	91	40.03
023	2.1366	51	42.30
213	2.1122	100	42.81
024	1.9730	30	46.00
214	1.9537	58	46.48
025	1.8092	1	50.44
215	1.7942	16	50.89
027	1.5158	4	61.40
230	1.3917	38	67.28
400	1.3715	18	68.40
041	1.2065	2	79.43
042	1.1925	6	80.55
421	1.1889	4	80.84
422	1.1755	11	81.96
043	1.1702	7	82.41
423	1.1542	14	83.82
044	1.1410	5	85.01
045	1.1065	2	88.33

Table AP-V

Atomic Positions in $NbPd_2$

orthorhombic, space group Immm (D_{2h}^{25})
6 atoms per unit cell, a = 2.839, b = 8.376, c = 3.886

body centering translations (0,0,0)+, (1/2,1/2,1/2)+

Nb	2(a)	(0,0,0)	
Pd	4(g)	$(0,y_g,0)$ $(0,-y_g,0)$	$y_g \approx 0.34$

Table AP-VI

Calculated XRD Pattern of $NbPd_2$

a = 2.839, b = 8.376, c = 3.886

hkl	d (angstroms)	I(%)	2θ Cu(K_α)
011	3.5251	1	25.26
110	2.6888	1	33.32
101	2.2924	100	39.30
031	2.2674	96	39.30
040	2.0940	1	43.20
130	1.9907	65	45.57
002	1.9430	30	46.75
141	1.5461	1	59.82
200	1.4195	11	65.79
060	1.3960	10	67.04
132	1.3904	39	67.34
231	1.2032	24	79.69
161	1.1923	23	80.57
103	1.1785	12	81.71
033	1.1750	11	82.00
202	1.1462	11	84.53
062	1.1337	10	85.69
260	0.9953	8	101.53
004	0.9715	4	105.03

Appendix 2

Computer Programs for the Calculation of XRD Patterns

The following three programs are provided to calculate the X-ray diffraction patterns of α–$NbPd_3$, β–$NbPd_3$, and $NbPd_2$. They are written in C so that they conform to the standard described by Brian W. Kernighan and Dennis M. Ritchie in "The C Programming Language", 1978, Prentice Hall Inc. Englewood Cliffs N.J.

```
#include "math.h"
#include "limits.h"
#include "stdio.h"

#define PI 3.141593 /* what else ! */
#define LAMBBY2 .77092 /* Cu K-alpha/2 */

/* scattering parameters for Nb */
#define NB0 41.510
#define NB1 -52.984
#define NB2 10.605
#define NB3 29.175
#define NB4 -16.454

/* scattering parameters for Pd */
#define PD0 46.497
#define PD1 -55.628
#define PD2 3.467
#define PD3 40.743
#define PD4 -21.262

struct complex {
        double r;
        double i;
        };

/*-----------------------------------------------------------------*/
/*                                                                 */
/*       XRNBPD3A  : Calculation of XRD pattern for alpha-NbPd3    */
/*                                                                 */
/*                  written by Michael Cima 1986                   */
/*                                                                 */
/*-----------------------------------------------------------------*/

main()
{
        double h,k,l,a,c,factr2(),sint,theta;
        double i,j(),cost,cos2t;


        printf("\nlattice parameter_______a = ");
        scanf("%lf",&a);
        printf("%5.3lf",a);

        printf("\nlattice parameter_______c = ");
        scanf("%lf",&c);
        printf("%5.3lf",c);

        for(;;) {

                printf("\n h,k,l = ");
                if(scanf("%lf %lf %lf",&h,&k,&l) != 3)
                        break;

                printf(" %1.0lf %1.0f %1.0f ",h,k,l);

                sint=LAMBBY2*sqrt((h/a)*(h/a)+(k/a)*(k/a)+(l/c)*(l/c));

                if(sint <= 1.0) {
```

```
                        theta=asin(sint);

                        cost=cos(theta);

                        cos2t=cos(2*theta);

                        i=j(h,k,l)*factr2(h,k,l,a,c)*
                                (1+cos2t*cos2t)/(sint*sint*cost)/4;

                        printf("   2theta %6.2lf  intens %10.1lf",
                                360*theta/PI,i);

                        }
                else
                        printf(" out of bounds");

                }
}
double factr2(h,k,l,a,c)
double h,k,l,a,c;
{
        double x,fnb,fpd,pow();
        struct complex f,nb1,pd1,pd2,pd3,pd4,pd5,pd6;

        x=.5*sqrt((h/a)*(h/a)+(k/a)*(k/a)+(l/c)*(l/c));

        fnb=NB0+NB1*x+NB2*pow(x,2.0)+NB3*pow(x,3.0)+NB4*pow(x,4.0);

        fpd=PD0+PD1*x+PD2*pow(x,2.0)+PD3*pow(x,3.0)+PD4*pow(x,4.0);

        cepi(&nb1,h+k+l);

        cepi(&pd1,l);

        cepi(&pd2,h+k);

        cepi(&pd3,k+l/2);

        cepi(&pd4,h+l/2);

        cepi(&pd5,h+1.5*l);

        cepi(&pd6,k+1.5*l);

        f.r = fnb*(1+nb1.r) +
                fpd*(pd1.r+pd2.r) +
                 fpd*(pd3.r+pd4.r+pd5.r+pd6.r);

        f.i = fnb*nb1.i +
                fpd*(pd1.i+pd2.i) +
                 fpd*(pd3.i+pd4.i+pd5.i+pd6.i);

        return((f.r)*(f.r)+(f.i)*(f.i));

}

cepi(p,x)
struct complex *p;
double x;
{
```

```
        x=PI*x;

        p->r=cos(x);

        p->i=sin(x);

}

double j(h,k,l)
double h,k,l;
{

        if( h == 0 && k == 0 )
                return(2);

        if((k == 0 && l == 0) || (h == 0 && l ==0))
                return(4);

        if( h == k && l == 0 )
                return(4);

        if( h != k && l == 0 )
                return(8);

        if((k == 0 && h != l) || (h == 0 && k != l))
                return(8);

        if( h == k && l != 0)
                return(8);

        return(16);

}
```

```
#include "math.h"
#include "limits.h"
#include "stdio.h"

#define PI 3.141593 /* what else ! */
#define LAMBBY2 .77092 /* Cu K-alpha/2 */

/* scattering parameters for Nb */
#define NB0 41.510
#define NB1 -52.984
#define NB2 10.605
#define NB3 29.175
#define NB4 -16.454

/* scattering parameters for Pd */
#define PD0 46.497
#define PD1 -55.628
#define PD2 3.467
#define PD3 40.743
#define PD4 -21.262

struct complex {
        double r;
        double i;
        };

/*-----------------------------------------------------------------------*/
/*                                                                       */
/*          XRNBPD2   : Calculation of the XRD pattern for NbPd2         */
/*                                                                       */
/*                 written by Michael Cima 1986                          */
/*                                                                       */
/*-----------------------------------------------------------------------*/


main()
{
        double h,k,l,a,b,c,y,factr2(),sint,theta;
        double i,j(),cost,cos2t;


        printf("\nlattice parameter_______a = ");
        scanf("%lf",&a);
        printf("%5.3lf",a);

        printf("\nlattice parameter--------b = ");
        scanf("%lf",&b);
        printf("%5.3lf",b);

        printf("\nlattice parameter_______c = ");
        scanf("%lf",&c);
        printf("%5.3lf",c);

        printf("\ny = ");
        scanf("%lf",&y);
        printf("%5.3lf",y);

        for(;;) {

                printf("\n h,k,l = ");
```

```
                if(scanf("%lf %lf %lf",&h,&k,&l) != 3)
                        break;

                printf(" %1.0lf %1.0f %1.0f ",h,k,l);

                sint=LAMBBY2*sqrt((h/a)*(h/a)+(k/b)*(k/b)+(l/c)*(l/c));

                if(sint <= 1.0) {

                        theta=asin(sint);

                        cost=cos(theta);

                        cos2t=cos(2*theta);

                        i=j(h,k,l)*factr2(h,k,l,a,b,c,y)
                                *(1+cos2t*cos2t)/(sint*sint*cost)/4;

                        printf("   2theta %6.2lf  intens %10.1lf",
                                360*theta/PI,i);

                        }
                else
                        printf(" out of bounds");

                }
}
/*-----------------------------------------------------------------------*/
double factr2(h,k,l,a,b,c,y)
double h,k,l,a,b,c,y;
{
        double x,fnb,fpd,pow();
        struct complex f;
        struct complex nb2,pd1,pd2,pd3,pd4;

        x=.5*sqrt((h/a)*(h/a)+(k/b)*(k/b)+(l/c)*(l/c));

        fnb=NB0+NB1*x+NB2*pow(x,2.0)+NB3*pow(x,3.0)+NB4*pow(x,4.0);

        fpd=PD0+PD1*x+PD2*pow(x,2.0)+PD3*pow(x,3.0)+PD4*pow(x,4.0);

        cepi(&nb2,h+k+l);

        cepi(&pd1,2*y*k);

        cepi(&pd2,-2*y*k);

        cepi(&pd3,h+(1+2*y)*k+l);

        cepi(&pd4,h+(1-2*y)*k+l);

        f.r = fnb*(1+nb2.r) +
                fpd*(pd1.r+pd2.r+pd3.r+pd4.r);

        f.i = fpd*(pd1.i+pd2.i+pd3.i+pd4.i);

        return((f.r)*(f.r)+(f.i)*(f.i));

}
/*-----------------------------------------------------------------------*/
```

```
cepi(p,x)
struct complex *p;
double x;
{
        x=PI*x;

        p->r=cos(x);

        p->i=sin(x);

}
/*-----------------------------------------------------------------------*/
double j(h,k,l)
double h,k,l;
{

        if( h == 0 && k == 0 )
                return(2);

        if((h == 0 && l == 0) || (k == 0 && l ==0))
                return(2);

        if( h == 0 || k == 0 || l == 0 )
                return(4);

        return(8);

}
/*-----------------------------------------------------------------------*/
```

```
#include "math.h"
#include "limits.h"
#include "stdio.h"

#define PI 3.141593 /* what else ! */
#define LAMBBY2 .77092 /* Cu K-alpha/2 */

/* scattering parameters for Nb */
#define NB0 41.510
#define NB1 -52.984
#define NB2 10.605
#define NB3 29.175
#define NB4 -16.454

/* scattering parameters for Pd */
#define PD0 46.497
#define PD1 -55.628
#define PD2 3.467
#define PD3 40.743
#define PD4 -21.262

struct complex {
        double r;
        double i;
        };

/*-----------------------------------------------------------------------*/
/*                                                                       */
/*     XRNBPD3B   : Calculation of the XRD pattern for beta-NbPd3        */
/*                                                                       */
/*                  written by Michael Cima 1986                         */
/*                                                                       */
/*-----------------------------------------------------------------------*/

main()
{
        double h,k,l,a,b,c,factr2(),sint,theta;
        double ay,e1y,e1z,by,e2y,e2z,fx,fy,gx,gy,gz;
        double i,j(),cost,cos2t;


        printf("\nlattice parameter_______a = ");
        scanf("%lf",&a);
        printf("%5.3lf",a);

        printf("\nlattice parameter--------b = ");
        scanf("%lf",&b);
        printf("%5.3lf",b);

        printf("\nlattice parameter_______c = ");
        scanf("%lf",&c);
        printf("%5.3lf",c);

        printf("\nay = ");
        scanf("%lf",&ay);
        printf("%5.3lf",ay);

        printf("\ne1y = ");
        scanf("%lf",&e1y);
        printf("%5.3lf",e1y);
```

```
printf("\ne1z = ");
scanf("%lf",&e1z);
printf("%5.3lf",e1z);

printf("\nby = ");
scanf("%lf",&by);
printf("%5.3lf",by);

printf("\ne2y = ");
scanf("%lf",&e2y);
printf("%5.3lf",e2y);

printf("\ne2z = ");
scanf("%lf",&e2z);
printf("%5.3lf",e2z);

printf("\nfx = ");
scanf("%lf",&fx);
printf("%5.3lf",fx);

printf("\nfy = ");
scanf("%lf",&fy);
printf("%5.3lf",fy);

printf("\ngx = ");
scanf("%lf",&gx);
printf("%5.3lf",gx);

printf("\ngy = ");
scanf("%lf",&gy);
printf("%5.3lf",gy);

printf("\ngz = ");
scanf("%lf",&gz);
printf("%5.3lf",gz);

for(;;) {

        printf("\n h,k,l = ");
        if(scanf("%lf %lf %lf",&h,&k,&l) != 3)
                break;

        printf(" %1.0lf %1.0f %1.0f ",h,k,l);

        sint=LAMBBY2*sqrt((h/a)*(h/a)+(k/b)*(k/b)+(l/c)*(l/c));

        if(sint <= 1.0) {

                theta=asin(sint);

                cost=cos(theta);

                cos2t=cos(2*theta);

                i=j(h,k,l)*factr2(h,k,l,a,b,c,ay,e1y,e1z,
                        by,e2y,e2z,fx,fy,gx,gy,gz)
                        *(1+cos2t*cos2t)/(sint*sint*cost)/4;

                printf("   2theta %6.2lf  intens %10.1lf",
```

```
                                360*theta/PI,i);

                        }
                else
                        printf(" out of bounds");

                }
}
/*-----------------------------------------------------------------------*/
double factr2(h,k,l,a,b,c,ay,e1y,e1z,by,e2y,e2z,fx,fy,gx,gy,gz)
double h,k,l,a,b,c,ay,e1y,e1z,by,e2y,e2z,fx,fy,gx,gy,gz;
{
        double x,fnb,fpd,pow();
        struct complex f;
        struct complex nb_a1,nb_a2,nb_e1,nb_e2,nb_e3,nb_e4;
        struct complex pd_b1,pd_b2,pd_f1,pd_f2,pd_f3,pd_f4;
        struct complex pd_e1,pd_e2,pd_e3,pd_e4;
        struct complex pd_g1,pd_g2,pd_g3,pd_g4,pd_g5,pd_g6;
        struct complex pd_g7,pd_g8;

        x=.5*sqrt((h/a)*(h/a)+(k/b)*(k/b)+(l/c)*(l/c));

        fnb=NB0+NB1*x+NB2*pow(x,2.0)+NB3*pow(x,3.0)+NB4*pow(x,4.0);

        fpd=PD0+PD1*x+PD2*pow(x,2.0)+PD3*pow(x,3.0)+PD4*pow(x,4.0);

        cepi(&nb_a1,h,k,l,    0.25,    ay,     0.25);
        cepi(&nb_a2,h,k,l,   -0.25,   -ay,    -0.25);

        cepi(&nb_e1,h,k,l,   0.25,      e1y,    e1z);
        cepi(&nb_e2,h,k,l,   0.25,      e1y, 0.5-e1z);
        cepi(&nb_e3,h,k,l,  -0.25,     -e1y,   -e1z);
        cepi(&nb_e4,h,k,l,  -0.25,     -e1y, -0.5+e1z);

        cepi(&pd_b1,h,k,l,   0.25,      by,    0.75);
        cepi(&pd_b2,h,k,l,  -0.25,     -by,   -0.75);

        cepi(&pd_e1,h,k,l,   0.25,      e2y,    e2z);
        cepi(&pd_e2,h,k,l,   0.25,      e2y, 0.5-e2z);
        cepi(&pd_e3,h,k,l,  -0.25,     -e2y,   -e2z);
        cepi(&pd_e4,h,k,l,  -0.25,     -e2y, -0.5+e2z);

        cepi(&pd_f1,h,k,l,    fx,       fy,     0.25);
        cepi(&pd_f2,h,k,l, 0.5-fx,      fy,     0.25);
        cepi(&pd_f3,h,k,l,   -fx,      -fy,    -0.25);
        cepi(&pd_f4,h,k,l, -0.5+fx,    -fy,    -0.25);

        cepi(&pd_g1,h,k,l,      gx,     gy,     gz);
        cepi(&pd_g2,h,k,l,  0.5-gx,     gy, 0.5-gz);
        cepi(&pd_g3,h,k,l,  0.5-gx,     gy,     gz);
        cepi(&pd_g4,h,k,l,      gx,     gy, 0.5-gz);
        cepi(&pd_g5,h,k,l,     -gx,    -gy,    -gz);
        cepi(&pd_g6,h,k,l,  -0.5+gx,   -gy, -0.5+gz);
        cepi(&pd_g7,h,k,l,  -0.5+gx,   -gy,    -gz);
        cepi(&pd_g8,h,k,l,     -gx,    -gy, -0.5+gz);


        f.r = fnb*(nb_a1.r + nb_a2.r + nb_e1.r + nb_e2.r +
                                nb_e3.r + nb_e4.r ) +
                fpd*(pd_b1.r + pd_b2.r + pd_f1.r + pd_f2.r +
```

```
                        pd_f3.r + pd_f4.r +
                        pd_e1.r + pd_e2.r +
                        pd_e3.r + pd_e4.r +
                        pd_g1.r + pd_g2.r +
                        pd_g3.r + pd_g4.r +
                        pd_g5.r + pd_g6.r +
                        pd_g7.r + pd_g8.r );

        f.i = fnb*(nb_a1.i + nb_a2.i + nb_e1.i + nb_e2.i +
                                nb_e3.i + nb_e4.i ) +
                fpd*(pd_b1.i + pd_b2.i + pd_f1.i + pd_f2.i +
                        pd_f3.i + pd_f4.i +
                        pd_e1.i + pd_e2.i +
                        pd_e3.i + pd_e4.i +
                        pd_g1.i + pd_g2.i +
                        pd_g3.i + pd_g4.i +
                        pd_g5.i + pd_g6.i +
                        pd_g7.i + pd_g8.i );

        return((f.r)*(f.r)+(f.i)*(f.i));

}
/*-----------------------------------------------------------------------*/
cepi(p,h,k,l,x,y,z)
struct complex *p;
double h,k,l,x,y,z;
{
        double arg;

        arg=2*PI*(h*x+k*y+l*z);

        p->r=cos(arg);

        p->i=sin(arg);

}
/*-----------------------------------------------------------------------*/
double j(h,k,l)
double h,k,l;
{

        if( h == 0 && k == 0 )
                return(2);

        if((h == 0 && l == 0) || (k == 0 && l ==0))
                return(2);

        if( h == 0 || k == 0 || l == 0 )
                return(4);

        return(8);

}
/*-----------------------------------------------------------------------*/
```

This report was done with support from the Department of Energy. Any conclusions or opinions expressed in this report represent solely those of the author(s) and not necessarily those of The Regents of the University of California, the Lawrence Berkeley Laboratory or the Department of Energy.

Reference to a company or product name does not imply approval or recommendation of the product by the University of California or the U.S. Department of Energy to the exclusion of others that may be suitable.

LAWRENCE BERKELEY LABORATORY
TECHNICAL INFORMATION DEPARTMENT
UNIVERSITY OF CALIFORNIA
BERKELEY, CALIFORNIA 94720